AUTOMATIC FAULT LOCATION SYSTEM FOR LOW VOLTAGE UNDERGROUND DISTRIBUTION NETWORKS

A DISSERTATION SUBMITTED
TO THE DEPARTMENT OF ELECTRONIC AND ELECTRICAL ENGINEERING
AND THE COMMITTEE FOR POSTGRADUATE STUDIES
OF THE UNIVERSITY OF STRATHCLYDE
IN PARTIAL FULFILLMENT OF THE REQUIREMENTS
FOR THE DEGREE OF
DOCTOR OF PHILOSOPHY

By

Senthivadivelu Navaneethan

December 2003

Declaration

I declare that this Thesis embodies my own research work and that it was composed by myself. Where appropriate, I have made acknowledgements to the work of others.

Senthivadivelu Navaneethan

Acknowledgements

I would like to thank my supervisors John J. Soraghan and W.H. Siew for their constant support and guidance throughout the course of this research. I would also like to thank Professor Tariq Durrani for his support.

I am grateful to ScottishPower plc for their sponsorship and to Hathaway Systems Ltd for their support for this research work.

Special thanks goes to Phil Gale and Barry Clegg from Hathaway Systems Ltd and to Fraser McPherson and Jim Livie from ScottishPower plc for their support and encouragement which proved invaluable to me.

I am truly grateful to all the past and present friends I made during my Ph.D studies in the Signal Processing Division. They supplied a friendly environment which offered a wide spectrum of technical discussion, interaction, and fun, for which I wish to thank them all.

To all my family back home and here, especially my Mother and Father, I wish to extend my utmost thanks for their love and continuous support and encouragement.

Finally, I offer my eternal thanks to my wife Saroja and my son Brendan. Without my wife huge support and sacrifices, this Ph.D would not have been possible. She has been my greatest source of encouragement and above all companionship.

Abstract

This thesis presents a novel approach to automating Time Domain Reflectrometry (TDR) waveform acquisition and automatic TDR based fault location in Low Voltage (450-1000V) Underground Distribution Networks (LVUDNs). First, the types of faults that occur in LVUDN and previously available fault location techniques are discussed and their relative advantages and limitations described. Adaptive Filter theory, Wavelet Transform Theory and Fuzzy Logic are presented.

Software is developed to automate: checking of the test lead connections, adjusting the internal balance network to match the cable surge impedance, blown fuse detection and backfeed identification, auto recording and storage of data, and voltage and current triggering for transient faults. Software is also developed for both direct and remote control of the instrument via a standard telephone line, GSM modem or direct serial link.

Adaptive and fuzzy based, and wavelet based automatic fault location systems are developed. Both systems pre-process the TDR waveforms by using a simple thresholding technique to identify single phase tees and to locate three phase faults. The adaptive and fuzzy based system uses an adaptive filter to produce a composite waveform from the healthy and faulty TDR waveforms and the fault distance is calculated using the composite waveform. If the result produces more than one possible fault distance either from the TDR waveforms or the error waveforms, the system uses fuzzy reasoning to find a common fault distance. In the wavelet based fault location process the TDR waveforms are split into four multi-scales before applying the adaptive filtering and calculating the fault distance using a selected scale. To improve the accuracy of fault distance calculation, local mean and gradient techniques are used in the adaptive and fuzzy based fault location system and latter technique is used in the wavelet enhanced fault location system. The performances of both systems were tested using data from a cable model and from real LVUDNs and gave an accuracy of ±4.3m of the actual fault distance.

Acronyms

AF	Audio Frequency
BN	Blue Neutral
C & C	Compare and Contrast
CWT	Continuous Wavelet Transform
DC	Direct Current
DWT	Discrete Wavelet Transform
EMTP	Electromagnetic Transient Program
HIF	High Impedance Fault
HV	High Voltage
LIF	Low Impedance Fault
LMS	Least Mean Square
LV	Low Voltage
LVUDN	Low Voltage Underground Distribution Networks
m	Metre
MSE	Mean Squared Error
MV	Medium Voltage
N	Neutral
NLMS	Normalised Least Mean Square
PE	Polyethylene
RB	Red Blue
RN	Red Neutral
RY	Red Yellow
RLS	Recursive Least Square
SCADA	Supervisory Control And Data Acquisition
SG	Surge Generator
S/Stn	Substation
STFT	Short Time Fourier Transform
TDR	Time Domain Reflectometry
TDL	Tapped Delay Line
WT	Wavelet Transform
YB	Yellow Blue

YN	Yellow Neutral

Contents

List of Tables

List of Figures

Chapter 1

1. Introduction

1.1. Introduction

This thesis is concerned with the practical problems of Time Domain Reflectometry (TDR) based fault location in Low Voltage Underground Distribution Networks (LVUDN), including data acquisition, interpretation of the TDR waveforms, and presents methods for automating the data analysis.

The sophisticated standards of living enjoyed today by people are dependent on a reliable uninterrupted supply of electricity. A perfect uninterrupted supply of electricity is not possible due to many acts of nature playing upon the transmission and distribution networks used for the supply of electricity. Outages occur more often under stormy weather conditions for overhead lines. Outages in LVUDN are often due to aging of the cables and accidental damage.

Transmission networks (22KV/33KV) that consist of high voltage lines are well managed with SCADA (Supervisory Control And Data Acquisition) systems [45]. The transmission network monitoring, control and operation of the entire network is carried out remotely from a centrally located control centre. Several methods, which use information from relays and breakers, have been proposed for location of outages in transmission systems [47-53]. Distribution networks on the other hand are not so well managed, mainly due to economic reasons and technological problems, which causes problems to the distribution engineers in monitoring, operation and control. Therefore an enormous amount of time is to spent attending to outages in distribution systems. However, some methods have been presented for location of outages in Medium Voltage (MV) distribution networks (615V/11KV): [45] is based on fuzzy set theory, [64] uses information from specially designed optical sensors located in the system, [75] is also based on information from specially designed sensors and uses a knowledge-based approach for outage location, [76, 77] use telephone calls from the customers experiencing outages for fault location, and [44] uses a statistical hypothesis based on using customer outage times. For Low Voltage (LV) distribution

networks (450V), not many methods are available due to a number of factors. They are: LV networks consist of a much higher number of tees, limited access points for testing, a large number of devices are required for monitoring that would be costly, customer loads are connected to cables all the time, and on-line fault location is required to minimise customer outage.

TDR is one of the most common methods used for locating faults on Underground cables and transmission lines [46, 57-63, 65]. TDR based fault location techniques have been developed and successfully applied to transmission and distribution network systems [46, 55, 58-62, 65]. The TDR waveforms that are obtained from transmission and distribution networks except LVUDN cables are easy to interpret. This is because they do not have many tees and customer loads whereas LVUDNs have multiple 3-phase and single-phase (service cable) tees, joints, and customer loads. Therefore, the TDR waveforms from LVUDNs are much more complicated than those obtained from high and medium voltage underground cables, and overhead lines.

TDR based fault location instruments that are currently commercially available for LVUDN fault location have two main problems: good TDR waveform acquisition, and interpretation of the TDR waveforms. TDR waveforms acquisition using the current commercial instruments have the following problems:

- Requirement of user interaction to acquire TDR waveforms and the lack of a facility to store data. Data storage facility is very important for transient faults. If TDR waveforms are not acquired just before the fault or just after the fault (i.e non-fault condition) and during the fault arc then fault location may not be possible for transient faults.
- Safeguard against user mistakes. At present commercial instruments do not have safeguards to check whether test leads are connected properly.
- If two phases become welded together then one of the phase fuses will blow and the other phase involved will feed the power (backfeed) the phase with the fuse blown. The existence of a backfeed will not be known unless a 3-phase customer reports the fault or a test lamp check is performed at the substation.
- Balancing is done manually. Manual balancing is required by the user to match the cable impedance and to compensate for the test leads.

- Do not have a facility to check whether fuses are blown or not. At present the test lamp is used.
- If the bus bar is connected to more than one cable then to record good reflected TDR waveforms fuses need to be removed or a blocking inductor is required to stop the pulses traveling to other cables so that most of the pulse energy will go into the test cable. To connect a blocking inductor the fuse needs to be removed. If there were a backfeed then one of the fuses would have blown. Therefore, good TDR waveforms can be recorded related to that phase.
- Currently available commercial TDR instruments employ an approach called compare and contrast, where the difference between the healthy TDR waveform and the fault TDR waveform is displayed or the healthy and fault waveforms are superimposed to identify the fault departure (split). An experienced engineer will usually use the compare and contrast result to find the fault location. Due to multiple tees and joints in LVUDN, the pulse launched into the cable reflects wherever mismatches are present, the cables have attenuation and dispersion characteristics, and together with noise this makes the TDR waveforms complicated. Ideally, the TDR waveforms from a cable are expected to be identical up to the fault. This is not true for a real LVUDN. Due to single phase tees, noise, impedance differences between phases, and attenuation and dispersion of pulses due to cable characteristics. Therefore, the TDR waveforms will have amplitude variations.

In this thesis, the above problems are addressed by automating most of the features to minimise the user interaction and to safeguard against the user making mistakes.

Due to changing staff working practice and low tariff charges to maintain a competitive edge, an automatic fault locator is required so that anyone can operate the instrument. In this thesis, two automatic fault location systems are developed that use the concept of similarity between the TDR waveforms.

1.2. Motivation for the Research

The motivation for the research is the problem of TDR based fault location in LVUDN.

(i) Instrumentation: At present most of the TDR waveform acquisition procedures, such as balancing, recording and storing TDR waveforms, and fuse blown checks are carried out manually.

(ii) Deskilling: Acquisition of good TDR waveforms is a crucial step in TDR based fault location. Current commercial instruments do not safeguard against the user making a mistake, such as with the test leads connection.

(iii) An experienced engineer is required for interpretation of TDR waveforms.

(iv) The application of Adaptive filtering, Fuzzy membership, and Wavelet Transform to these challenging problems have not been effectively considered to date.

In this thesis, the above motivations of automatic TDR waveform acquisition and fault location for LVUDN are addressed. Adaptive filtering is considered to exploit the similarity between the TDR waveforms from the same cable network up to the fault point except where single-phase tees are present. Fuzzy membership is considered to calculate fault distance where there is more than one fault distance. Wavelet Transform is used to decompose the TDR waveforms into multi scales, so those waveforms can be analysed using individual scales that will have certain frequency components only.

1.3. Organisation of Thesis

The organisation of the thesis as follows:

Chapter 2

In Chapter 2, the types of faults that exist in LVUDN and the currently available fault techniques are reviewed. Four types of faults are classified: transitory, intermittent, persistent, and permanent. Followed by, the fault location techniques that are currently available for fault location in LVUDN and non-LVUDN. The LVUDN fault location techniques reviewed in this chapter are based on TDR, audio frequency, transient gradient, and Resistance Bridge. The non-LVUDN techniques reviewed are based on application of waveform processing techniques either to improve the existing fault location methods or to provide new fault location techniques.

Chapter 3

Chapter 3 reviews the basic waveform processing techniques that form the preliminary platform for the subsequent research. These include the concept of Adaptive Filter theory, Wavelet Transform (WT) theory, and Fuzzy Set theory. The adaptive filtering theory includes Least Mean Square (LMS), Normalised-LMS (NLMS), and Recursive Least Square (RLS) that allows comparing two TDR waveforms to produce a composite waveform in chapter 5. The Wavelet transform section covers Short Time Fourier Transform (STFT), Continuous WT (CWT), and Discrete WT (DWT), which is the engine for multi scale waveform analysis in Chapter 6.

Chapter 4

Chapter 4 presents an automatic TDR waveform acquisition system, which minimises user interaction and safeguards against user mistakes. This chapter presents an auto test lead connection check, auto balancing, auto fuse blown and backfeed supply check, auto recording and storage of data, auto voltage and current triggering, and auto re-arming. The test leads connection check is to safeguard against a user mistake in connecting the test leads. The auto balancing is to match the cable under test and to compensate for the test leads. The auto fuse(s) blown and backfeed check is to select appropriate TDR waveforms to record. The auto recording and storage of TDR waveforms are based on which fuses are blown and which phases have a backfeed supply. If the instrument is armed for a transient fault trigger then it automatically triggers from either a voltage disturbance or from a fault current. Finally, if the instrument is set for transient fault trigger then it automatically re-arms after a transient fault trigger. Some of the above features are demonstrated using cable model examples. Some real LVUDN data that were recorded by new prototype P2000 (TDR instrument) are also presented.

Chapter 5

Chapter 2 demonstrated the requirement of an automatic fault location system for LVUDN. TDR based fault location is one of the most commonly used fault location techniques in LVUDN.

In this chapter, an automatic adaptive and fuzzy based fault location system for LVUDN using TDR waveforms is presented. This automated system pre-processes

the TDR waveforms to identify single-phase tees and to locate 3-phase faults. Followed the pre-processing, if no 3-phase fault is located, then TDR waveforms are processed in pairs with an adaptive filter that will yield an error waveform as its output. The error waveforms from the adaptive filter are analysed to find the departure that is related to the fault. Due to more than one TDR waveform being used during the fault location process, it is possible to have more than one fault location. If more than one fault location is found then Fuzzy membership is applied to the fault locations to find a common fault location. Finally, fault distance is calculated from the common fault location.

The performance of the automatic fault location system is demonstrated using field and cable model data.

Chapter 6

In this chapter, an automatic WT based fault location system, gradient based fault distance calculation, and local mean based fault distance calculation are presented. As described in Chapter 3, the WT can be used to extract multi scale decomposition of a waveform and then to reconstruct the original waveform from the decomposed multi scale waveforms.

Decomposing a waveform into multi scales allows it to be processed in individual scales. As mentioned in Chapter 2, the power cable has dispersion and attenuation characteristics and therefore different frequency components travel at different velocities of propagation [46, 65, 66]. Waveform analysis into individual scales will therefore minimise the effects of dispersion and attenuation. WT based automatic fault location uses this to advantage, by decomposing the waveform into multi scales and then applying adaptive filtering to the waveform at each scale.

An alternative to zero (Distance-axis) crossing point based fault distance calculation is also presented in this chapter to improve the accuracy of the fault distance calculation.

Chapter 7

Finally, Chapter 7 concludes with a summary of the contributions that are presented in this thesis. There is also a discussion of extensions and possible future research directions which may be undertaken within fault location in power cables using TDR waveforms and other means of fault location using data from the P2000.

1.4. Summary of Original Contributions

The research described in this thesis includes original contributions to the fields of automatic TDR waveform acquisition and fault location in LVUDN.

These contributions are as follows:

(i) To automate TDR waveform acquisition, software is developed. The automation facility includes auto check on test leads connection, auto balancing, auto fuse blown and backfeed power supply detection, auto recording and storage of TDR waveforms, and auto trigger and auto re-arm for transient faults either from a voltage disturbance or from fault current.

(ii) An automatic adaptive and fuzzy based fault location algorithm for LVUDN using TDR waveforms is developed. The adaptive filtering is used to produce a difference waveform between a pair of TDR waveforms, which will have significant difference at the fault point. Fuzzy membership is used to find the fault distance when there are more than one-fault distances.

(iii) An automatic Wavelet Transform (WT) enhanced fault location system has been developed. This system uses WT to extract waveforms in multi scales and uses the lowpass scale 4 error waveform to find the fault distance. The error waveform is analysed in the same way as the adaptive and fuzzy based fault location system.

(iv) To improve the zero-crossing based fault distance calculation, a gradient based fault distance calculation has been developed for the both methods of fault location systems and a local mean based fault distance calculation has been developed for adaptive and fuzzy based fault location system.

Chapter 2

2. Classification of LV Faults, and Fault Location Techniques

2.1. Introduction

Fault location on multi-branched and loaded Low Voltage (LV) systems is complex and pre-location is never easy and often impossible. This is due to a number of reasons, some of which are listed below:

- LV Cable network is loaded
- Multiple tees (3-phase and single phase)
- Live line fault location required to avoid customer power outage
- Test access points are limited
- Voltage restriction for test equipment

In Underground Low Voltage Distribution Networks (LVUDN) there are four types of fault: transitory, intermittent, persistent and permanent. These are discussed in detail in section 2.2. In section 2.3, LVUDN, and non-LVUDN fault location techniques are reviewed. Each of the location techniques that are discussed in section 2.3 is intended for the location of particular types of fault. In section 2.4, conclusions to this chapter are drawn.

2.2. Classification of Faults

Faults that can exist in LVUDN may be classified into four types: transitory, intermittent, persistent, and permanent. Normally, a fault in LVUDN starts as a transitory fault and then becomes intermittent. The intermittent fault then becomes persistent and finally the persistent fault becomes permanent [46].

Transitory faults do not cause significant service disruption, except for possible voltage fluctuations. No fuse ruptures due to a transitory fault. Typical voltage and current waveforms for a transitory fault are shown in Fig.2.1. The waveforms clearly

show how the voltage recovers quickly after a transitory fault while the current increases only during the fault arcing process. Therefore, the current drawn by a transitory fault does not flow long enough to cause a fuse to rupture. The arcing due to a transitory fault is not stable or repeatable but the arcing process will eventually draw current on enough successive half cycles that will blow a fuse. This condition of a fault is defined as intermittent. If the fuse is replaced, it often does not immediately blow but may take weeks or months before it ruptures again. Normally the duration between fuse operations diminishes with time. Typical voltage and current waveforms for an intermittent fault are shown in Fig. 2.2. The voltage waveform in Fig.2.2a shows voltage reduction due to an intermittent fault. The current waveform in Fig.2.2b shows the current drawn due to an intermittent fault. The arcing process due to an intermittent fault continues for several successive cycles as shown in Fig.2.2. and therefore results in operation of the fuse. If, on replacing the fuse, it ruptures immediately or very soon afterwards the fault is defined as persistent.

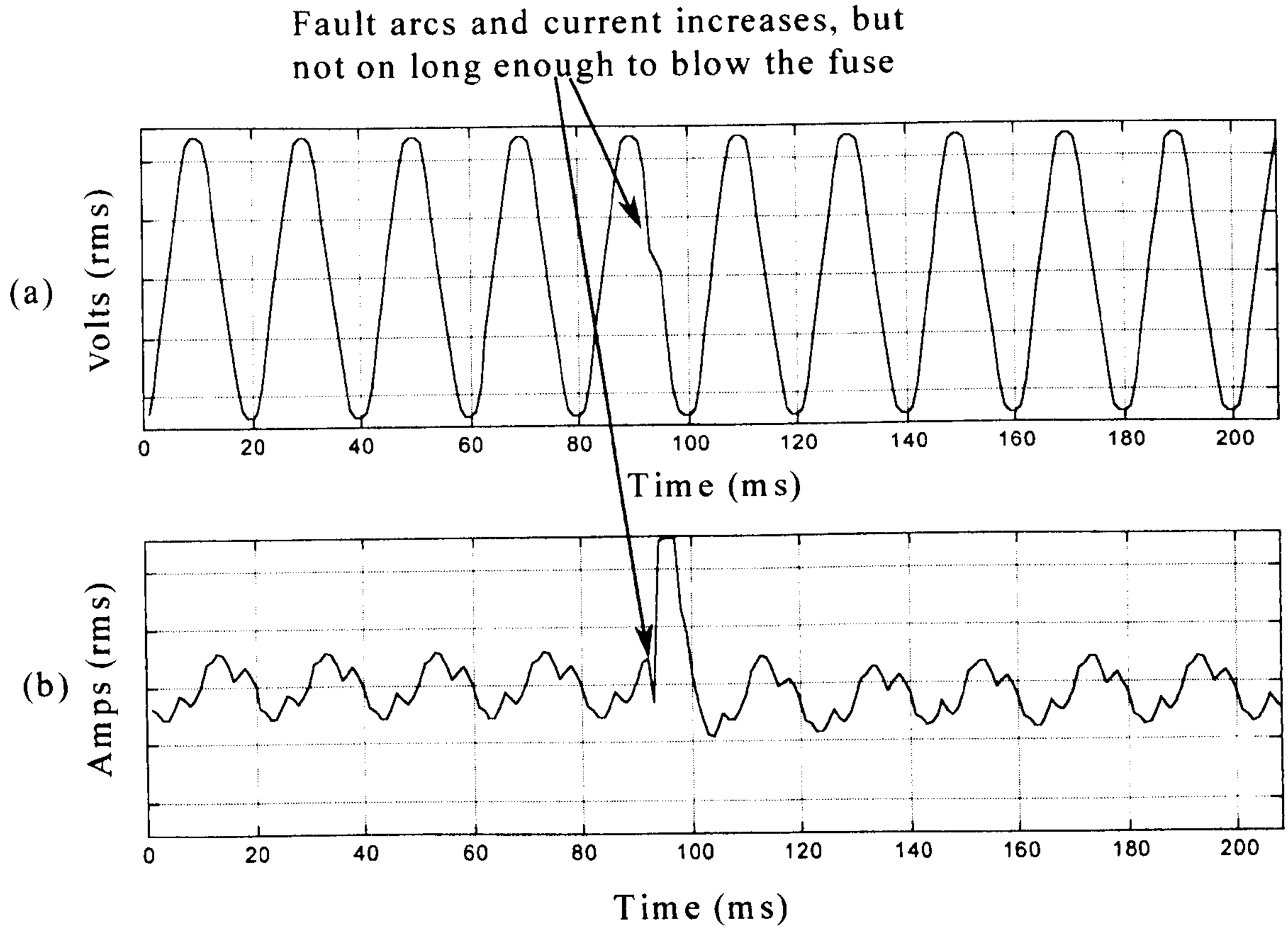

Figure 2.1: Transitory fault waveforms (a) Voltage, (b) Current

All of the above types of fault have a non-linear characteristic due to the underlying arcing process [46]. Eventually a persistent fault becomes a permanent fault when the arcing process becomes a metallic contact, i.e. the fault path is permanently in a state of low resistance which causes a sustained fault current, which is high enough to rupture the fuse. The fault path may be a massive carbon deposit exhibiting a very low resistance or a metal-to-metal weld (Short circuit fault). If two or more conductors are permanently in contact (welded together) then it is called a short circuit fault. If one or more conductors are broken then it is called an open circuit fault. Typical values of resistance between the break and adjacent metal are very high or infinite for this type of fault.

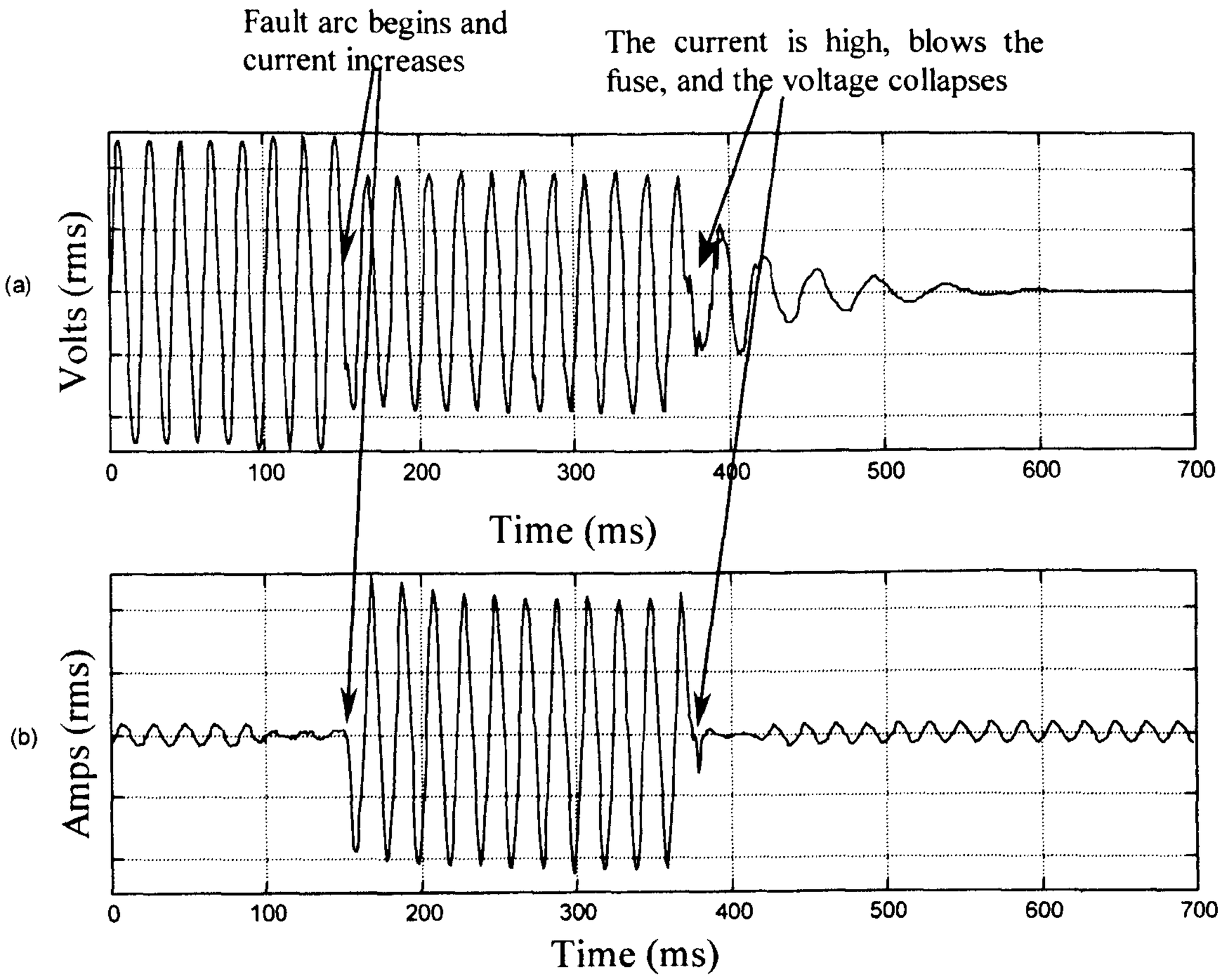

Figure 2.2: Intermittent fault waveforms (a) Voltage, (b) Current

2.3. Fault Location Techniques

An overview of fault location techniques is illustrated in Fig. 2.3. Fault location techniques can be divided into two main parts: LVUDN and non-LVUDN. Detailed explanations of these are described in the following sections.

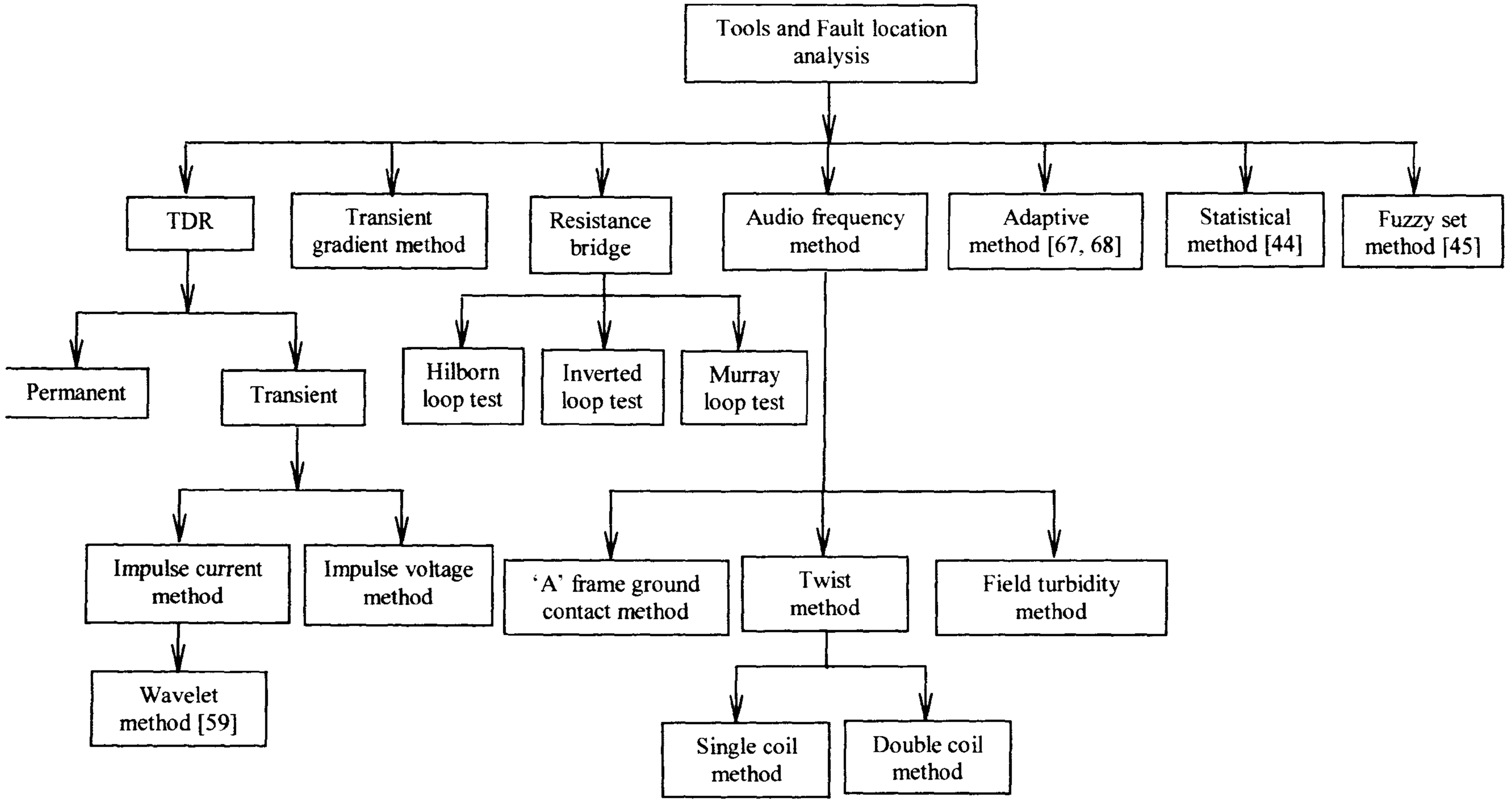

Figure 2.3: An overview of fault location techniques

2.3.1. Transient Gradient Method

The transient gradient method has been used for fault location in power cables for many years [46]. The process of this fault location technique is as follows: Initially, voltage readings are taken at several access points on the LVUDN. These access points can be the substation, feeder pillars, and customer meter points. To find a fault at least two voltage readings before the fault and one voltage reading after the fault are required. The voltage readings are then plotted on a graph against the distance where the voltage readings were taken, as shown in Fig. 2.4. The voltage readings before the fault will gradually reduce as shown in Fig. 2.4. The voltage reading beyond the fault is low and constant as shown in Fig.2.4 and depends on the fault arc voltage (*If the reference conductor beyond the fault is carrying some of the return current then the voltage beyond the fault will rise slightly)*. There will be two lines: one is the *gradient to fault* line (as shown Fig. 2.4) which will represent the voltage readings before the fault and the other one is the *beyond the fault* line (as shown in Fig. 2.4) that is represents the voltage reading(s) beyond the fault. The intersection point of the *gradient to* fault line and *beyond the fault line* will give the approximate distance of the fault.

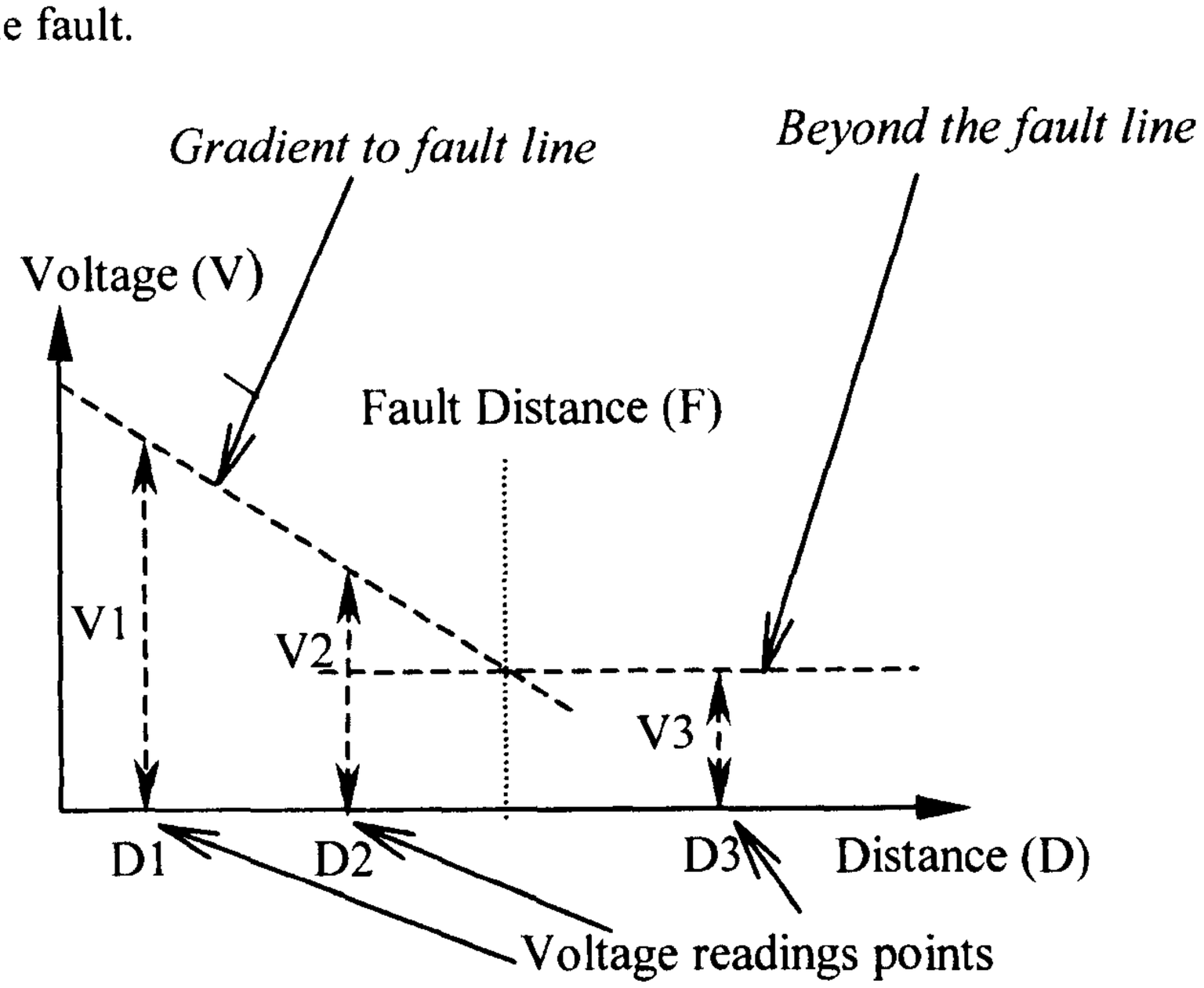

Figure 2.4: Typical gradient test

For example, consider a part of the real LVUDN network shown in Fig. 2.5. It has a fault between pot end (branch end) A and B. To apply the transient gradient method to locate the fault voltage readings need to be taken at the substation X, pot end A,

and pot end B. These voltage readings are then plotted as described for Fig 2.4. A line is drawn between the voltage readings of the substation X and pot end A will give the *gradient to the fault line*. Similarly, a horizontal line that is parallel to the Distance-axis at the voltage read at pot end B will give the *beyond the fault line*. The intersection point, between these lines will give the fault distance.

The disadvantage with the voltage gradient method is that loads are permanently connected, access points are few, and they are not always suitably spaced, and most of the LV faults are transitory [45]. If the faults are transitory then, voltage readings have to be taken by several measuring devices spread along the cable *when the fault arcs over*. This method can only be used successfully, if the reference conductor is not carrying return current. Otherwise, the voltage after the fault can rise slightly and may mislead the intersection point. If the fault is a phase to neutral fault then voltage readings between that the faulty phase and neutral are required. However, if the fault is between two phases then voltage readings need to be taken between the two faulty phases. The transient fault can be either phase to neutral or phase-to-phase. Therefore, 3-phase voltage measurement is desirable. When drawing the graph the voltage readings need to be plotted against the distances in the right order.

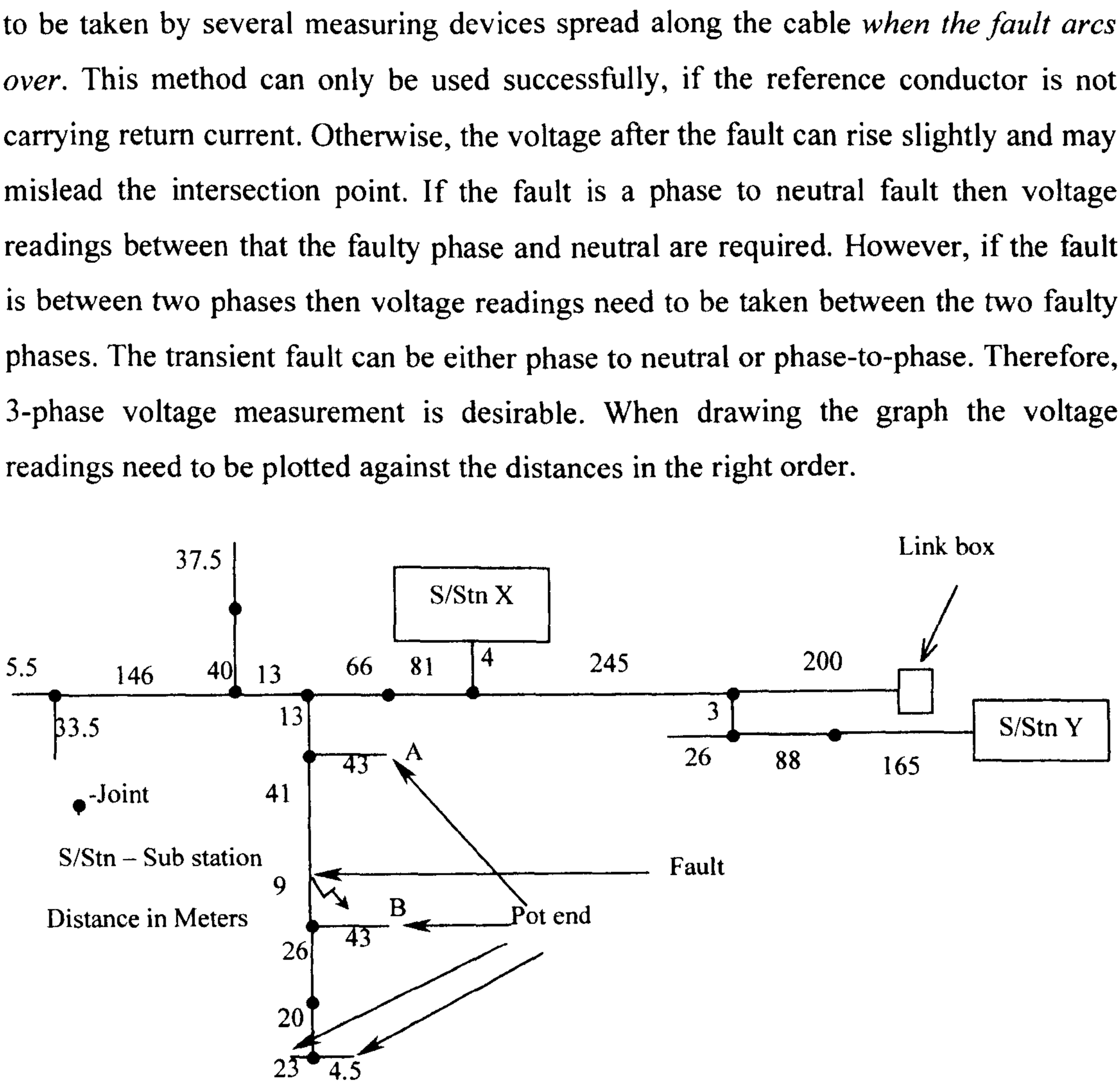

Figure 2.5 Part of a real LV network

2.3.2. Audio Frequency Methods

The direct overground audio frequency method is one of the most powerful tools in the LV fault location engineer's armoury, providing it is understood and only

applied in the particular circumstances in which it is effective such as low resistance faults [46, 66]. These methods are:

- Twist method for core to core faults using either single or double coil
- Twist method for core to sheath faults using either single or double coil
- Field turbidity method for core to sheath faults
- 'A' frame ground contact method for core to earth faults where there is no sheath

2.3.2.1. Twist Method

The Twist method is the most well known audio frequency technique in fault location and is based on the fact that cores of the cable are laid up twisted [46, 66]. In this method, two types of coils are used for the receiver. They are known as single coil and double coil. The procedure for this method of LV fault location is as follows: Firstly, the neutral earth link should be removed to reduce other possible signal paths. Then the Audio Frequency (AF) generator is connected between the two faulty cores (phases). The AF current passes through one core and returns via the fault path and the other core to the generator. At any point before the fault, therefore, there is a *go* and *return* current present in the cable. These currents produce a magnetic field maxima and minima at each half-twist of the cores. Therefore, if a search coil and receiver are moved along the cable, a series of signal maxima and minima will be detected as illustrated in Fig.2.6. As shown in Fig.2.6, this pattern will continue up to the fault point where a greater maximum is detected [46, 66]. Beyond the fault point, the signal tails off to a steady but very low level.

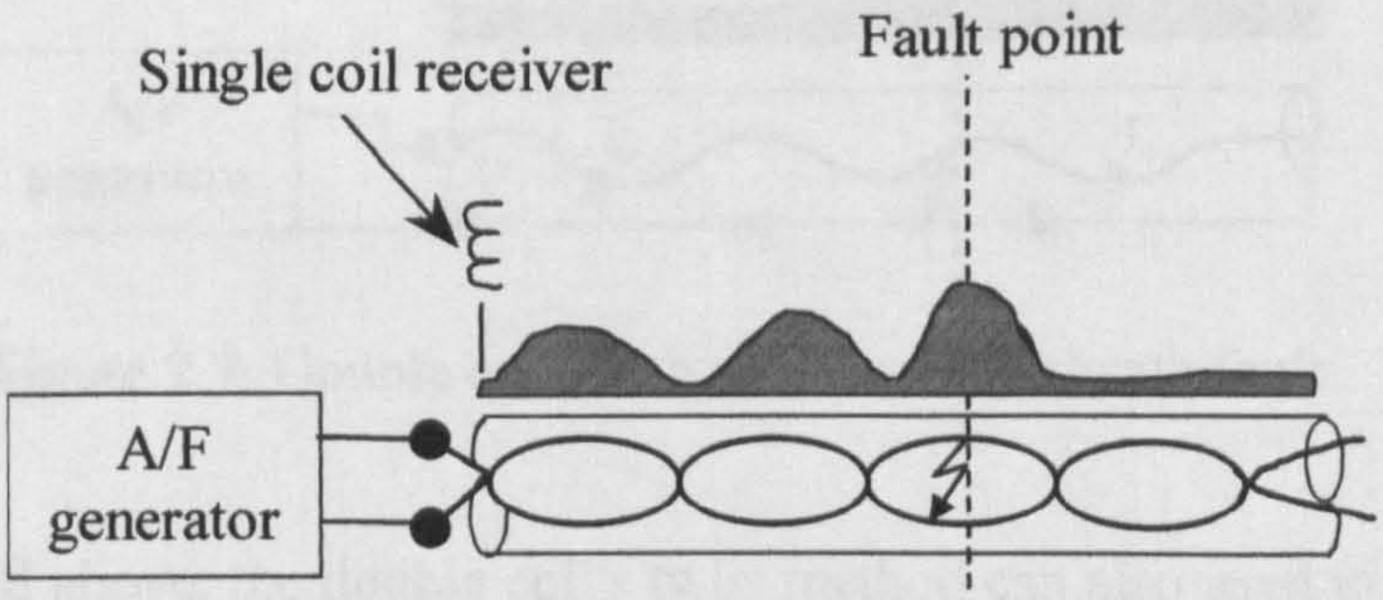

Figure 2.6: Twist Method

Before commencing the fault location, it is essential that the route or route section of the cable be traced and marked. This is because the twist method test will be

carried out at a brisk walking pace to be most effective. If one tried to trace the cable at the same time as fault detection, the recognition of the rhythm of the rising and falling tone pattern can be missed.

One of the disadvantages of the single coil's twist method is interference from other signal paths such as adjacent metal lines and cables and earth neutral links. To reduce the effect of other signal paths, the double coil can be used instead of single coil. The procedure for this method is the same as the single coil twist method. The two coils are separated at a distance equal to the separation between adjacent signal peaks of the magnetic field. Then subtracting the signals from the coils, the interference can be removed. This is because normally the interference field will be more or less the same in magnitude and polarity in both coils.

The procedure for locating sheath to core faults using the single coil's twist method is the same as core-to-core faults. This time the AF generator is connected between a healthy core and sheath and the healthy core is shorted with the faulty core at the remote end. This allows the test current to pass along the healthy core and return to the sheath along the faulty core, resulting in a rise and fall signal pattern between the fault and the remote end. The signal is checked from the remote end whereas for the core-to-core faults the signal is checked from the source end. The rise and fall will continue from the remote end until the fault point but after the fault, the signal tails off to a steady low level.

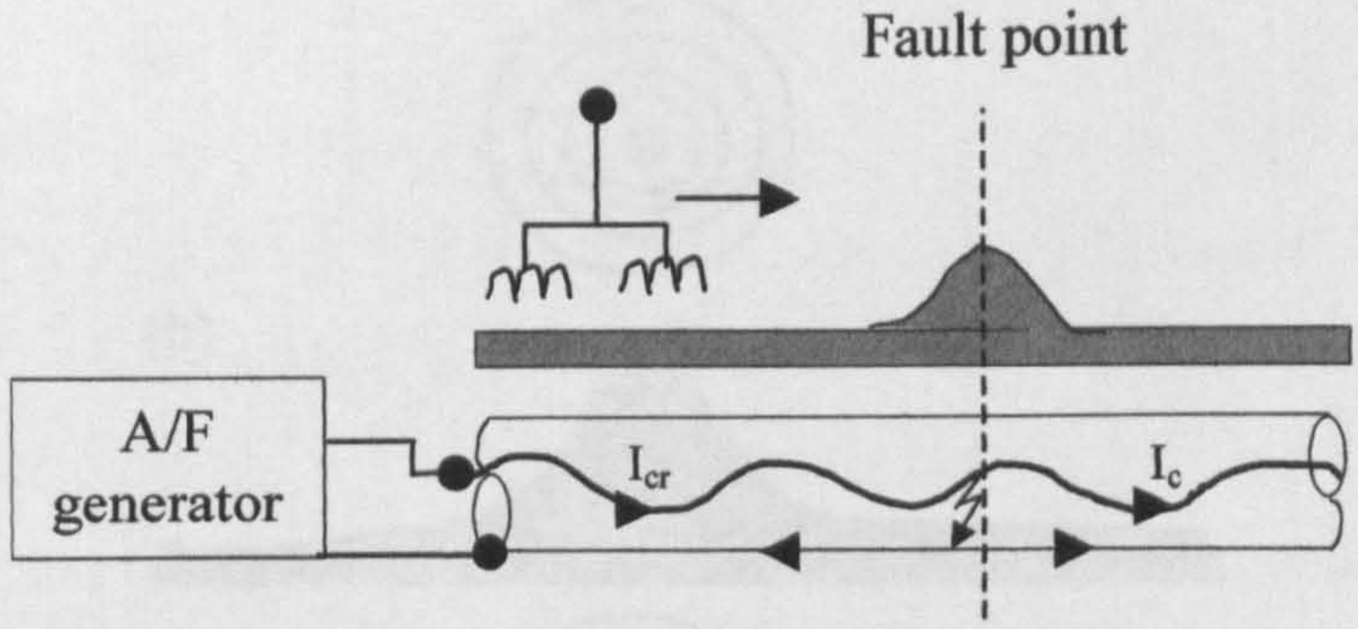

Figure 2.7: Double coil method for core to sheath fault

As mentioned above, the double coil's twist method can also used to locate sheath to core faults to reduce the interference signal. The procedure for this is as follows: the AF generator is connected between the faulty core and the sheath. Therefore, when the two coils are placed before and after the fault, the resultant signal will be almost zero as shown in Fig. 2.7. This is due to the same magnitude and opposite

polarity current travelling on the faulty core and sheath. The current before the fault will be due to the capacitive drain of the whole cable plus the in-phase current through the fault (I_{cr}) whereas after the fault the current will be due to the remaining length of the cable (I_c). This method can only be used if the fault is a low resistance and the suspect zone of the fault is certain. The disadvantage of this method is that a sudden deviation in the cable or joints can also produce peaks. This will lead to wrong a fault location. Furthermore, the distances to the cable terminations before and beyond the fault influence the levels of capacitive currents at any points [46, 66].

2.3.2.2. Field Turbidity Method

Field turbidity is another audio frequency method that is used for locating core to sheath faults. In route tracing for a cable, a search coil is placed perpendicular to a cable carrying an audio frequency current to give a maximum signal. If the search coil is placed in-line with the cable then it will produce a minimum signal [46]. Fig. 2.8a illustrates a typical signal pattern across a cable with the coil vertical while Fig. 2.8b shows a typical signal pattern across a cable with the coil horizontal.

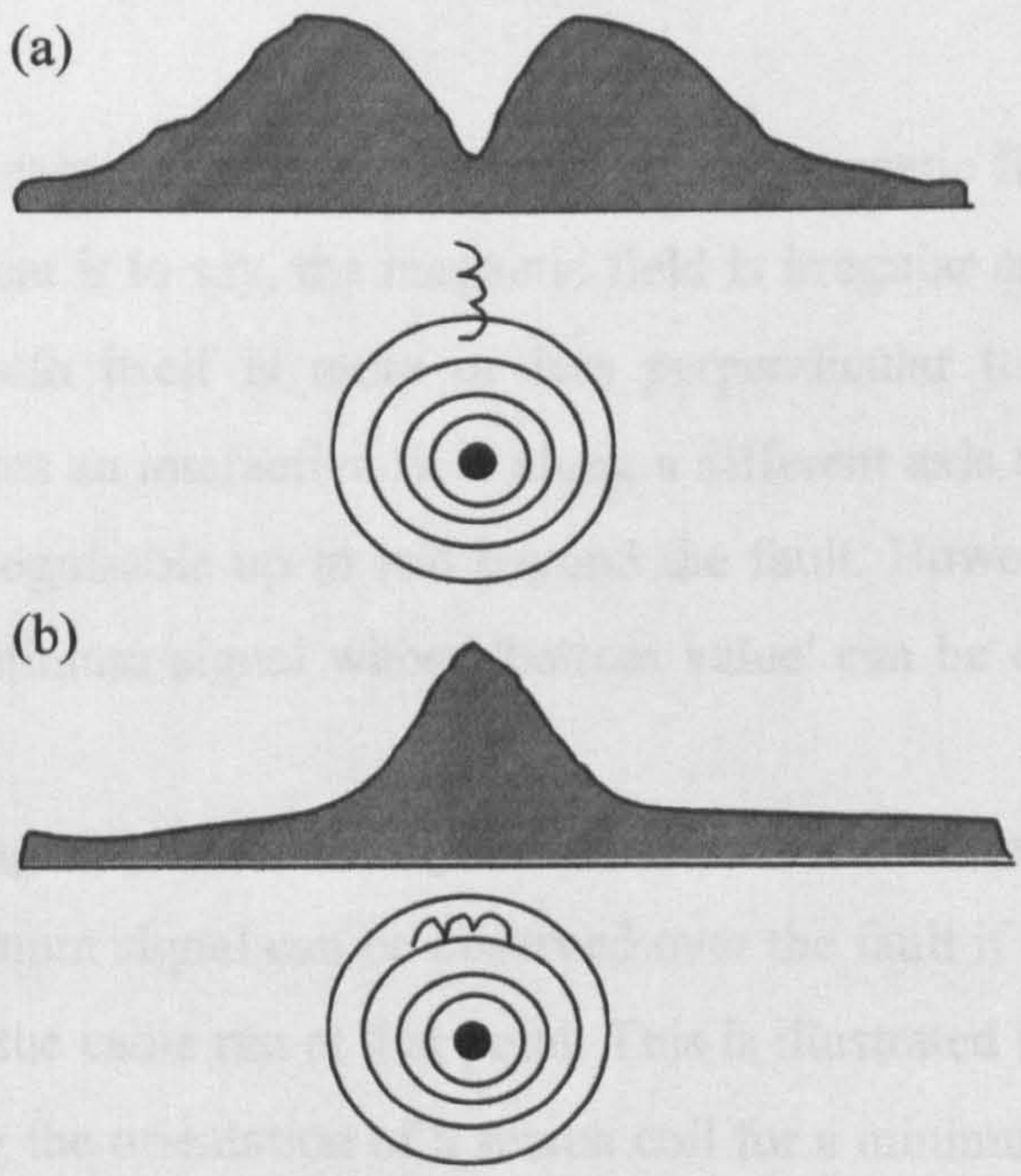

Figure 2.8: A search coil signal pattern (a) across line with coil vertical (b) across line with coil horizontal

These maxima and minima can be noted when the audio frequency source is being applied to an open ended core, a core shorted at the far end or a core with a fault. The magnetic field will be the same form, but the current may be in phase or at a leading angle.

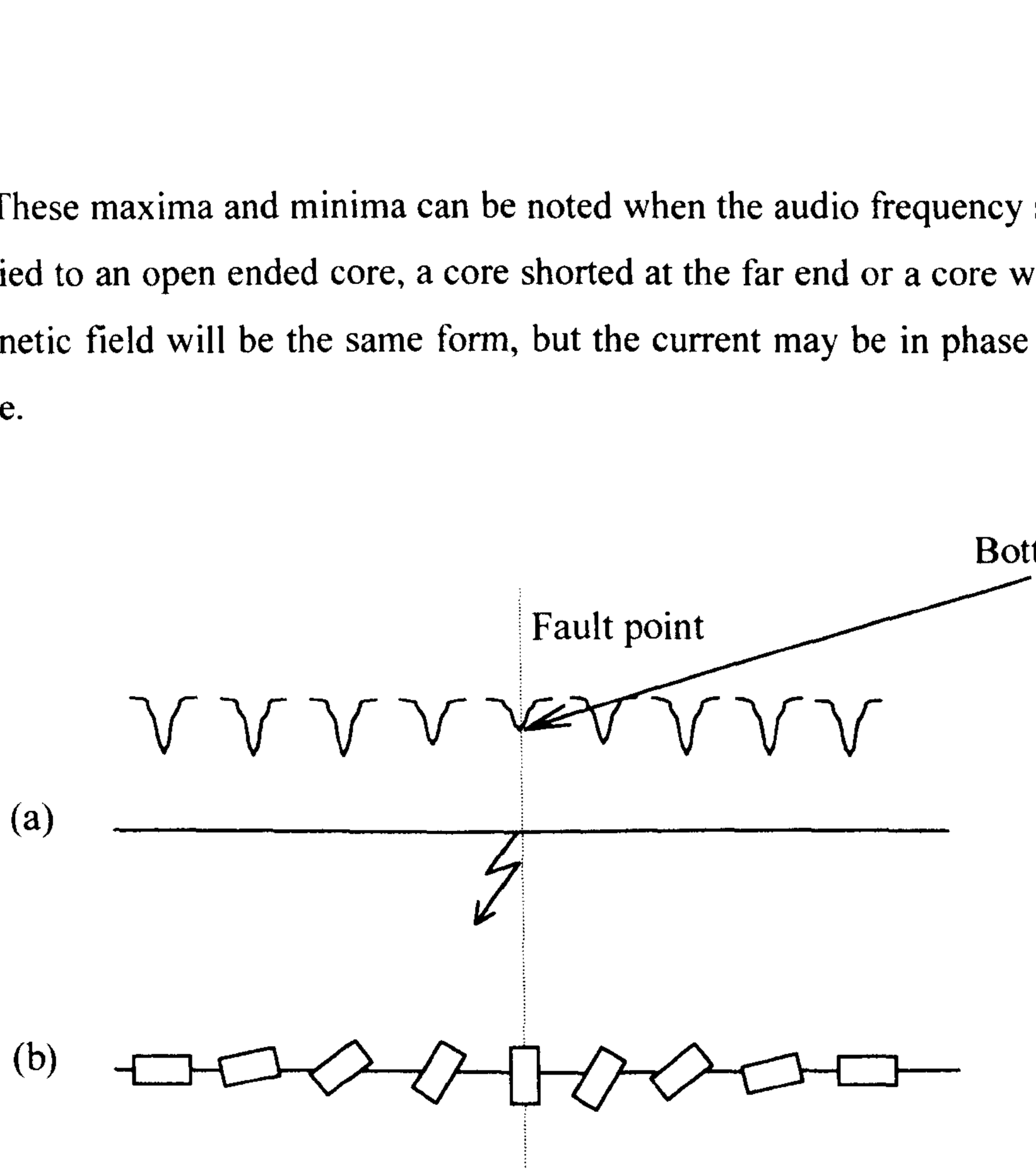

Figure 2.9: Field turbidity method (a) variation signal in field turbidity method
(b) Plan view showing the search coil orientation for the minimum signal

However, in the case of a core to sheath fault, the magnetic field is often *turbid* at the point of fault. That is to say, the magnetic field is irregular and deformed. This is because the fault path itself is more or less perpendicular to the core direction. Therefore, it generates an interactive field along a different axis to the axis producing the regular field recognisable up to and beyond the fault. However, it will display a much less sharp minimum signal whose 'bottom value' can be checked as shown in Fig. 2.9a.

The resultant magnetic field directly over the fault exhibits a different 'minimum signal axis'. A minimum signal can be observed over the fault if the search coil is not exactly in-line with the cable run at that point. This is illustrated in Fig. 2.9b, which is a plan view showing the orientation of a search coil for a minimum signal as it moves along the cable over the fault. As stated in the other audio frequency methods, this method cannot be used other than on low resistance faults.

2.3.2.3. 'A' Frame Ground Contact Method

The 'A' frame ground contact method that is illustrated in Fig. 2.10 can only be used for a relatively short length of unloaded cable, such as between two cuts, and a core or the sheath is in contact with the ground at the fault [46].

The procedure is as follows: first at the source cable termination, the faulty core or the sheath is checked to make sure that there is no solid earth connection. Then the AF generator is connected between the faulty conductor and a ground spike or general earth. The matching and amplitude controls are adjusted for a maximum value. After that the receiver/amplifier, together with headphones and the 'A' frame are taken to a point on the cable close to the source and connected up. The transmitter frequency is selected and tuned in and levels of audible and visible signals are set. It is possible that only a low signal will be heard at this point if the fault is close. The 'A' frame is then advanced along the route of the cable and stuck into the ground every few metres and the signal level checked. The signal level along the cable is illustrated in Fig.2.10. At some point along the route, a small but noticeable rise in the signal level will become apparent. This will develop rapidly into a very strong signal and then will drop to zero minimum within the length of one pace and then suddenly rise to another crescendo before slowly dying away again. This detected zero minimum point of the signal will be marked as the fault location [46].

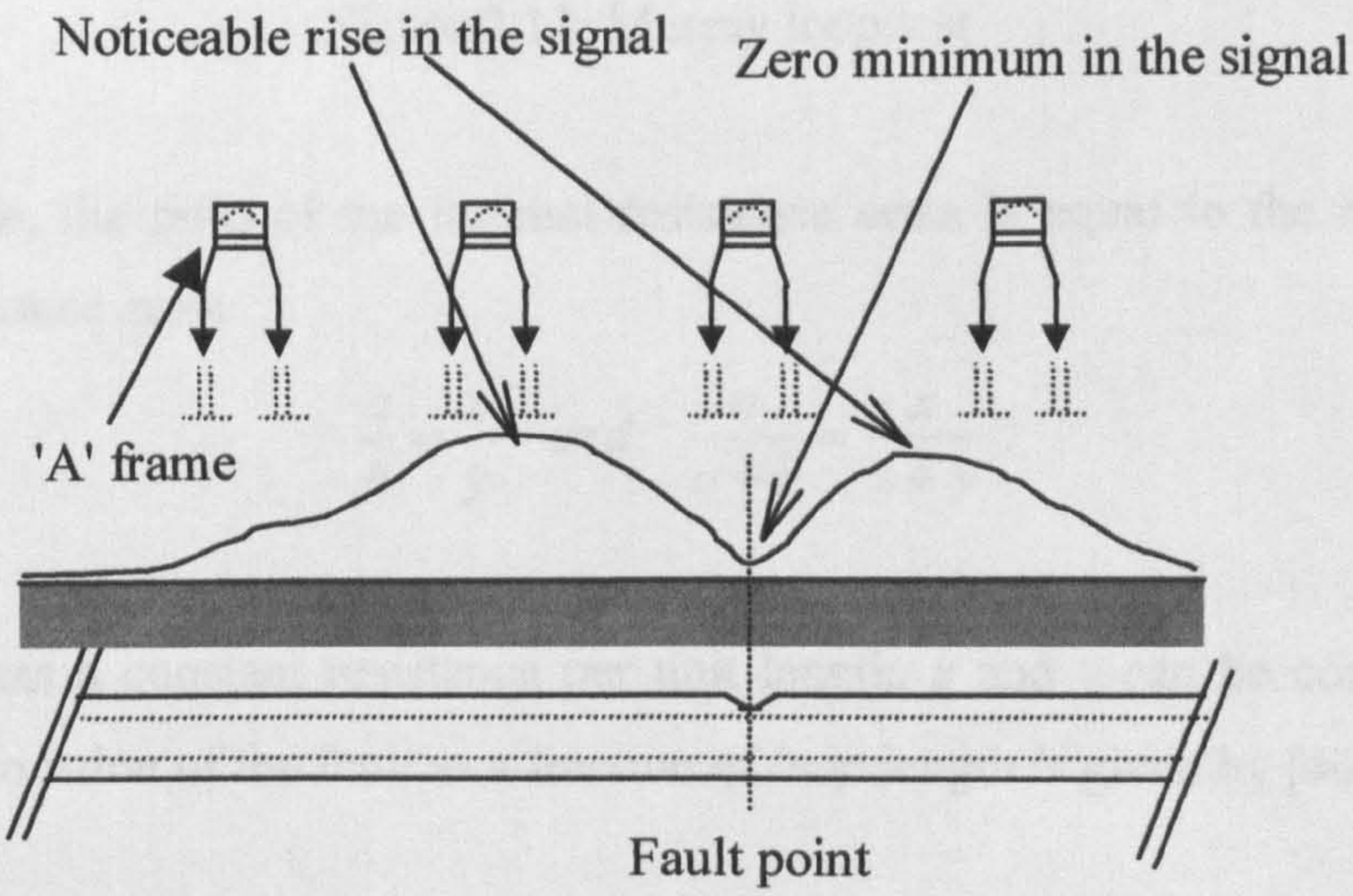

Figure 2.10: Ground voltage signal pattern

2.3.3. Resistance Bridge

This method is used for locating medium and high resistance faults, where neither Time Domain Reflectometry (TDR) nor transient methods can be used. Three types of resistance bridge configuration are available: *Murray loop*, *Inverted loop*, and *Hilborn loop* [46, 54, 67].

2.3.3.1. Murray Loop Resistance Bridge

This method is used for locating medium and high resistance faults and is still employed today [46, 54]. The method can only be used if the conductor is continuous (not "burnt" open). It can only be applied to contact (shunt) faults. The measurement is done by balancing two internal resistance arms (a, b) against the two external resistance arms (x, y) represented by the length of cable conductor up to the fault as shown in Fig. 2.11. In order to create an external loop a zero ohm short circuit is made at the remote end (B) between the healthy and faulty cores as illustrated in Fig. 2.11.

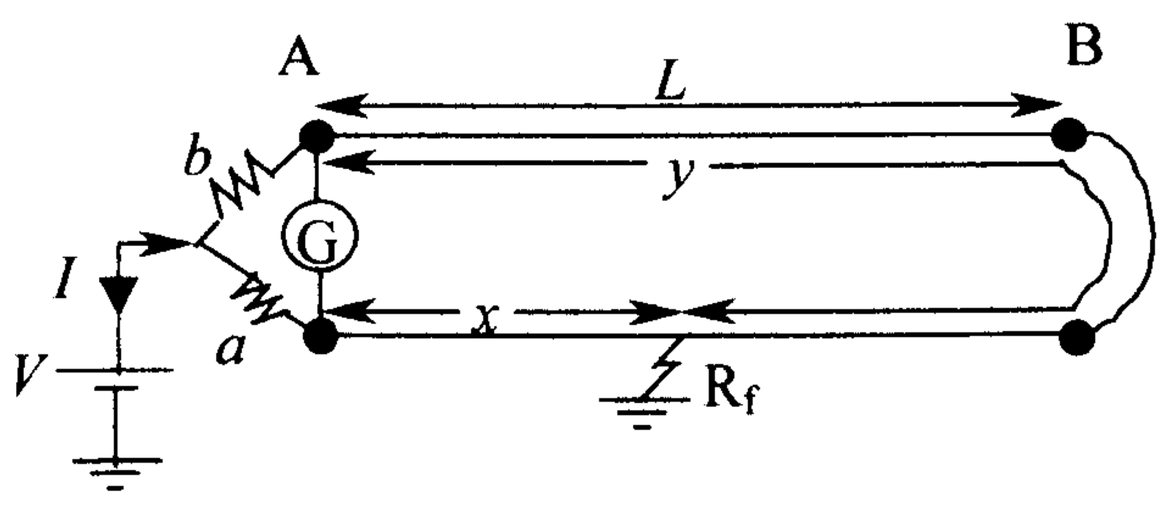

Figure 2.11: Murray loop test

At balance, the ratio of the internal resistance arms is equal to the ratio of the external resistance arms:

$$\frac{a}{b} = \frac{x}{y} \quad and \quad \frac{a}{a+b} = \frac{x}{x+y} \,. \tag{2.1}$$

If the cable has a constant resistance per unit length, x and y can be considered as lengths. The location of the fault as a fraction of *loop* length is given by [46]:

$$x = \frac{a(x+y)}{a+b} \quad or \quad x = \frac{a}{a+b}(2L) \tag{2.2}$$

The above equation is only valid if the measurements are made in ohms with a decade switching system [46]. If a potentiometer is used then the dial reading is a percentage of the loop length $2L$. The location of the fault depends on the linearity of resistance per unit length along the cable core. The main disadvantage of this test method, on cables with varying cross-sections of the cores, is that the positions at any point of change of cross-section must be known. It is also essential, that the user have access to the remote end of the cable in order to loop the healthy and faulty cores.

If a single pair of test leads is used, this will introduce the resistances of the test leads into the external loop. Therefore, the test lead resistance needs to be added to the external loop resistances. If the test lead resistance is small compared to the external resistance (x, y) and if it is ignored during the fault distance calculation then any error due the test lead resistance will be small. However, if the fault lies close to the test end (A) it will produce a higher percentage error in the fault distance.

The main advantage of the Murray loop test is accuracy. The accuracy can be up to 0.1 percent, provided that there are no other sources of error, e.g. poor route length measurement. To pass current through the fault a D.C voltage is required and at balance, the galvanometer will indicate zero volts. The sensitivity of the bridge depends on two factors:

- The sensitivity of the galvanometer
- The current being driven through the fault

The current being driven through the fault is equal to the applied voltage divided by the total resistance of the test circuit (the main component is the fault resistance)[46]. A better balance can be achieved by either raising the applied voltage or lowering the current level at which a zero can be detected.

If a cable network has tee branches as shown in Fig. 2.12, the test needs to be done more than once. If the fault lies on the main cable (*F1* in Fig.2.12), normally one test will be enough, i.e. closing the loop at the remote end of the main cable (B in Fig.2.12). If the fault lies on the branch tee (*F2* in Fig.2.12) or tee joint (C in Fig.2.12) then the test needs to be done twice. First, close the loop at the remote end of the main cable (B in Fig.2.12) only and do the test as shown Fig.2.12. This will give a location at the tee joint (C in Fig.2.12). Then do a second test by closing the loop at the branch tee end (D in Fig.2.12) only.

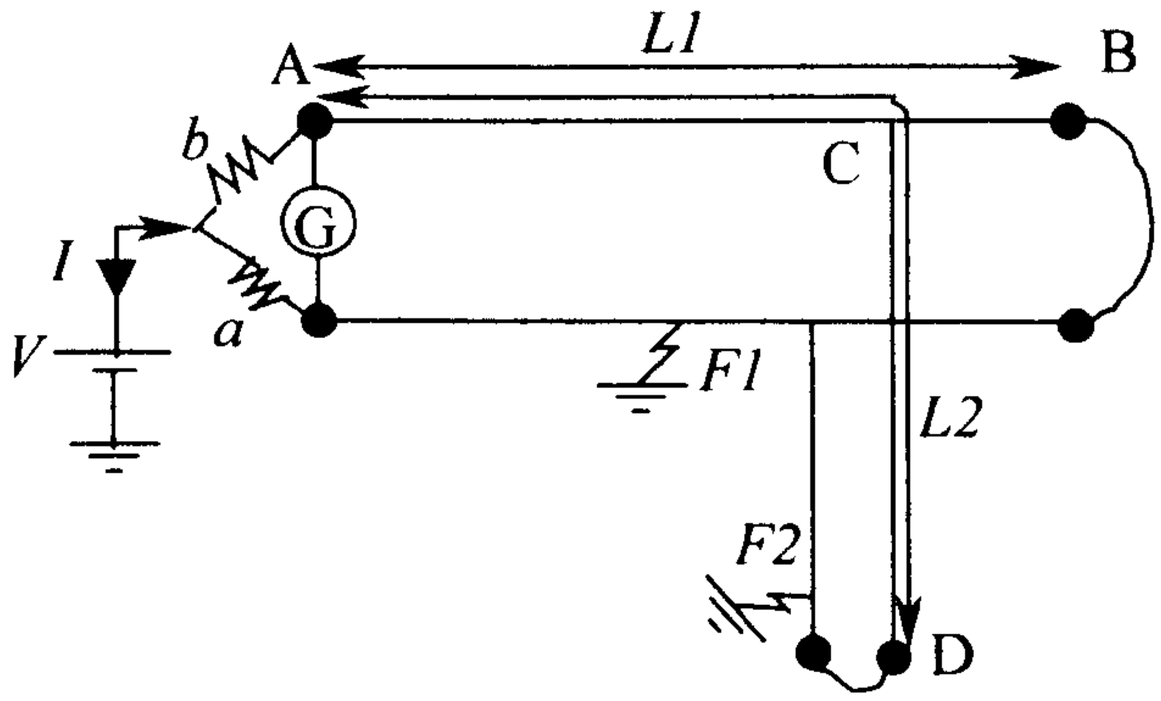

Figure 2.12: Murray loop test for teed cable

When the loop is closed at the main end of the cable, the cable length has to be considered as *L1*. If the loop is closed at the branch tee, the cable length has to be considered as *L2*. This will clearly indicate whether the fault is at the tee joint or somewhere along the branch.

2.3.3.2. Inverted Loop Test

The *Inverted loop test* is an extremely effective method for locating a high resistance fault. The basic set up is shown in Fig.2.13. It can be seen that the positions of the galvanometer (or null detector 'D') and the battery are interchanged. Therefore, the battery voltage V drives the current I around the external loop (x, y) and the current i through the internal arms (a, b). For this test, no more than 6V is required but may produce roughly between one and one hundred amperes. Therefore, it should be possible to connect and disconnect the battery quickly and conveniently. A heavy duty 6V lead should be used, so that it has the capacity to drive the heavy currents around the cable loop and still maintain the potential difference not below the nominal 6V.

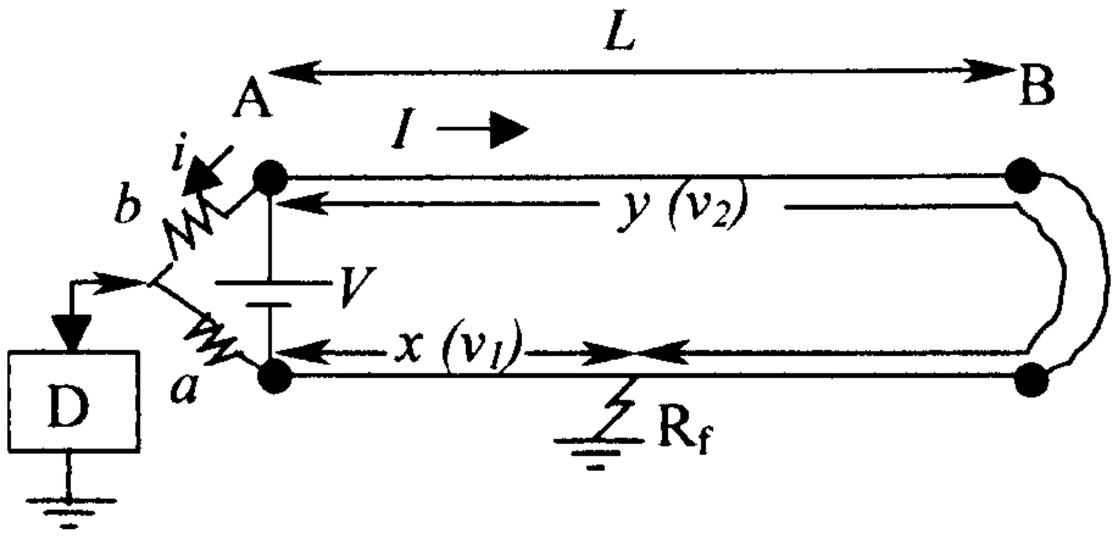

Figure 2.13: Inverted loop test

This test is capable of locating faults up to 200 mega *ohms*. However, the following points need to be considered when it is used for locating such high resistance faults [46]:

1. Most LV cables have a 200 mega *ohms* insulation resistance if they are healthy!
2. If the cable is long enough to have a significant capacitance then there will be a large time constant involved when testing shunt resistance values in the order of hundreds of mega *ohms*.
3. Effects of stray capacitance are observed.
4. Guard terminals should be connected to the insulation at the test end A to cancel out surface leakage.

Therefore, in practice the inverted loop test is extremely effective in locating faults that have fault resistance from zero to 20 mega *ohms*.

2.3.3.3. Hilborn Loop Test

In the case where two healthy cores, or cores in an auxiliary cable such as a pilot or control cable terminated in the same location, are available then the *Hilborn loop* can be used for locating faults. If the cable is short, it may be possible to run out an auxiliary cable overground. The configuration of this loop test is shown in Fig. 2.14.

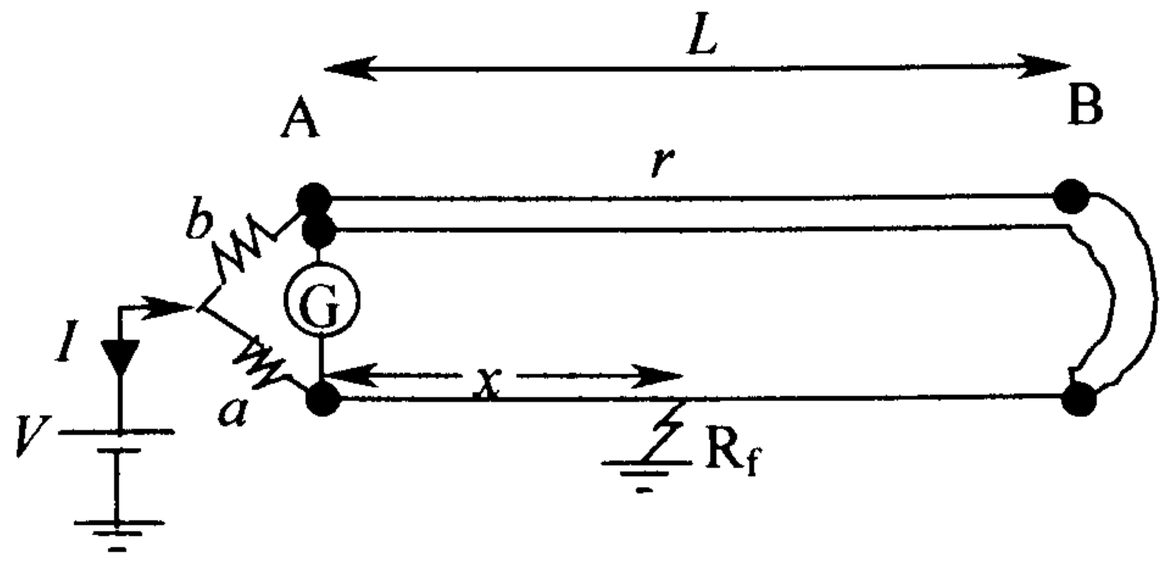

Figure 2.14: Hilborn loop test

It is a powerful technique for the following reasons:

- The resistances of the two auxiliary conductors are unimportant as they appear in the internal arms and the galvanometer circuit respectively. The small connection at the remote end B is also not important. This is a most useful factor when the faulty core has a large cross-section.
- The bridge is in effect connected directly across the faulty core and the loop length is the route length. Therefore, the error is small.

At balance the fault location is given by [46]

$$x = \frac{a}{a+b+r} \times L \tag{2.3}$$

where r is the resistance of the auxiliary cable or the healthy cores.

This method is often used for locating sheath faults, because the cores of the cable are usually healthy and available for use as auxiliary connections.

2.3.4. Time Domain Reflectometry (TDR) or Pulse Echo

Time Domain Reflectometry (TDR) is one of the most common methods used for locating faults in underground cables and transmission lines [46, 55-64, 66] The procedure for TDR based pre-location is as follows: A short duration pulse is launched into one end of the cable. This pulse is partially or completely reflected by any impedance mismatches in the cable. The impedance mismatches can be a shunt path (e.g. short circuit fault) or a series path (e.g. an open circuit or end). Then the return (reflected) waveforms are analysed to locate the fault. The measurement of the distance to the mismatch is calculated using the time (t) taken for the pulse to return to the source end and the velocity of propagation (v) that is assumed to be constant for the given cable. The formula for the fault distance, (D) calculation is

$$D = \frac{t * v}{2}. \tag{2.4}$$

The velocity of propagation depends on the cable dielectric and is defined as

$$v = \frac{c}{\sqrt{\varepsilon}}. \tag{2.5}$$

where c is the velocity of light in free space ($300 m/\mu s$), and ε is the relative permittivity of the dielectric.

Table 2.1 shows typical velocities of propagation for different dielectrics [46]. These values are approximate and vary due to differences in the particular type of insulation, temperature, and ageing of the insulation. In practice, a value of v should be derived using a known length of same cable.

Dielectric of the cable	Velocity of propagation ($m/\mu s$)
Impregnated paper	150-171
Dry paper	216-264
PE	Approx. 200
XLPE	156-174
PVC	152-175
PTFE	Approx. 213
Air insulated	Approx. 282

Table 2.1: Typical velocity of propagation of different dielectrics

Any pulse travelling in the cable is a high frequency phenomenon that sees a cable of infinite length before it with an impedance of Z_o, the characteristic impedance defined as

$$Z_o = \sqrt{\frac{L}{C}}. \tag{2.6}$$

Values of Z_o for power cables vary between 15 and 80 *ohms* [46].

When a voltage pulse is applied to a cable, it will travel along it. Along with the voltage pulse there will be a corresponding current pulse that travels along the cable at the same velocity. The ratio of the voltage pulse, V, to the current pulse, I, is the characteristic impedance of the cable, Z_o [74]

$$Z_o = \frac{V}{I} \tag{2.7}$$

When an impedance discontinuity is encountered on the cable, some energy is reflected back according to the following relationship [74]

$$V_{rfl} = V\rho_V \tag{2.8}$$

and

$$I_{rfl} = I\rho_I \tag{2.9}$$

where V_{rfl} and I_{rfl} are the voltage and current reflections, and ρ_V and ρ_I are the voltage and current reflection coefficients respectively.

The reflection coefficient given by [74]

$$\rho_V = \frac{Z_{dscnt} - Z_o}{Z_{dscnt} + Z_o} \tag{2.10}$$

and

$$\rho_I = -\rho_V \tag{2.11}$$

where Z_{dscnt} is the impedance discontinuity on the cable.

For shunt faults, the impedance discontinuity on the cable is the parallel combination of the fault impedance, Z_{flt}, and the characteristic impedance of the cable [66]. Therefore, the Z_{dscnt} is given by

$$Z_{dscnt} = \frac{Z_o Z_{flt}}{Z_o + Z_{flt}} \tag{2.12}$$

and the voltage reflection coefficient for shunt faults becomes

$$\rho_{Vshunt}(x) = \frac{-Z_o}{2Z_{flt} + Z_o} \tag{2.13}$$

Similarly, for series faults, the impedance discontinuity on the cable can be defined as the series combination of the fault impedance and the characteristic impedance of the cable [66]. Therefore, the Z_{dscnt} is given by

$$Z_{dscnt} = Z_{flt} + Z_o \tag{2.14}$$

and the voltage reflection coefficient for a series fault will become

$$\rho_{Vseries}(x) = \frac{Z_{flt}}{2Z_o + Z_{flt}} \tag{2.15}$$

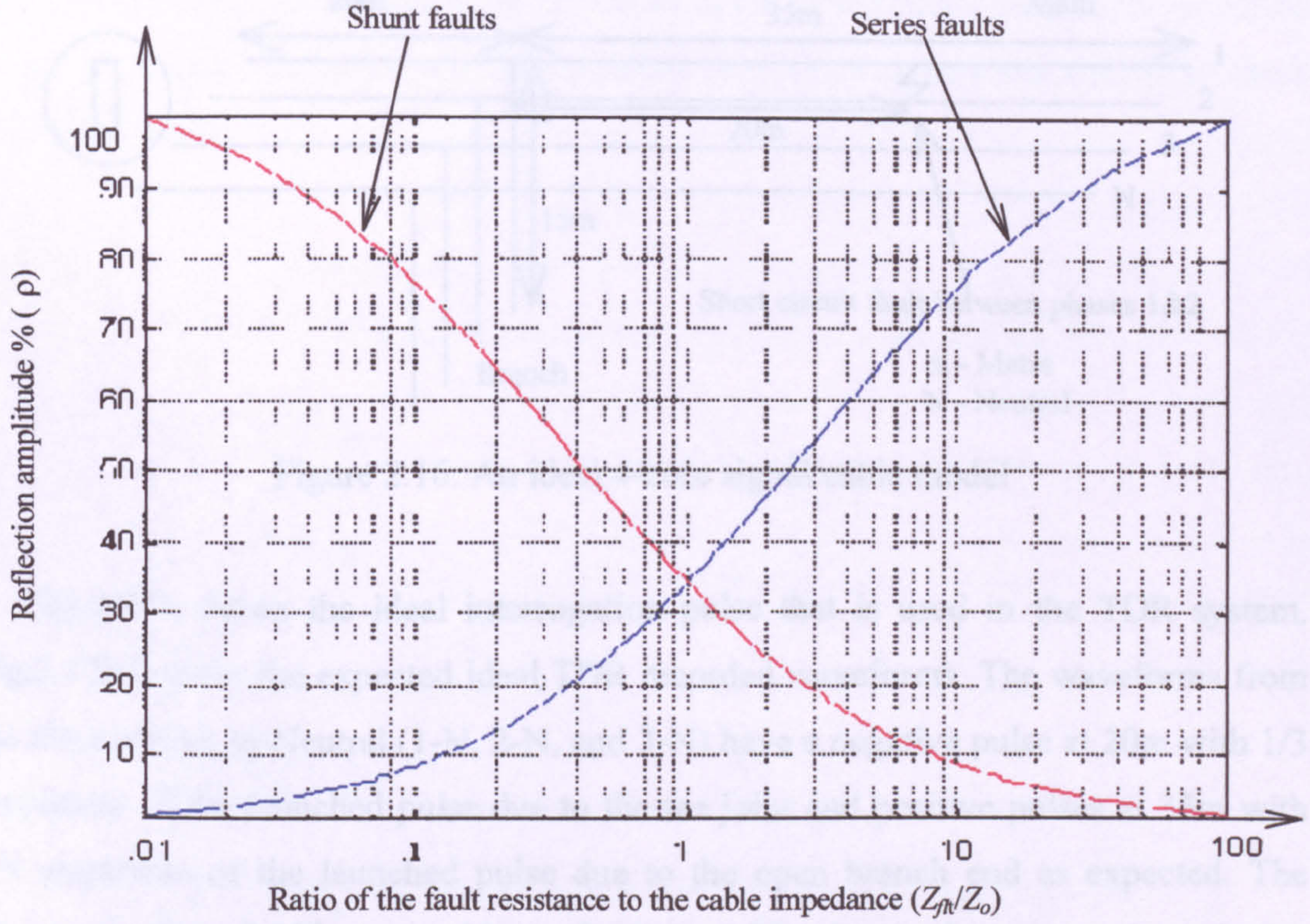

Figure 2.15: TDR voltage reflection factors for power cables

Therefore, to get a good visible reflection the fault resistance must be low for shunt faults and high for series faults [55, 66].

The reflection of the pulse amplitude diminishes due losses in the cable and the pulse energy being steadily dissipated the further the pulse travels. As well as faults and ends, other features such as joints, changes in cable cross-section, core splits and re-splits, and waterlogged zones can give rise to reflections. Tee joints and ends of tee branches cause more significant mismatches that produce trace features of greater magnitude.

2.3.4.1. Ideal TDR Waveforms

Consider the simple 4-core cable model shown in Fig.2.16. It comprises a 55m main 4-core cable with a tee branch at 20m of length 15m. There is a short circuit fault 40m along the main cable between cores 1&2. The ideal TDR input pulse,

expected waveforms, and expected results for the cable model in Fig.2.16 are illustrated in Fig.2.17.

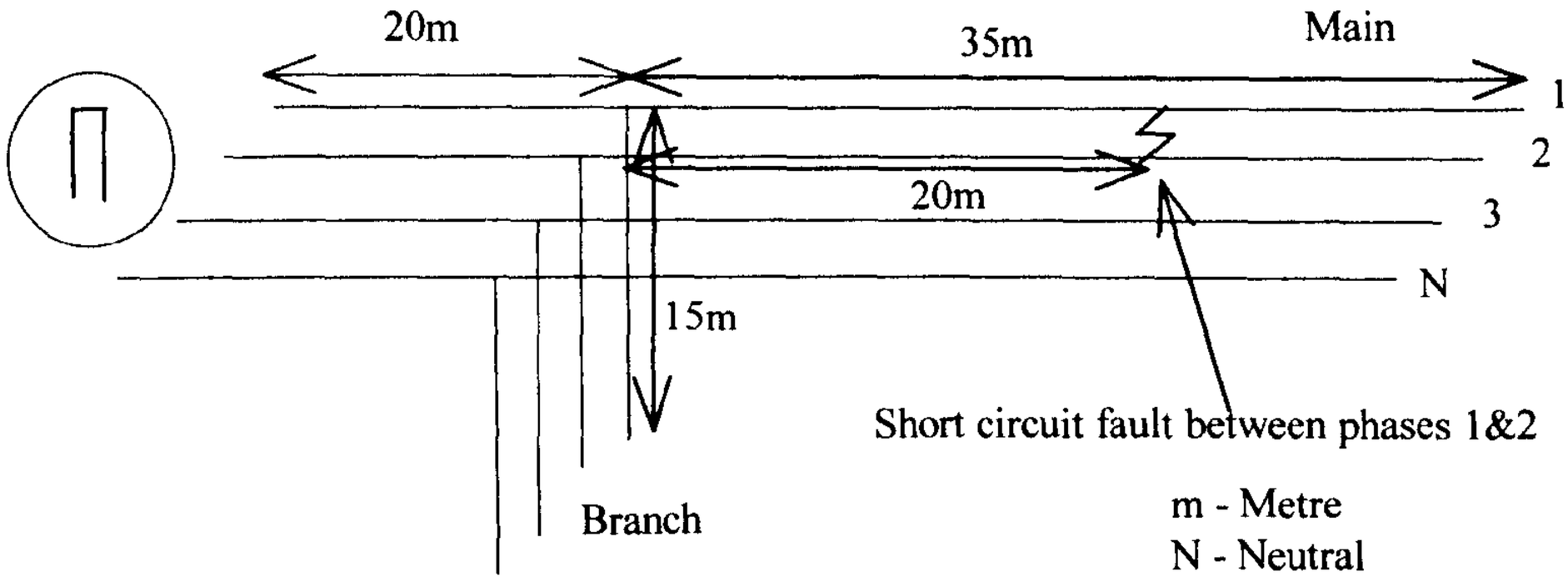

Figure 2.16: An ideal 4-core signal cable model

Fig.2.17a shows the ideal interrogation pulse that is used in the TDR system. Fig.2.17b-d show the expected ideal TDR recorded waveforms. The waveforms from the three phases to Neutral (1-N, 2-N, and 3-N) have a negative pulse at 20m with 1/3 amplitude of the launched pulse due to the tee joint and positive pulses at 35m with 4/9 amplitude of the launched pulse due to the open branch end as expected. The phase waveform 3-N has a positive reflection at 55m due to the open main end with 4/9 amplitude of the launched pulse. The phase waveforms 1-N and 2-N have a second negative pulse at 40m with 2/9 amplitude of the launched pulse due to the short circuit fault and a positive reflection at 55m due to the main open end with 1/9 amplitude of the launched pulse. In Fig.2.17e, the superimposed waveforms of 1-N & 3-N are illustrated. The bold pulses in Fig.2.16e indicate that two reflected pulses are in the same position. Fig.2.17f shows the difference between the 1-N & 3-N waveforms which shows a negative pulse at 40m due to the short circuit fault at 40m and a further negative pulse at 55m due to the main open end. The waveform at 40m is clearly seen because the TDR waveforms are ideal. In practice TDR waveforms are much more complicated as is illustrated in the next section.

In TDR based fault location, the difference or the superimposed waveform of the healthy and the faulty phases is examined by an experienced engineer to discover if any key departures exist in the waveform caused by the fault. This conventional method is sometimes referred to as the Compare and Contrast (C&C) method.

Key departures only exist if one of the waveforms under test is faulted or there is a mismatch due to a single-phase tee. Otherwise there will not be any significant key departures in the ideal situation. In reality, this is not true due to other impedance differences along the cable and the effects of noise which cause amplitude variations in the waveform. These amplitude variations may show departures similar to those caused by faults.

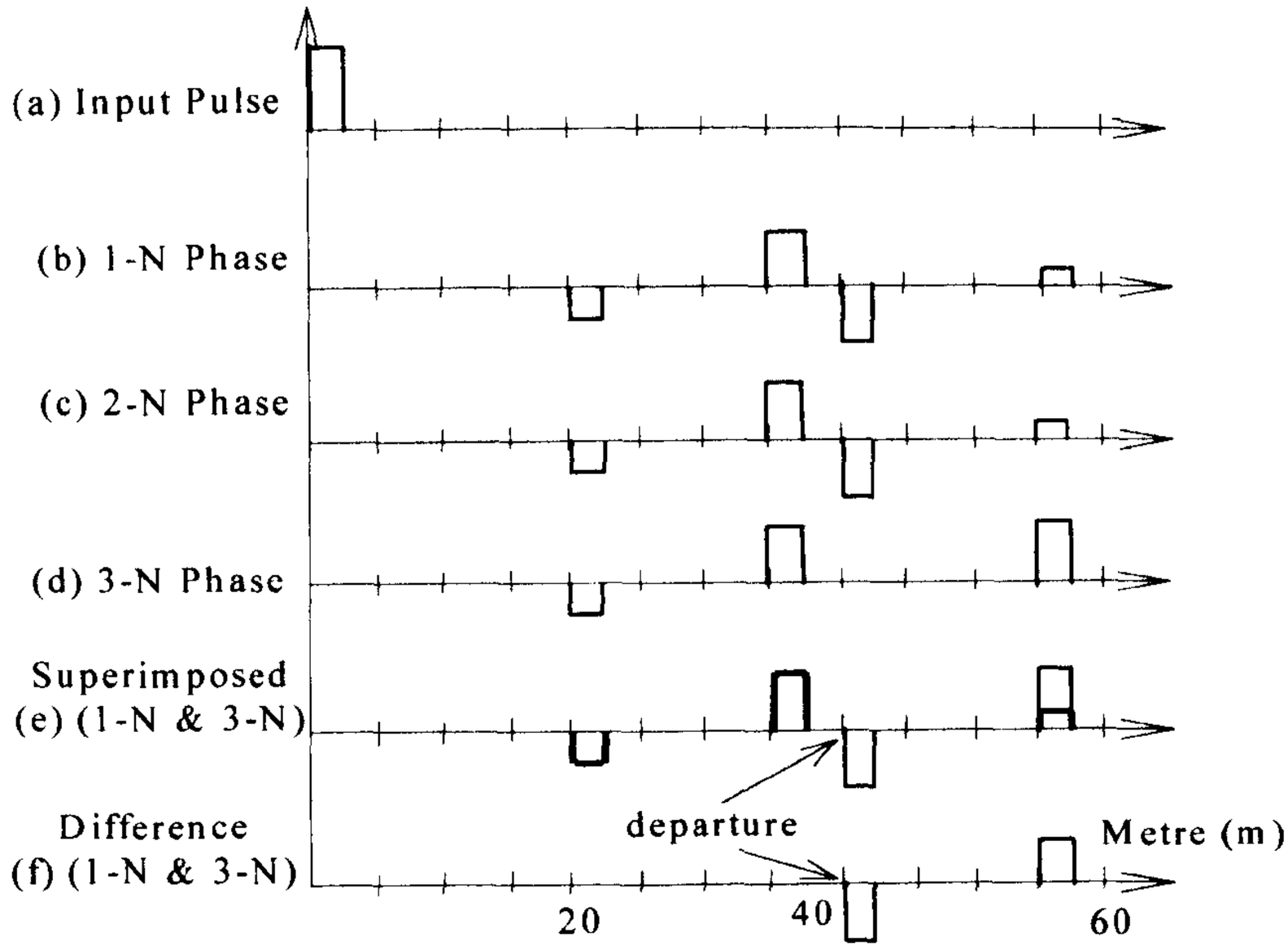

Figure 2.17: An ideal TDR input pulse, recorded waveforms, and expected results for the model in Fig.2.16

The C&C method of fault location has three main disadvantages. First, as explained earlier amplitude variation may cause problems in interpreting the waveforms. Second, this method can only deal with two waveforms at any instant. Third, multi-phase waveform recording in LVUDN is restricted. This is due to live line testing as mentioned in the introduction whereby it is not always possible to record healthy and faulty phase waveforms without customer power outage.

The pulse width is very important. Narrow pulses will give rise to very sharp trace features, which are easy to measure, but they attenuate very quickly and therefore are only useful over short distances. Wide pulses, on the other hand, produce wider and more rounded trace features whose 'start points' are more difficult to identify. However, they are not so quickly attenuated and therefore travel further. The TDR method is used in many commercial LVUDN fault location instruments [46]. The

main disadvantage of these instruments when used for LVUDN is the need for experienced engineers to interpret the results due to the complexity of the waveforms. Detailed explanations of the above points are illustrated in section 4.4.

2.3.4.2. Impulse Voltage Transient Method

In the sixties a transient method became available to locate very high resistance and flashing faults which are very difficult to find [46, 55, 56]. The typical connection for this method is shown in Fig. 2.18. It shows a Surge Generator (SG) connected to the faulty core and a high voltage capacitor (C). The 'cold' end of the high voltage capacitor is connected to the TDR oscilloscope via a low voltage capacitor (c) that is normally incorporated within the instrument. Both low and high voltage capacitors (C, c respectively in Fig. 2.18) constitute a capacitor divider. This produces a safe low voltage signal of the same form as the high voltage phenomenon present on the cable core.

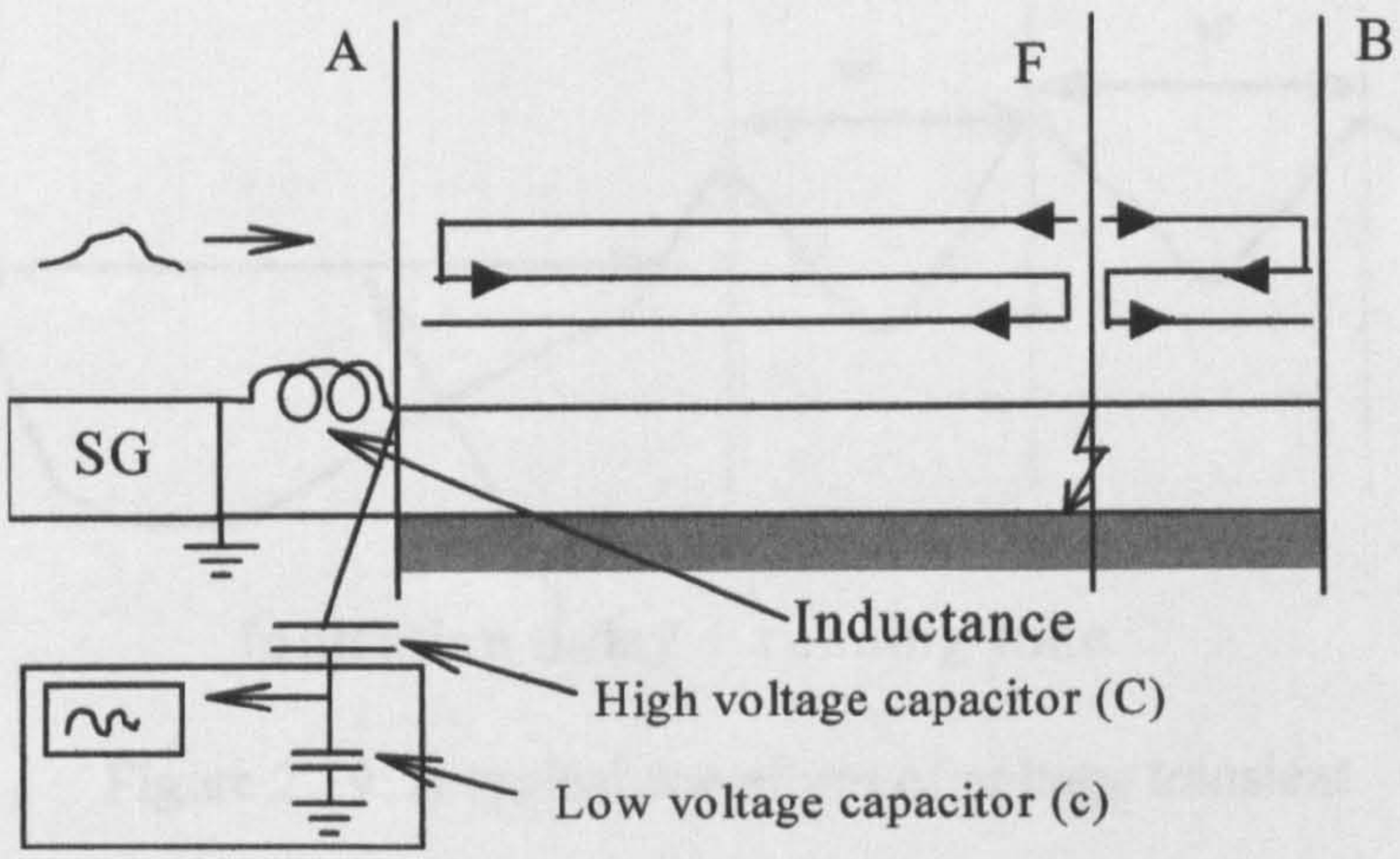

Figure 2.18: Connection for the impulse voltage transient method

The operation of this method is as follows: the high voltage surge wave travels along the cable until it reaches the fault. After a certain time lapse the fault ionises and arcs over and two voltage transients are set up which travel from the site of the fault in both directions, one towards the far end and one towards the test end. The latter transient will be displayed on the oscilloscope. When it arrives at the test end, it is reflected with no change of polarity due to the high impedance of the inductance that is placed in series with the SG output. On arriving back at the fault position it is again reflected, this time with a change in polarity, by the fault arc that appears as a permanent short circuit. This is because the duration of the arc is long in comparison

with the time of flight of the transient wave. This reflection and re-reflection continues until the energy in the transient has been dissipated due to losses in the cable.

A typical waveform of a voltage transient is shown in Fig 2.19 [46]. As shown, the resulting trace displays constant wavelength *w* but diminishing amplitude. This is due to the cable loss. This wavelength, *w*, is related to the fault distance which, in terms of time (*t*), is 1/2 *w*, i.e. it is equal to the time taken for the transient to travel from the fault to the test point and back. Therefore, the fault distance is given by

$$D = t \times v \quad or \quad D = \frac{w}{2} \times v \tag{2.16}$$

where t is the time of flight in microseconds and *v* is the velocity of propagation of the cable under test in metres per microsecond.

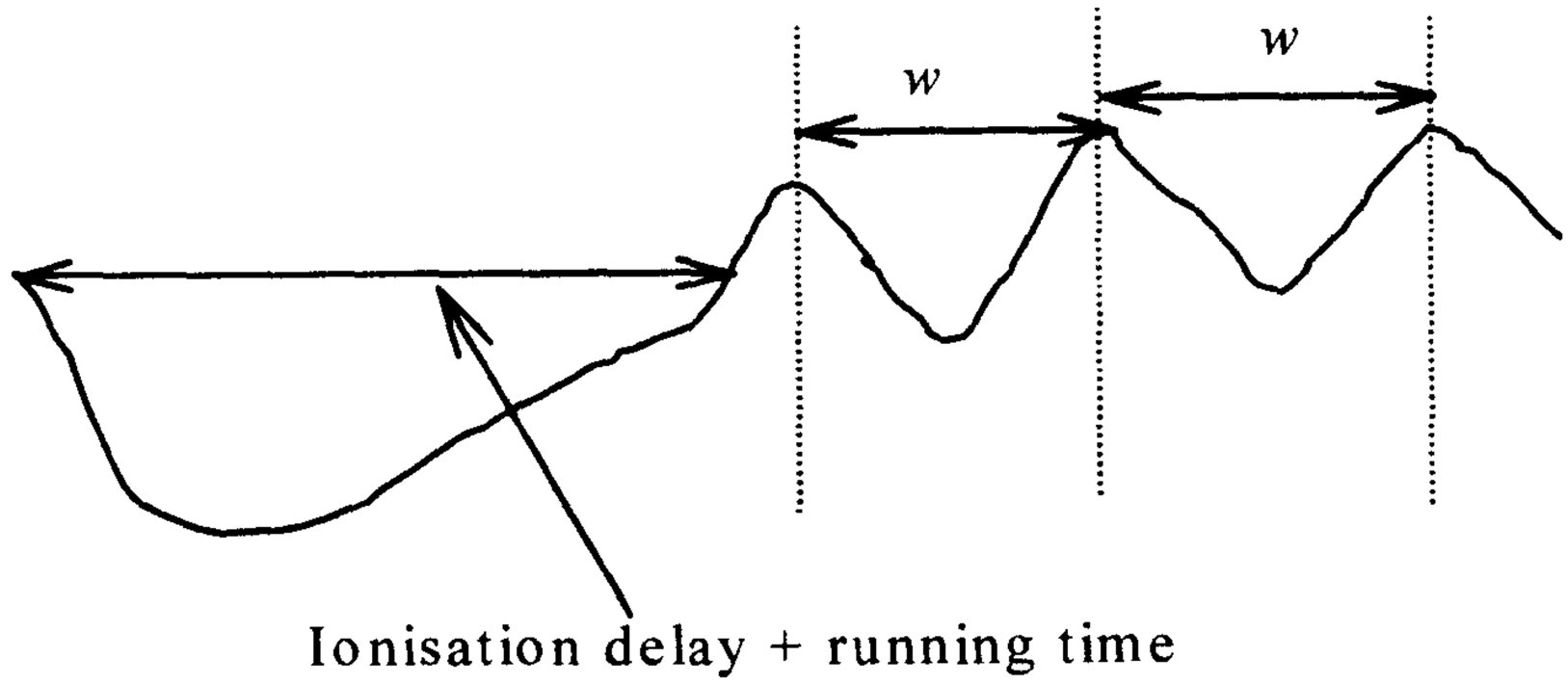

Figure 2.19: A typical waveform of voltage transient

It is important to note that until the arc occurs there will be no transient. The time duration between the start of the travelling wave and the arc includes *ionisation delay* and should be ignored for the transient analysis.

The gap may take many microseconds to ionise and breakdown or, occasionally, a few milliseconds as shown in Fig. 2.19. It may be possible that the arc strikes when the surge wave has just passed the fault or after it has travelled to the end, been reflected and is on its way back. Sometimes, the surge wave breaks the fault on the return journey because the voltage has been doubled due to the positive reflection coefficient at the open circuit end.

2.3.4.3. Impulse Current Transient Method

In the late seventies, the impulse current method was developed by P. F. Gale [46, 55, 66]. This method is successfully used for transmission lines (TWS by Hathaway Systems Ltd.]. The method has many advantages one of which is safety. This is because the current signal is derived from a simple linear coupler normally attached to the 'earthy' return lead of the surge generator. The linear coupler also has an earthed screen between the secondary and the earth return (primary) because, in certain circumstances, the potential of the earth return can be raised. The linear coupler comprises a short length of insulated wire, the secondary winding, in close proximity to the earth-return conductor, the primary winding. The typical connection arrangement for the impulse current method is shown in Fig.2.20

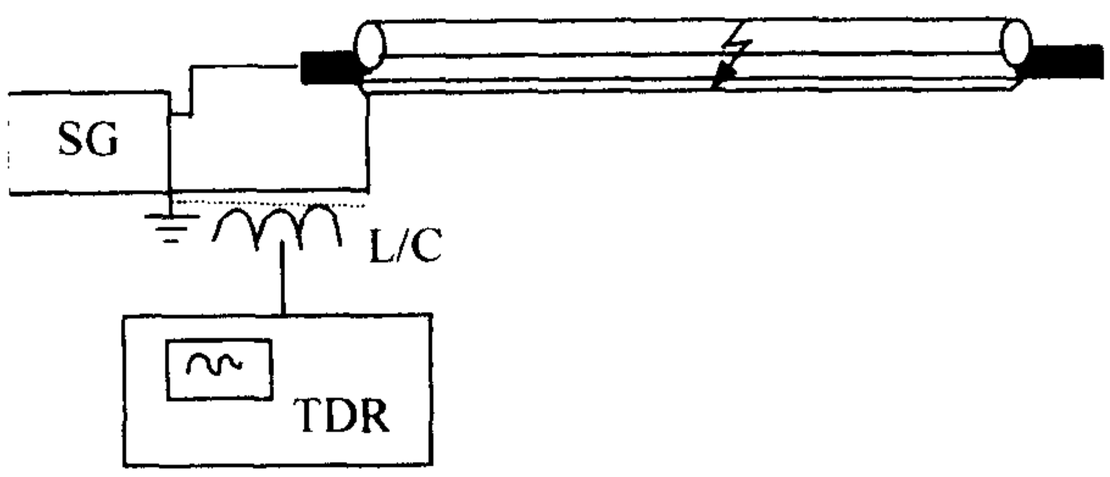

Figure 2.20: Connection for the impulse current method

This method does not need a blocking capacitor/capacitor divider and by eliminating the need for a series inductance does not reduce the efficiency of the surge generator. Another advantage of looking at current displays is that the signal in the secondary is proportional to the rate of change of current in the primary so the leading edges of the trace features are accentuated.

The disadvantage of this method is the waiting time for the transient. For example in LVUDN, if a customer reports flickering lights due to a transient fault then the user must set-up the unit at the substation and leave it there until another transient occurs. The time between flickers will vary depending on the type of transient fault as mentioned in section 2.2. Another disadvantage in using this method for LVUDN is that the signal generated by the fault will be attenuated due to the multiple tees and customer loads and also will travel along all the tees. Therefore, the signal arriving at the recording end may not have significant detail to allow the fault to be located.

2.3.5. Adaptive Method

In [67], an adaptive method was used to detect high impedance faults in HV networks. The adaptive model is shown in Fig. 2.21. It has multiple inputs and a learning algorithm for weight correction.

The detection system uses multiple pieces of information from the algorithms such as energy [69], randomness [70], phase relationship [71], sequence component [72] and amplitude ratio [73]. Each algorithm produces, as its attribute, the number of fault indications in a certain time interval. From the adaptive weights and the number of fault indications, the adjusted weights are obtained. Then, with these adjusted weights and the fault or non-fault indicating information from the detection algorithms, the supportive and non-supportive evidence is calculated. The combinations of this multiple information are the combination of the two pieces of evidence.

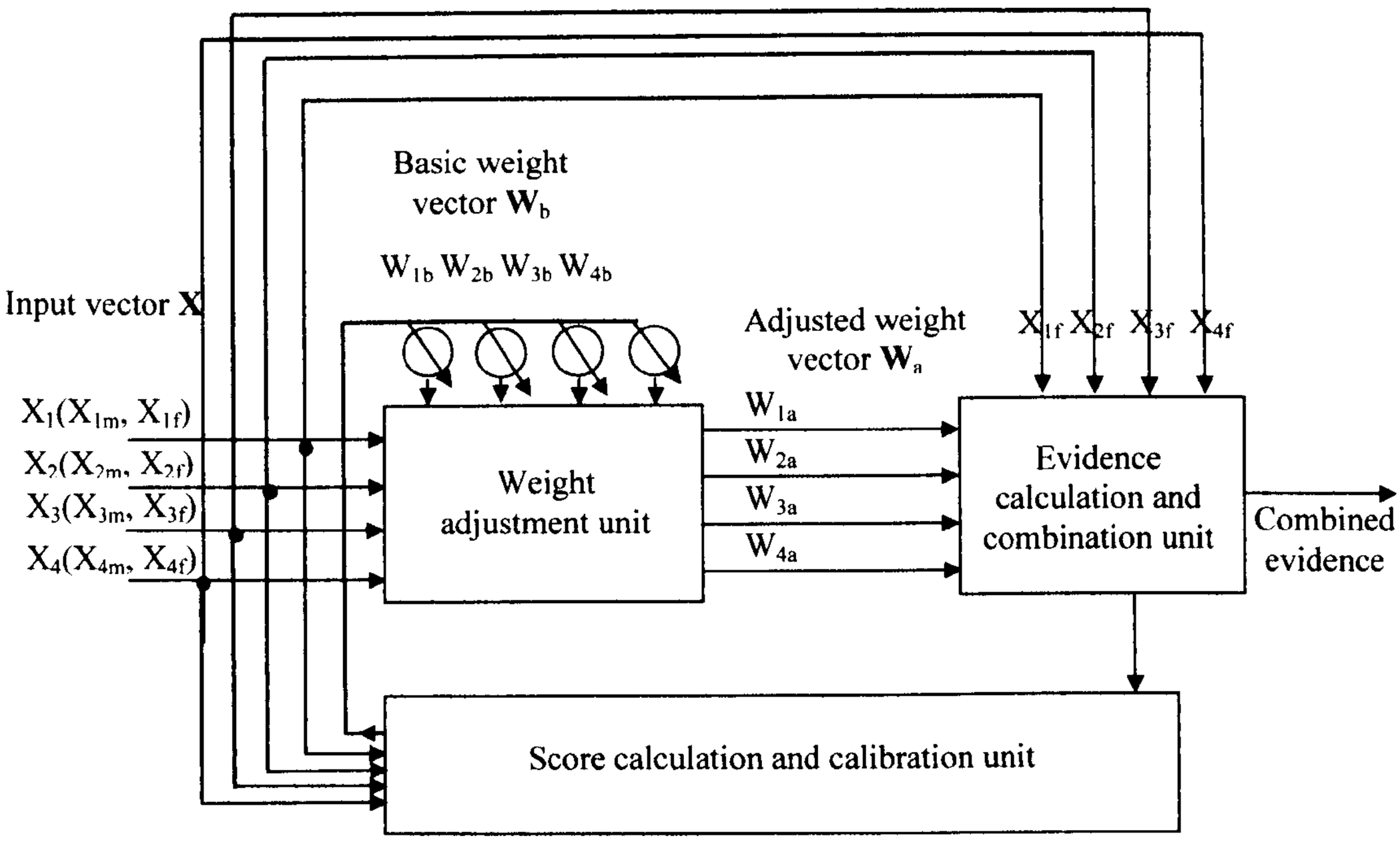

Figure 2.21: Structure of adaptive detection system

The variables used in the adaptive method are three columns vectors: the input vector (X), the basic weight vector (W_b) and the adjusted weight vector (W_a) as indicated in Fig. 2.21.

The input vector has two components: the maximum indication number (X_m) and the number of fault indications (X_f). The reason there are two components is that during the time process there can be more than one fault occurring. Therefore, it has to be taken into account.

The output indications of each detection algorithm have different uncertainty levels, so experts assign basic weights on the detection algorithms. The basic weights indicate the expert's confidence level on the detection algorithm in the assumed situation where only one detection algorithm was employed to detect a fault. Therefore, a basic weight is independent of other weights similarly derived from the corresponding detection algorithms.

The adjusted weight is used to adjust the basic weight when X_f is greater than 1. This is because the basic weight is set based on the original scheme of each detection algorithm with just one fault indication (i.e. $X_f = 1$) and it is not appropriate. Therefore, the basic weight needs to be adjusted if $X_f > 1$, but this adjustment of basic weight is not easy.

This method was applied to HV networks and high impedance fault detection and only gave correct indication of faults 70% of the time while keeping false fault indication at 0%. Increasing the false indication will decrease the correct indication of faults. This method also relies on an expert's confidence level to set the basic weights, so it is not an automatic operation.

The method described in [68] is based on the characteristics of High Impedance Faults (HIF). The characteristics of HIF are fault current magnitude, magnitude of the 3rd harmonic current, magnitude of the 5^{th} harmonic current, the angle of the third harmonic current, the angle difference between the third harmonic current, the fundamental voltage, and the negative sequence current of HIF. These characteristics are identified from models of distribution feeders using the Electromagnetic Transient Program (EMTP). This adaptive method calculates and stores the average load current and the average negative sequence current. The average currents are calculated at 5 minute intervals. The measured rms load and negative sequence current are compared with the stored average values. If there is an increase or decrease in the load current by 20% (adjustable) or an increase in the negative sequence currents by 20% (adjustable), then that phase is identified as exhibiting HIF.

A fault current above the maximum expected load current is defined as Low Impedance Fault (LIF). LIF current can be detected easily by over current relays. Detection of LIF is based on threshold settings for the average load current.

The magnitudes of the 3^{rd} and 5^{th} harmonic current are used to distinguish capacitor switching, load switching, or an arc furnace from HIF. This adaptive method is implemented using logic circuits for HIF and LIF.

The magnitude of the fault current is calculated as follows: the load current measured at the substation is compared with the over current relay pickup value for LIF detection. It is also compared with the normal average load current for HIF. If the load current is greater than the over current pickup value, then it is classified as LIF. If the load current magnitude is less than the normal average load current, then it is identified as HIF. When HIF occurs, the 3rd harmonic current is higher than the 3rd harmonic current when load switching occurs. Furthermore, when HIF occurs, the 3rd harmonic current is higher than the 5th harmonic current. It is also shown that during a HIF, the phase of the 3rd harmonic current lagged the corresponding voltage by about 180 to 220 degrees. Finally, when HIF occurs, the negative sequence current will be superimposed with the negative sequence fault current. Therefore, the magnitude of the negative sequence current will increase during the HIF. All this information is implemented in the logic circuit to detect LIF and HIF. The logic circuit provided for both LIF and HIF detection is in one module. This method has been implemented for HV network fault detection only [67, 68].

2.3.6. Statistical Hypotheses Testing Method

In [44], a statistical hypothesis method is applied to find fault locations on distribution networks. This method only requires the information of the time when power is lost for an extended period at various customer ends in the distribution system. Such outages will be due to a permanent fault resulting in fuse operation or breaker lock out. The time measurements do not have to be precise. The timer will not record for temporary loss of power such as the "dead times" of re-closer operations, and it will not trigger for the transient during faults such as low voltage. This method can also give information about the fault type. The information about the time of outage is recorded via a communication medium, such as high frequency radio or fibre optic. To record the time of outage, the meters at the customer need modification. The meters also require battery power for data storage and for communication with the control centre.

This method first categorises the types of fault, so that they can be analysed in a statistical manner. The types of fault that this method dealt with are high impedance faults with a broken conductor, low impedance faults with a broken conductor, and low impedance faults without a broken conductor. The first type of fault occurs when the fault current is not large enough to operate the over current protective device, but

it forces a power outage only to the customers connected downstream of the point of fault. The second one will operate the closest protective device upstream of the fault. It will provide two sets of outage data. One from the customers downstream of the point of fault and the other representing the time at which the fuse blew or breaker locked out. The latter one will be recorded by the customer upstream from the fault point up to the fuse or breaker location. For the last type of fault, all customers on the feeder will lose power simultaneously. Therefore, only one value for the time of outage will be recorded at all customer ends that will be the time when the fuse ruptured or the breaker locked out.

The method proceeds by hypothesising a fault point. The data is then clustered into two groups. One belongs to the upstream and the other to the downstream of the hypothesised point of fault. Then the statistical difference between the upstream and the downstream values are calculated. To compare the mean of two normal populations with equal variances, the Student's t-test is used. It was assumed that the variances of the two populations are the same, because the timers used for measurements of time at each location will be similar. To determine the correct fault location, the hypotheses of faults are then moved to another location and a t-statistic is determined. Similarly, t-statistic values are determined for all possible locations in the distribution system. The location at which the t-statistic has the highest value is chosen as the correct location of the fault. This is because at that point, the difference in the mean values of the two populations will be the maximum and the pooled standard deviation will be minimum.

This method will help to identify the fault location between two nodes, but cannot identify the exact fault location. To find the outage time equipment needs to be installed on every single node, which will be costly.

2.3.7. Fuzzy Set Method

Modelling uncertainty in the fault location process of distribution networks is discussed in this method [45]. This uses the heuristic knowledge of the control centre operators together with the information obtained from the network database and Supervisory Control And Data Acquisition (SCADA) system. The information is obtained from the above sources and grouped into membership functions of fuzzy sets. The membership functions used in this paper are estimates of fault location, operation of fault detectors, fault sensitive components, and overhead line section

information. By linking the information to these membership functions obtained from the system the fault location can be identified. The highest value of a line section will be identified as the fault line. This method only applies to the location of permanent faults in distribution networks.

2.3.8. Fault Location Using Wavelets

This method uses the wavelet transform to analyse travelling wave transient signals to locate faults [59]. The wavelet transform is localised in frequency as well as in time. Therefore, it is used to extract time resolution for the high frequency components of the fault transient. Wavelet transform theory can be found in chapter 3. This method of fault location is demonstrated using data from double ended and single ended recording from transmission line. This method is only demonstrated for a transmission line with no branches. This method is similar to the impulse current method except that the wavelet transform is used to analyse the signal.

2.4. Conclusion

In this chapter, fault classifications in LVUDN and fault location techniques were discussed. Some of the fault location techniques cannot be applied to LVUDN fault location. This is because:

- Voltage restrictions for testing instrument due to live line fault location,
- Multiple tees in the network,
- Limited test access points, and
- Network is loaded.

Presently, there is no single fault location technique that can be used for locating all four types of faults that are described in section 2.2. This is because, the behaviour of the faults is different. The fault location techniques that were described in section 2.3 can only locate one or two of the types of fault that were described in section 2.2. All the fault location techniques described above require at least some user input, and interpretation of results.

In the next chapter, signal processing tools are described.

Chapter 3

3. Signal Processing Tools

3.1. Introduction

Novel signal processing tools such as adaptive filters, wavelet transforms, and fuzzy logic have been used in a number of applications such as image processing, instrumentation and control, speech and audio processing, military applications, telecommunications, biomedical engineering, and power engineering. This chapter reviews signal processing tools that are used in this research work. They are adaptive filters, wavelet transform, and fuzzy logic.

In section 3.2, linear adaptive filtering, Least Mean Square (LMS), Normalised LMS (NLMS), and Recursive Least Square (RLS) adaptive algorithms are discussed. The Short-Time Fourier transform, Discrete Wavelet Transform, Continuous Wavelet Transform, and Subband Coding Scheme theories are discussed in section 3.3. In the next section, Fuzzy set theory, Set theoretic operators, α-cuts, and fuzzy decisions are discussed in detail. Finally conclusion of this chapter is presented.

3.2. Adaptive Filtering

Adaptive filters have found usage in many applications such as echo cancellation [34-36], speech modelling [34, 36], multipath compensation [34], radar signal processing [34-36], noise cancelling [35, 36], navigation systems [34], and biomedical signals enhancement [34]. This is because of their time-varying and self-adjusting performance. There is a considerable number of adaptive filtering algorithms available [34-36, 68].

An adaptive filter is a filter containing coefficients that are updated by an adaptive algorithm to optimise the filter's response to a desired performance criterion. It also has the property that its frequency response is adjustable or modifiable automatically to improve the performance in accordance with some criterion, allowing the filter to adapt to changes in the input signal characteristics. They are used in a number of application areas with different input and output configurations.

3.2.1. Linear Adaptive Filters

The basic structure of an adaptive filter is shown in Fig 3.1. It consists of an input signal *x(k)*, a desired(reference) signal *d(k)*, an output filtered signal *y(k)*, and an error signal *e(k)* which are related as follows:

$$e(k) = d(k) - y(k) \tag{3.1}$$

where

$$y(k) = Filter\ [\ x(k)\ ] \tag{3.2}$$

Filter [.] is an adaptive linear filter.

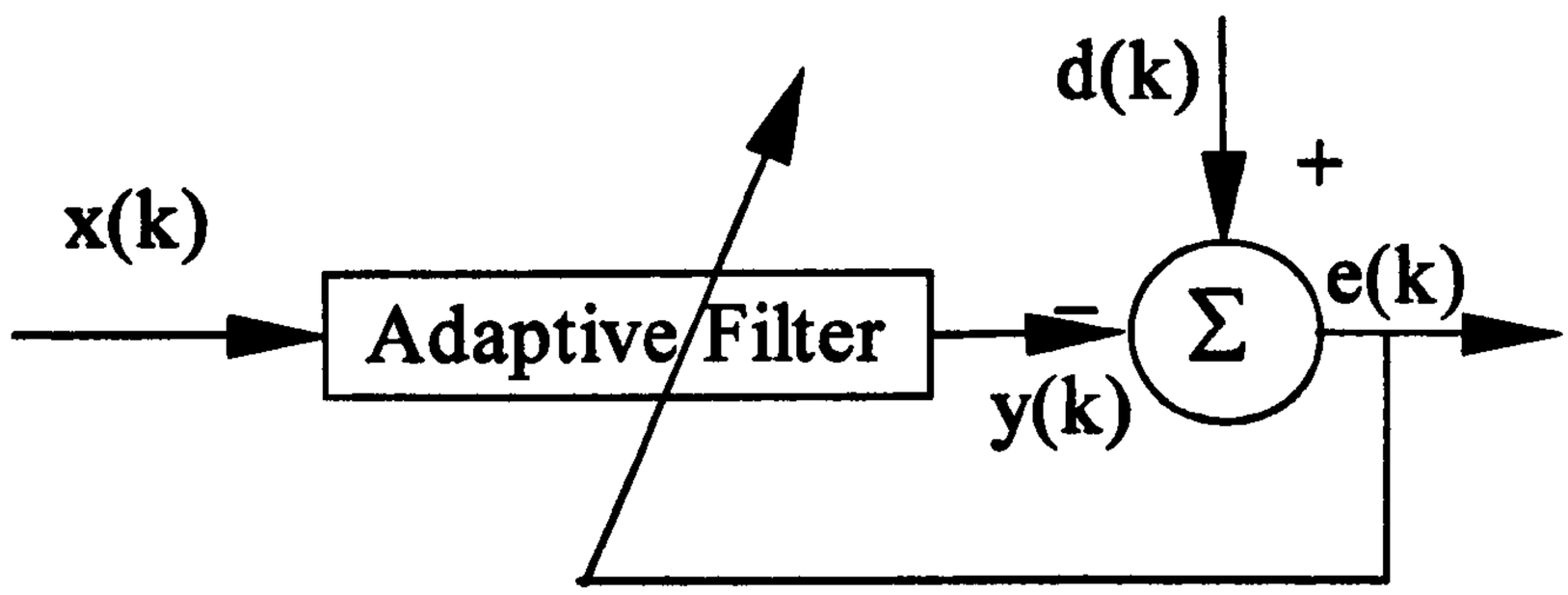

Figure 3.1: A basic adaptive filter structure

If we consider the filter to be a Tapped Delay Line (TDL) then the output of the filter *y(k)* is expressed as:

$$y(k) = \sum_{i=0}^{N-1} w(i)x(k-i) = \mathbf{w}^T \mathbf{x}(k) \tag{3.3}$$

where *x(k)* represents the sequence of the input data, w*(i)* represents the weights (filter coefficients), *N* is the number of weights (or taps) in the adaptive filter.

The adaptive filter attempts to exploit any correlation between *x(k)* and *d(k)*. The characteristics of the filter are changed in an iterative manner, such that its output approximates the correlated component of the desired signal [34, 36] as illustrated in Fig. 3.2.

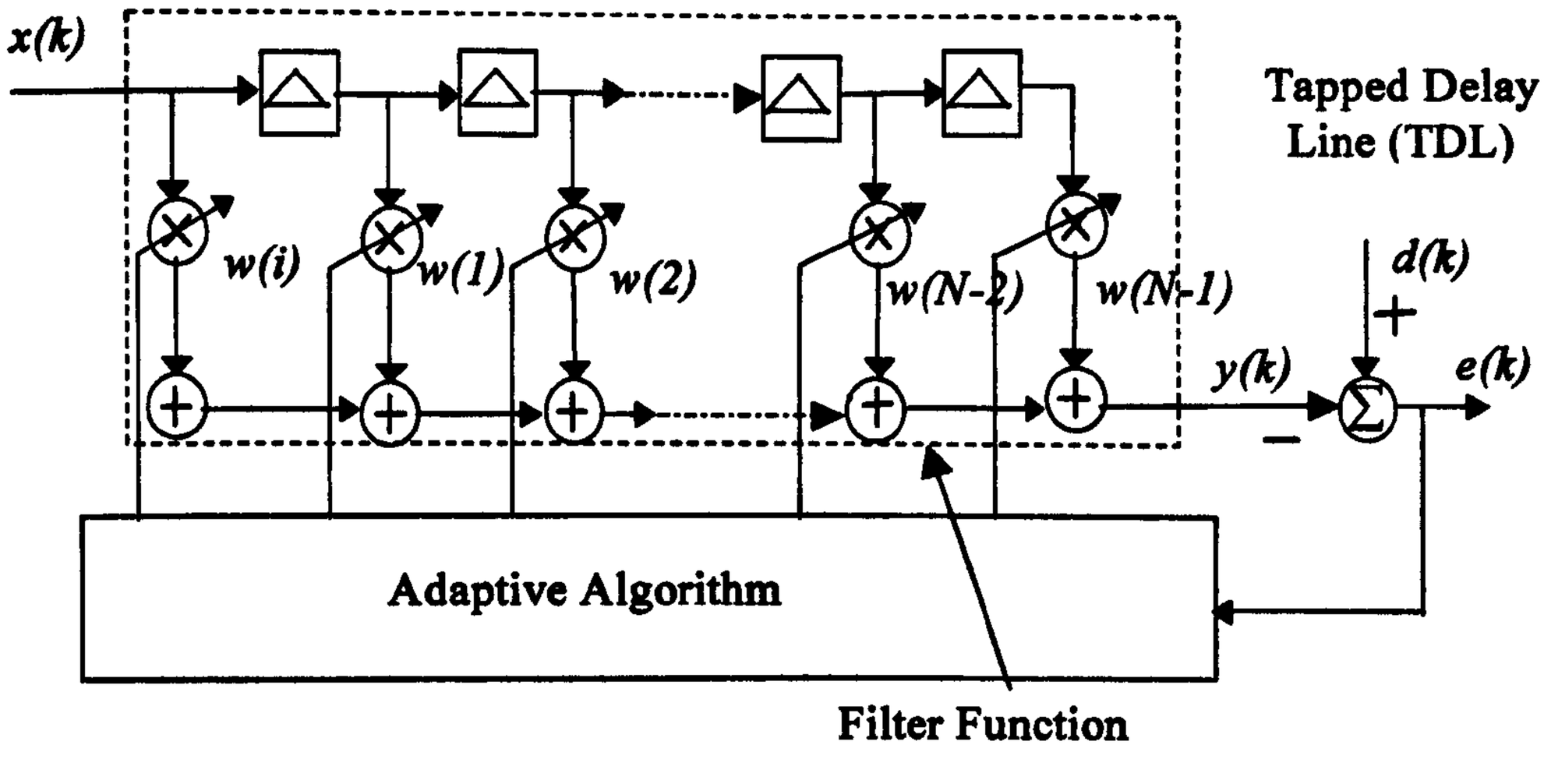

Figure 3.2: Detailed structure of an adaptive filter

The error signal is given by:

$$e(k) = d(k) - y(k) = d(k) - w^T \mathbf{x}(\mathbf{k}) \tag{3.5}$$

The Mean Squared Error, *MSE*, is given by $E[e^2(k)]$ and it can be shown [5] that the *MSE* is

$$MSE = \xi = E[e^2(k)] = E[d^2(k)] + w^{\mathrm{T}}\mathbf{R}w + 2\mathbf{P}^{\mathrm{T}}w \tag{3.6}$$

where $E[.]$ represents the statistical expectation operator, $E[d^2(k)]$ is the variance of d(k), $\mathbf{P} = E[d(k)\mathbf{x}(k)]$ is the m length cross-correlation vector and $\mathbf{R} = E[\mathbf{x}(k)\mathbf{x}(k)^T]$ is the $m \times m$ auto correlation matrix.

A plot of the *MSE* against the filter coefficients (assuming 2 tap weights *w(0)* and *w(1)*) is a bowl shaped (parabola) with a unique vertex as shown in Fig. 3.3. This figure is known as the performance surface and is non-negative.

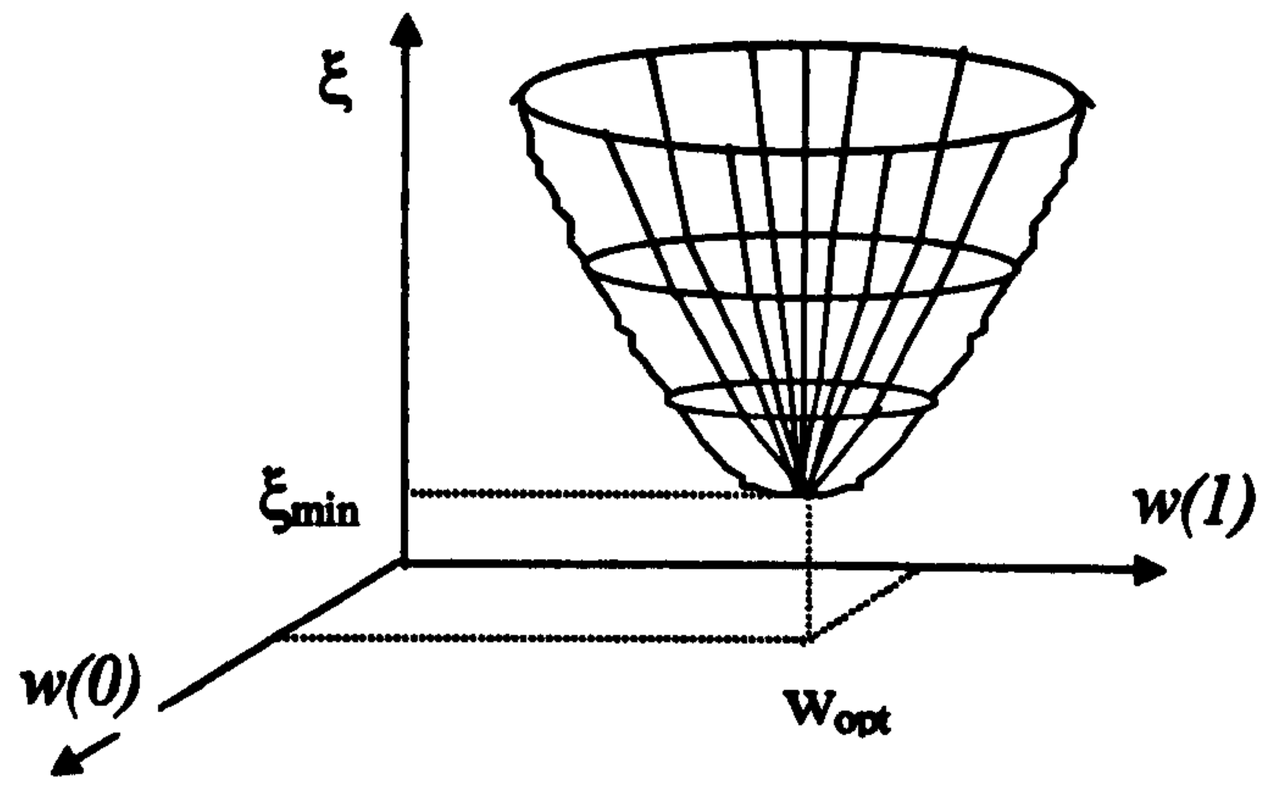

Figure 3.3: Error performance surface

The gradient of the *MSE* is given by Eq. (3.7) [2].

$$\nabla(\xi) = \frac{\partial \xi}{\partial w} = 2\mathbf{R}w - 2\mathbf{P} \tag{3.7}$$

To find the minimum value for the *MSE* the gradient is set to zero and the filter weight vector has its optimum value, w_{opt} is given by Eq. (3.8).

$$w_{opt} = \mathbf{R}^{-1}\mathbf{P} \tag{3.8}$$

This solution in Eq. (3.8), known as the Wiener-Hopf solution [37], gives us the optimum set of values for the weight w. Unfortunately, this method is limited [34] because

- it requires the auto-correlation matrix, **R**, and the cross-correlation vector, **P**, both of which are normally not known *a priori*,
- it involves matrix inversion, which is time consuming, and
- if the signals are non-stationary, then both **R** and **P** will change with time and so w_{opt} will have to be computed repeatedly.

Therefore, for real-time applications, a method for obtaining w_{opt} on a sample-by-sample basis is required. A widely used method for optimisation is the steepest descent algorithm [35, 36]. This will now be used to develop the classical LMS adaptive algorithm.

3.2.2. Least Mean Square (LMS) Algorithm

One of the most successful adaptive algorithms is the LMS algorithm, which was developed by Widrow and his co-workers [33, 35]. Instead of calculating w_{opt} using the Wiener-Hopf solution, in LMS it was calculated using the steepest descent algorithm. The Steepest descent algorithm is a way of calculating an optimum value of a multidimensional performance surface [37]. The steepest descent algorithm uses an initial value for the tap-weight vectors, which provides guess of the *MSE* and then it calculates the gradient vector for that particular value. The next guess of the tap-weight is made by changing the tap-weight vector in a direction opposite to the gradient vector as indicated in the following equation.

$$w(i+1) = w(i) - \mu\nabla(k) \tag{3.9}$$

where $w(i)$ is the weight, μ is the step size, and $\nabla(k)$ is true gradient. The true gradient ($\nabla(k)$) is calculated from the instantaneous squared error $|e(k)|^2$. The above process is repeated until it reaches the minimum gradient vector of the *MSE*.

The step size, μ, is chosen in such a way that the minimum *MSE* is approached. If the μ value is chosen too large, the variance of the *MSE* will be large and potentially unstable. On the other hand, if the value of μ is chosen too small, the convergence time will be excessive.

The weight update can be re-written as:

$$w(i+1) = w(i) - \mu\left(\frac{\partial}{\partial w(i)} e^2(k)\right) \tag{3.10}$$

The calculation of the gradient is as follows:

$$\frac{\partial}{\partial w(i)} e^2(k) = 2e(k)\left(\frac{\partial e(k)}{\partial w(i)}\right) = 2e(k)\left\{\left(\frac{\partial d(k)}{\partial w(i)}\right) - \left(\frac{\partial y(k)}{\partial w(i)}\right)\right\} = -2e(k)\mathbf{x}(k) \tag{3.11}$$

Eq. (3.10) now becomes:

$$w(i+1) = w(i) + 2\mu e(k)\mathbf{x}(k) \tag{3.12}$$

This is the classical LMS developed by Widrow and his co-workers [33, 35].

An example of LMS adaptive filtering algorithm process is illustrated in Fig. 3.4. In this figure x(k) is the input signal that consists of noise and g(k), d(k) is the desired

signal, y(k) is the output of the filter, and e(k) is the error signal. It is assumed that g(k) and d(k) are correlated each other. In this example the adaptive filter tries to exploit the correlation between the x(k) and d(k).

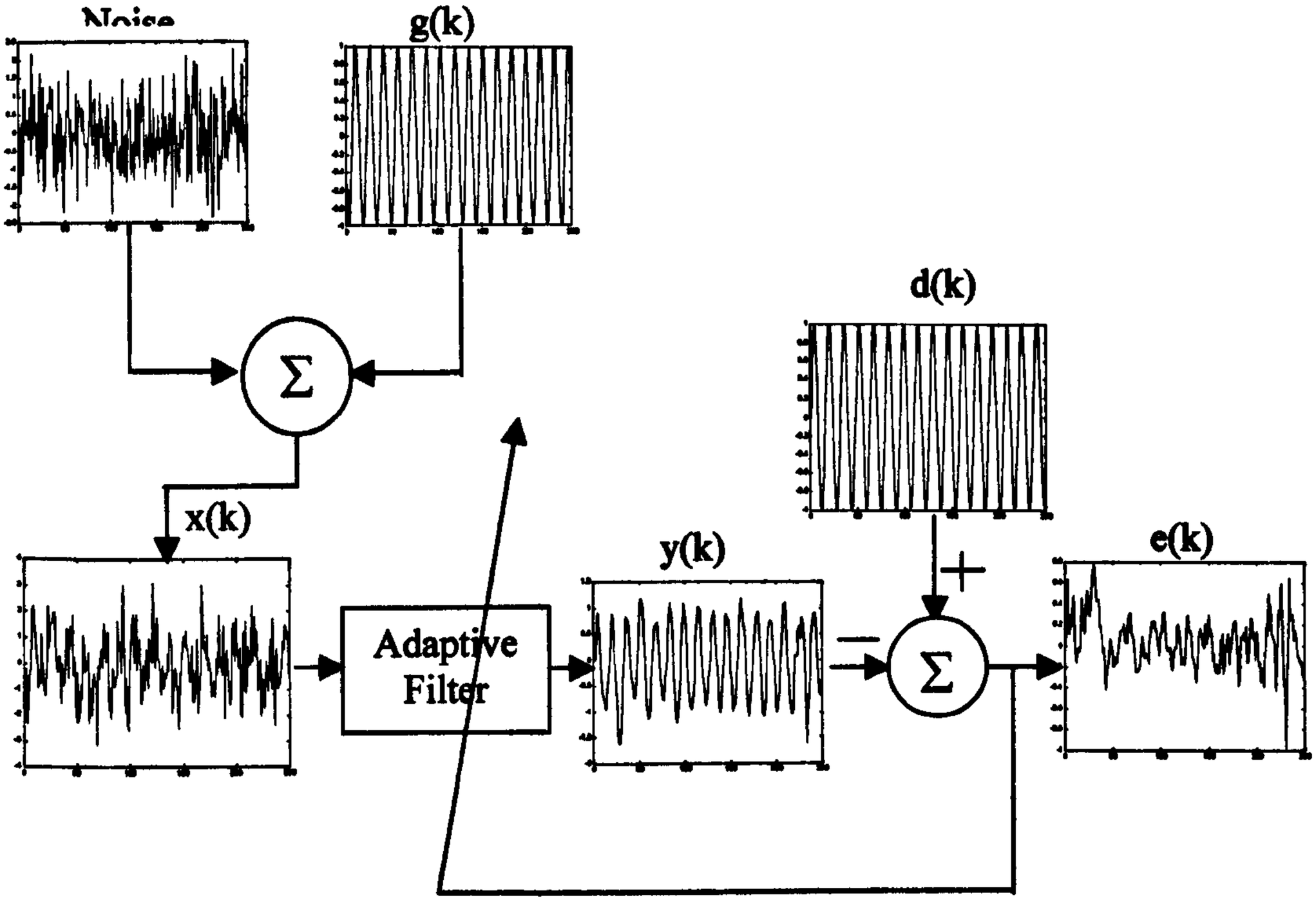

Figure 3.4: An example of LMS adaptive algorithm process

The weights obtained by the LMS algorithm are estimates, but these estimates improve gradually with time as the weights are adjusted and the filter learns the characteristics of the signals. Eventually, the weights converge. The condition for convergence is [33]:

$$0 < \mu < \frac{1}{\lambda_{max}} \tag{3.13}$$

where λ_{max} is the maximum eigenvalue of the input signal auto correlation matrix.

If the step size is chosen outside these bound, it is likely that the algorithm would become unstable and hence fail to adapt to an optimum value. In practice, w never reaches the theoretical optimum (the Wiener solution), but fluctuates about it [34].

3.2.3. Normalised LMS (N-LMS) Algorithm

In the standard LMS algorithm, the correction $\mu e(k)\mathbf{x}(k)$ applied to the tap-weight vector $w(i)$ at iteration $i+1$ is directly proportional to the input vector $\mathbf{x}(k)$.

Therefore, when $\mathbf{x}(k)$ is large, the LMS algorithm experiences a gradient noise amplification problem [36]. This is particularly important in non-stationary environments [34]. To overcome this problem, the normalised LMS algorithm can be used. In this method, the correction of the tap-weight vector *w(i)* takes place at iteration *i+1*. It is "normalised" with respect to the square Euclidean norm of the input vector $\mathbf{x}(k)$ at iteration *k*. The update of the weight vector is given by [36]:

$$w(i+1) = w(i) + \frac{\hat{\mu}}{a + \|\mathbf{x}(k)\|^2}\mathbf{x}(k)e(k) \tag{3.14}$$

where $\hat{\mu}$ is the adaptation constant, *a* is a positive small constant, and $\|\mathbf{x}(k)\|^2$ is the squared norm of the input vector

The adaptation constant, $\hat{\mu}$, is used to exercise control over the changes in the weight vector from one iteration to the next without changing its direction. The effective value of $\hat{\mu}$ is as follows:

$$0 < \hat{\mu} < 2 \tag{3.15}$$

When the input vector $\mathbf{x}(k)$ is small, numerical difficulties may arise because then we have to divide by a small value for the squared norm $\|\mathbf{x}(k)\|^2$. To overcome this problem, a small positive constant *a* is used.

3.2.4. Recursive Least Square (RLS) Algorithm

The Recursive Least Squares (RLS) algorithm is an extension of the method of least squares [36]. In this method a least squares estimate of the transversal adaptive filter tap-weight vector at iteration (*m-1*), is recursively updated to form a new estimate of this vector at iteration (*m*) upon arrival of new data. An important feature of the RLS algorithm is that it utilises information contained in the input data, extending back to the instant of time when the algorithm is initiated. The resulting rate of convergence is faster by an order of magnitude than the LMS algorithm. This improves the performance, but increases the computational complexity.

If $e(k)$ is the difference between the desired response d(k) and the output y(k) of the transversal filter then the cost function $\xi(m)$ [36] can be defined as

$$\xi(m) = \sum_{k=1}^{m} \lambda^{m-k} |e(k)|^2 \tag{3.19}$$

where λ^{m-k} forms the exponential weighting (or forgetting) factor with λ a positive constant close to, but less than, 1.

The RLS algorithm is summarised below [36]:

$$\mathbf{K}(k) = \frac{\lambda^{-1}\mathbf{P}(k-1)\mathbf{x}(k)}{1+\lambda^{-1}\mathbf{x}^{H}(k)\mathbf{P}(k-1)\mathbf{x}(k)} \tag{3.20}$$

$$\varepsilon(k) = d(k) - \hat{w}\,\mathbf{x}(k) \tag{3.21}$$

$$\hat{w}(i) = \hat{w}(i-1) + \mathbf{K}(k)\varepsilon^{*}(k) \tag{3.22}$$

$$\mathbf{P}(k) = \lambda^{-1}\mathbf{P}(k-1) - \lambda^{-1}\mathbf{K}(k)\mathbf{x}^{H}(k)\mathbf{P}(k-1) \tag{3.23}$$

where $\mathbf{P}(k)$ is the inverse of the exponentially weighted autocorrelation matrix, $\mathbf{x}(k)$ is the input tap-weight vector for the transversal filter, $\varepsilon(k)$ is the priori estimation error, $\mathbf{K}(k)$ is gain vector, and $\hat{w}$ is the tap-weight vector.

Equation (3.21) describes the filtering operation of the algorithm, whereby the transversal filter is able to compute the *a priori* estimation error $\varepsilon(k)$. The tap-weight vector is updated by the equation (3.22) and the gain vector is updated by the equations (3.20), and (3.23).

The performance and computation of the above three adaptive algorithms are given in table 3.1.

Algorithms	LMS	N-LMS	RLS
Addition(+)/Subtraction(−)	2N	3N	$2N^2+2N$
Multiplication (×)	2N+1	3N+1	$2N^2+4N$
Division (÷)	0	1	1
Data Storage	2N+3	2N+4	N^2+4N+4

Table 3.1: Summary of Computational Complexity and Data Storage Requirements of the Three Adaptive Algorithms

3.3. Wavelet Transform Theory

Wavelet theory has been developed rapidly in recent years and it has been widely used for a number of applications in different fields of science and engineering. For example, multi-resolution signal processing, computer vision such as; subband coding, developed for speech and image compression; wavelet series expansions, fault location, and power distribution relaying [8-14]. Wavelet theory covers a wide area and deals with both continuous and discrete-time bases. It provides a very general technique that can be applied to many tasks in signal processing and therefore has numerous potential applications.

There are several types of wavelet transforms based upon its applications. For a continuous input signal, the time and scale parameters can be continuous [23], leading to the Continuous Wavelet Transform (CWT) [1-7]. On the other hand, discrete parameters [11, 24, 25, 27], lead to Wavelet Series expansion and the discrete time signals represented by the Discrete Wavelet Transform (DWT) [27].

The Wavelet Transform (WT) is of interest for the analysis of non-stationary signals, because it provides an alternative to the classical Short-Time Fourier Transform (STFT) [17-19]. The basic difference is that STFT uses a single analysis window whereas the WT uses short windows at high frequencies and long windows at low frequencies.

3.3.1. Short-Time Fourier Transform (STFT)

The aim of signal analysis is to extract relevant information from a signal by transforming it. For a stationary signal whose properties do not change in time, the well-known Fourier Transform (FT) is used. The FT (3.24) and its inverse (3.25) are defined by:

$$X(f) = \int_{-\infty}^{\infty} x(t) e^{-2j\pi ft}\, dt \tag{3.24}$$

$$x(t) = \frac{1}{2\pi} \int_{-\infty}^{\infty} X(f) e^{2j\pi ft}\, df \tag{3.35}$$

The FT works well if the signal *x(t)* is composed of a few stationary components such as sine waves. However, any abrupt change in time in a non-stationary signal *x(t)*

is spread out over the whole frequency axis in $X(f)$. Therefore, an analysis adapted to non-stationary signal requires more than the Fourier Transform.

For non-stationary signal analysis, Gabor [17] introduced the Short-Time Fourier Transform (STFT). The idea was to use an analysis window so that the signal is analysed through the window over which the signal is approximately stationary. The STFT decomposes the signal into a two-dimensional time-frequency representation $S(\tau,f)$ of the signal $x(t)$ is composed of spectral characteristics depending on time. The signal $x(t)$ is assumed to be stationary when seen through a window $g(t)$ of limited length, centred at time location τ. The Fourier Transform of the windowed signals $x(t)g^*(t-\tau)$ yields the Short-Time Frequency Transform (STFT):

$$STFT(\tau,f)=\int_{-\infty}^{\infty}x(t)g^*(t-\tau)e^{-2j\pi ft}\,dt \qquad (3.26)$$

Equation (3.26), maps the signal onto a two-dimensional function in a time-frequency plane (τ, f).

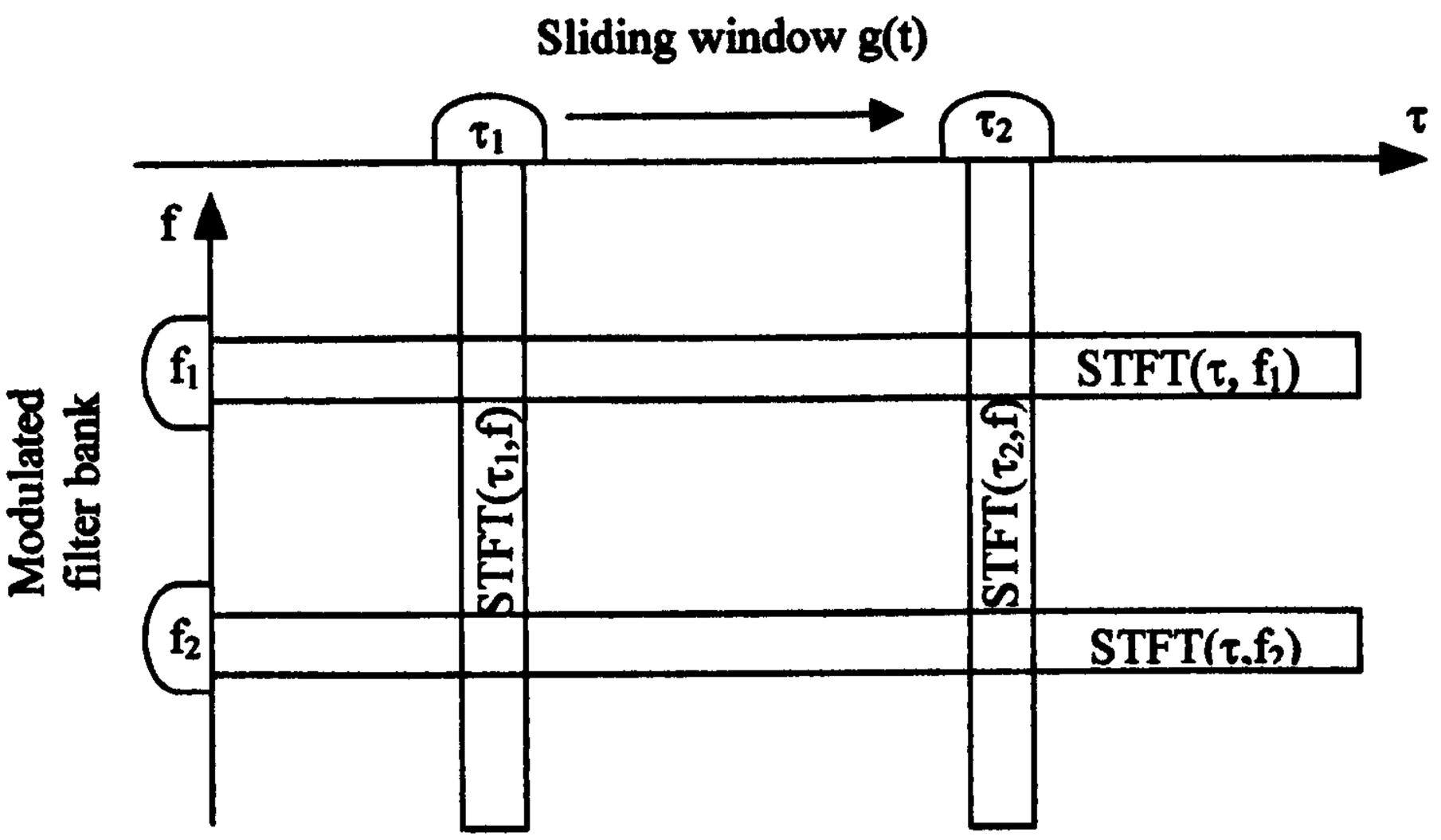

Figure 3.5: Time-frequency plane corresponding to the Short-Time Fourier Transform

The analysis of the STFT depends on the choice of window g(t). Fig. 3.5 shows vertical stripes in the time-frequency plane, illustrating this "window of the signal" view of STFT.

The main disadvantage of STFT is that once the window has been chosen, the time-frequency resolution is fixed over the entire time-frequency plane (since the same window is used at all frequencies). This is shown in Fig. 3.6.

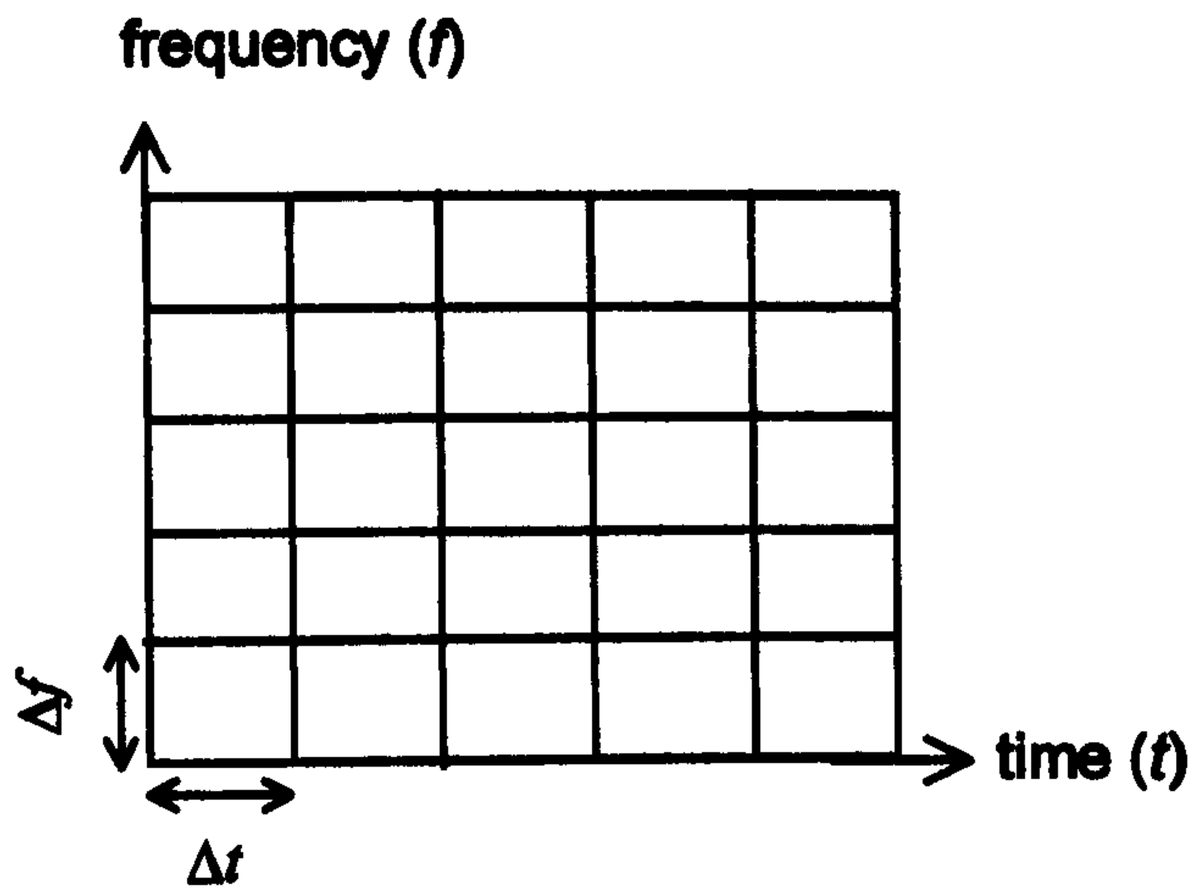

Figure 3.6: Coverage of time-frequency plane for the STFT

For better time resolution a smaller size window, and for better frequency resolution a larger size window is needed. The problem with STFT is that the same size window is used for all frequencies, so we can analyse with either good time resolution or good frequency resolution, but not both.

3.3.2. Wavelet Transform (WT)

In the last section, the time-frequency window was shown to be rigid when analysing a signal with STFT. This is because the width of the window was fixed when observing the frequency bands. Since the frequency is proportional to the number of cycles per unit time, it takes narrow time-window to locate high frequency component detail more precisely and a wide time-window to analyse low frequency components in more detail. The Wavelet transform provides a flexible time-frequency window that narrows when observing high frequency components and widens when analysing low frequencies. The Continuous Wavelet Transform (CWT) follows the ideas of changing resolution at different frequencies without depending on the signal. The next section discusses the Continuous Wavelet Transform.

3.3.2.1. Continuous Wavelet Transform (CWT)

The impulse responses of the filter in the CWT are defined as scaled versions of the same prototype $h(t)$:

$$h_a(t) = \frac{1}{\sqrt{|a|}} h\left(\frac{t}{a}\right) \tag{3.27}$$

where a is the scale factor that is defined as $1/f$ and $\frac{1}{\sqrt{|a|}}$ is used for energy normalisation. The definition of the CWT is [14]:

$$CWT(\tau, a) = \frac{1}{\sqrt{|a|}} \int_{-\infty}^{\infty} x(t) h^*\left(\frac{t-\tau}{a}\right) dt \tag{3.28}$$

The prototype function $h(t)$ is called the *basic* or *mother* wavelet and is used for all type of the filter responses. The explanation of Eq. (3.28) is that as the scale increases the filter impulse response $h\left(\frac{t-\tau}{a}\right)$ becomes spread out in time, and only takes into account long-time behaviour. If a is large then a global view is obtained and if it is small then a detailed local view is obtained. This is shown and compared to the STFT in Fig. 3.7.

To compare with STFT, the basic wavelet $h_a(t)$ in Eq. (3.24) can be chosen as modulated window [15, 23]:

$$h_a(t) = g(t) e^{-2\pi f_o t} \tag{3.29}$$

In general, $h_a(t)$ can be a band-pass function.

Another way to introduce the CWT is to define *wavelets* as basis functions and by rewriting the Eq. (3.28) as:

$$CWT(\tau, a) = \int_{-\infty}^{\infty} x(t) h_a^* dt \tag{3.30}$$

It measures the "similarity" between the signal and the basis functions:

$$h_{a,\tau}(t) = \frac{1}{\sqrt{|a|}} h\left(\frac{t-\tau}{a}\right) \tag{3.31}$$

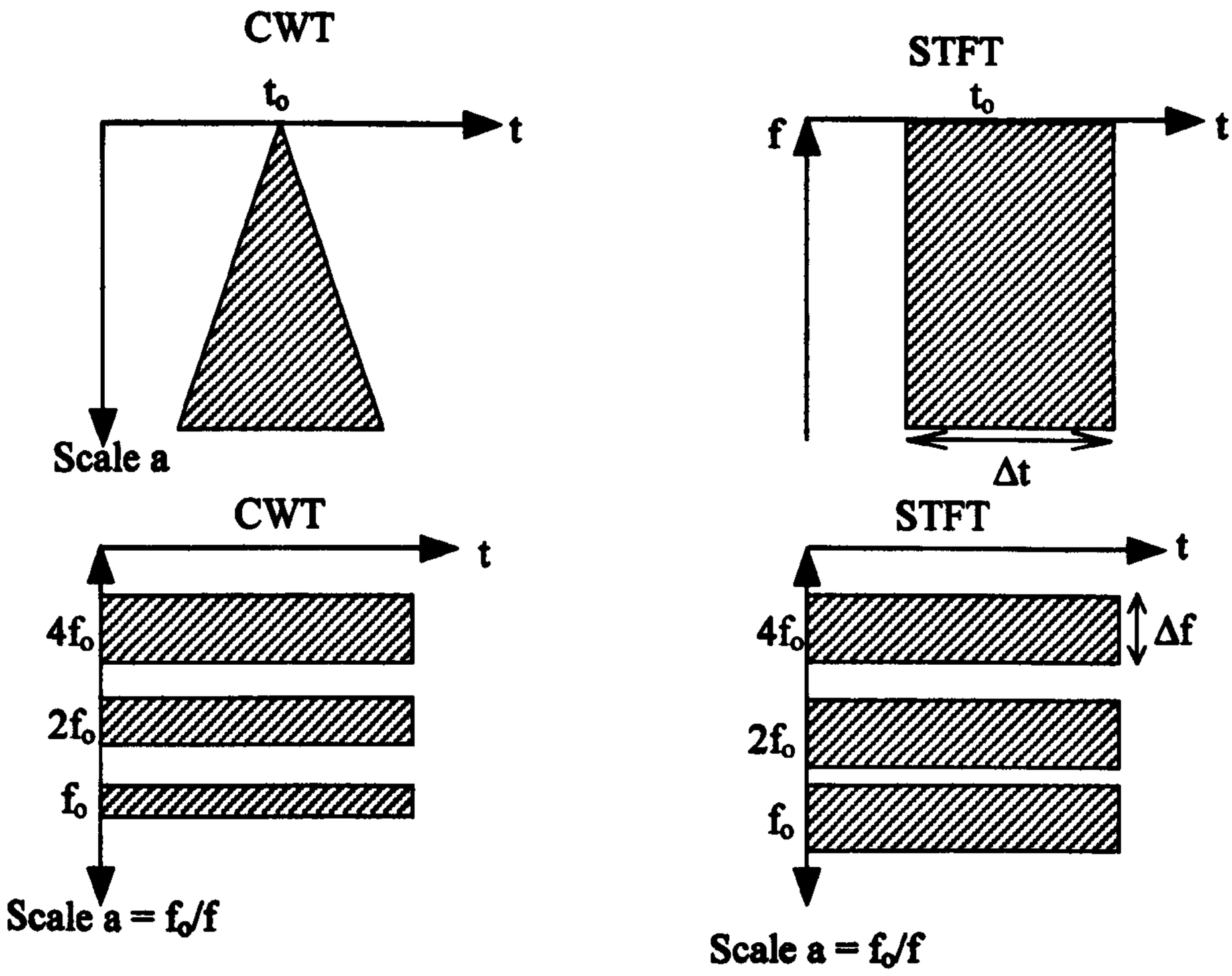

Figure 3.7: Scaled time and frequency domain responses of scaled wavelet transform

3.3.2.2. Discrete Wavelet Transform (DWT)

The CWT is highly redundant when the parameters (a, τ) are continuous, therefore if a and τ are discretised, the Discrete Wavelet Transform (DWT) is obtained. The natural way to discretise the time-scale parameters a and τ [24], is through Nyquist's rule. For the two scales $a_0 < a_1$, which correspond to two frequencies $f_0 > f_1$, the wavelet coefficients at scale a_1 can be sub-sampled at $(f_0/f_1)^{th}$ the rate of the coefficients at scale a_0, according to Nyquist's rule. The wavelets in Eq. (3.31) can be discretised by letting $a = a_0^j$ and $\tau = k a_0^j T$ in Eq. (3.31). where j and k are integers.

The corresponding wavelets are:

$$h_{j,k}(t) = a_0^{-j/2} h\left(a_0^{-j} t - kT\right) \tag{3.32}$$

that result in wavelets coefficients

$$C_{j,k}(x) = \int x(t) h_{j,k}^{*}(t) dt \tag{3.33}$$

The reconstruction of the signal can be obtained as follows [14]:

$$x(t) = \sum_j \sum_k C_{j,k} h_{j,k}(t) \tag{3.34}$$

3.3.2.3. Subband Coding Scheme

The subband coding scheme was first introduced in speech compression in the late seventies [20-22]. This scheme filters the signal with lowpass and highpass filters independently. An example of subband coding scheme is shown in Fig. 3.8.

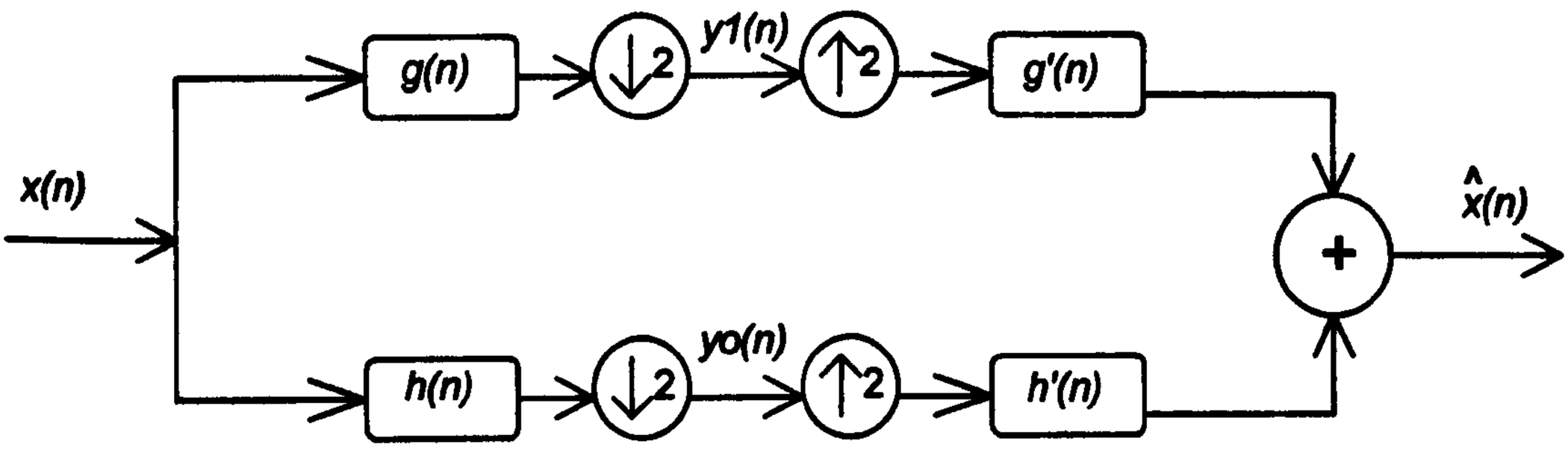

Figure 3.8: Subband Coding Scheme

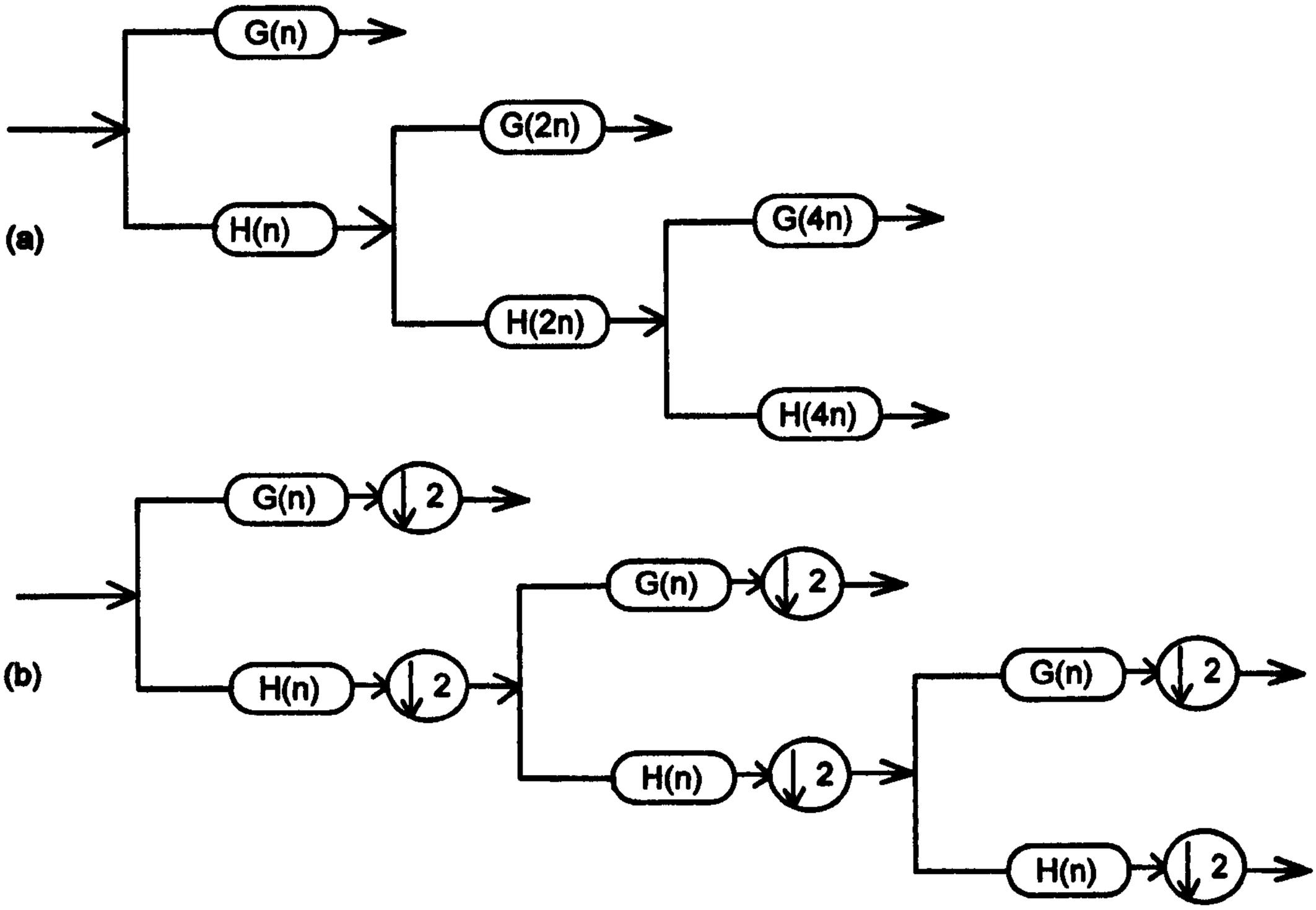

Figure 3.9: Subband coding scheme, Discrete Wavelet Transform implemented with discrete filters. (a) Without subsampling and with dilated filters, (b) With subsampling by a factor of two.

where $h(n)$ and $g(n)$ are the impulse responses of the lowpass and highpass filters respectively.

Once the process of the highpass and lowpass filtering is done then the filter outputs are down sampled by two. For the reconstruction the down sampled signal $y_1(n)$ and $y_0(n)$ are then upsampled and filtered with synthesis filters $g'(n)$ and $h'(n)$ respectively. The reconstructed signal $\hat{x}(n)$is not identical to the signal $x(n)$, unless the filters meet some specific constraints. There are number of papers investigating the design of perfect reconstruction filter banks [27- 30].

An iterated subband coding scheme with subsampling and without subsampling is shown in Fig. 3.9. The above iterated subband coding scheme is that the lowpass filtered signal is only further process with both highpass and lowpass filters independently. This process is continued until the required number of the iteration is reached. The highpass filtered signals are not involved in any further processing. Finally, the reconstruction of the signal is achieved as mentioned earlier. If subsampling is applied during the subband coding scheme then up sampling is applied before reconstructing the signals with dilated filters. Some recent subband coding scheme were published on multiresolution analysis [9, 16].

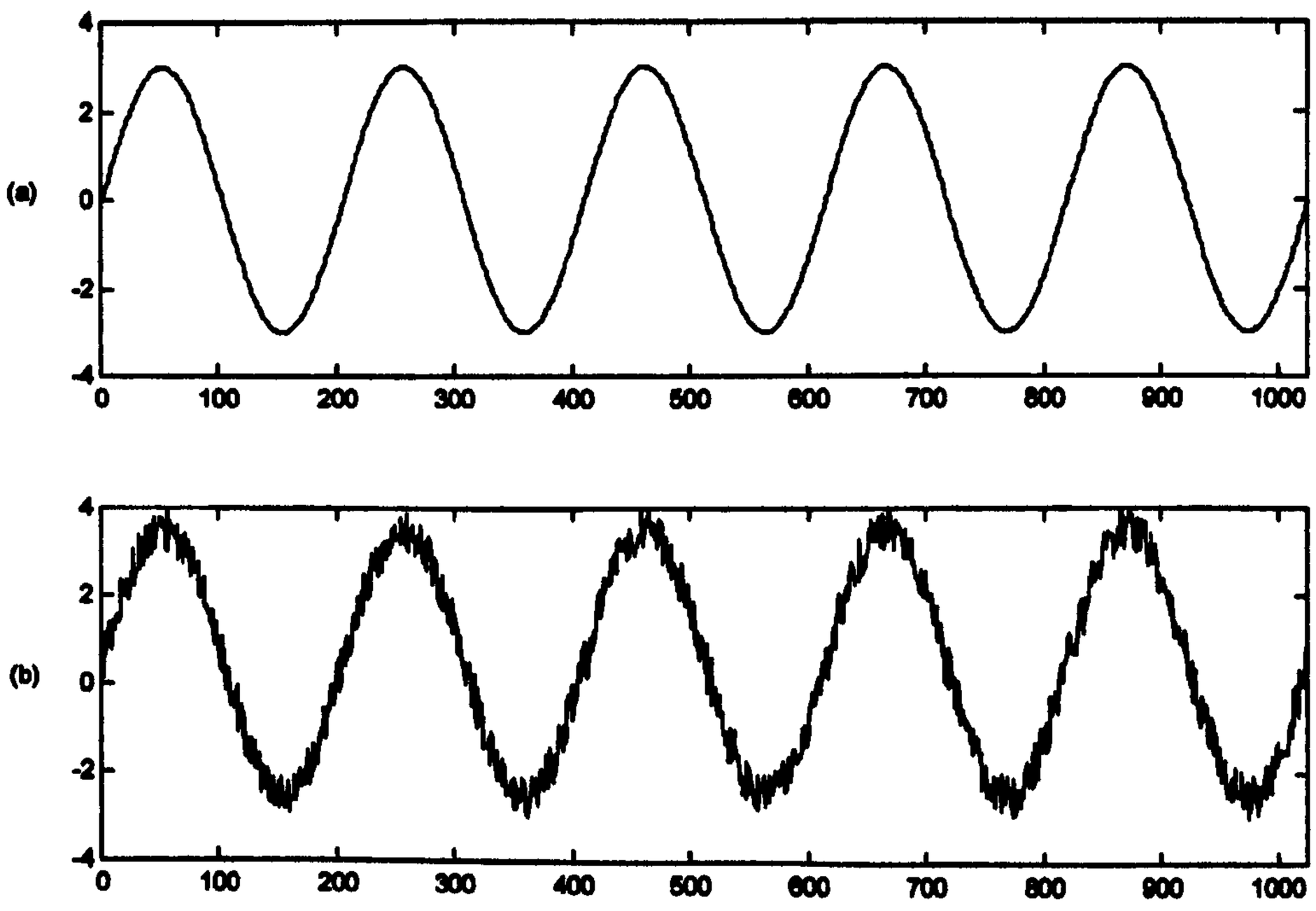

Fig.3.10 Sinusoidal Signal (a) Without noise, (b) Noise added

Fast numerical implementations, can be done by imposing the scale variation in a dyadic sequence (2^j) [9]. Where j is the number of scales.

A simple sinusoidal signal is shown in Fig. 3.10a and noisy sinusoidal signal is shown in Fig. 3.10b. The dyadic wavelet transform is applied to the noisy sinusoidal signal in Fig. 3.10b with 4 scales.

The resultant 4 scales for the lowpass and highpass filters are shown in Fig.3.11, 3.12 respectively. These lowpass and highpass filters allow processing the signal into individual scales. The process can be either to remove noise or for purpose of compression. Followed by processing, the signal can be reconstructed by applying the inverse wavelet transform to the scales. The reconstructed signal without denoising is shown in Fig. 3.13a. This figure shows that the wavelet transform can reconstruct the original signal. The denoised reconstructed signal is shown in Fig. 3.13b. This figure shows that the signal can be processed in each scale and then the signal can be reconstructed.

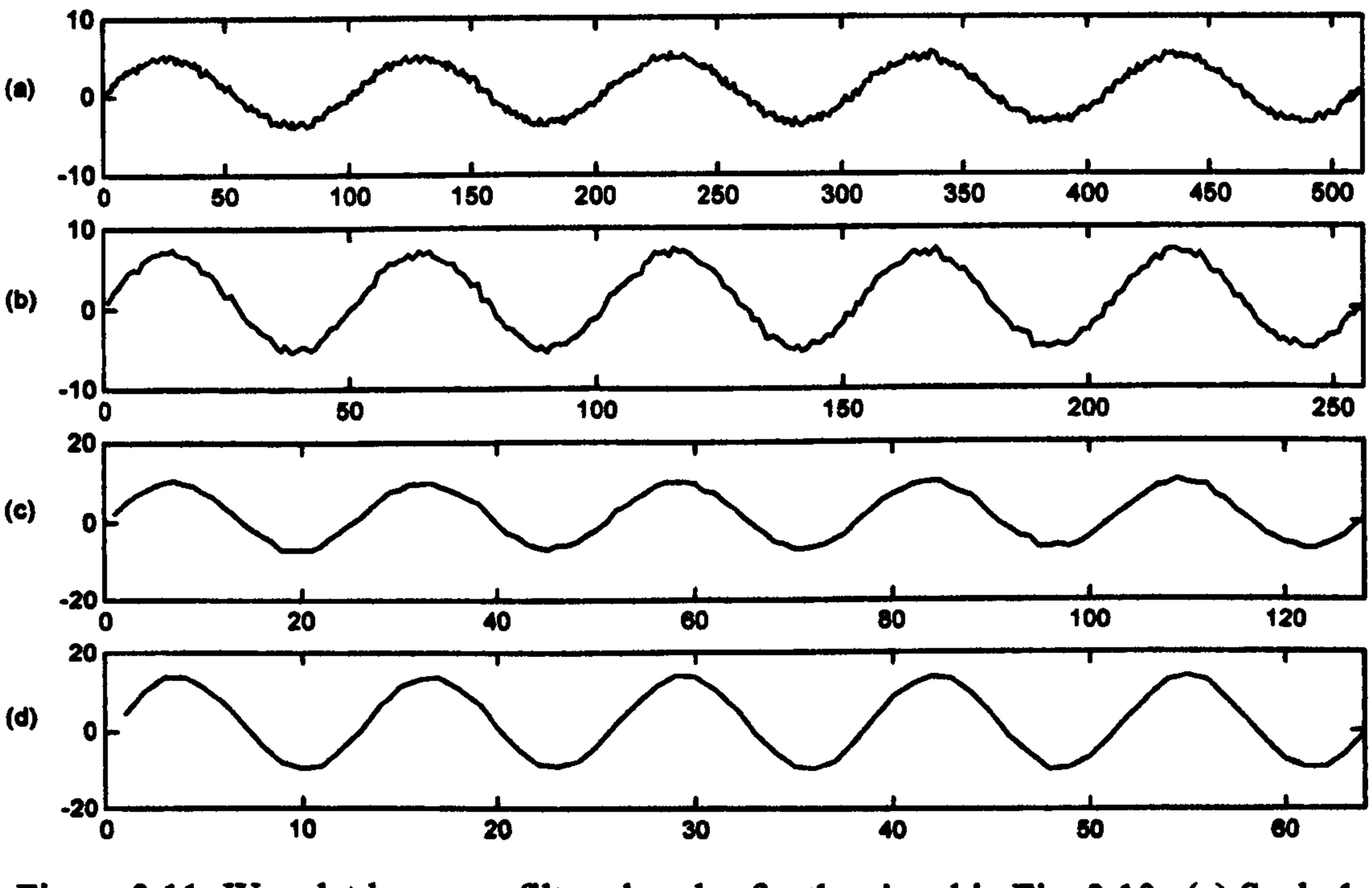

Figure 3.11: Wavelet low pass filtered scales for the signal in Fig. 3.10a (a) Scale 1, (b) Scale2, (c) Scale3, and (d) Scale4.

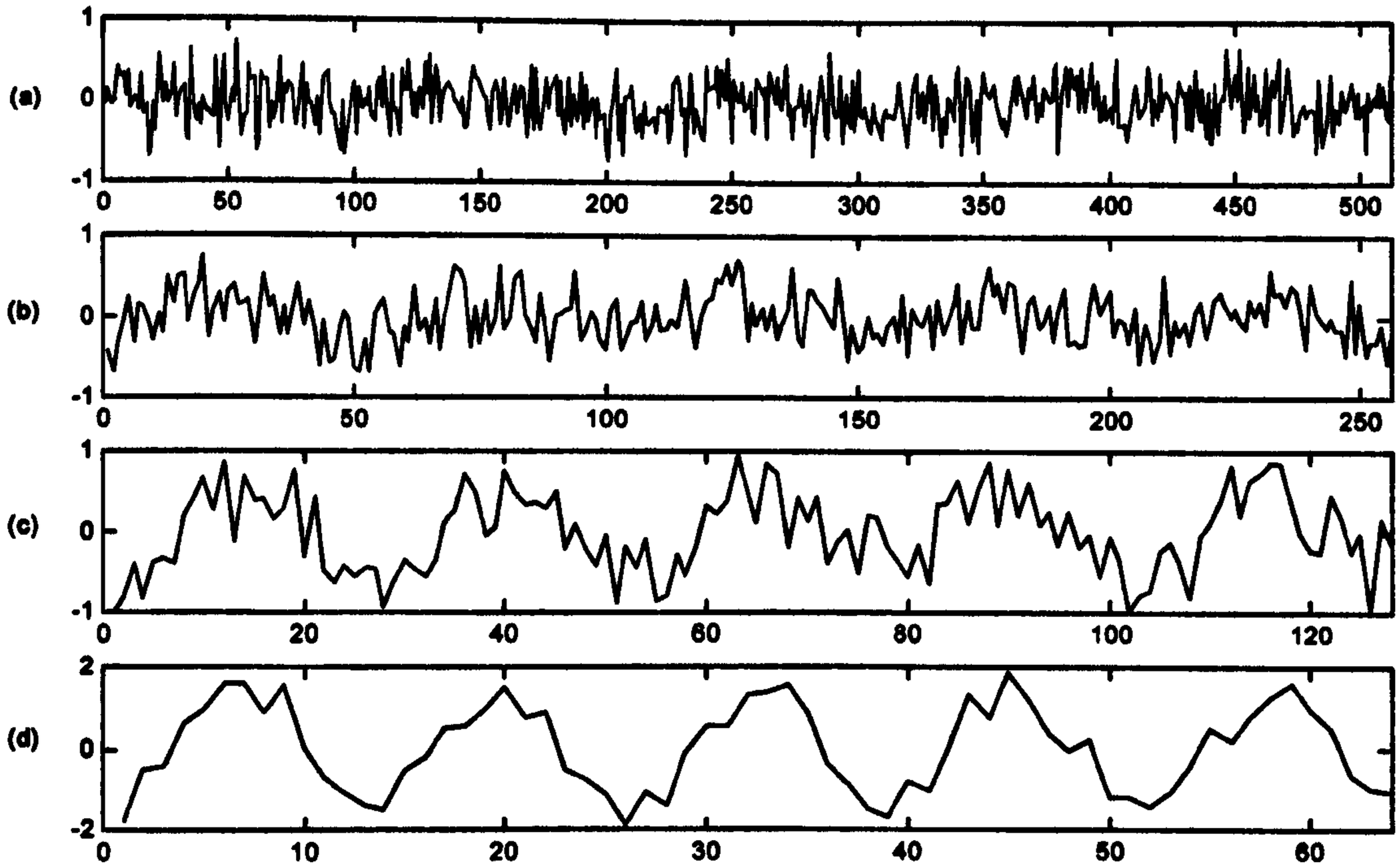

Figure 3.12: Wavelet high pass filtered scales for the signal in Fig. 3.10a (a) Scale 1, (b) Scale2, (c) Scale3, and (d) Scale4.

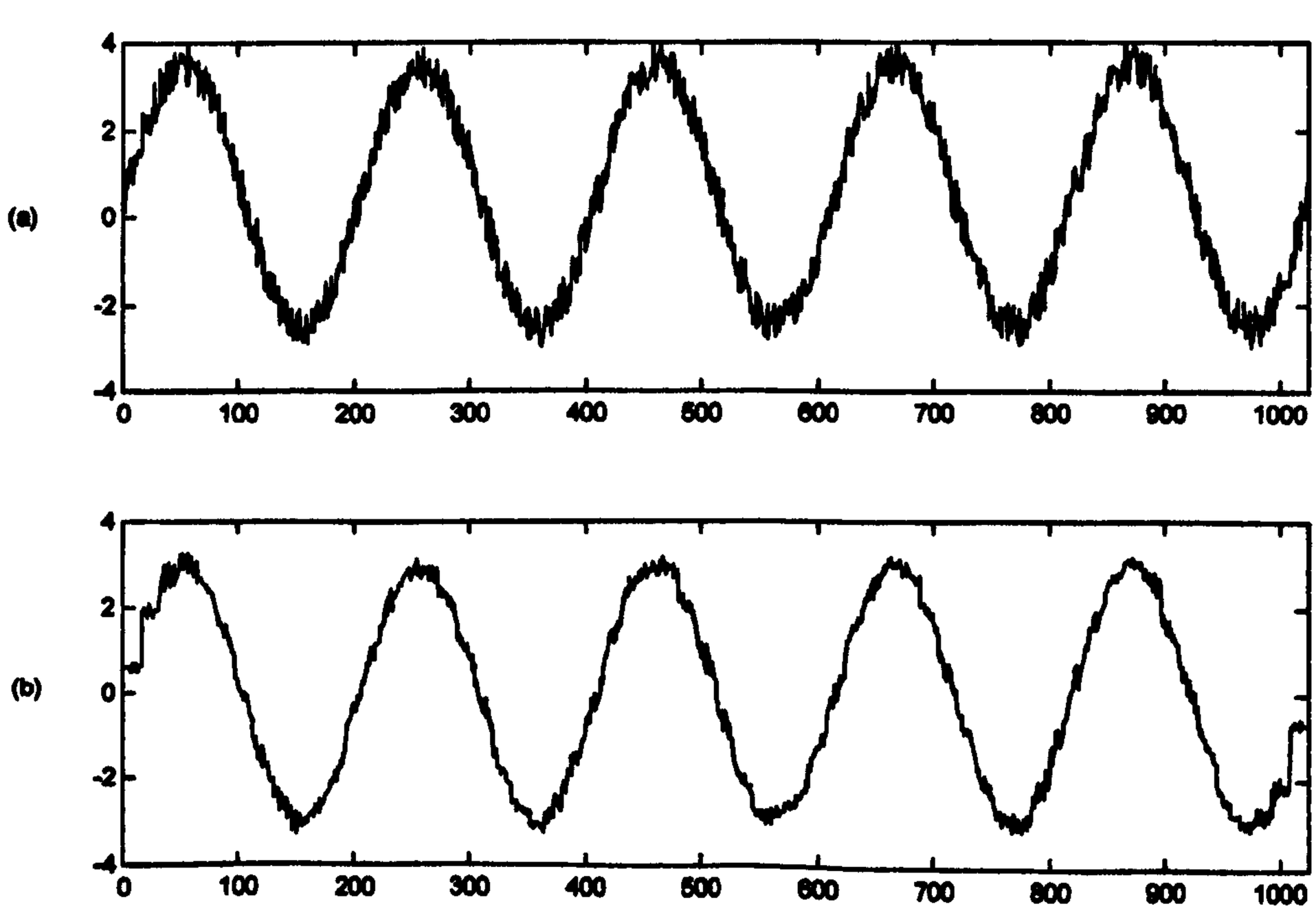

Figure 3.13: Wavelet Reconstructed signal (a) Without denoising , (b) With denoised

3.4. Fuzzy Set Theory

In 1965, Zadeh first introduced the theory of fuzzy sets [38]. Fuzzy set theory offers new methods for modelling the in-exactness and uncertainty associated with decision making. The fuzzy approach improves the potential for modelling human reasoning, presenting, and utilising linguistic descriptions in computerised inferencing.

In fuzzy set theory, the concept of possibility is used instead of the concept of probability. Where the possibility is defined by a number between one (completely possible) and zero (totally impossible). Probability is an appropriate measure of uncertainty if statistical information is available. In uncommon situations where no statistics are available, an expert may be able to express degrees of confidence in various hypotheses. In the latter case, the concept of possibility can be utilised [39].

A classical (crisp) set includes elements that can either belong to or not belong to the set, whereas elements of a fuzzy set may have various degrees of belonging. The classical set theory is defined if X is a *universe* and its subset is S then the characteristic function μ_s from X to the *valuation set* {0,1} is defined as

$$\mu_s(x) = \begin{cases} 1 \, if \; x \in S, \\ 0 \, if \; x \notin S. \end{cases} \tag{3.35}$$

where x is the generic element of X.

If the valuation set is chosen to be in the real interval {0,1}, S is defined by Zadeh[38] as a *fuzzy set* in the universe X. In this case, $\mu_s(x)$ is the grade of membership or the membership function (also degree of compatibility or degree of truth) of x in S. The membership function ($\mu_s(x)$) describes the degree to which the elements x belongs to the fuzzy set S. S can be characterised by the set of pairs as

$$\mathbf{S} = \{(x, \mu_s(x)), x \in X\}. \tag{3.36}$$

If X is a finite set $\{x_1, x_2, \ldots., x_n\}$ then a fuzzy set on X is expressed as [40]

$$S = \sum_{i=1}^{n} \mu_s(x_i)/x_i \, . \tag{3.37}$$

If X is not finite then S is expressed as

$$S = \int \mu_s(x)/x. \tag{3.38}$$

The *support* of a fuzzy set S is the ordinary subset of X is given by

$$\text{supp}S = \{x \in X, \mu_s(x) > 0\}. \tag{3.39}$$

S reaches its *crossover* points when $\mu_s(x) = \frac{1}{2}$. The *height* of S is defined as

$$hgt(S) = sup_{x \in X}\, \mu_s(x). \tag{3.40}$$

i.e., the least upper bound of $\mu_s(x)$.

S is *normalised* if and only if $\exists x \in X$, and $\mu_s = 1$. This definition implies that $\text{hgt(S)} = 1$. The *empty set* $\varnothing$ is defined as $\forall x \in X, \mu_0(x) = 0$ and $\forall x, \mu_x(x) = 1$.

3.4.1. Set-Theoretic Operators

Zadeh extended the above fuzzy set definitions to set theoretic operators such as *union* ($\cup$) and *intersection* ($\cap$). They are defined by the following formulas [38]:

$$\forall x \in X, \mu_{s_1 \cup s_2}(x) = max(\mu_{s_1}(x), \mu_{s_2}(x)) \tag{3.41}$$

$$\forall x \in X, \mu_{s_1 \cap s_2}(x) = min(\mu_{s_1}(x), \mu_{s_2}(x)) \tag{3.42}$$

where $\mu_{s_1 \cup s_2}$, $\mu_{s_1 \cap s_2}$ are the membership functions for the fuzzy sets $s_1 \cup s_2$ and $s_1 \cap s_2$. These formulas give the usual *union* and *intersection* when the valuation set is reduced to {1,0}. There are other extensions of $\cup$ and $\cap$ coinciding with the binary operator. The choice of the *max* and *min* was justified in [41].

Fig.3.14 shows an illustration of equation (3.41) and (3.42). Fig. 3.14a shows the characteristic function μ_{s_1} that has a fuzzy interval *between* 5 and 8. Similarly, Fig.3.14b shows the characteristic function μ_{s_2} that has a fuzzy number *about* 4. Fig.3.14c shows the fuzzy set *between* 5 *and* 8 **OR** *about* 4 (the dashed line). Similarly the fuzzy set *between* 5 and 8 **AND** *about* 4 is shown in Fig 3.14d (the dashed line).

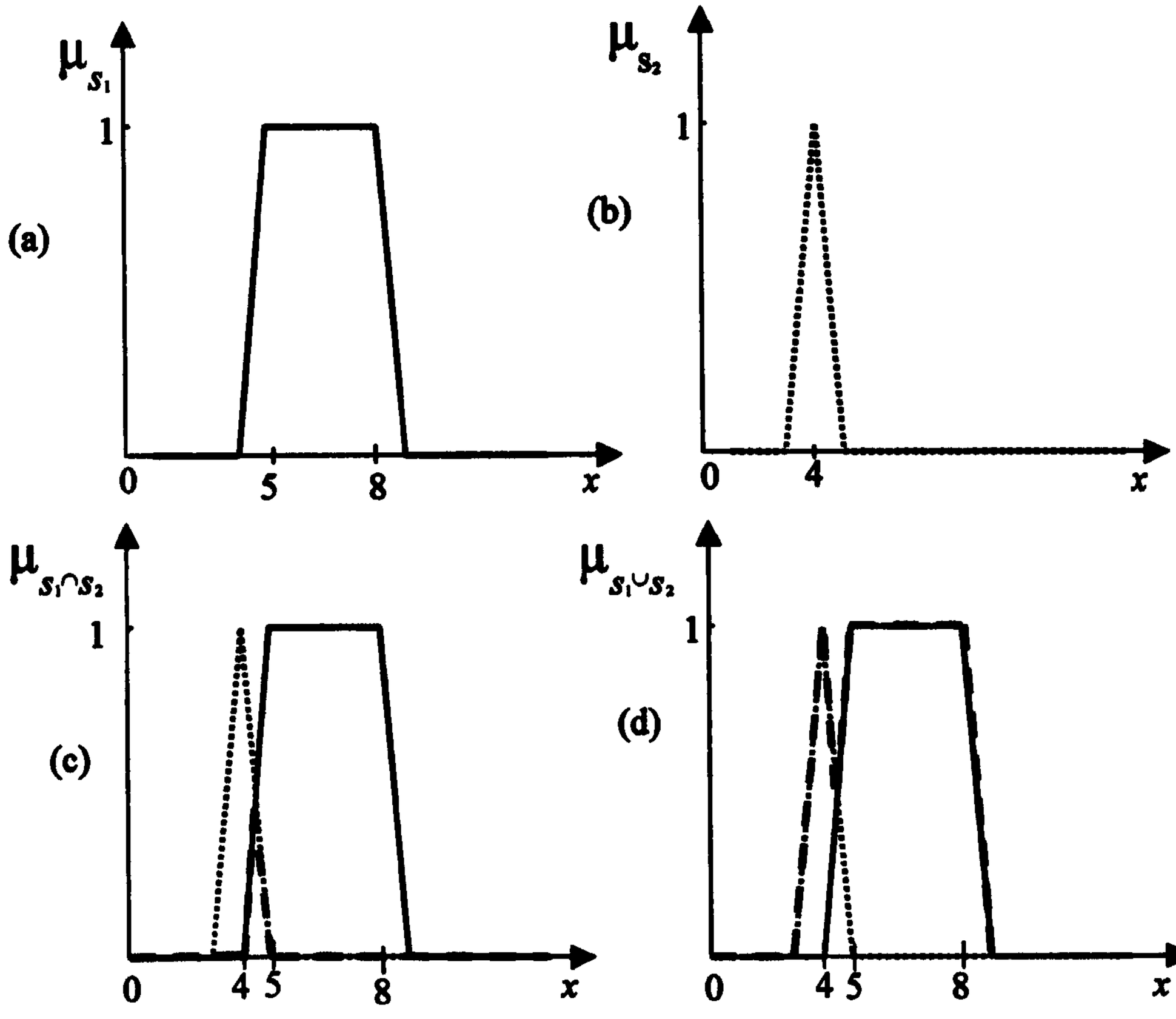

Figure 3.14: Illustrations of set theoretic operators (*union and intersection*) (a) The characteristic function μ_{s_1}, (b) The characteristic function μ_{s_2}, (c) Membership function for fuzzy set $s_1 \cap s_2$, (d) Membership function for fuzzy set $s_1 \cup s_2$

Another important operator is *complement* that is defined by the following formula [38]:

$$\forall x \in X, \mu_{\bar{s}}(x) = 1 - \mu_s(x) \tag{3.43}$$

Another useful set theoretic operator is *mth power of fuzzy set*, s^m, which is defined by Zadeh as:

$$\forall x \in X, \forall m \in \Re^+, \mu_{s^m}(x) = [\mu_s(x)]^m \tag{3.44}$$

It is used to model linguistic hedges like 'more' or 'less'. It is also used in fuzzy set to either concentrate or dilute the fuzzy membership functions that is depending on whether m is greater than 1 or less than 1 respectively. More details of the above operators and other operators can be found in [40].

3.4.2. α-Cuts

To exhibit if an element $x \in X$ belongs to a fuzzy set S or not, its membership value is required to be greater than some threshold value $\alpha \in]0,1]$. The ordinary set of such elements is the α-*cut* S_α of S,

$$s_\alpha = \{x \in X, \mu_x(x) \geq \alpha\}. \tag{3.45}$$

The *strong* α-*cut* of $S_\alpha$can be defined as:

$$s_{\bar{\alpha}} = \{x \in X, \mu_s(x) \rangle \alpha\}. \tag{3.46}$$

The membership function of a fuzzy set S can be expressed in terms of the characteristics functions of its α-cuts by the following formula

$$\mu_s(x) = \sup_{\alpha \in]0,1]} \min(\alpha, \mu_{s_\alpha}(x)), \tag{3.47}$$

where

$$\mu_{s_\alpha}(x) = \begin{cases} 1 & iff\ x \in s_\alpha \\ 0 & otherwise.' \end{cases} \tag{3.48}$$

S_α can be written as $\mu_\alpha^{-1}([\alpha,1])$ that is the inverse image of the interval [α, 1]. By assuming $\mu_{[\alpha,1]}$ to be a characteristic function of the interval [α, 1] in the universe [0,1] then we can derive

$$\mu_{s_\alpha}(x) = \mu_{[\alpha,1]}(\mu_s(x)) \quad \forall x \in X \tag{3.49}$$

A fuzzy α-cut can be understood as the set of elements whose membership values are greater than "approximately α" i.e., belong to a fuzzy interval $[\tilde{\alpha},1]$. Semantically, the fuzzy interval means something like "high". Therefore, the equation (3.49) can be extended as follows into:

$$\mu_{s_\alpha}(x) = \mu_{[\tilde{\alpha},1]}(\mu_s(x)) \quad \forall x \in X \tag{3.50}$$

where $s_{\tilde{\alpha}}$ is the fuzzy α-cut of S. The Fuzzy α-cut is an extended operator and is results from the extension principal that was introduced by Zadeh [42].

3.4.3. Fuzzy Decision

Optimisation models in operations research assume that the data are precisely known, that constraints delimit a crisp set of feasible decisions, and that criteria are well defined and easy to formalise. However, in the real world such assumptions are only approximately true. Bellman and Zadeh [43] pointed out that in a fuzzy environment goals and constraints formally have the same nature and can be represented by fuzzy sets. If it is assume that C_i be the fuzzy domain delimited by the *i*th constraint (*i*=1, m) and G_j the fuzzy domain associated with *j*th goal (*j*=1, n). When goals and constraints have the same importance then it is called a *fuzzy decision* which is defined as a fuzzy set D on X [43]

$$D=\left(\bigcap_{i=1,m} C_i\right)\cap\left(\bigcap_{j=1,n} G_j\right), \tag{3.51}$$

that is

$$\forall x\in X,\quad \mu_D(x)=\left[\min_{i=1,m}\mu_{C_i}(x),\min_{j=1,n}\mu_{G_j}(x)\right] \tag{3.52}$$

The final decision x_f can be chosen in the set as

$$\forall x\in X,\quad M_f=\{x_f,\mu_D(x_f)\geq\mu_D(x). \tag{3.53}$$

where M_f is called the *maximal decision set*[40].

When criteria and constraints have unequal importance then membership functions can be weighted by x-dependent coefficients [40].

3.4.4. Fuzzy Membership Functions

In order to benefit from fuzzy techniques and methods in real applications, it is necessary to convert the numerical information (obtained from, for example, sensors) or linguistic information (obtained from human experts) to fuzzy sets. This needs appropriate fuzzy membership functions to be defined first. The calculation of membership functions is central to application of fuzzy set theory.

The membership function is supposed to be a good model of the way people perceive categories, therefore, membership functions themselves are fuzzy. There is no general way to define membership functions for particular applications. However, some ideas and methods have been suggested by several authors independently, which were reviewed in [40].

In practical applications, S shape functions and $\prod$ shape functions were usually used [78] for fuzzification of real data which are defined as follows:

$$S(x;a,b,c)=\begin{cases}0 & x\le a\\ 2\left(\frac{x-a}{c-a}\right)^2 & a\le x<b\\ 1-2\left(\frac{x-a}{c-a}\right)^2 & b\le x<c\\ 1 & c<x\end{cases} \tag{3.54}$$

where $b=\frac{a+c}{2}$ and

$$\Pi(x;b,c)=\begin{cases}S(x;c-b,c-\frac{b}{2},c & x\le c\\ 1-S(x;c,c+\frac{b}{2},c+b & c<x\end{cases} \tag{3.55}$$

These functions are symmetric, but can be easily made non-symmetric by relaxing the requirement that b be the midpoint of a and c. The parameters a, b, and c are estimated from statistical data, usually considering the examples of the problem under consideration which may be referred to as 'learning from examples' [79].

3.5. Conclusion

In this chapter, novel signal processing tools such as adaptive filters, the wavelet transform, and fuzzy logic theories have been reviewed that form the foundation for the remaining research chapters of this thesis. The characteristics of adaptive algorithms (LMS, NLMS, and RLS) were introduced that will be used in chapter 5 and 6 to exploit the correlation between two signals. Fuzzy set theory provides us with a powerful mathematical tool for modelling the approximate reasoning process of humans and their ability to reach conclusions when the available information is imprecise, was reviewed and will be utilised in the algorithms in chapter 5 and 6. Finally, the concept of wavelet decomposition was introduced that will be used in chapter 6 for multi scale representation of noisy waveforms.

Chapter 4

4. Data Acquisition and Prototype Instrument

4.1. Introduction

Staff working practices, and pressure from customers and the electricity regulator to restore power quickly, make fault location more difficult. Therefore, fault location instruments need to have some capability to detect and correct the user's mistakes automatically or to give warnings to the user so that mistakes can be corrected. Fault location instruments should also require minimal user interaction and expertise. This chapter presents a new prototype fault locator (P2000) that was developed for data acquisition in LVUDN. It minimises the requirement for user interaction through automation of many of the operations. The equipment is used to demonstrate the complexity of TDR waveforms which can be produced by a LVUDN.

In section 4.2, the difficulties associated with acquiring TDR waveforms using previous commercial instruments in LVUDN, and issues regarding TDR waveform acquisition on live lines, are discussed.

In section 4.3, real TDR waveforms that were obtained using P2000 from cable models are presented. These TDR waveforms demonstrate the possible mismatches that can be expected in a LVUDN and also illustrate the additional complexity of TDR waveforms caused by multiple reflections from the mismatches.

In section 4.4, a new prototype instrument (P2000) for TDR waveform acquisition in LVUDN is presented. This prototype automates some of the data acquisition processes and minimises user interaction. Software development for the P2000 is also illustrated with examples in this section. A comparison between a previous generation of fault location instrument (P240 by Hathaway Systems Ltd) and the new prototype (P2000) are also presented in this section.

Section 4.5 presents data recorded using P2000 on a selection of real transient faults on LVUDN's. Conclusions to this chapter are presented in section 4.6.

4.2. Data Acquisition Difficulties in LVUDN

The data acquisition problems can be grouped into two parts. One is due to the LVUDN configuration at the testing point (substation) and other is due to TDR instrument limitations. The first one is explained in section 4.2.1 and the latter is discussed in section 4.2.2.

4.2.1. Difficulties of Data Acquisition on energised cables

When fault location is carried out from a substation on an energised cable it will only be possible to record good waveforms on the phases of the cable which are isolated from the busbar. If a phase is not isolated the injected pulse will be launched into all the cables connected to the busbar and not just the cable to be tested. Therefore, the only recordings that can be made are those related to the faulty phase, because the fuse of the faulty phase would have been ruptured, or withdrawn. To record waveforms for another (healthy) phase would require additional fuses to be removed which would result in un-desirable power outages to additional single phase customers. To overcome this problem, when the faulty is re-energised, a blocking inductor is connected in series with the replacement fuse. Testing from points other than the feeding substation, for example a link box, will also usually present the same problem of the injected pulse propagating along several branches. The one exception is where the cable can be accessed at a normally open end, for example a feeder pillar provided to allow interconnection between substations.

The number of waveforms which can be recorded on a faulted 3-phase live LVUDN cable (without the need for blocking inductors, or additional fuse withdrawals) fall into three categories namely:

- One fuse ruptured, or withdrawn, allows three waveforms to be recorded from the test point. For example, if the Red phase fuse is blown, or withdrawn, the only waveforms that can be recorded are those associated with the Red phase. Therefore Red-Neutral (RN), Red-Blue (RB), and Red-Yellow (RY) waveforms can be recorded.
- Two fuses ruptured, or withdrawn, allows five waveforms to be recorded from the test point. In this case if the Red and Blue fuses are blown, or withdrawn, then RN, BN, RB, RY, and YB waveforms can be recorded.

- Three fuses ruptured, or withdrawn, allows all six waveforms (RN, BN, YN, RB, RY, and YB) to be recorded from the test point.

In the case of a backfeed, one or two fuses may be ruptured depending on how many phases are involved in the fault. If two phases are involved then only one fuse will be ruptured. If all three phases are involved then two fuses will be ruptured. If a fuse is ruptured then good TDR waveforms can be recorded associated with that phase. Therefore, by recording all the TDR waveforms that are related to the backfed phase(s) and then analysing the TDR waveforms it is possible to identify which fuse is ruptured. Once the ruptured fuse has been identified, the TDR waveforms that are related to that phase are retained and the rest of the waveforms discarded. The process of analysing the waveforms is explained in section 4.4.6.

4.2.2. Instrumentation Problems in Data Acquisition

Good TDR waveform acquisition is important for accurate TDR based fault location in LVUDN. Acquiring good TDR waveforms depends on how the TDR instrument has been used to collect the data. The previous TDR instruments require manual operation, provide no safeguard against user mistakes, do not have the facility to check which fuses are blown and do not have the facility to recognise the presence of a backfeed.

Manual operation is required for balancing, setting the triggering level for transient fault detection and, most importantly, for fault location analysis. Balancing is used to minimise the amplitude of the injected signal at the start of the recorded waveform and to compensate for the mismatch produced by the test leads. Trigger level settings are selected so that the instrument launches a pulse when the fault is in an arcing (i.e. low impedance state). In previous instruments, triggering was found to be more reliable if based on *increases in current* rather than *decreases in voltage*. This was because the 'voltage dip' trigger device was non-selective and did not discriminate between a 'dip' due to a transient fault and a 'spike' due to re-energisation of the cable. The final, manual, identification of the fault position was highly dependent on the expertise of the operator in analysing TDR waveforms.

Presently, blown fuses are identified by the user using a test lamp – although knowledge of which consumers are without power often provides the same information.

4.3. Characteristics of TDR Waveforms

This section presents some of the complexities associated with TDR based fault location and shows examples of real TDR waveforms that were recorded using the new prototype P2000 (see next section for more details about P2000). The TDR waveforms illustrated in this section were recorded on a model network consisting of 4-core signal cable. Single and three phase tees, as well as faults, were modelled.

TDR based fault location on LVUDN is complicated for a number of reasons:

- TDR recorded waveforms are not easy to interpret due to reflections from the many possible tee connections in the network as mentioned earlier.
- Single-phase tees produce reflections similar to short circuits, therefore it is difficult to distinguish between a single-phase tee and a short circuit fault from the recorded waveform.
- Cables exhibit attenuation and dispersion which distorts the reflected pulses and makes analysis of TDR waveforms more complicated.
- Once the reflection from the fault has been identified, any errors in the assumed velocity of propagation will result in an error in the calculated fault distance.

The following cable models (Fig. 4.1a, 4.3, 4.5, 4.7, 4.9, 4.11, and 4.13) and the respective TDR waveforms (4.2, 4.4, 4.6, 4.8, 4.10, 4.12, and 4.14) illustrate some of the above points. All the cable models used a 4-core signal cable with multi-stranded copper conductors. The cross section of the cable is shown Fig. 4.1b. All the TDR waveforms in the following examples were recorded using P2000.

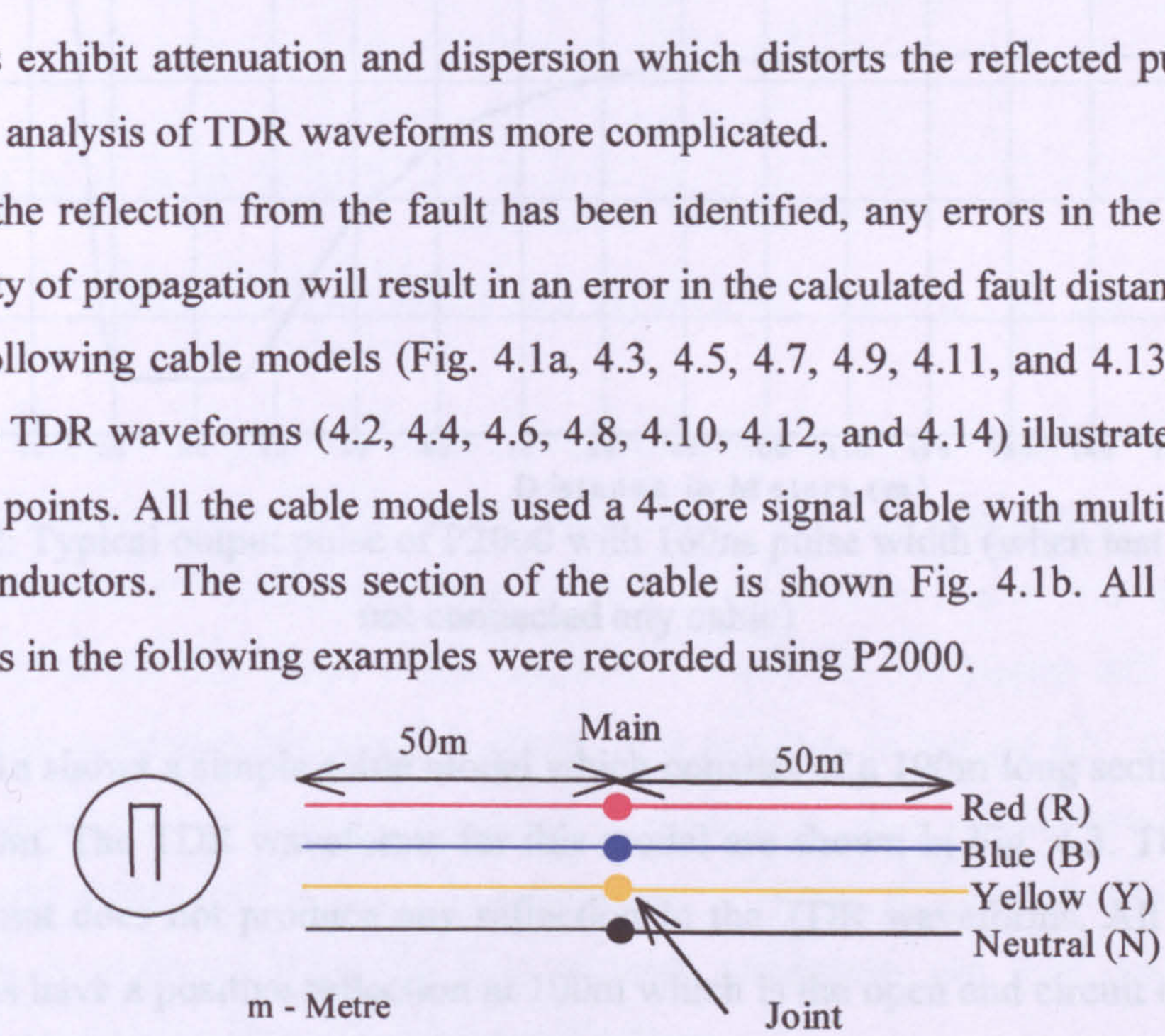

(a)

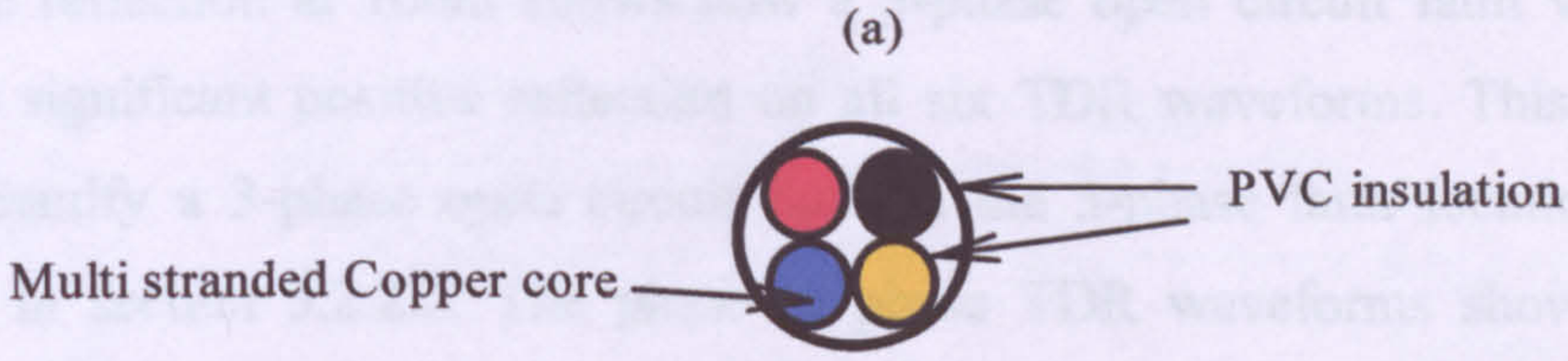

(b)

Figure 4.1: (a) Cable model with a 3-phase straight joint
(b) View of the model cable cross-section

The pulse generated by P2000 is a rectangular shape and it is generated by charging and discharging a capacitor. The minimum rise time of the pulse is about 20ns. However, the rise time depends on the test leads of P2000 and the cable inductance that is under test. The narrowest pulse width that can be generated by P2000 is 160ns. The pulse width can be increased by factor of 2 and the maximum pulse width that can be generated is 20.48μs. Typical output pulse of P2000 is shown in Fig.4.2, when the test leads of the P2000 are not connected to any cable. In this figure, narrowest pulse width is used.

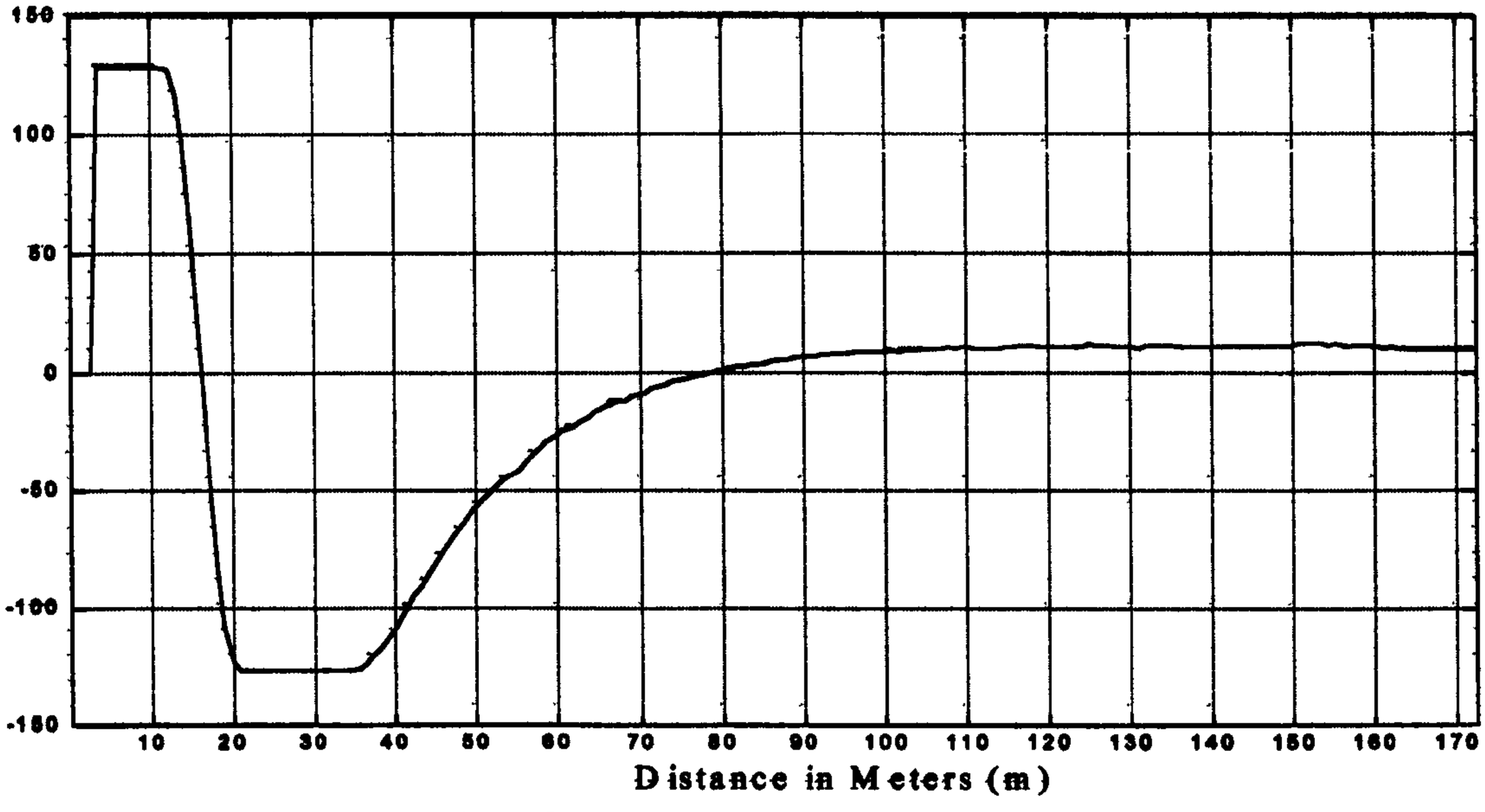

Figure 4.2: Typical output pulse of P2000 with 160ns pulse width (when test leads are not connected any cable)

Fig.4.1a shows a simple cable model which consists of a 100m long section with a joint at 50m. The TDR waveforms for this model are shown in Fig. 4.3. This shows that the joint does not produce any reflection in the TDR waveforms. All the TDR waveforms have a positive reflection at 100m which is the open end circuit end of the cable. The reflection at 100m shows how a 3-phase open circuit fault would also produce a significant positive reflection on all six TDR waveforms. This feature is used to identify a 3-phase open circuit fault in the 3-phase fault location process described in section 5.2.2.2. The phase to phase TDR waveforms show a higher reflection than the phase to neutral TDR waveforms due to the lower attenuation experienced by pulses which are injected between phases. These TDR waveforms show how the reflected pulses are distorted by the cable attenuation and dispersion when compared with the rectangular pulse injected by the P2000. (NOTE: In these

example waveforms the balancing network has been adjusted to minimise the displayed amplitude of the injected pulse).

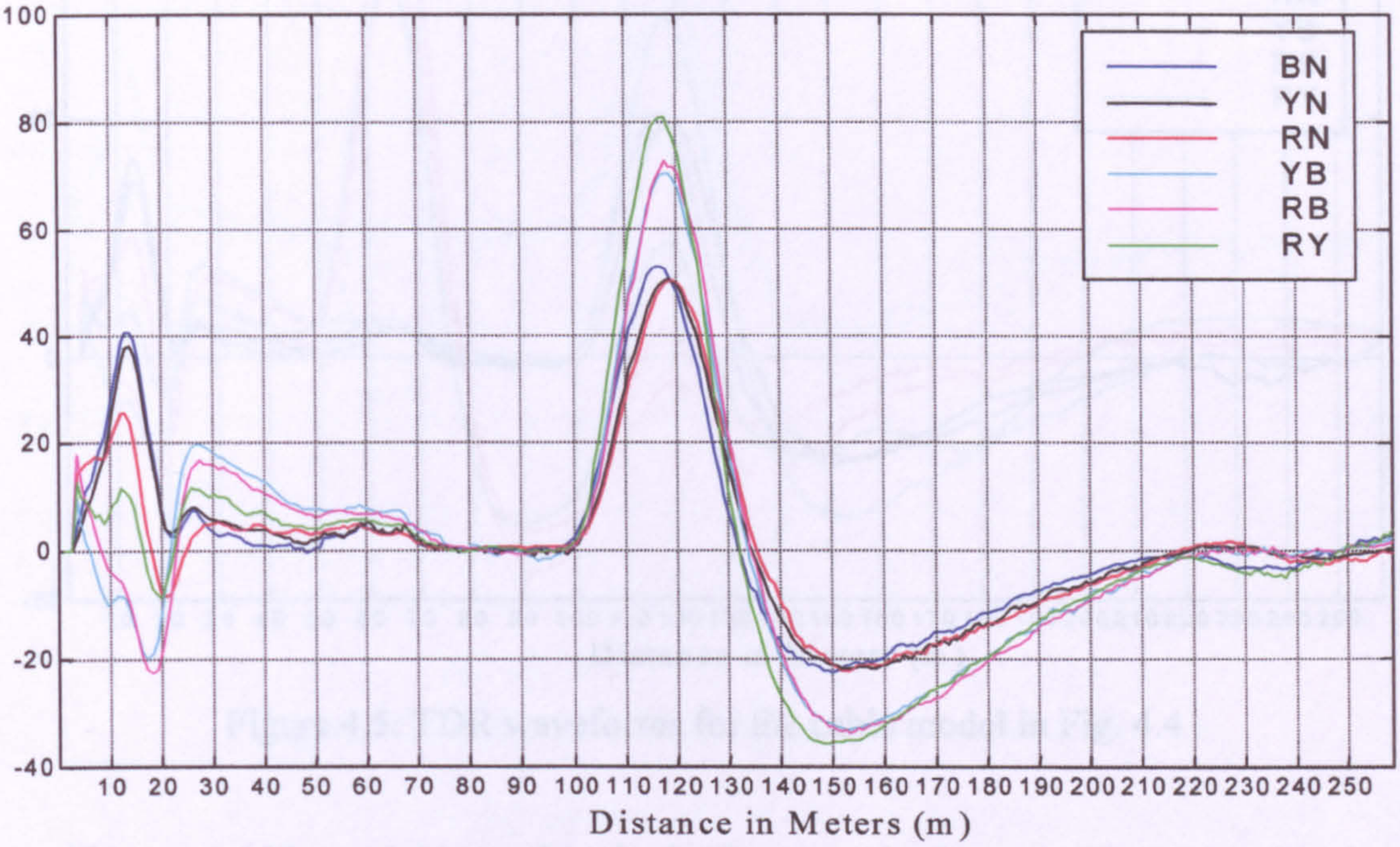

Figure 4.3: TDR waveforms for the cable model in Fig. 4.1a

Fig. 4.4 shows the previous cable model but now with an open circuit fault on the Red phase at 50m. The recorded TDR waveforms for this model are shown in Fig.4.5. The RN, RB and RY waveforms show a large positive reflection at 50m due to the open circuit on the Red phase whilst the BN, YN and YB waveforms still show the large positive reflection from the end of the cable at 100m. In fact the RN, RB and RY waveforms also show a (reduced amplitude) reflection at 100m which starts below the zero axis and is the result of which is a secondary reflection of the open circuit fault at 50m. This is example illustrates how multiple reflections can arise and become (partially) combined with other primary reflections.

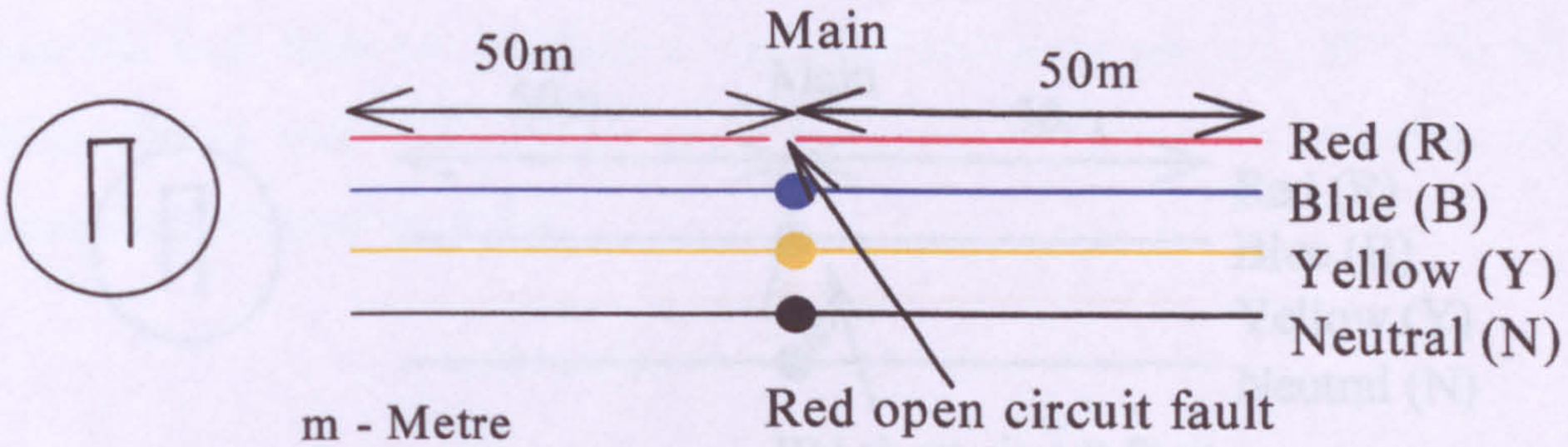

Figure 4.4: Cable model for an open circuit fault

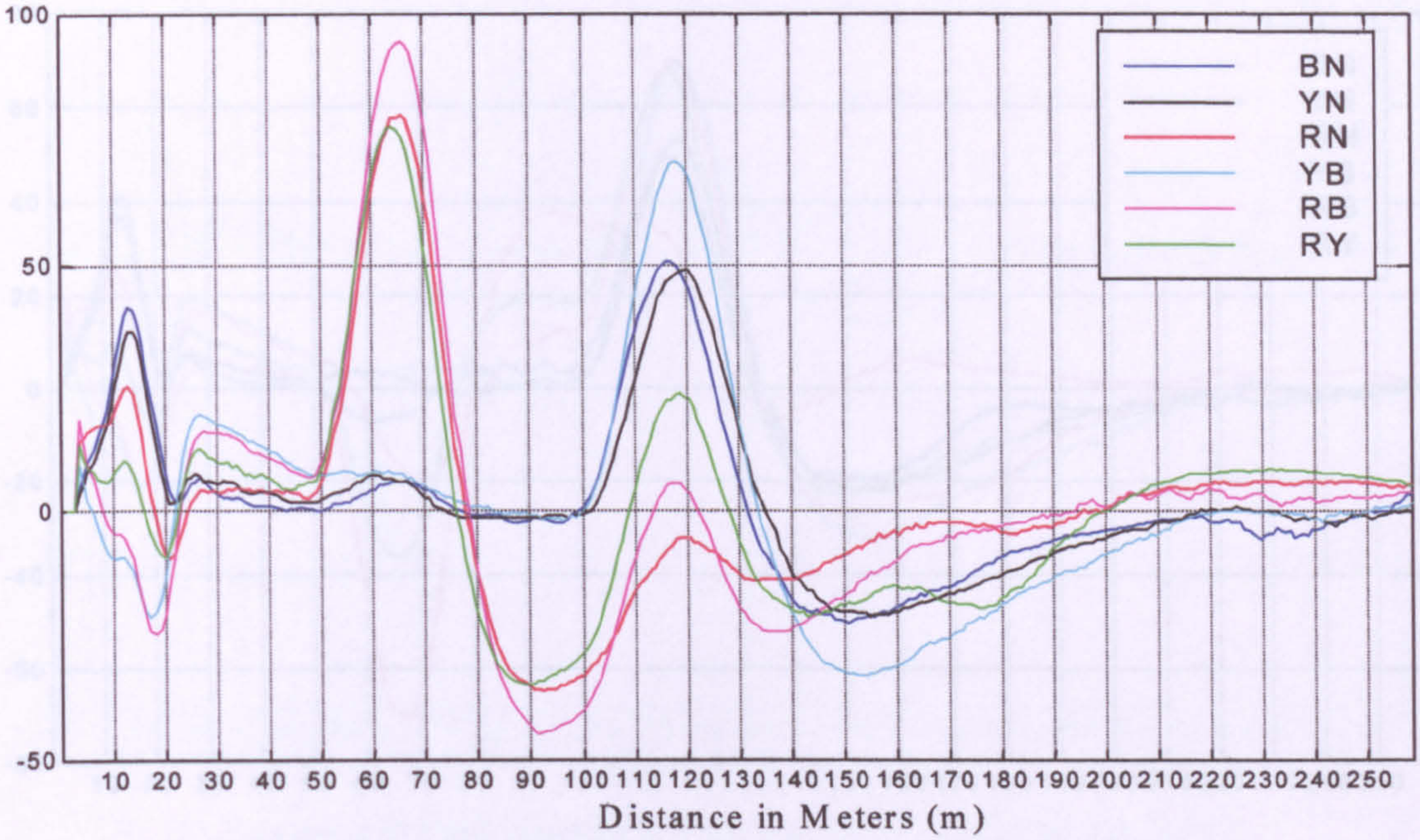

Figure 4.5: TDR waveforms for the cable model in Fig. 4.4

The same cable model is used again for the example shown in Fig.4.6 but this time with a Red phase to Neutral short circuit at 50m. The TDR waveforms for this are shown in Fig. 4.7. The RN, RB, and RY waveforms all show negative reflections at 50m but with RN being the largest. This is quite different from the single phase open circuit case where RN, RB, and RY all exhibited positive reflections of a similar magnitude. The reason the RB and RY reflections are smaller for the Red phase to neutral fault is that the fault reflection factor is approximately 50%, compared with 100% in the open circuit case. Since pulses injected into the RB and RY combinations are only partially reflected at the fault the waveforms still show very clear positive reflections from the open circuit terminals at 100m albeit with a DC offset compared to the reflections produced on BN, YN and YB.

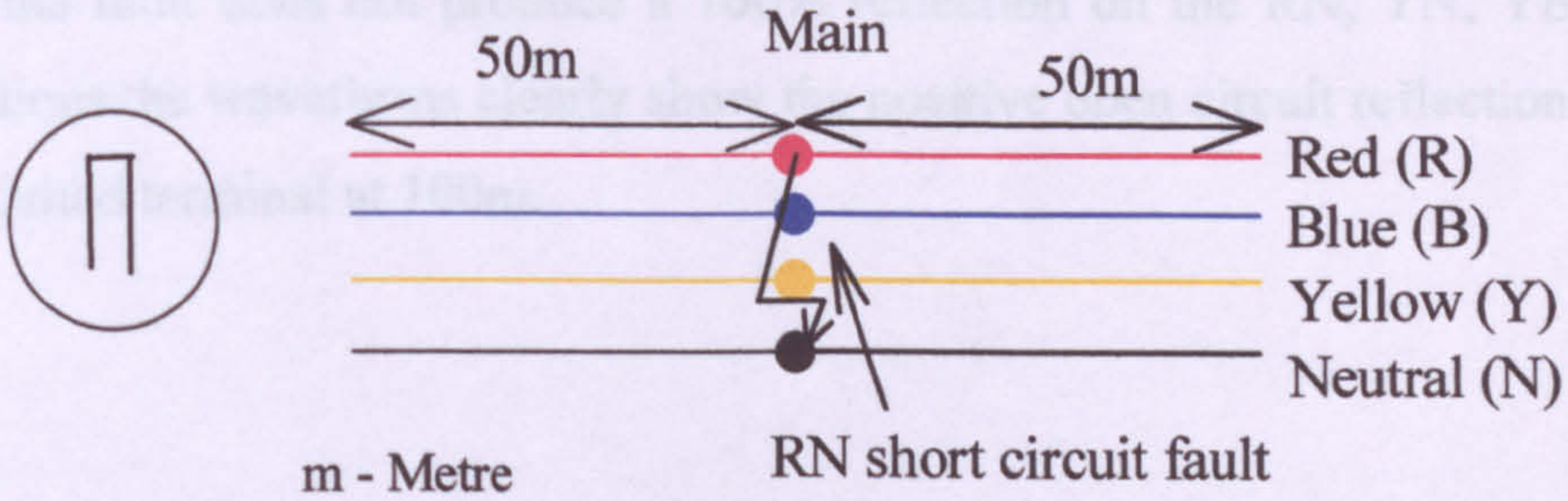

Figure 4.6: Cable model for phase to Neutral fault

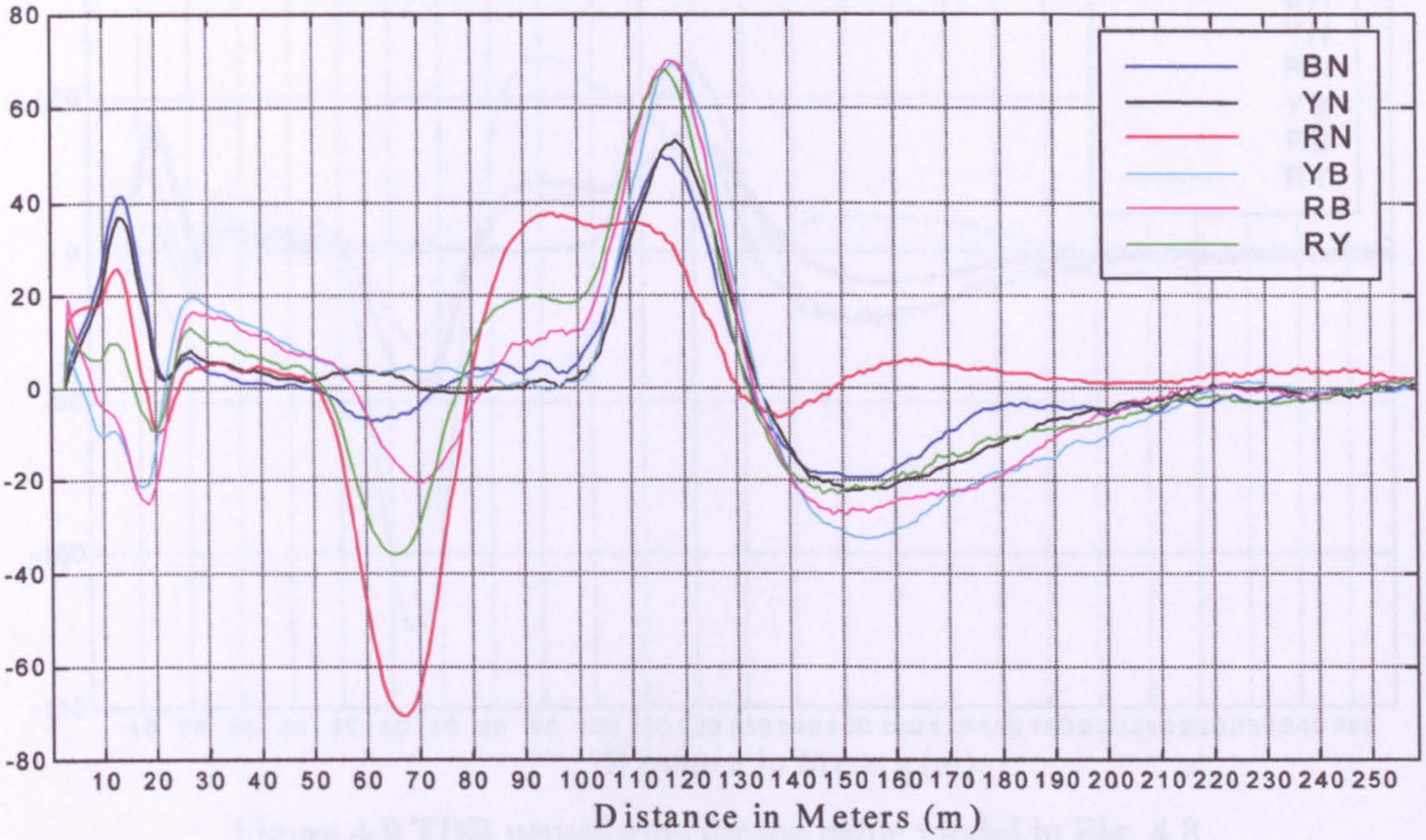

Figure 4.7: TDR waveforms for the cable model in Fig. 4.6

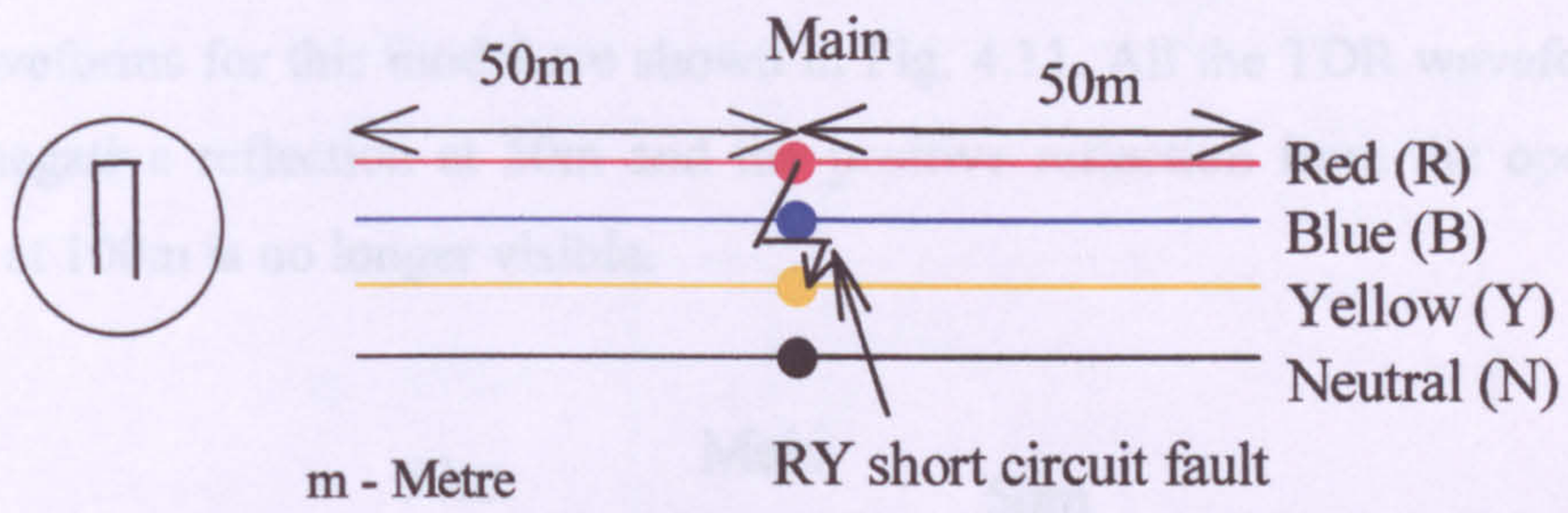

Figure 4.8: Cable model for a phase to phase fault

Fig. 4.8 shows an example of a phase to phase (RY) short circuit fault at 50m on the same cable model. The TDR waveforms for this model are shown in Fig. 4.9. Now all the TDR waveforms, except BN, have a negative reflection at 50m due to the short circuit fault with RY (the faulted pair) producing the largest reflection. Again, because the fault does not produce a 100% reflection on the RN, YN, YB and RB combinations the waveforms clearly show the positive open circuit reflection from the open circuited terminal at 100m.

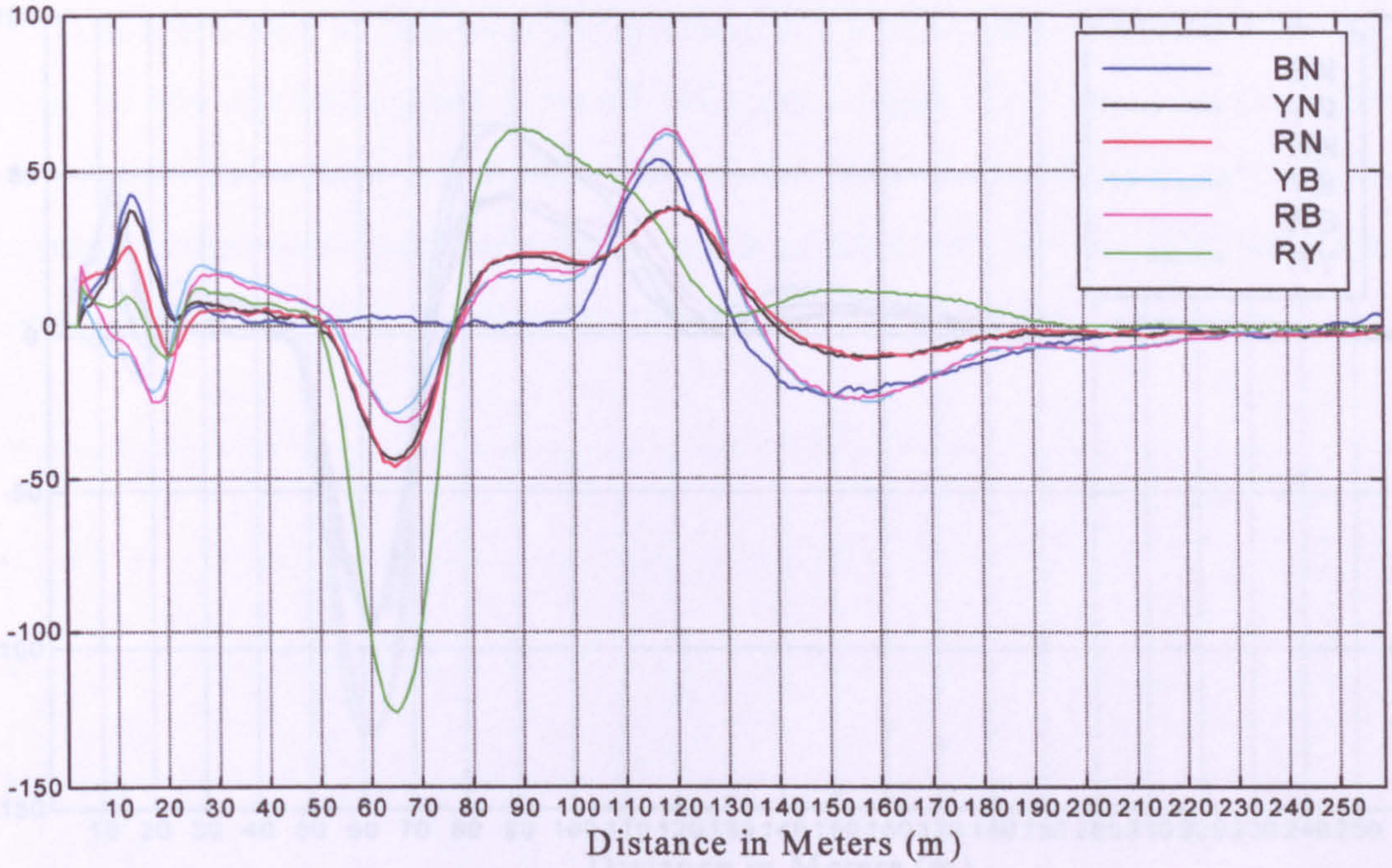

Figure 4.9 TDR waveforms for the cable model in Fig. 4.8

In Fig. 4.10 a 3-phase and neutral short circuit fault has been applied at 50m. The TDR waveforms for this model are shown in Fig. 4.11. All the TDR waveforms now have a negative reflection at 50m and the positive reflection from the open circuit terminal at 100m is no longer visible.

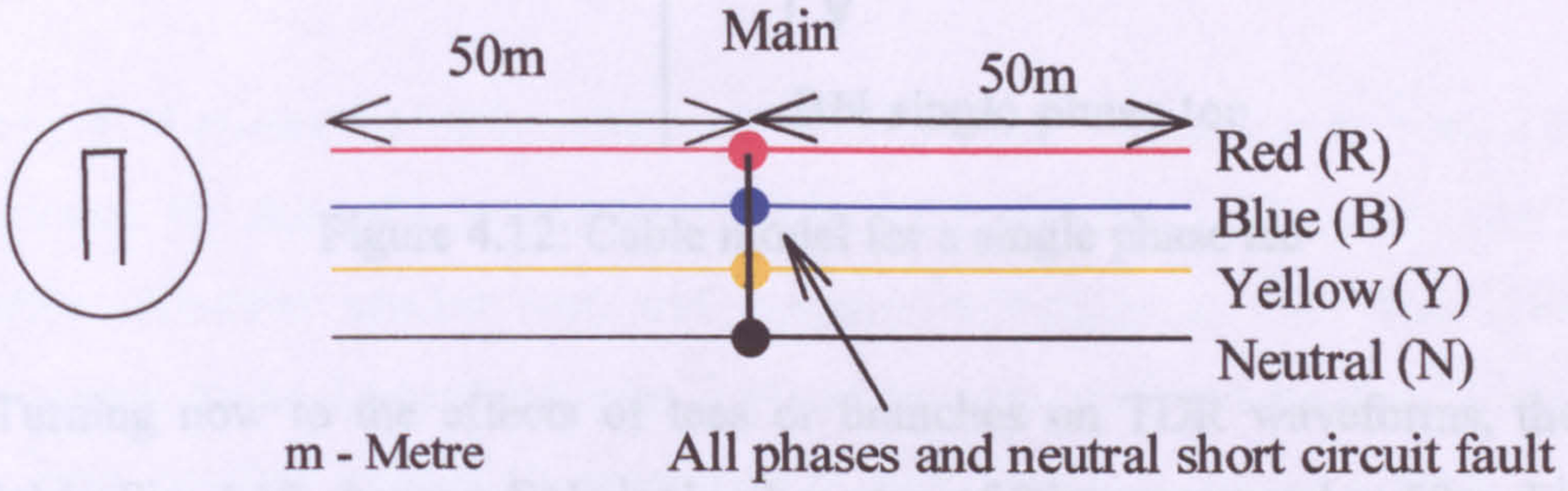

Figure 4.10: Cable model for all 3 phases to Neutral fault

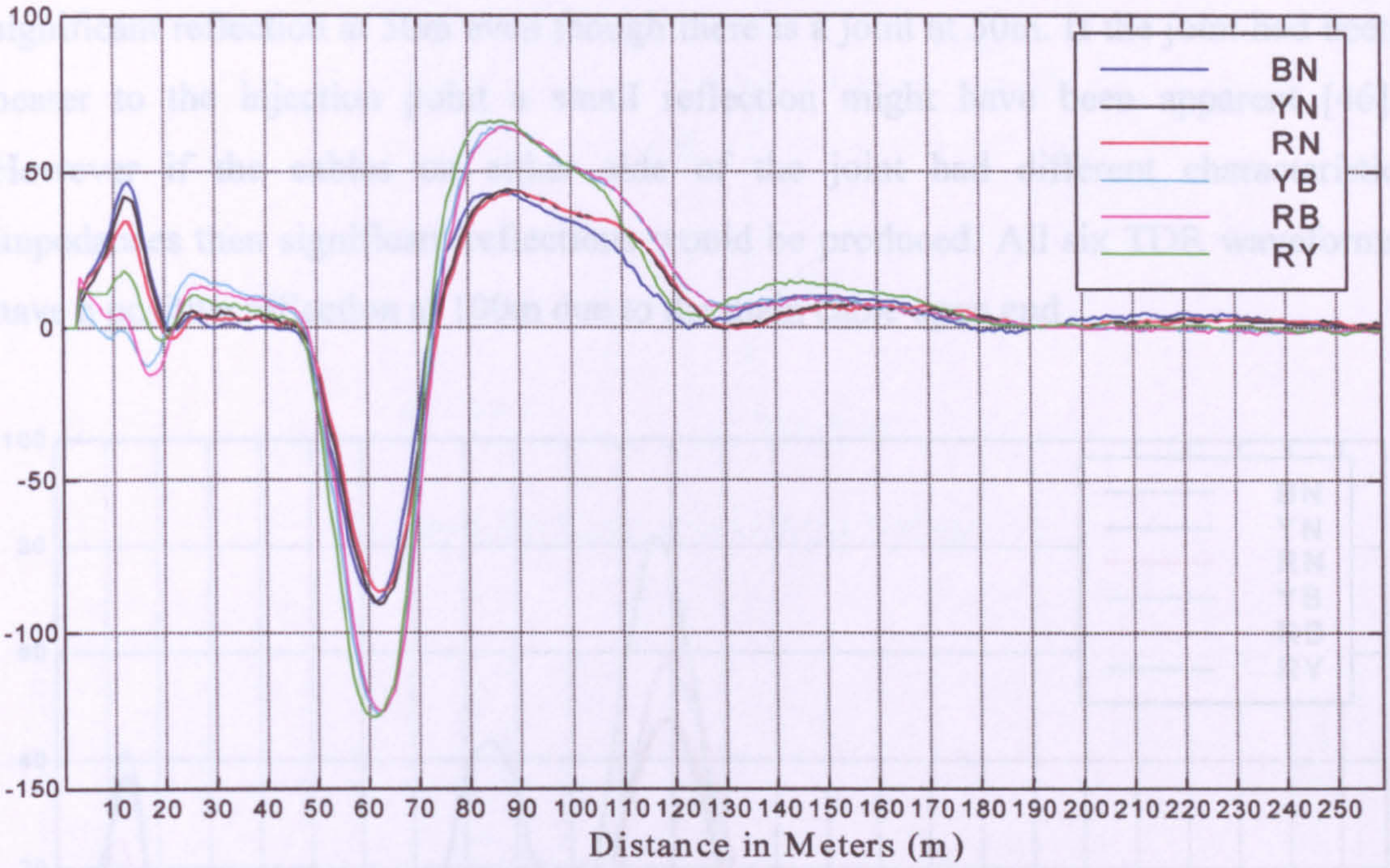

Figure 4.11: TDR waveforms for the cable model in Fig. 4.10

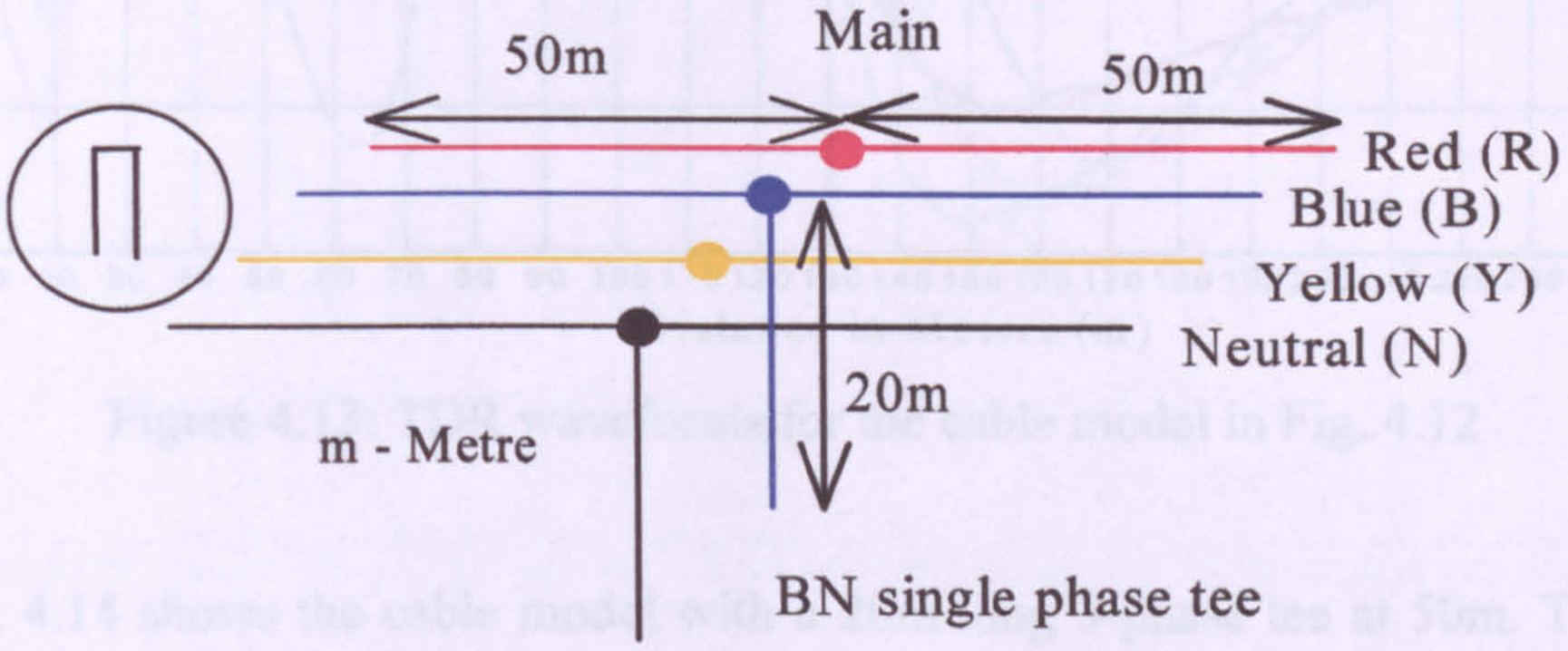

Figure 4.12: Cable model for a single phase tee

Turning now to the effects of tees or branches on TDR waveforms, the cable model in Fig. 4.12 shows a BN single-phase tee of 20m connected at 50m. Fig. 4.13 shows the TDR waveforms for the model in Fig. 4.12. All the TDR waveforms have a positive reflection at 100m due to the main cable open end. The BN, RB, and YB waveforms have a negative reflection at 50m and another positive reflection at 70m due to the BN single-phase tee joint and open end respectively. The RB and YB waveforms have much smaller reflections compared to BN at both positions. This is because the single-phase tee is on BN only. This feature is used in the single-phase identification process in section 5.2.2.1 to identify single-phase tee reflections from other reflections. Other TDR waveforms (RN, YN, and RY) do not have the

significant reflection at 50m even though there is a joint at 50m. If the joint had been nearer to the injection point a small reflection might have been apparent [46]. However if the cables on either side of the joint had different characteristic impedances then significant reflections would be produced. All six TDR waveforms have a positive reflection at 100m due to the main cable open end.

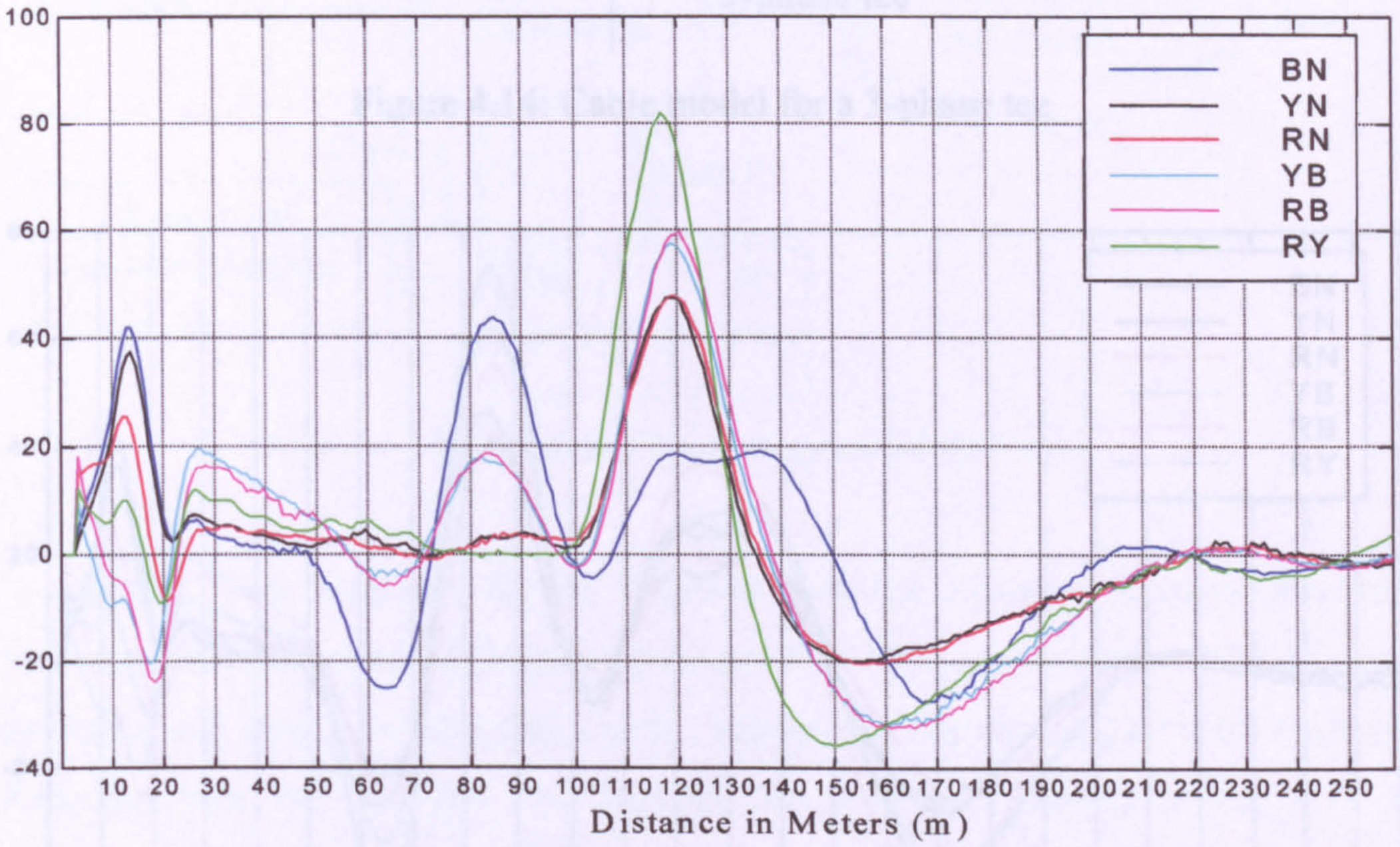

Figure 4.13: TDR waveforms for the cable model in Fig. 4.12

Fig. 4.14 shows the cable model with a 20m long 3-phase tee at 50m. The TDR waveforms for this case are shown in Fig. 4.15. All the TDR waveforms have a negative reflection around 50m and positive reflections at 70m and 100m due, respectively, to the 3-phase tee joint, 3-phase tee open end, and main cable open end. The 100m positive reflection's amplitude is reduced due to the secondary reflection from the 3-phase tee joint. This shows how composite reflections can cause problems to the user of a TDR instrument when trying to interpret the TDR waveforms. This example shows how a 3-phase tee joint can produce a negative reflection on all six TDR waveforms. The 3-phase tee joint reflection on all TDR waveforms are similar to the 3-phase short circuit fault that is shown in Fig. 4.10 except the short circuit fault produces higher amplitude reflections. This feature is used in the 3-phase fault location process in section 5.2.2.2 to distinguish between them.

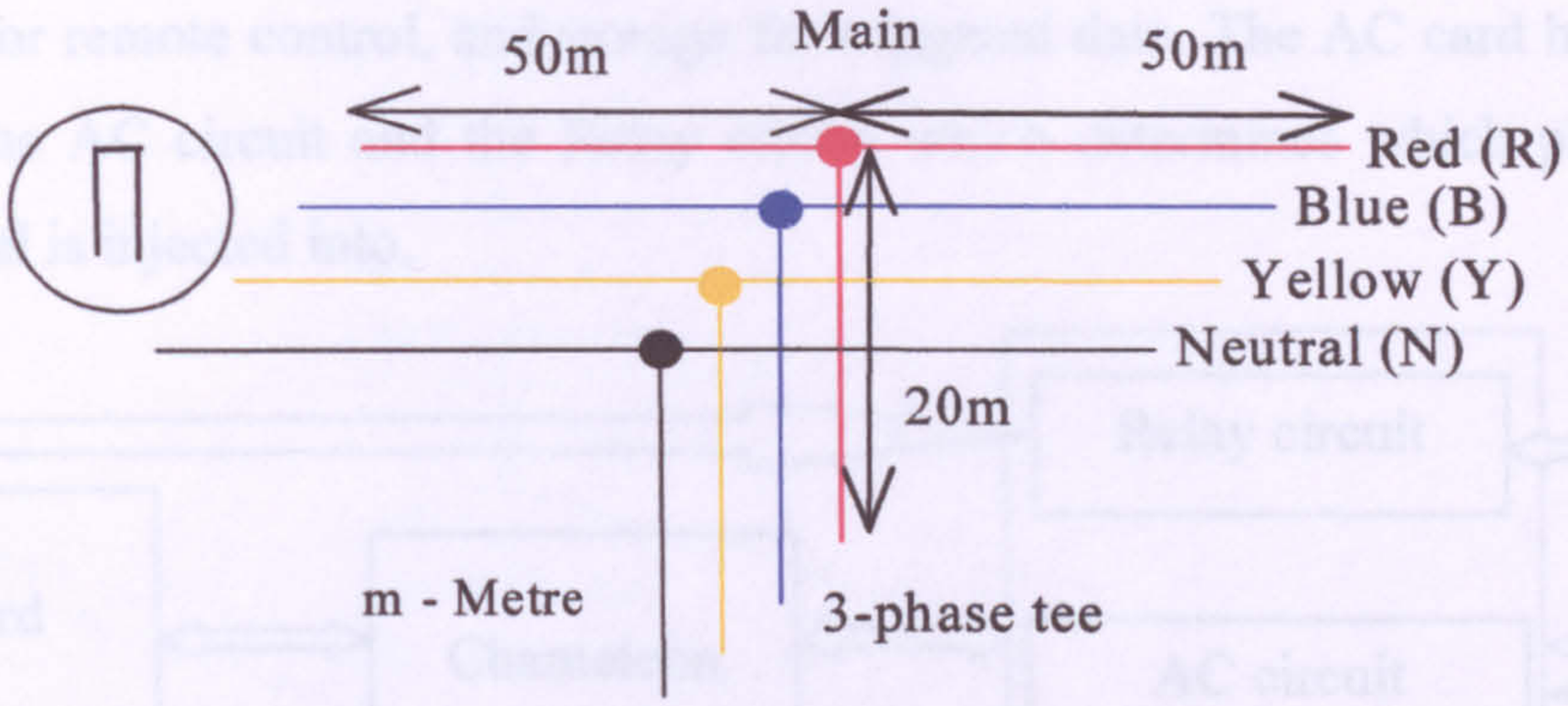

Figure 4.14: Cable model for a 3-phase tee

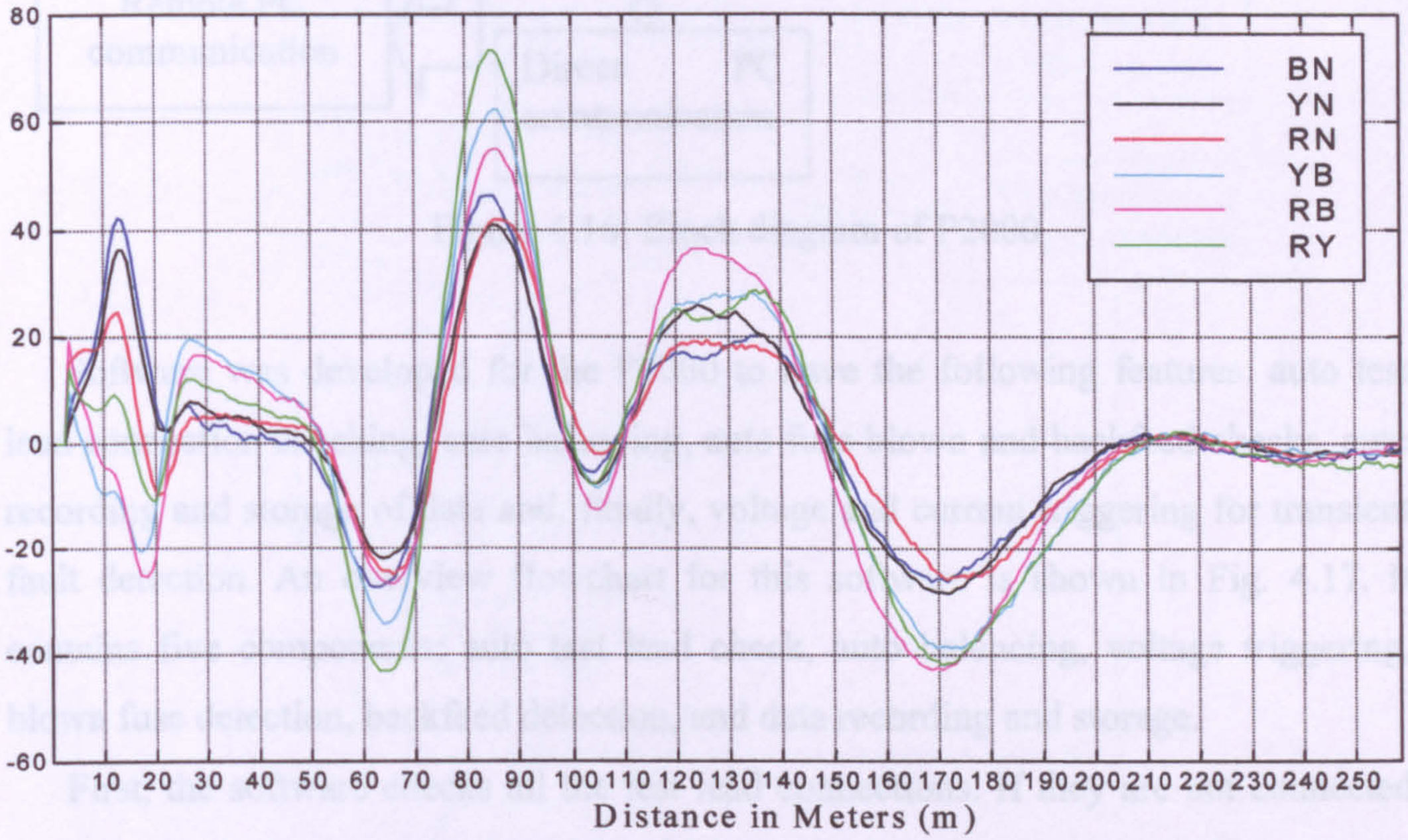

Figure 4.15: TDR waveforms for the cable model in Fig. 4.14

The relatively simple cable models and TDR waveforms presented above illustrate the complexity of TDR waveforms and the effects of tees, and faults in TDR waveforms. These cable models are simple, but real LVUDNs are much more complicated. The different features associated with tees and faults, illustrated using the cable models, are used in chapter 5 to automate the process of fault location.

4.4. Prototype P2000 and Data Acquisition

The block diagram of the P2000, Fig 4.16 shows that it consists of three main components: Chameleon processor, AC card, and TDR card. The Chameleon is an embedded processor with software to control the AC and TDR cards, communication

software for remote control, and storage for triggered data. The AC card has two sub circuits: the AC circuit and the Relay circuit which determines which phase(s) the TDR signal is injected into.

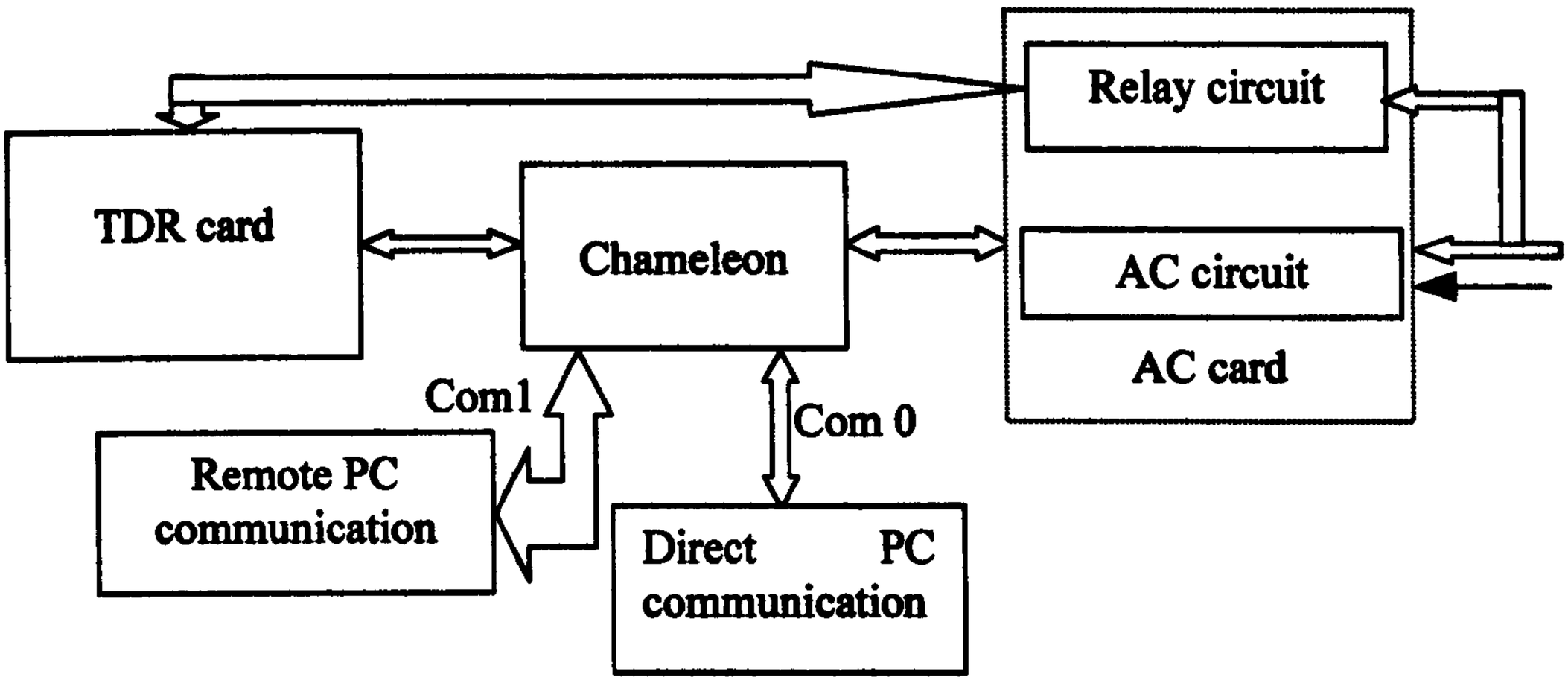

Figure 4.16: Block diagram of P2000

Software was developed for the P2000 to have the following features: auto test lead connection checking, auto balancing, auto fuse blown and backfeed checks, auto recording and storage of data and, finally, voltage and current triggering for transient fault detection. An overview flowchart for this software is shown in Fig. 4.17. It contains five components: auto test lead check, auto balancing, voltage triggering, blown fuse detection, backfeed detection, and data recording and storage.

First, the software checks all the test lead connections. If they are not connected properly, it displays a message saying which test leads are not connected. This process is repeated until the test leads are connected properly. Auto balancing is carried out to adjust the settings of a passive network within the P2000 to replicate the surge impedance of the cable under test and stray inductance of the test leads. The system then checks whether the user requires to enable voltage and/or current triggering. If either voltage or current triggering is required the software checks which fuses are blown and then checks for any backfeed. Once these tests are completed the appropriate TDR waveforms are recorded. The following sections describe these components in detail.

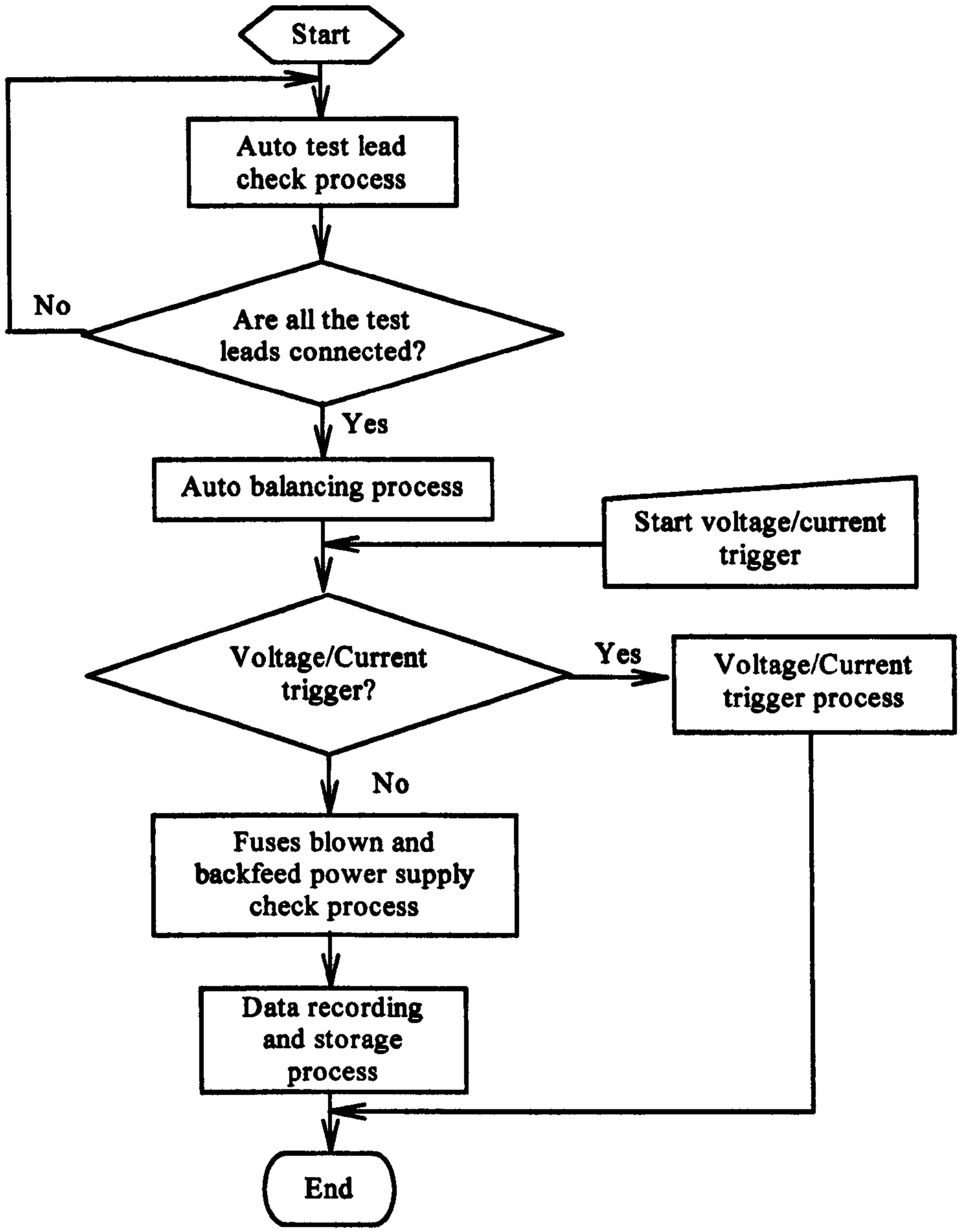

Figure 4.17: An overview flowchart for the P2000 software

4.4.1. Auto Test Lead Check Process

This process is to check for proper connection of the four test leads with each phase and neutral. The flowchart for this process is shown in Fig. 4.18. First, the process records the Blue phase to Neutral (BN), Red phase to Neutral (RN), and Yellow phase to Neutral (YN) TDR waveforms using the instrument's default settings of gain, pulse width and balance. It then retrieves pre-stored BN, RN, and YN TDR waveforms from its archive and compares them with the recently recorded waveforms as illustrated in Fig. 4.18. Based on the difference or similarity of the waveforms the software decides which test leads are not connected and displays a message indicating

what is wrong to the operator. The operator is then requested to (re)-connect the test leads and the software waits for the operator to confirm that this has been done by pressing the <ENTER> or <ESCAPE> keys. If the <ENTER> key is pressed, the auto test lead check is repeated until the leads appear to be connected properly. However, if the <ESCAPE> key is pressed the process can be aborted if the instrument is only to be used for single phase cable fault location where all the test leads will not require to be connected.

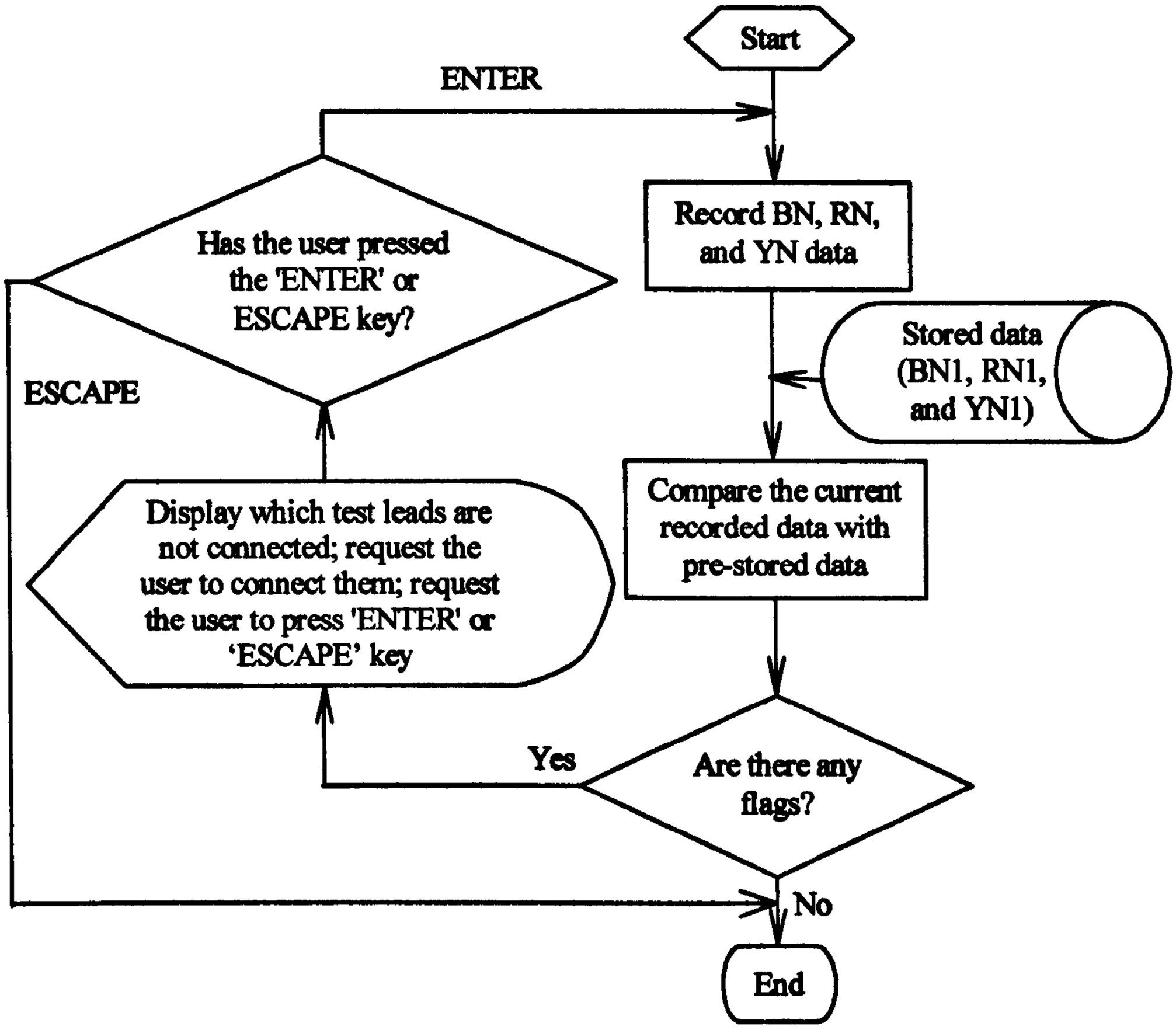

Figure 4.18: Flowchart for the auto test leads check

A flowchart for the process of comparing the TDR waveforms is shown in Fig.4.19. As mentioned in the above paragraph, the pre-stored and recently acquired waveforms are compared to check for proper connection of the test leads. Comparison of the waveforms is done over a 'distance' of 20m to 35m. The reason for choosing this region is explained in the next paragraph. If the comparison shows that both waveforms are similar during the whole period then the appropriate flag is set. After confirming that all the waveforms are similar up to 30m a check is done on the data beyond 30m and, if differences are now detected, the Neutral flag is set.

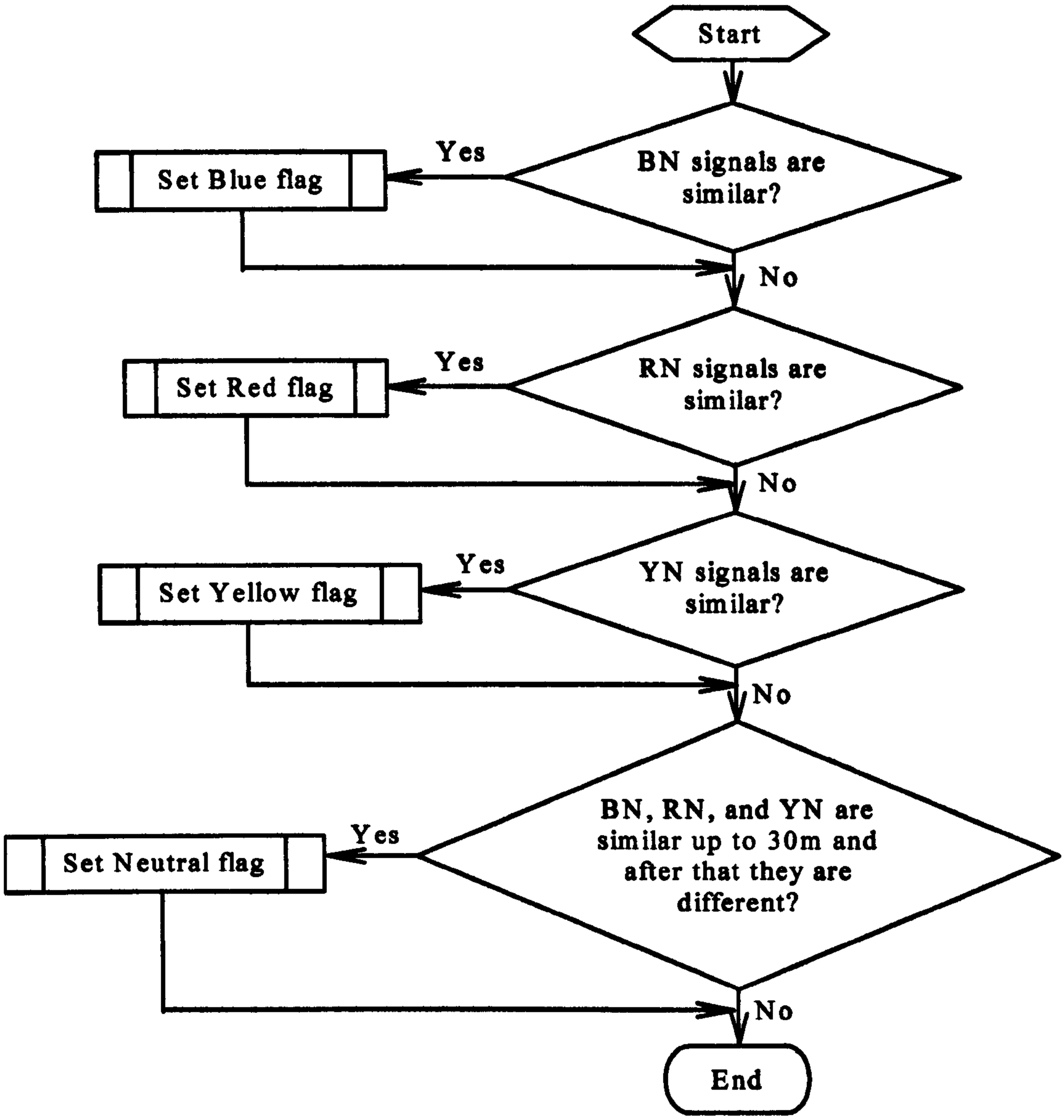

Figure 4.19: Flowchart for the TDR waveforms comparison

Three cases will now be examined: (i) where all four test leads (Red, Yellow, Blue, and Neutral) are disconnected, (ii) where all four test leads are connected, and (iii) where the Neutral is disconnected but the three phase leads are connected. Fig.4.20 shows the TDR waveforms of RN for the above three cases. As explained in the last paragraph if we compare the first two cases for the RN waveforms then they begin to separate within the 20 to 30m region. For the first case, the RN waveform values do not change between 20 to 35m. Therefore, this region was chosen for the comparison of TDR waveforms to check the test lead connections. If the waveforms show differences during the selected period then it is concluded that all the test leads

are dis-connected. If the RN waveforms show no differences up to 30m, but differences thereafter, it is concluded that the Neutral test lead is not connected.

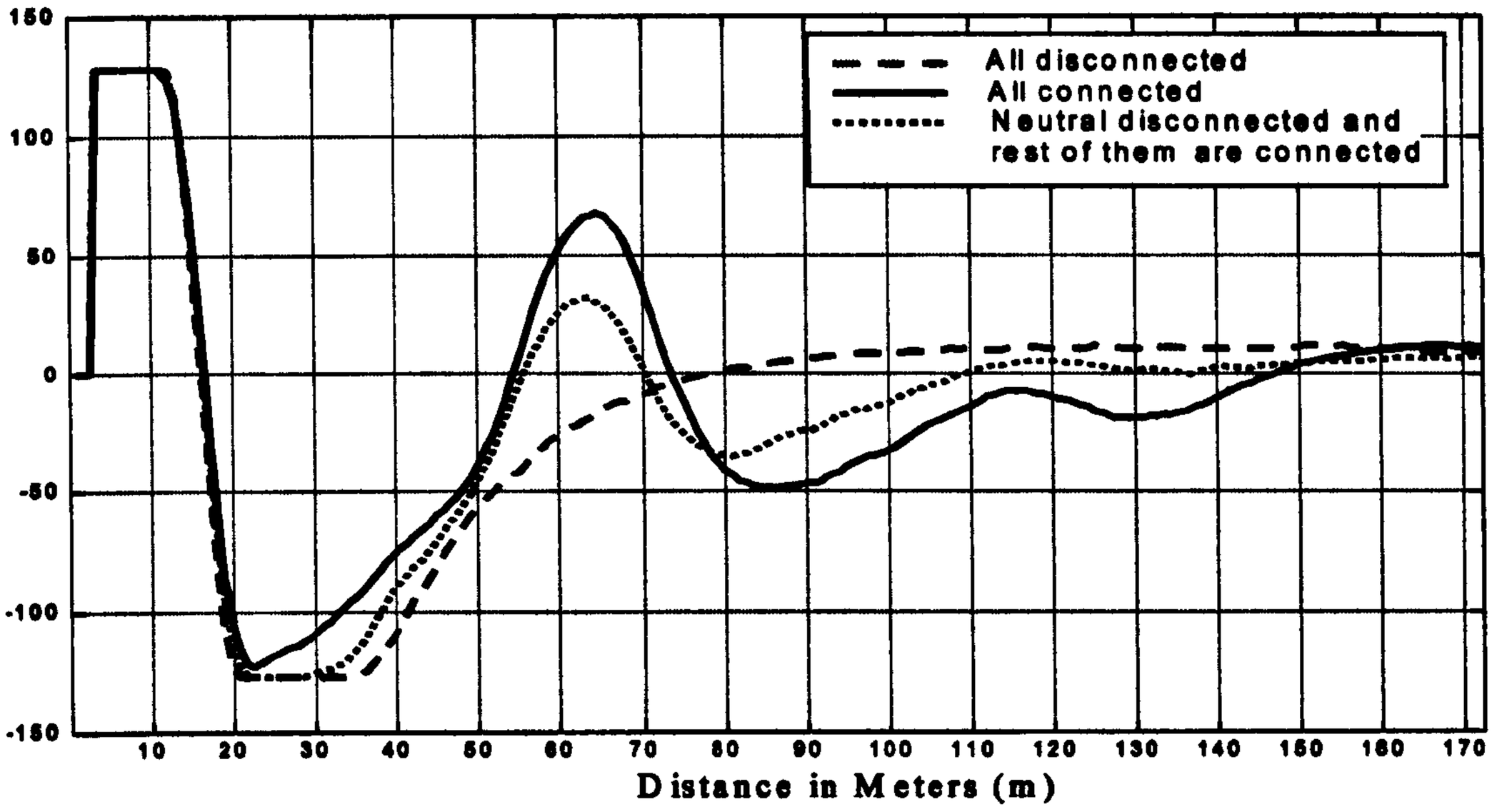

Figure 4.20: RN TDR waveforms on the model cable when: (i) all the test leads are dis-connected, (ii) all the test leads are connected and (iii) the neutral is not connected but the phase leads are connected

4.4.2. Auto Balancing Process

In this process the components of an internal passive network are adjusted to produce a replica of the surge impedance of the cable under test and the stray inductance of the connection between the test leads and the cable under test. Fig. 4.21 shows the flowchart of the auto balancing process. The procedure of this process is as follows: initially, the TDR waveform for each phase is recorded with a pre-set resistor value of 5 *ohms*. The software then calculates the absolute maximum value for the first 20 samples of the TDR waveform. The resistor value is then increased in 1 *ohm* steps and the absolute maximum value determined at each step. The process is repeated until the absolute maximum reaches a minimum value. The resistor value which produces this minimum is the value nearest to the surge impedance of the cable under test. This process has to be repeated for all six (BN, RN, YN, RY, RB, and YB) TDR waveforms because the cable surge impedance is slightly different for each of the six combinations.

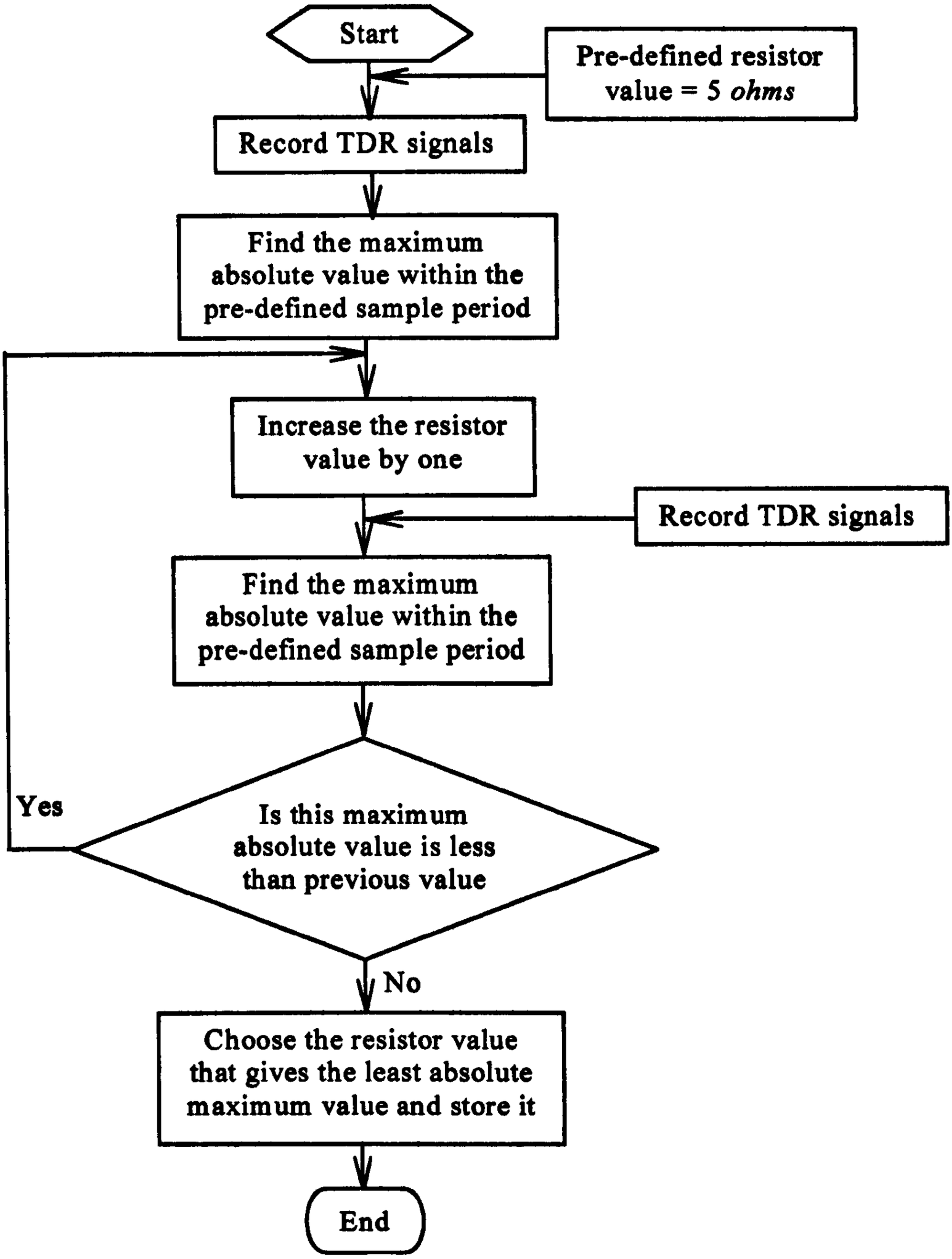

Figure 4.21: Flowchart for auto balancing process

Typical examples of RN waveforms that were recorded for a 50m open ended cable when matching resistor value is greater or less than and more or less equal to the cable impedance are shown in Fig. 4.22. The figure shows that if the matching resistor is not matched to the cable then we will have a mismatch at the beginning of the waveform. This also affects the 50m open end reflection. This shows the important of

balancing in order to get good TDR waveforms. The next section discusses how the system operates the voltage trigger for transient faults.

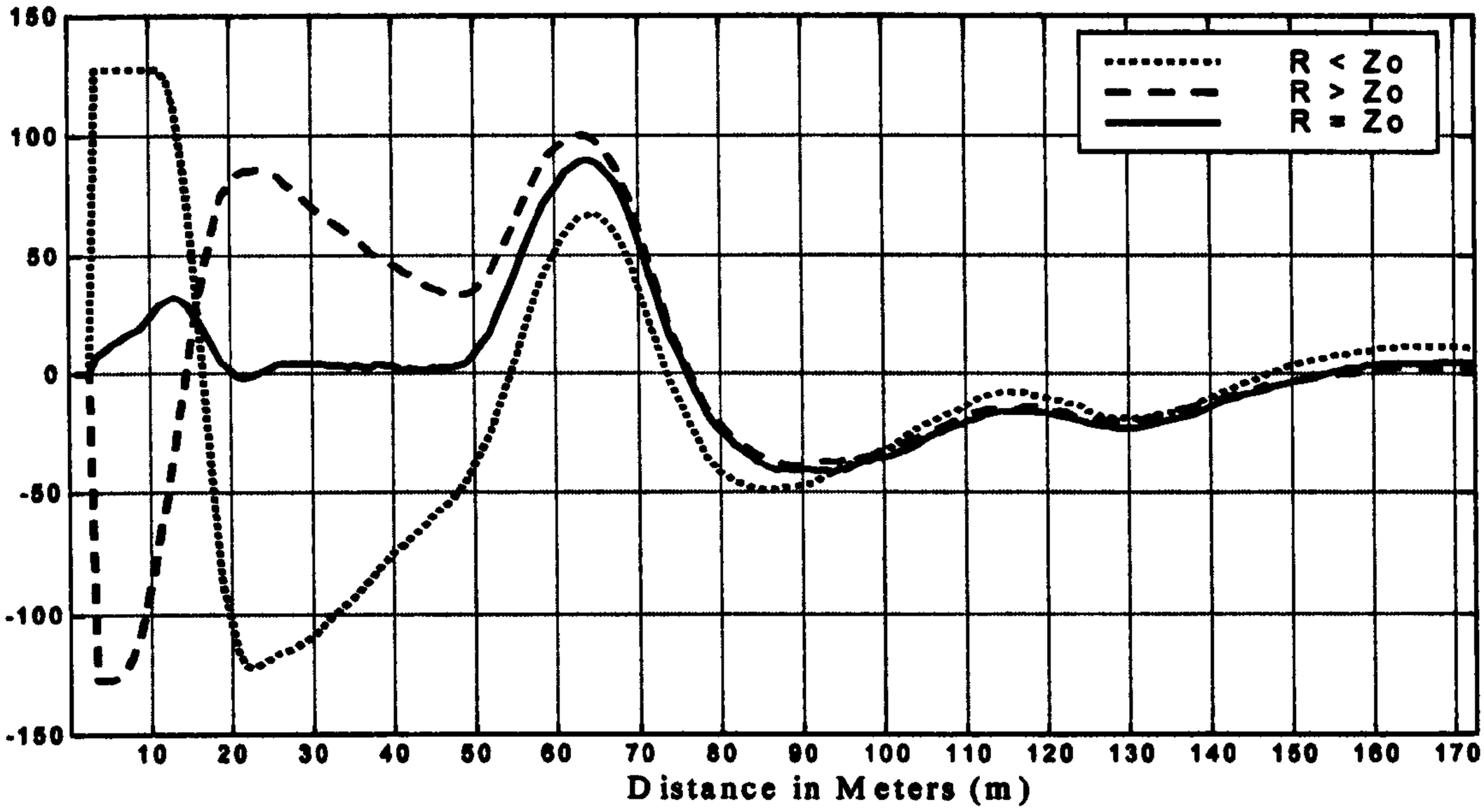

Figure 4.22: RN TDR waveforms when the balance resistor (R) is less that cable impedance (Zo), greater than Zo, and equal to Zo

4.4.3. Voltage/Current Trigger Process

This process records TDR waveforms before and during transient faults in the LVUDN. This is done by either using the voltage trigger or the current trigger. For the voltage trigger, it monitors for voltage disturbance on any of the three phases in the LVUDN. If any disturbance occurs then it triggers the P2000. Similarly for the current trigger, monitors for an increase in the current value. The current level is set by the user. If the current value exceeds the pre-set value then it triggers the P2000.

The user needs to specify which phase-to-neutral or phase-to-phase is to be monitored by the TDR for a transient fault. This is because the instrument has only one TDR card. Therefore, it can only monitor one of the six possible combinations and there will not be enough time to switch the TDR to another connection during the fault arc. The flowchart for this process is illustrated in Fig. 4.23. Initially, the system records the selected phase-to-neutral or phase-to-phase TDR waveform that is under test and stores it. This will give the healthy TDR waveform of the combination. Then it waits for a current or voltage trigger. When the fault occurs, the current or the

voltage will exceed the pre-set value and the P2000 will launch a pulse into the cable and record the TDR waveform. This will give the faulty TDR waveform. The faulty and healthy TDR waveforms can then be compared to find the fault distance. The comparison of TDR waveforms and fault location is explained in more detail in chapter 5.

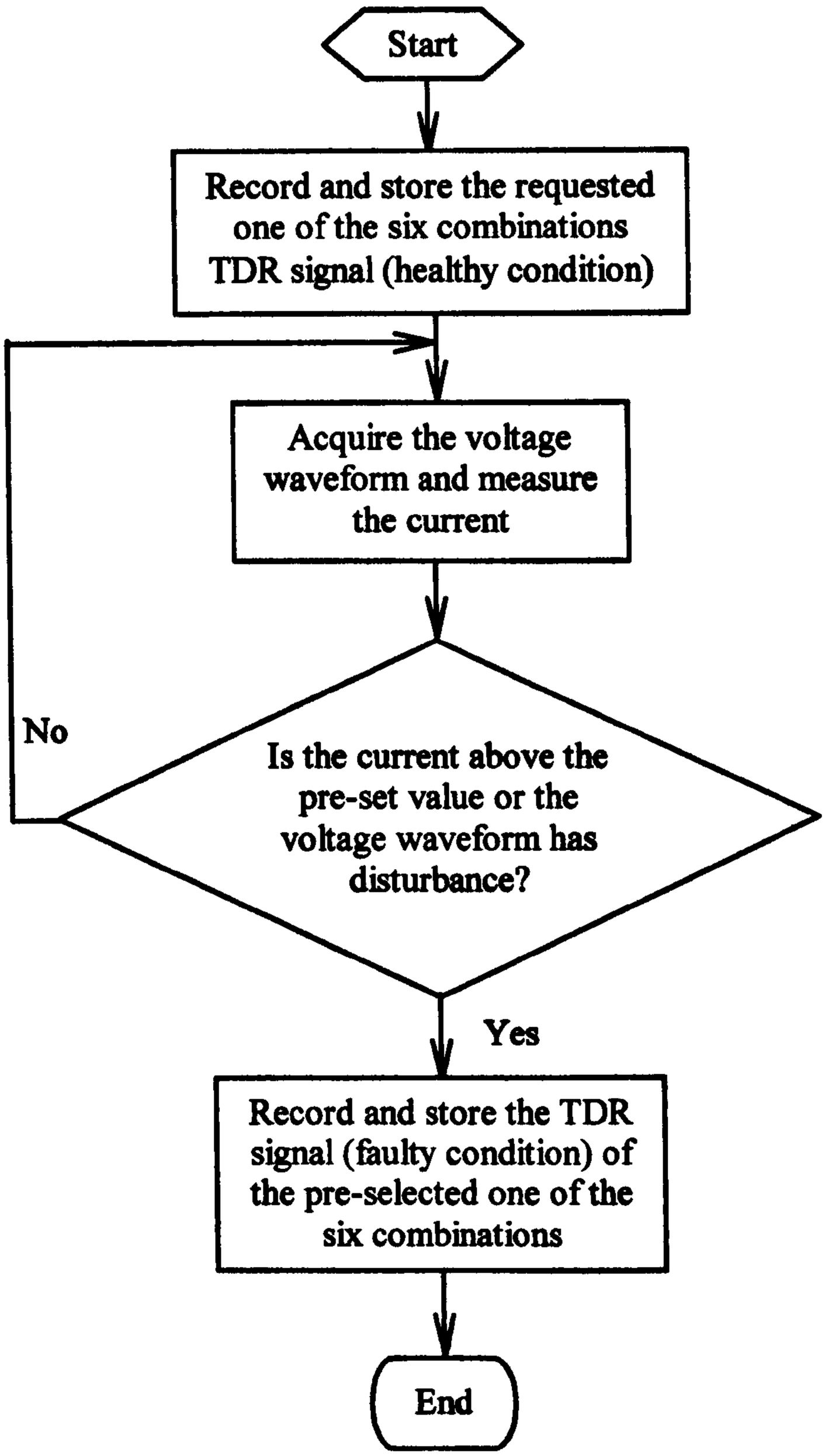

Figure 4.23: Flowchart for the voltage trigger process

The following section discusses how the system detects which fuses are blown and backfeed supply.

4.4.4. Fuse Blown and Backfeed Power Supply Check Process

This process has two main components as shown in Fig. 4.24. They are fuses blown and backfeed power supply check processes. The first component checks, which fuses are blown and then set the flags accordingly. The second component checks which phases have a backfeed and set the flags accordingly.

The flowchart for the fuse blown check process is shown in Fig. 4.25. Initially, the process will acquire all three phases' voltage waveforms. Following this, each phase waveform individually analysed to see whether they are energised or not. If they are energised then flag is set accordingly as shown in Fig. 4.25 and the process ends.

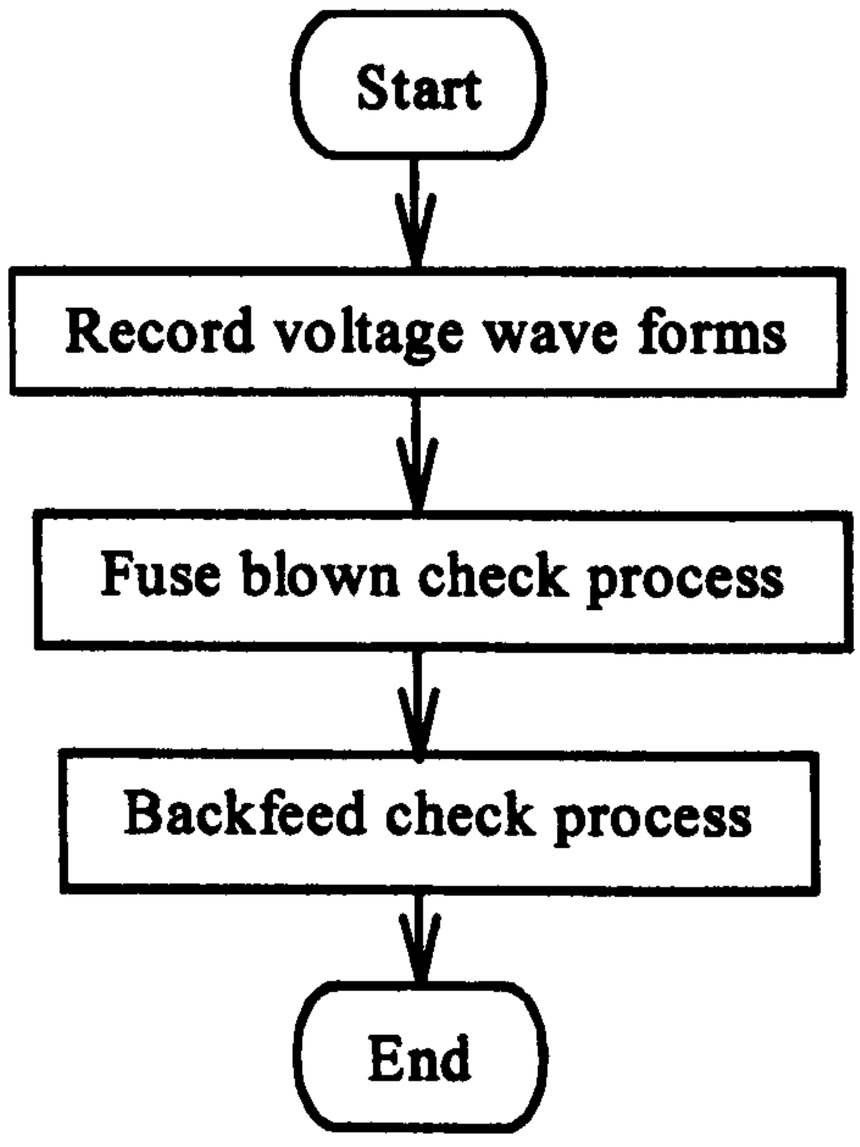

Figure 4.24: An overview flowchart for the fuse blown and backfeed check

The flowchart for the backfeed power supply check process is illustrated in Fig.4.26. The backfeed power supply is identified as follows: first, all possible combinations of pairs of voltage waveforms are taken and compared. If the pairs of voltage waveform have different phase angles they are identified as not having a backfeed (i.e. no phase to phase fault exists). If there is no phase angle difference then a flag is set to indicate the existence of a backfeed as shown in Fig. 4.26. For example, if the Red and Blue phases are found to have a backfeed supply then the process will set the Red-Blue flag.

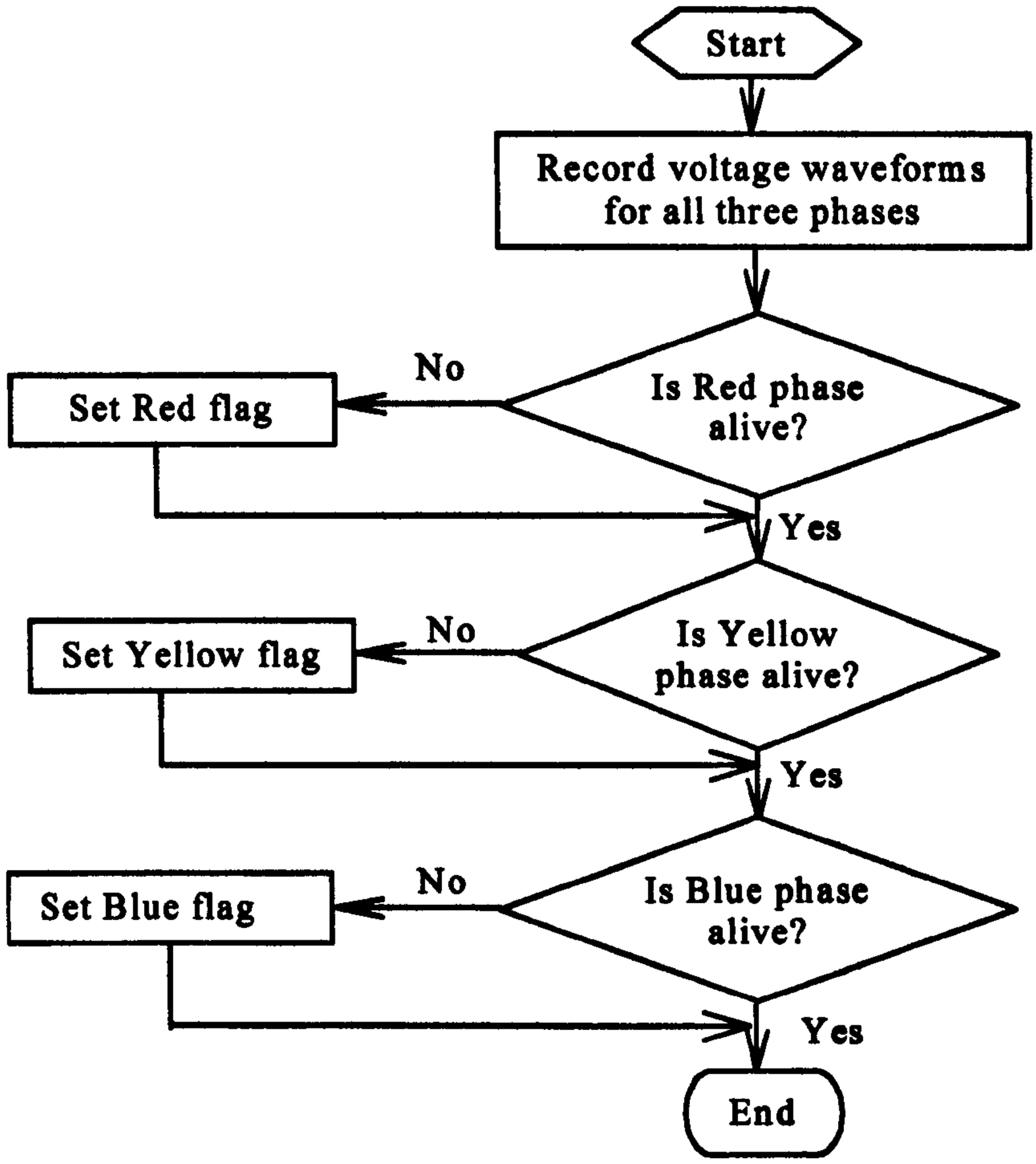

Figure 4.25: Fuse blown check process

The flags that were set during the fuse blown and backfeed check processes are then passed to the recording and storage data process to identify which TDR waveforms need to be recorded.

In the case where all three phases are alive then typically all three (Red, Yellow and Blue) phases will have the voltage waveforms as illustrated in Fig. 4.27. All three phases have a 120° phase angle difference between them. If any phase is not alive then the voltage waveform amplitude for that phase will be zero. This allows identification of which fuses are blown. If there is a backfeed from one phase to another the phase angle of the voltage waveforms will be the same - although the amplitude of the voltage on the backfed phase will usually be lower. For example, if Red and Yellow phases have a phase to phase fault between them and the Red phase is backfeeding the Yellow phase, then the Yellow phase voltage will be in phase with that of the Red phase thereby identifying the backfeed condition.

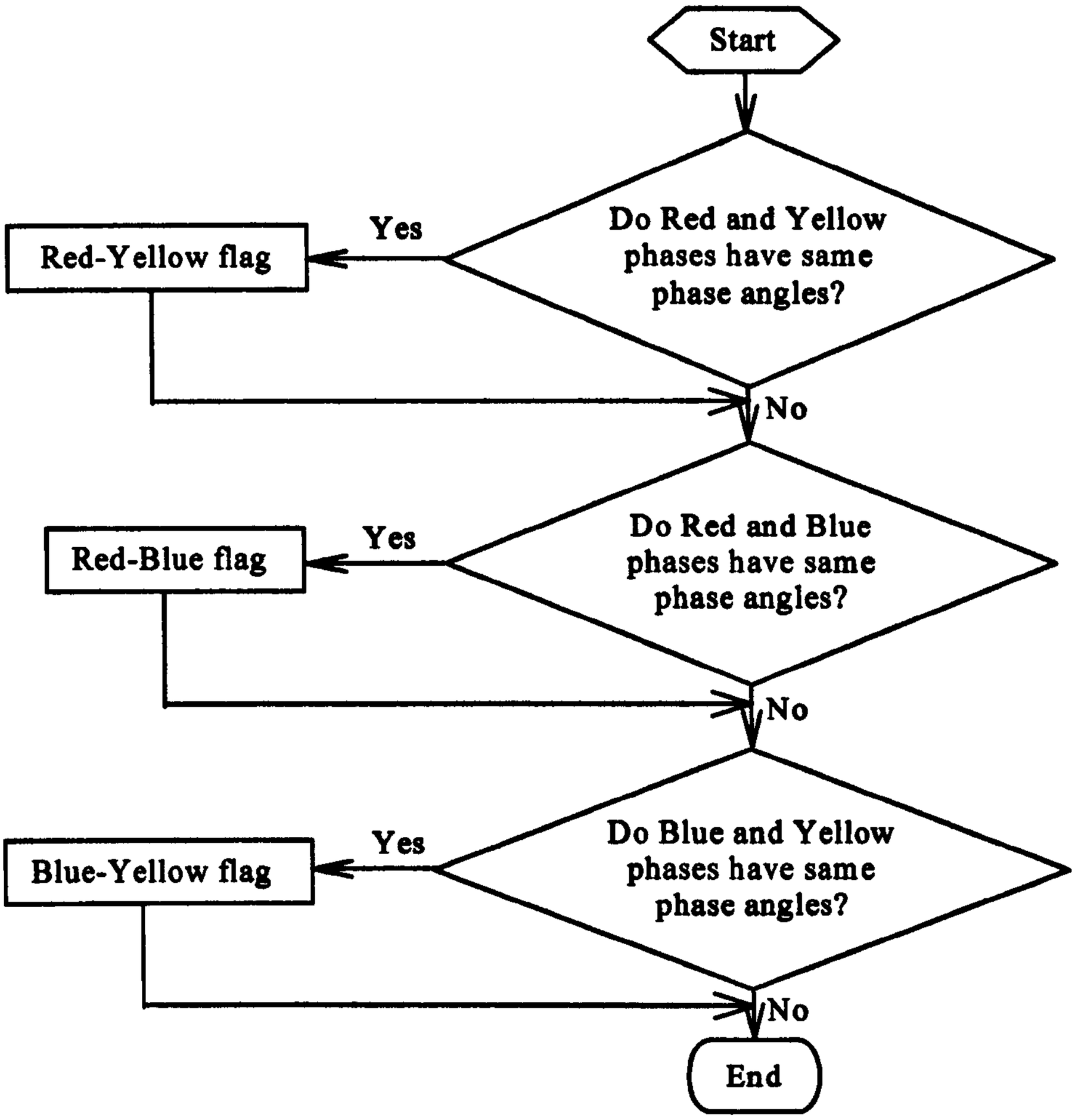

Figure 4.26: Flowchart for the backfeed check process

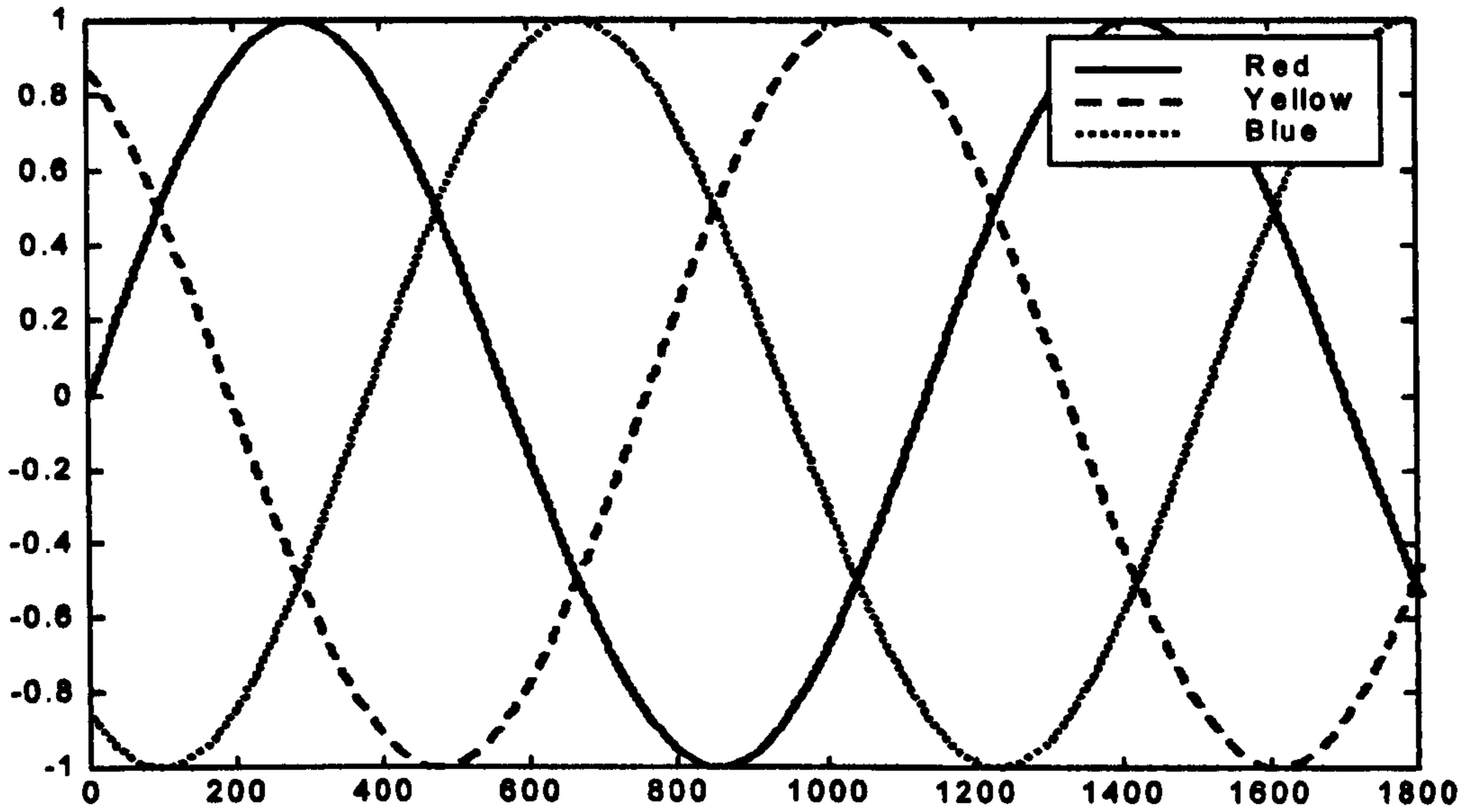

Figure 4.27: Typical Red, Yellow and Blue phase's voltage waveforms

4.4.5. Data Recording and Storage Process

This process records and stores the appropriate data. First, the process checks if the fuse flags of all three phase (Red, Yellow, and Blue) are set or not. If all three flags are set then it will record all six TDR waveforms (BN, RN, YN, RY, RB, and YB) and store them.

If only two fuse flags are set then five TDR waveforms will be recorded. The waveform which will not be recorded is the phase to neutral waveform for the phase whose flag is not set. For example, if Yellow flag is not set then the process will not record YN TDR waveform but records the rest of the five TDR waveforms.

If only one fuse flag is set then the backfeed flags of the other two phases are checked. For example, if the Yellow fuse flag is set, then the process will check whether the Red-Blue backfeed flag is set or not. If the backfeed flag is set then all six TDR waveforms will be recorded. Next one of the phase to Neutral TDR waveforms is examined to see if it is below a threshold value of 30. This is to identify which phase fuse is blown. If the selected TDR waveform is below the threshold value then the process will discard it and store all the other the TDR waveforms. If it is above the threshold value then the process will discard the other phase to Neutral waveform involved in the backfeed and store the rest of the five TDR waveforms. For the above example, where Yellow fuse flag and Red-Blue backfeed flags are set, and the Red phase fuse of the backfed phases is blown, the process will not store BN but will store the rest of the five TDR waveforms.

If there are no flags set, the process will check if any backfeed flags are set or not, and then record and store the TDR waveforms accordingly. For example if there is only one backfeed the process will record and store three TDR waveforms only because only one fuse would have been blown in this case. If two backfeed flags are set then the process will record and store five TDR waveforms. This time two fuses would have blown, so the process can record five TDR waveforms.

4.4.6. Comparison between P240 and Prototype (P2000)

Previous commercial TDR-based fault location instruments have some limitations for data acquisition and fault location (see section 4.4 for more details). The P240 is one of the commercial TDR instruments that was developed by Hathaway Instruments Ltd. in the mid 1980s. The P240 is illustrated in Fig. 4.28. Features of the P240 and its

limitations are illustrated in Table 4.1. To overcome some of the limitations of the P240, the new prototype P2000, shown in Fig. 4.29, was developed.

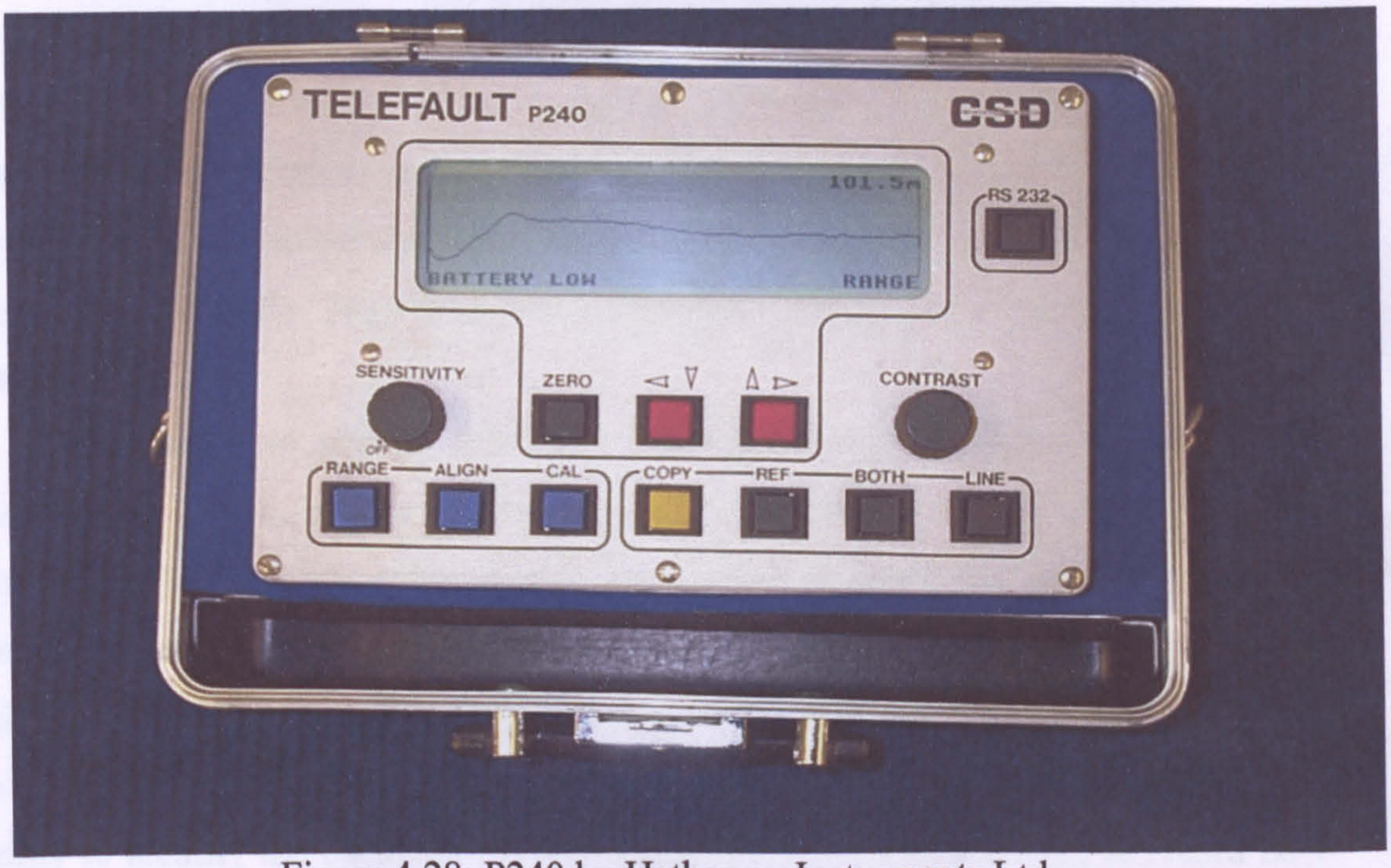

Figure 4.28: P240 by Hathaway Instruments Ltd.

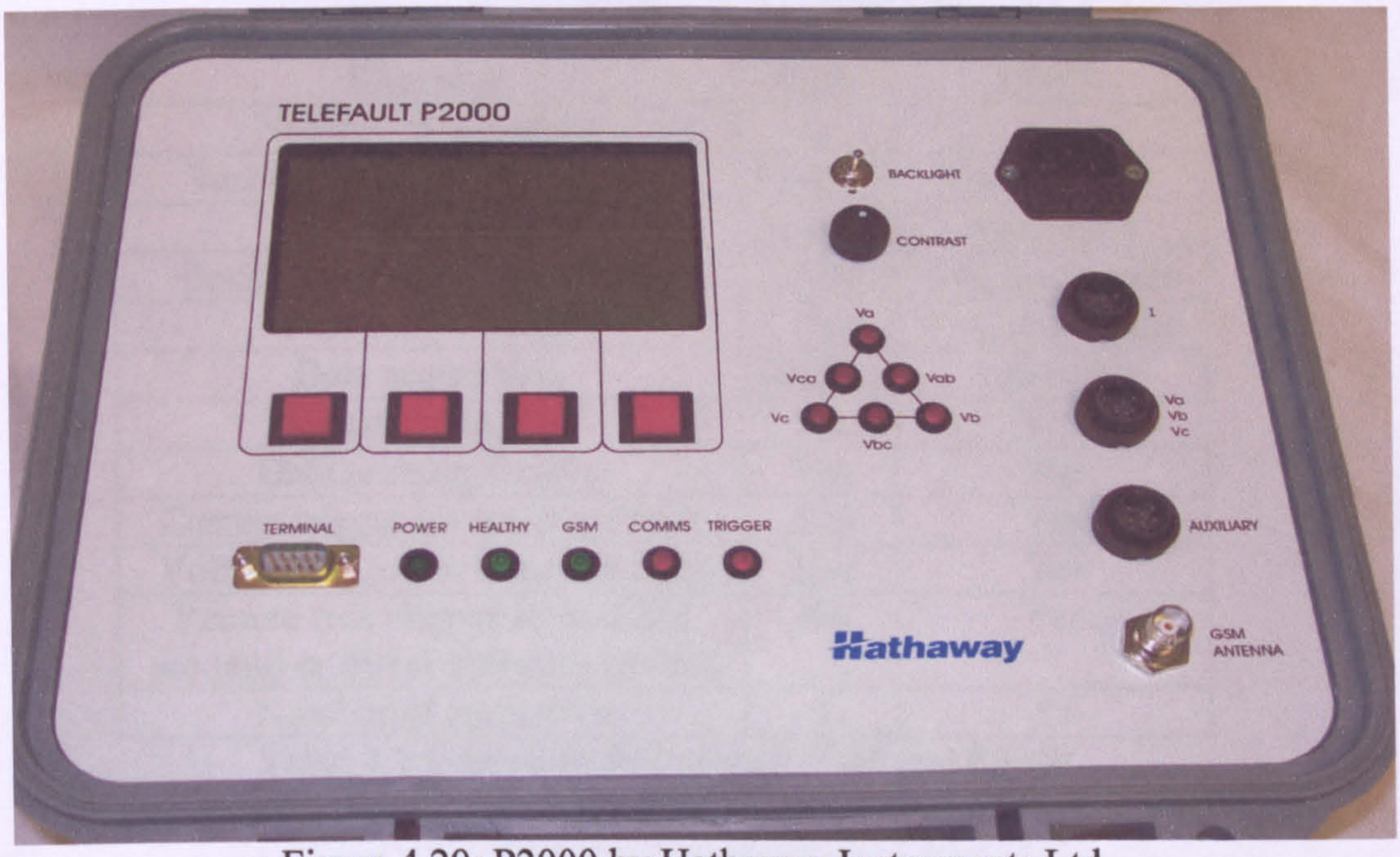

Figure 4.29: P2000 by Hathaway Instruments Ltd.

Table 4.1 shows the functionality of both instruments. The P240 has a single pair of test leads. They can be connected between phase to phase or phase to neutral. The

test leads therefore need to be manually interchanged to acquire different TDR waveforms. The P2000 has four test leads. All phases and neutral are connected at the time and the data acquisition is done by the software automatically. The P240 does not have the capability to check whether the user has connected the test leads properly or not. However, the P2000 has the facility to check this and warn the user which test leads are not connected as explained in section 4.4.1. In the P240, to match the cable impedance and to minimise the effect of the test lead, the user is required to adjust the balance box manually. The balancing is done automatically in the P2000 as explained in section 4.4.2.

Before starting to acquire TDR waveforms, the user is required to know which fuse(s) is/are blown, so that the appropriate TDR waveforms can be recorded (see section 4.2.1). The P240 does not have the facility to check this and a separate test lamp procedure must be used. The P2000 has the facility to check this automatically and record the TDR waveforms appropriately as explained in section 4.4.5. If one of the phases in a LVUDN has a backfeed from another phase then the P2000 has the facility to identify the backfeed automatically (section 4.4.4) and then to record only the appropriate TDR waveforms (section 4.4.5).

Function	P240	P2000
Number of test leads	2	4
Test leads connections check	Manual	Automatic
Balancing	Manual	Automatic
Backfeed power supply check	No	Yes, Automatic
Fuse blown check	No	Yes, Automatic
Data acquisition	Manual	Automatic
Data storage	No	Yes
Data printing facility	Yes	No
Current trigger for transient fault	Yes	Yes
Voltage trigger for transient fault	Yes	Yes
Remote (via telephone or GSM modem) or direct software control	No	Yes
Number of memories	1	25

Table 4.1 Comparisons between P240 and P2000

As mentioned above, the P2000 records the appropriate TDR waveforms automatically (section 4.4.5), whereas with the P240 the user has to know which TDR waveforms need to be recorded. The P240 has the facility to print TDR waveforms whereas the P2000 does not have a print facility but does have 25 non-volatile

memories. Both instruments have the facility to acquire TDR waveforms before and during transient faults using either current or voltage triggering (section 4.4.3).

4.5. Real LVUDN's Transient Faults Data Analysis

In this section, a selection of transient faults that were recorded using the P2000 on real LVUDNs are presented. When the P2000 is installed to detect and locate transient faults, it is normally setup to record three phase voltage waveforms, a single current waveform and a single TDR waveform. The voltage and current waveforms are recorded for a 10 cycle period that includes two cycles before the fault and 8 cycles after the fault. Six TDR waveforms are usually recorded before the fault for all combinations of phase to phase and phase to neutral connections. Although the P2000 has only one TDR card, as mentioned in sectioned 4.4.3, six TDR waveforms are recorded in case the fault becomes permanent at which time these waveforms can then be used for comparison purposes in locating the fault. The particular phase to phase or phase to neutral injection is selected by the user based on the previous fault history (e.g. fuse operations) and the P2000 is armed for transient capture. After each transient recording the P2000 is automatically re-armed for further transients.

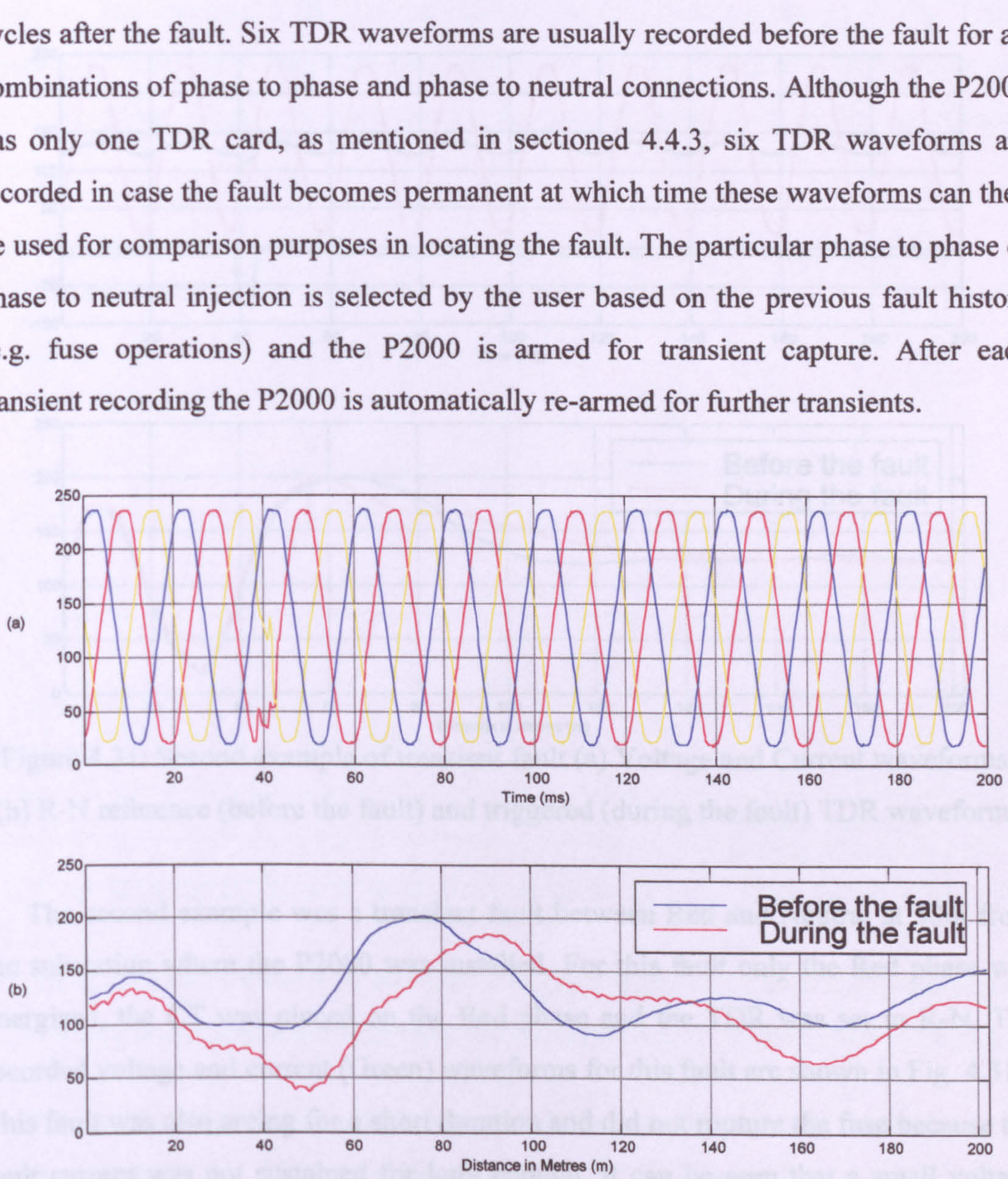

Figure 4.30: First example of transient fault (a) Voltage waveforms, (b) R-Y reference (before the fault) and triggered (during the fault) TDR waveforms

First example was a transient fault between Red and Yellow phases at 36m from the substation where the P2000 was installed. The three phases voltage waveforms for this fault are shown in Fig. 4.30a. It can be seen that the fault was arcing for a short duration. Therefore, the fuse did not rupture for this transient. No CT was installed on this fault and therefore the current waveform was not recorded. Fig 4.30b shows the R-Y reference (before the fault) and the triggered (during the fault) TDR waveforms for this fault. A split is shown between the two TDR waveforms at 36m, i.e. the actual location of the fault. The DC offset between the two TDR waveforms can be eliminated by using the vertical alignment function on the P2000.

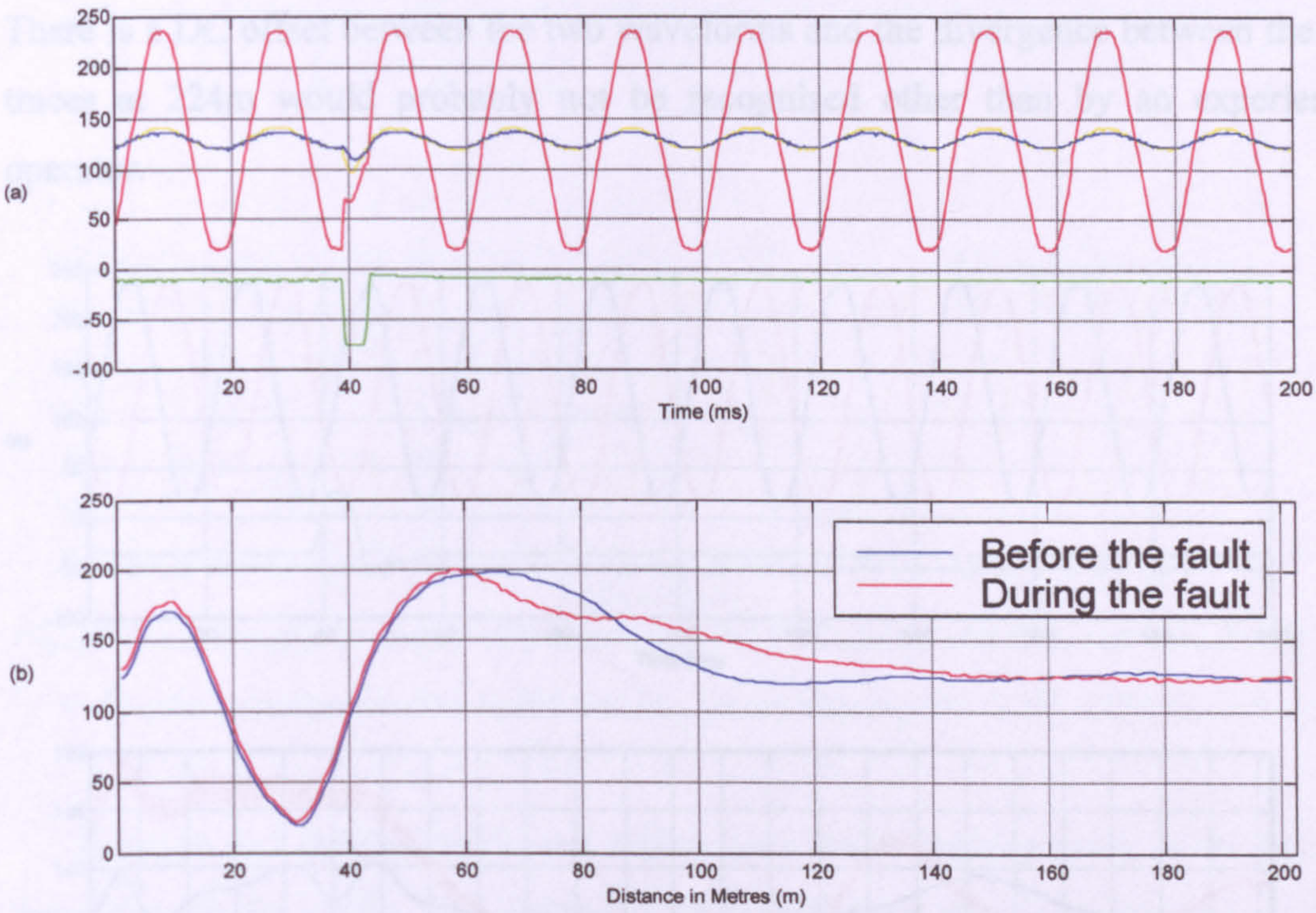

Figure 4.31: Second example of transient fault (a) Voltage and Current waveforms, (b) R-N reference (before the fault) and triggered (during the fault) TDR waveforms

The second example was a transient fault between Red and Neutral at 58m from the substation where the P2000 was installed. For this fault only the Red phase was energised, the CT was placed on the Red phase and the TDR was set to R-N. The recorded voltage and current (Green) waveforms for this fault are shown in Fig. 4.31a. This fault was also arcing for a short duration and did not rupture the fuse because the fault current was not sustained for long enough. It can be seen that a small voltage was induced in the de-energised phases (Yellow and Blue) due to mutual coupling

from the Red phase. The induced voltage increased during the fault. The R-N reference and triggered TDR waveforms for this fault are shown in Fig. 4.31b which shows a spilt between the TDR waveforms at 58m.

The third example was a transient fault, involving all three phases, at 224m from the substation where the P2000 was installed. The CT was installed on the Yellow phase and the TDR was set to inject on Y-B. Fig. 4.32a shows the voltage and current waveforms of this example. It can be seen that the fault initially started between Yellow and Blue phases only and then involved Red phase as well. The Yellow phase was affected more than the other two phases. The fault was arcing for only a short duration. The recorded Y-B TDR waveforms for this fault are shown in Fig. 4.32b. There is a DC offset between the two waveforms and the divergence between the two traces at 224m would probably not be recognised other than by an experienced operator.

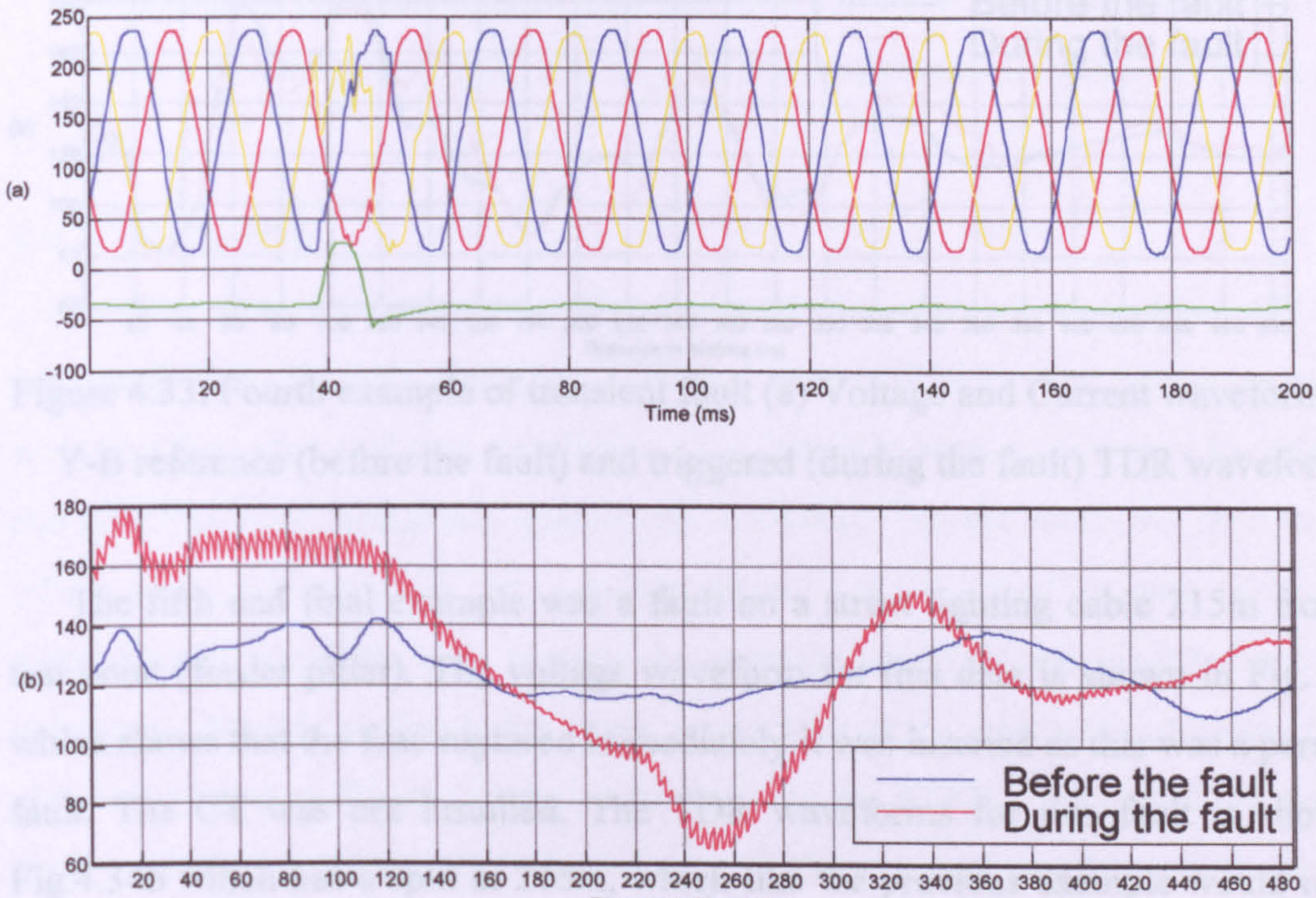

Figure 4.32: Third example of transient fault (a) Voltage and Current waveforms, (b) Y-B reference (before the fault) and triggered (during the fault) TDR waveforms

The fourth example was a fault between Yellow and Blue phases at 59m from the substation where the P2000 was installed. The CT was installed on the Blue phase. The voltage and current waveforms for this fault are shown in Fig. 4.33a which shows

that the fault was arcing for several cycles. In this case the fault current duration and amplitude were sufficient to rupture the Blue phase fuse and cause the voltage on the Blue phase to collapse. The Yellow phase voltage recovers after the fuse operation on the Blue phase. The TDR waveforms for this data are shown in Fig. 4.33b which shows a split at 59m.

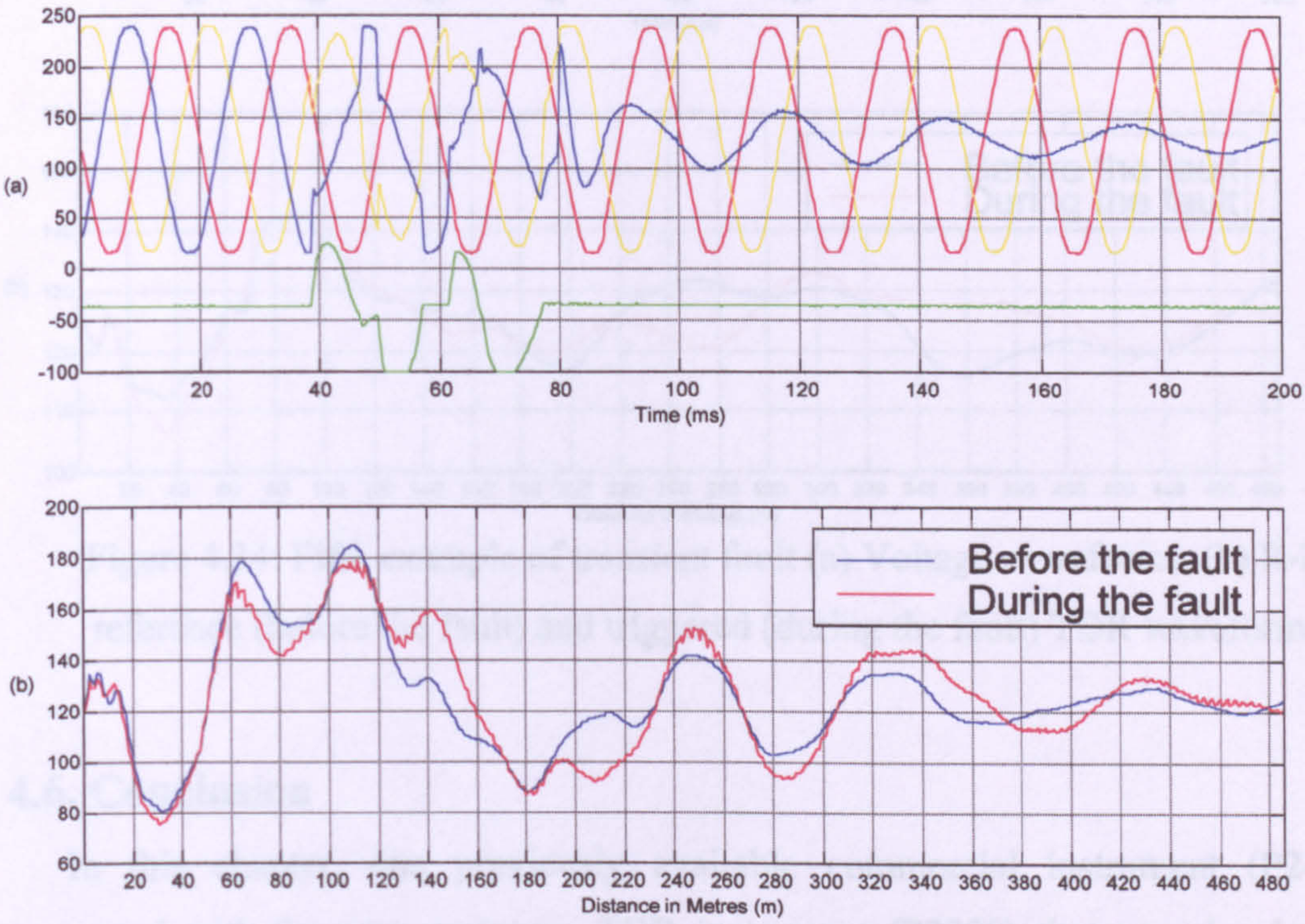

Figure 4.33: Fourth example of transient fault (a) Voltage and Current waveforms, (b) Y-B reference (before the fault) and triggered (during the fault) TDR waveforms

The fifth and final example was a fault on a street lighting cable 215m from the test point (feeder pillar). The voltage waveform for this data is shown in Fig. 4.34a which shows that the fuse ruptured immediately it was inserted as this was a persistent fault. The CT was not installed. The TDR waveforms for this fault is shown in Fig.4.34b which has a split at 215m, which like the previous example would require skill to recognise.

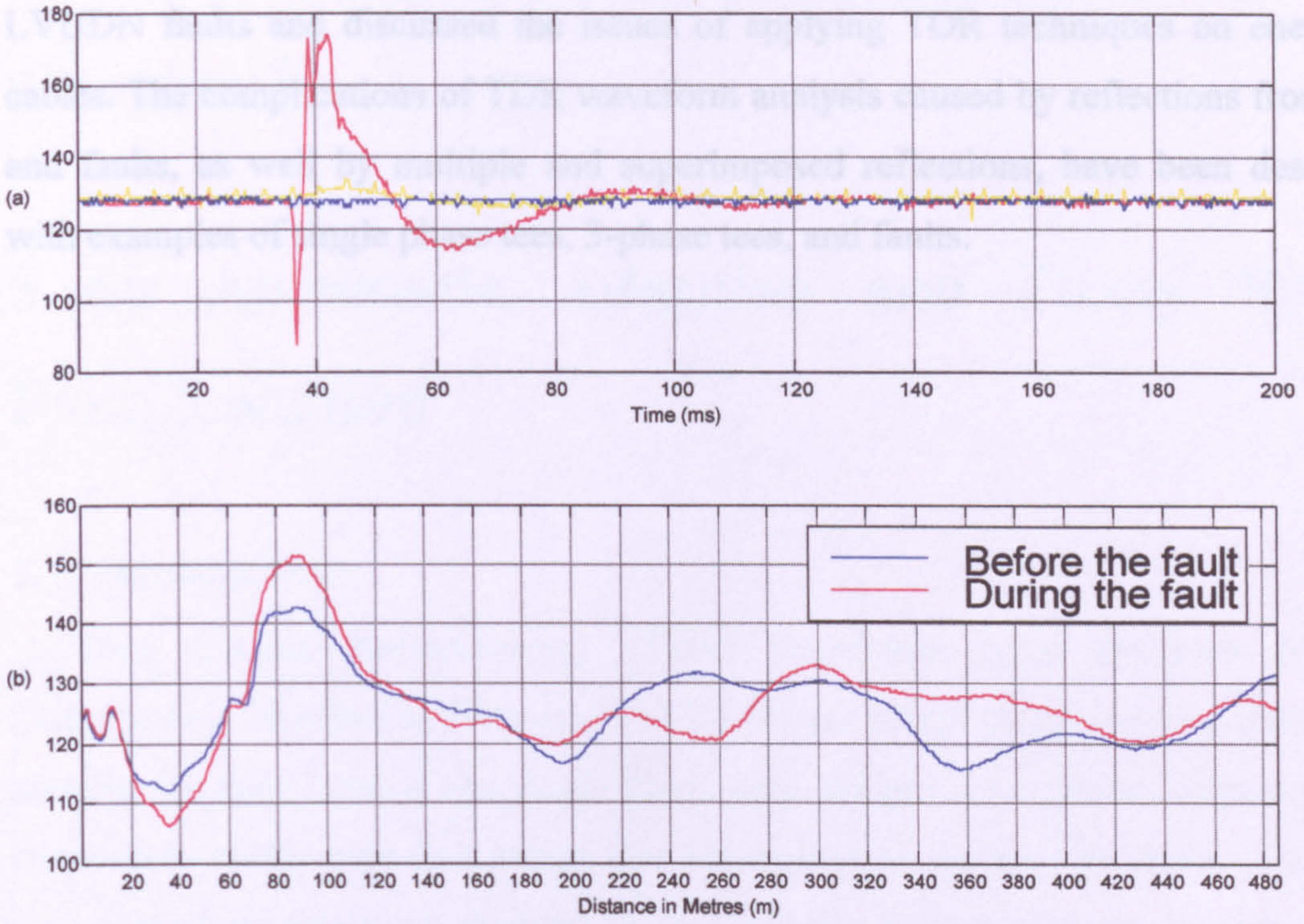

Figure 4.34: Fifth example of transient fault (a) Voltage waveforms, (b) R-N reference (before the fault) and triggered (during the fault) TDR waveforms

4.6. Conclusion

In this chapter, one previously available commercial instrument (P240) is compared with the new prototype TDR instrument (P2000) that was developed to automate the process of data acquisition. The P2000 minimises the need for user skill and provides some safeguards against user mistakes. The user does not need to know which fuses are ruptured nor whether there is a backfeed or not. The P2000 automatically identifies and records the appropriate TDR waveforms. Setting the balancing network to match the cable surge impedance and to compensate for the stray inductance of the test leads is automated in the P2000. The P2000 has four test leads to connect to all three phases and neutral, thereby avoiding the need to move the connections manually. The instrument automatically detects if the user accidentally does not connect the test leads properly and informs the user which test lead(s) are not connected. The P2000 also has the facility for triggering on voltage depressions and current surges. The features of the P2000 are illustrated with example of TDR waveforms.

This chapter has presented examples of the ideal TDR waveforms which can be obtained on model networks. It has also presented TDR waveforms obtained on real

LVUDN faults and discussed the issues of applying TDR techniques on energised cables. The complications of TDR waveform analysis caused by reflections from tees and faults, as well by multiple and superimposed reflections, have been described with examples of single phase tees, 3-phase tees, and faults.

Chapter 5

5. An Automatic Adaptive and Fuzzy Based Fault Location

5.1. Introduction

Time Domain Reflectrometry (TDR) waveforms from the Low Voltage Underground Distribution Networks (LVUDN) are complicated due to a number of reasons: multiple 3-phase and single phase tees, straight joints, noise, dispersion and attenuation of the reflected pulses due to cable loss, as well as faults. Therefore experienced engineers are required to interpret the TDR waveforms to identify the fault reflection from them. There are two approaches currently employed to locate faults using TDR waveforms. One is to subtract the faulty waveform from the healthy waveform to produce a departure for the fault. The second one is to superimpose the healthy and faulty waveforms to find a split (departure) for the fault. The detailed explanations of these two approaches are contained in section 2.3.4.1, chapter 2.

In this chapter, an automatic fault location system for LVUDN using TDR waveforms is presented. There are three distinct stages in this automatic fault location system. One is pre-processing to identify single-phase tees and locate 3-phase faults. The second one is intelligent processing that uses adaptive filtering to produce error waveforms that will only give a significant difference at the fault point. Finally, fuzzy membership is used to find a unique fault distance when there is more than one error or TDR waveform. This is because each error or TDR waveform may give different apparent fault distances.

In section 5.2, an overview of the automatic fault location system for LVUDN and its overall flowchart is presented. Section 5.3 explains why pre-processing is needed and describes in detail how it is used to identify single-phase tees and to locate 3-phase faults. Section 5.4 introduces intelligent processing and shows how adaptive filtering is applied to TDR waveforms to produce an error waveform. It also shows how these error waveforms are analysed automatically to find the fault departure. In section 5.5, the fault distance calculation is demonstrated. It uses fuzzy membership to

find a unique fault distance when there is more than one fault distance. i.e. if there are more than two reflected waveforms there will be more than one error waveform. Each error waveform will have one fault distance and they may not all have the same fault distance.

In section 5.6, the performance of the system is tested using some field data and the analysis of these results is given. Finally, the optimisation of the adaptive filter's parameters for the three adaptive algorithms (LMS, NLMS, and RLS) is given in section 5.7.

5.2. System Overview

An overview flowchart of the adaptive based automatic fault location system for LVUDN is illustrated in Fig. 5.1. It consists of three stages: pre-processing, intelligent processing, and a fault distance calculation.

In the pre-processing stage, the cable network is characterised to detect single-phase tees and also to locate 3-phase faults (open/short) based on the gathered data. The single-phase tee locations are then stored for later use in the intelligent processing stage. If a 3-phase fault is detected it then moves to fuzzy based distance calculation stage bypassing the intelligent processing stage to calculate the fault distance. The intelligent processing stage produces error waveforms between the TDR waveforms using an adaptive filter. These error waveforms are processed with the earlier information stored in the pre-processing stage to detect faults. Once the fault is detected, the fuzzy based distance calculation stage calculates the fault distance.

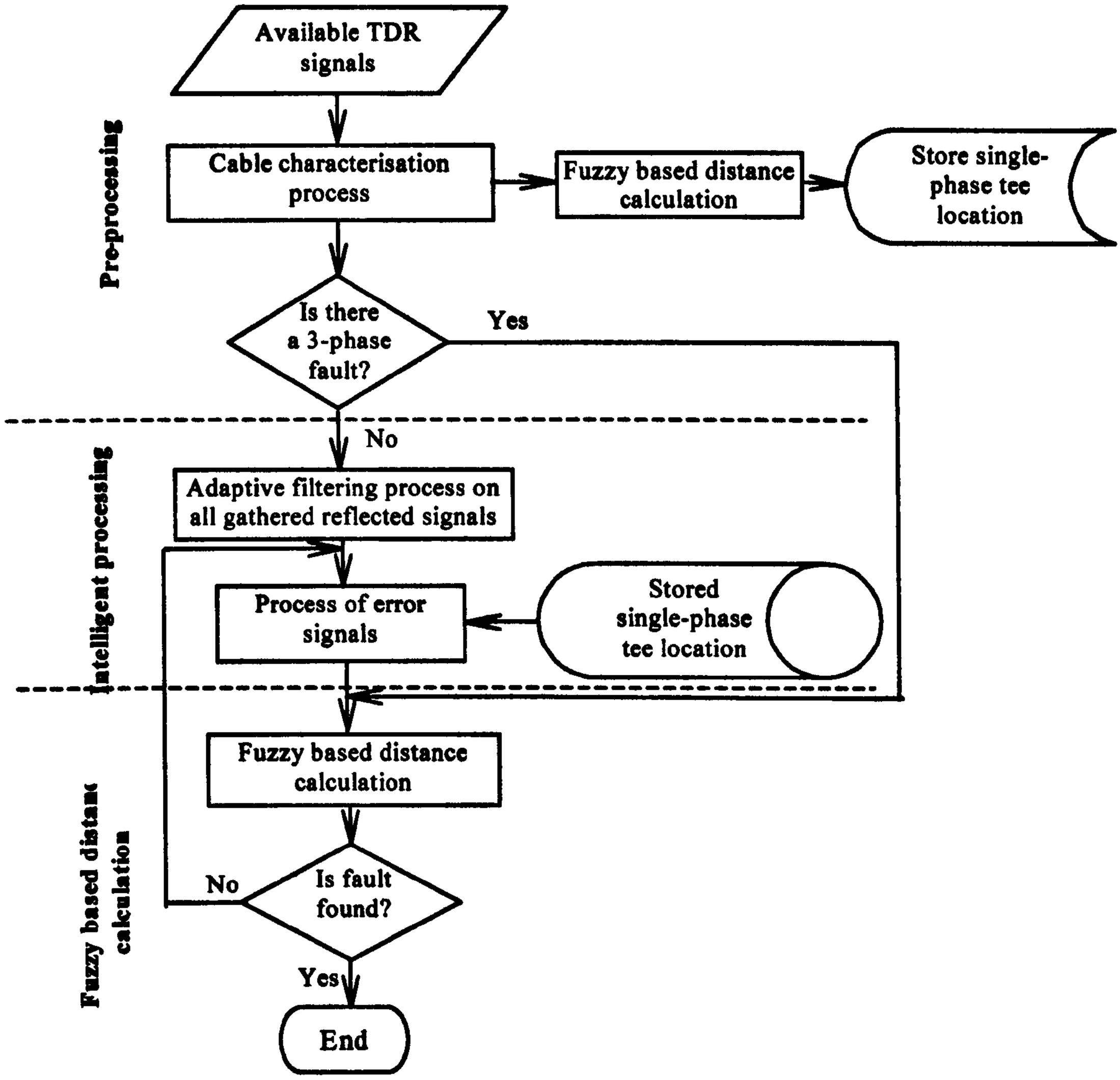

Figure 5.1: An adaptive based automatic fault location system's overview flowchart

5.3. Pre-processing

5.3.1. Why Pre-processing?

There are two reasons for pre-processing, one is to identify the existence of any single-phase tees (service cables) and the other is to locate 3-phase faults. The TDR waveforms for all 3 phases have similar characteristics for a cable network, unless the cable network under test has a fault or single-phase tee(s) (or due to noise). The effect of the single-phase tee will be more visible on phase to neutral TDR waveforms than the phase- to-phase TDR waveform as explained in section 4.3. The single-phase tee will give a reflection similar to that of a short circuit fault, but will have less

amplitude as demonstrated in section 4.3. Therefore, before processing waveforms with adaptive filters, it is useful to identify the single-phase tee location(s). These single-phase tee locations will be cross-referenced with the fault location that may found during the intelligent processing to eliminate the confusion between them.

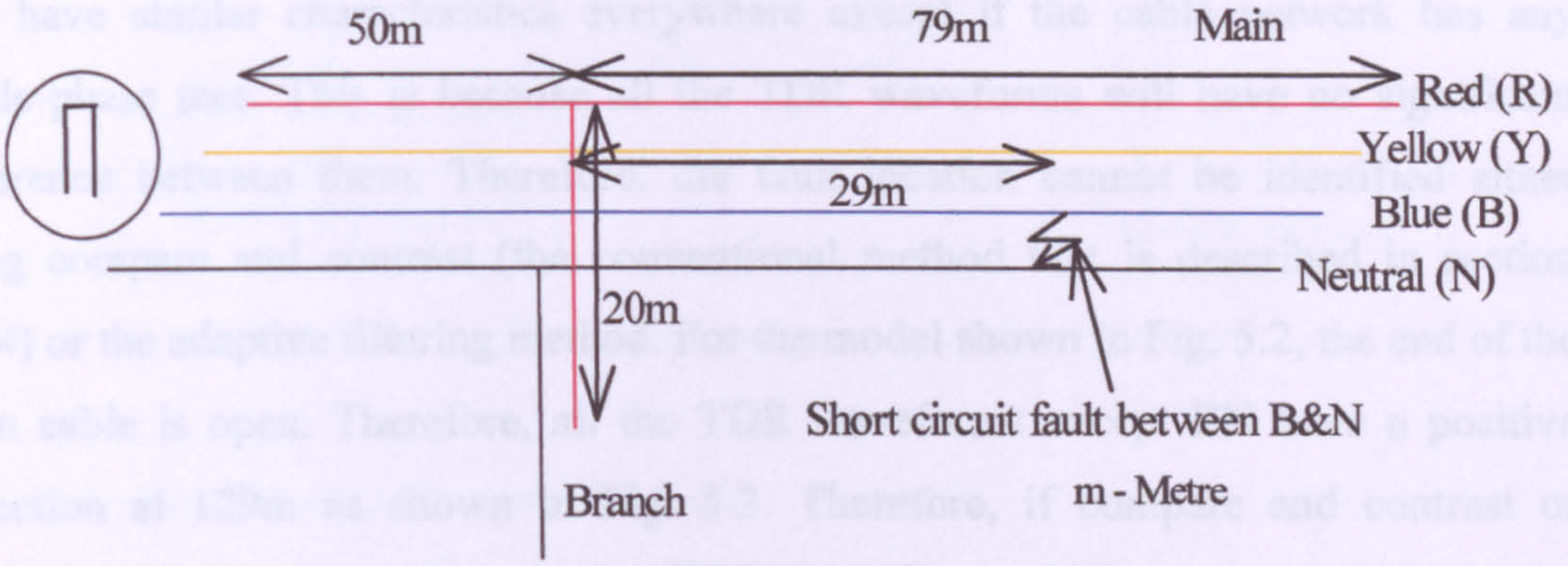

Figure 5.2: A 4-core cable model

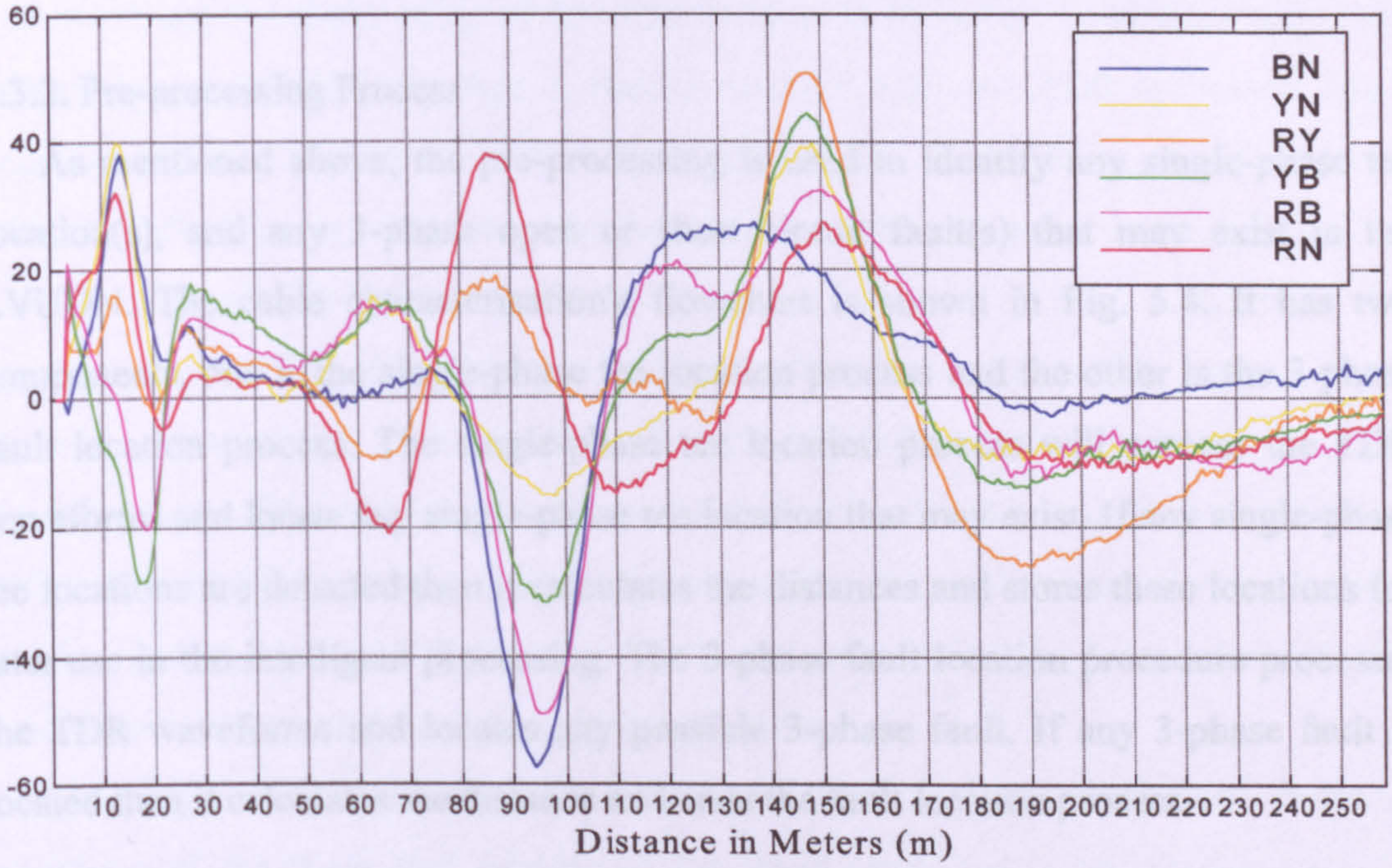

Figure 5.3: TDR waveforms (BN, YN, RY, YB, RB, and RN) for model in Fig. 5.2

Consider the example network of a 4-core cable model is shown in Fig. 5.2. It comprises a 129m main cable with a single-phase (RN) tee at 50m of length 20m. The main cable has straight joints at 50m and 79m. It has a short circuit fault at 79m along the main cable between Blue and Neutral. The TDR waveforms (RN, YN, BN, RB, YB, and RY) for the model in Fig. 5.2 are shown in Fig. 5.3. The RN waveform has a

negative reflection at 50m due to the single-phase tee whereas other waveforms do not have any significant reflection at 50m similar to the RN waveform. Therefore, if the RN phase waveform is used for the adaptive process it may show that location as a fault position.

If the cable network under test has a 3-phase fault then all the TDR waveforms will have similar characteristics everywhere except if the cable network has any single-phase tees. This is because all the TDR waveforms will have no significant difference between them. Therefore, the fault location cannot be identified either using compare and contrast (the conventional method that is described in section 2.3.4) or the adaptive filtering method. For the model shown in Fig. 5.2, the end of the main cable is open. Therefore, all the TDR waveforms except BN have a positive reflection at 129m as shown in Fig. 5.3. Therefore, if compare and contrast or adaptive filtering is applied to the TDR waveforms this open end will not be identified. Therefore, some pre-processing is required to tackle these problems.

5.3.2. Pre-processing Process

As mentioned above, the pre-processing is used to identify any single-phase tee location(s), and any 3-phase open or short circuit fault(s) that may exist in the LVUDN. The cable characterisation's flowchart is shown in Fig. 5.4. It has two components, one is the single-phase tee location process and the other is the 3-phase fault location process. The single-phase tee location process will process the TDR waveforms and locate any single-phase tee location that may exist. If any single-phase tee locations are detected then it calculates the distances and stores these locations for later use in the intelligent processing. The 3-phase fault location procedure processes the TDR waveforms and locates any possible 3-phase fault. If any 3-phase fault is located then it calculates the distance and ends the fault location process.

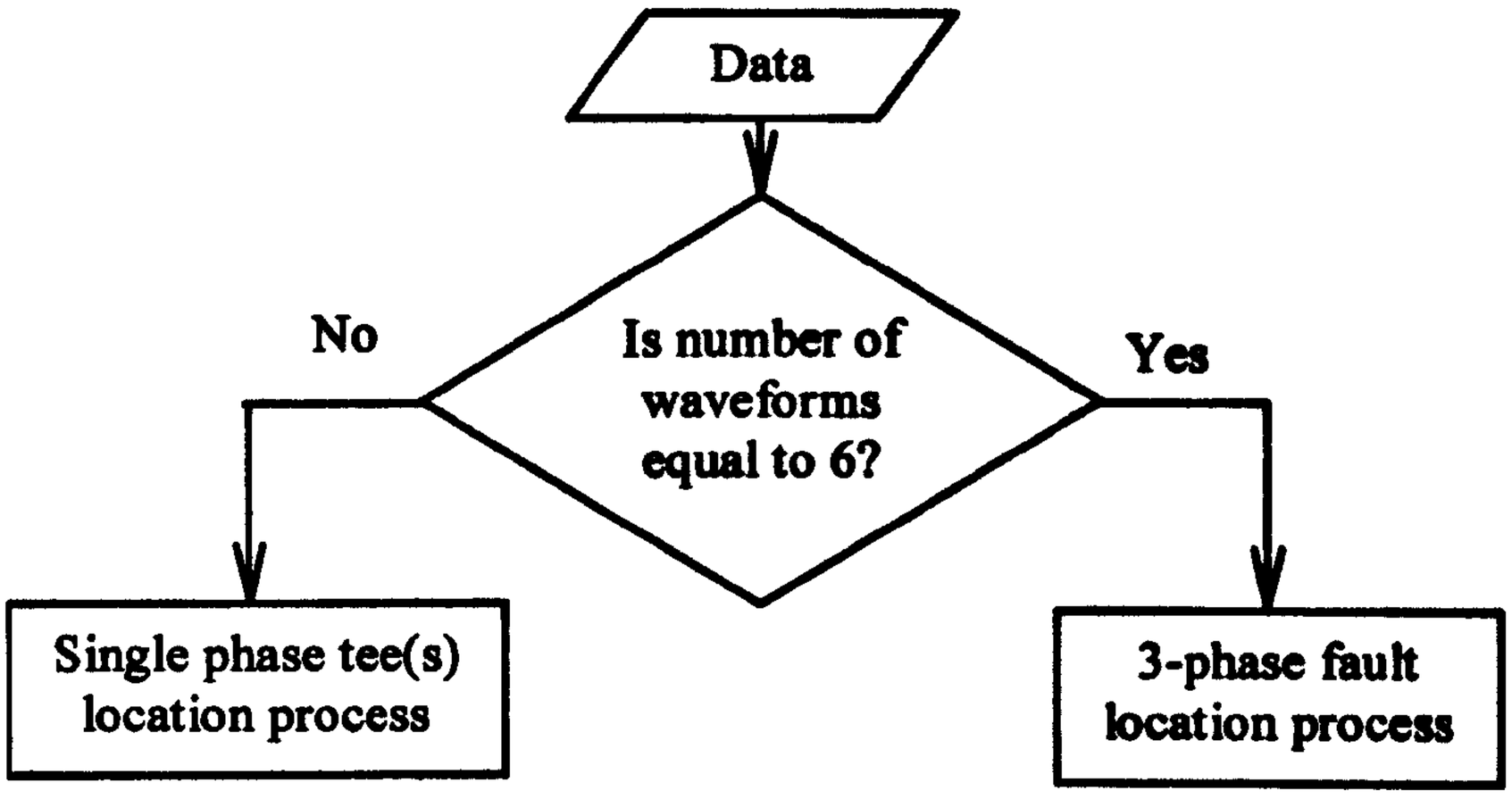

Figure 5.4: Cable characterisation overview flowchart

5.3.2.1. Single Phase Tee Location Process

A flowchart for the single-phase tee location process is illustrated in Fig.5.5. The procedure for this process is as follows: Firstly, the TDR waveforms are thresholded with a pre-set threshold value of 20. This process is to isolate significant amplitude reflections only. Following then it checks whether only one TDR waveform has a negative value at any position. This is to identify the single-phase tee. If only one TDR waveform has a negative value then it checks that the peak value is below the pre-set value. If it is below the pre-set threshold value of 30 then it identifies this location as a possible single-phase tee location. This is to differentiate a single-phase tee from a short circuit fault. As shown Fig. 5.3, the RN waveform has a single phase tee reflection at 50m and has a smaller amplitude than the short circuit fault reflect on BN at 79m. If this location is a single-phase tee then it calculates the distance for that location and stores it. The distance calculation process is explained in section 5.5. The process is then repeated for the whole length of data.

The single phase tee may not be identified if the phase-to-neutral reflected waveform of the phase that consists of the single-phase tee is not available for the fault location process as explained in section 4.3. i.e the cable model shown in Fig. 5.2 has a single phase tee on the Red phase at 50m. If RN is phase is not used in the fault location then the single phase tee will not be identified. This is because, the single phase tee reflection on RY and RB waveforms will not have significant reflection as RN waveform. Since the fault is on the Blue phase, BN, RB, and YB reflected phase waveforms would only be recorded as mentioned in Chapter 4. This does not include the RN reflected waveform. As a consequence the RN single-phase

tee may not be identified during the single-phase classification process. This is because the single-phase tee on the red phase will have only minimal amplitude on RB, BN and YB as illustrated in Fig 5.3. It will therefore not be identified during the pre-processing, because this will be filtered out during the thresholding process. Since the amplitude is small, it will also not cause a problem during the intelligent processing stage.

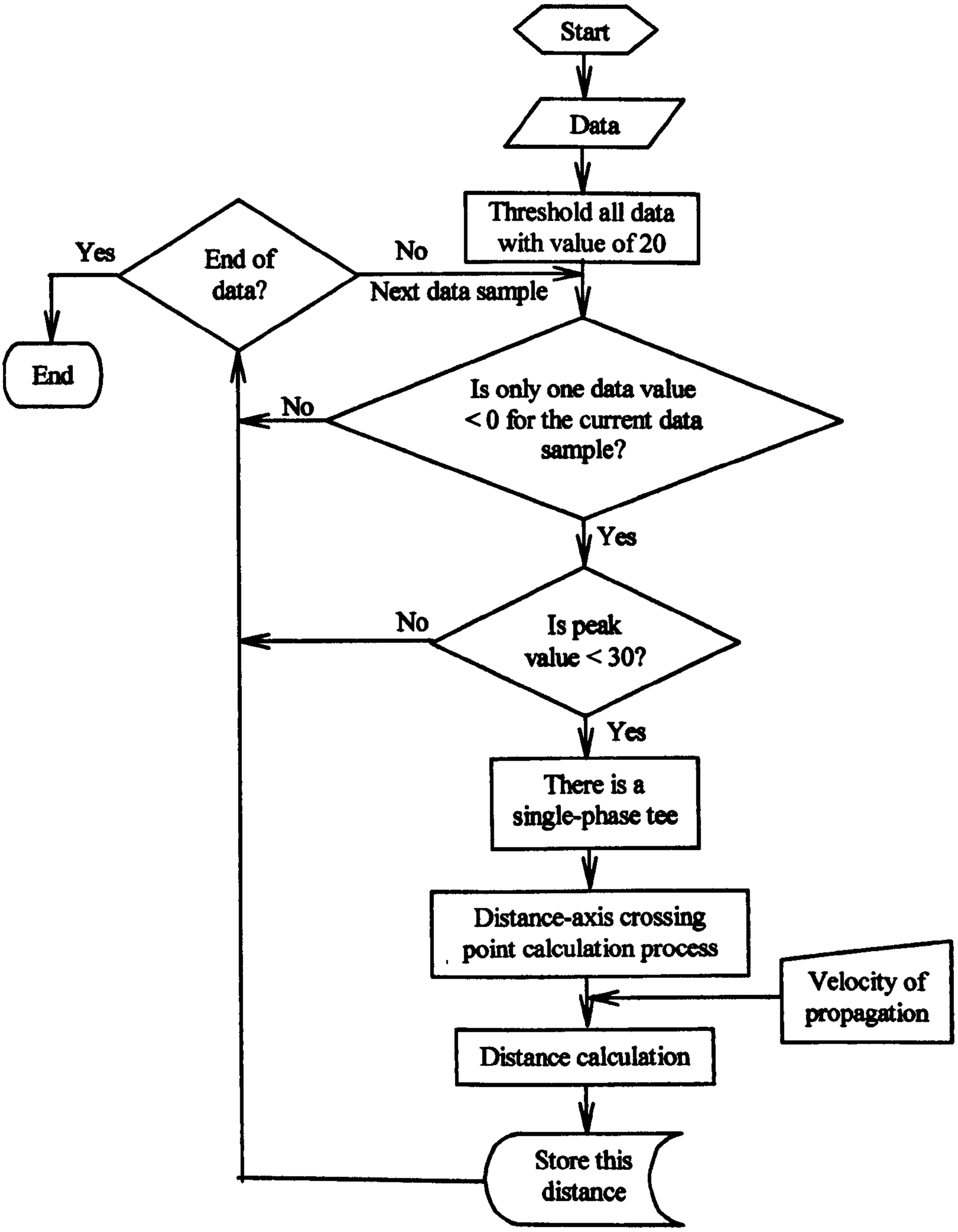

Figure 5.5: Flowchart for the single-phase tee location process

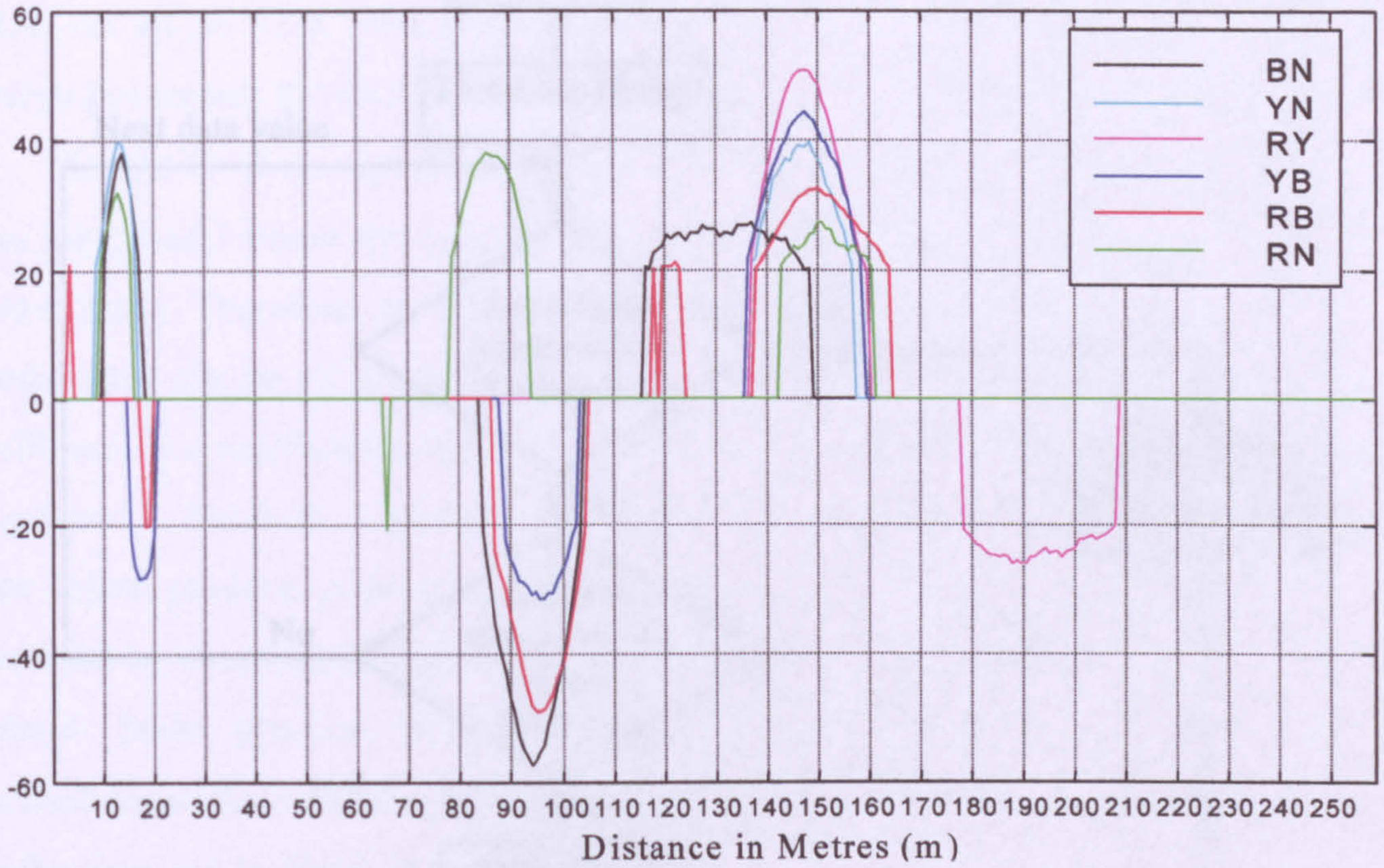

Figure 5.6: Thresholded TDR waveform for waveforms shown in Fig. 5.3

Consider the case where the single-phase identification process is applied to all six TDR waveforms that are shown in Fig. 5.3 for the model in Fig. 5.2 (assume that all six TDR waveforms are available). First, all the TDR waveforms are thresholded as shown in Fig.5.6. The process then checks for a negative value in one TDR waveform only. The RN and RY waveforms only have negative value just after 60m and just before 180m respectively. Therefore, these locations are identified as possible single-phase tee locations. However, as mentioned in section 4.3 these two (RN and RY) waveforms will not normally available for in the fault location process for this particular example. Therefore, no single-phase tee will be detected. This also clarifies the point that was mentioned earlier in this section that if the TDR waveform (phase to Neutral) that consists of the single-phase tee is not included in the fault location process then single phase tee might not be identified.

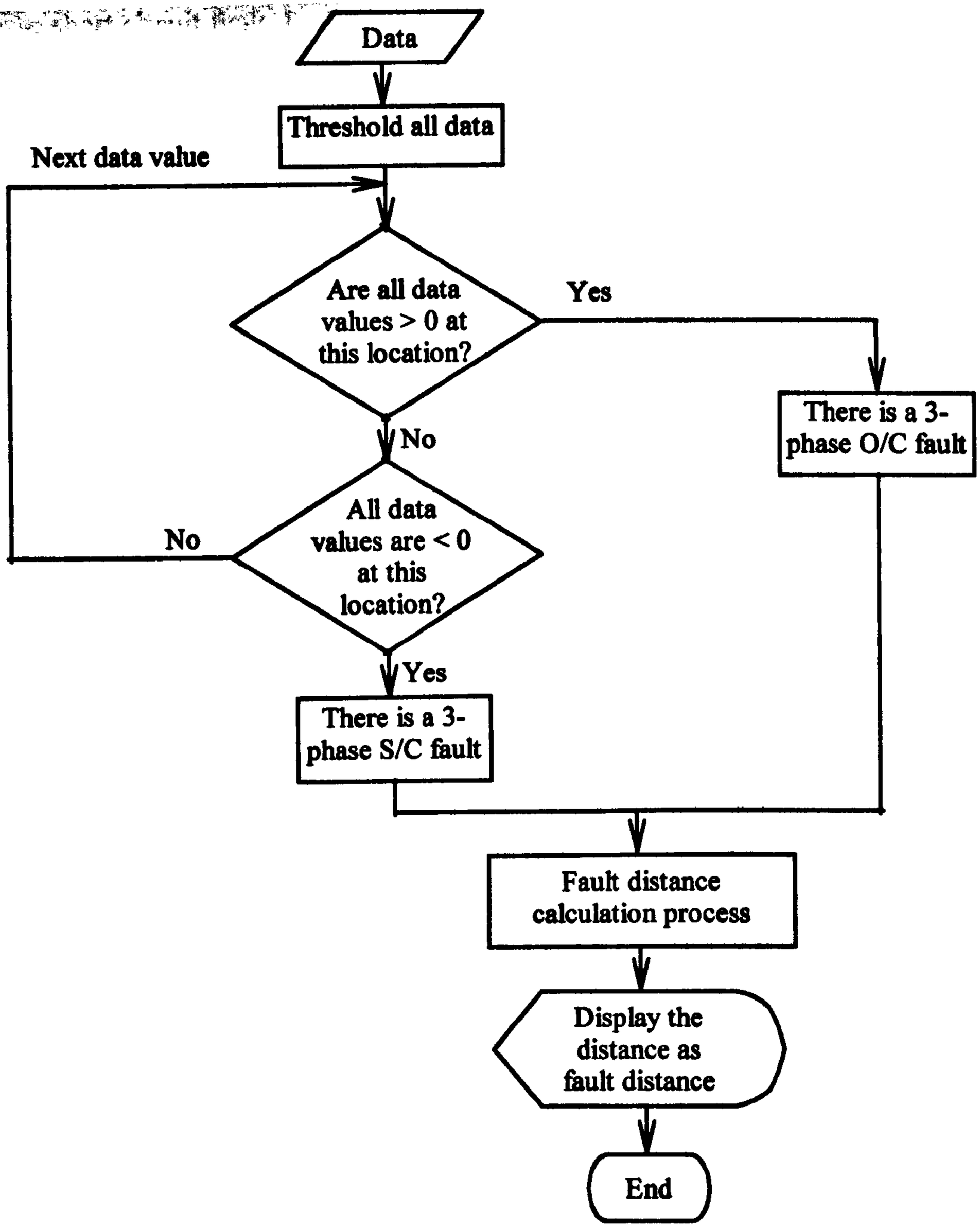

Figure 5.7: Flowchart for the 3-phase fault location process

5.3.2.2. 3-Phase Fault Location Process

The flowchart for the 3-phase fault location process is illustrated in Fig.5.7. Firstly, all the TDR waveforms are thresholded with a pre-set threshold value of 30. Following the thresholding, it checks whether all TDR waveforms have a positive value. If all have a positive value then it identifies that location as a 3-phase open circuit fault. It then calculates and displays the fault distance. If the TDR waveforms do not all have positive values then it checks whether all TDR waveforms have negative values. If all of them have a negative value then it identifies that location as a

3-phase short circuit fault. Following that, it calculates the fault distance and displays it. If not all the TDR waveforms have negative values then it moves to the next data value and repeats the above process until it finds the 3-phase fault (open/short).

The choice of an appropriate threshold value is important. This is because 3-phase tee joints and 3-phase short circuit faults also produce negative reflections on all TDR waveforms. Therefore, by choosing a higher threshold value the 3-phase tee joints reflections can be eliminated during this process. The 3-phase tee joints reflections will have less amplitude compared to the 3-phase short circuit fault as demonstrated in section 4.3. Similarly, 3-phase open circuit faults and secondary reflections of 3-phase tee joints produce positive reflections on all TDR waveforms. This also can be avoided by choosing an appropriate threshold value. This is because the 3-phase open circuit faults produce higher amplitude reflections compared to the secondary reflections of the 3-phase tee joints. More details of 3-phase fault and 3-phase tee joint reflections can be found in section 4.3.

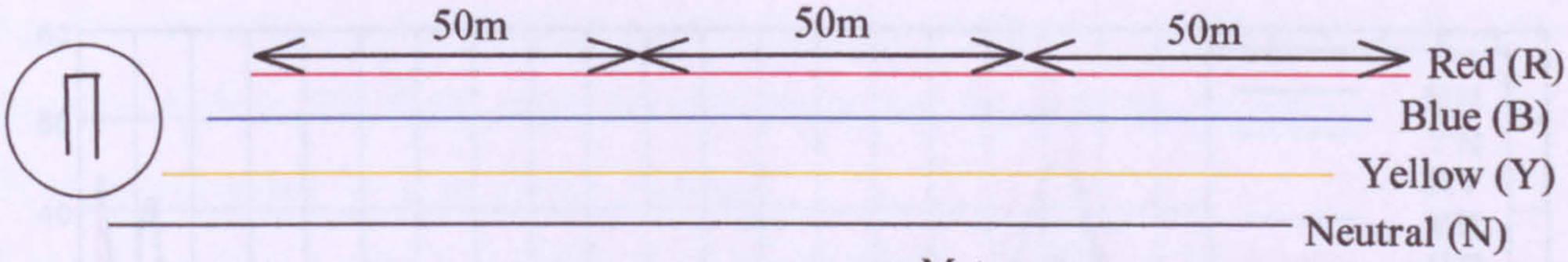

Figure 5.8: 4-core cable model that consists of three 50m cables joined together in series

The cable model shown in Fig. 5.8 consists of three 50m 4-core cables are joined together in series to make a 150m length of cable. The end of the cable was left open, so that it has a 3-phase open circuit fault. The TDR waveforms that are recorded for this model are shown in Fig. 5.9.

It is clearly seen that all six TDR waveforms (RN, BN, YN, RY, YB, and RB) have a positive reflection at 150m. This is due to the 150m 3-phase open circuit fault. For these TDR waveforms, if we apply the pre-processing process then the resulting thresholded TDR waveforms are shown in Fig. 5.10. All the thresholded waveforms (in Fig.5.10) have a positive reflection only at 160m approximately. It therefore identifies this location as a possible 3-phase open circuit fault and rejects other cases.

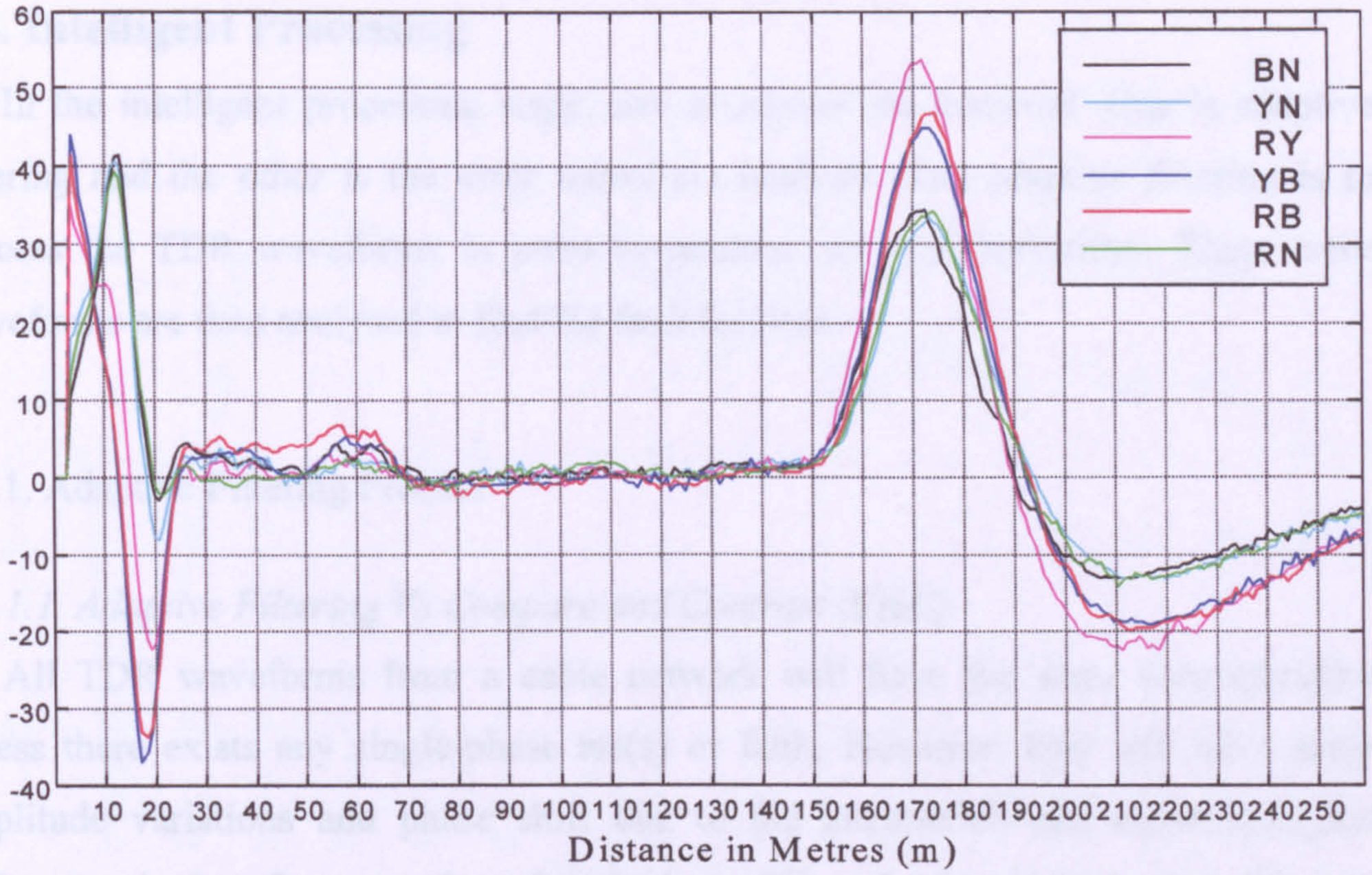

Figure 5.9: TDR waveforms for the cable model in Fig. 5.8

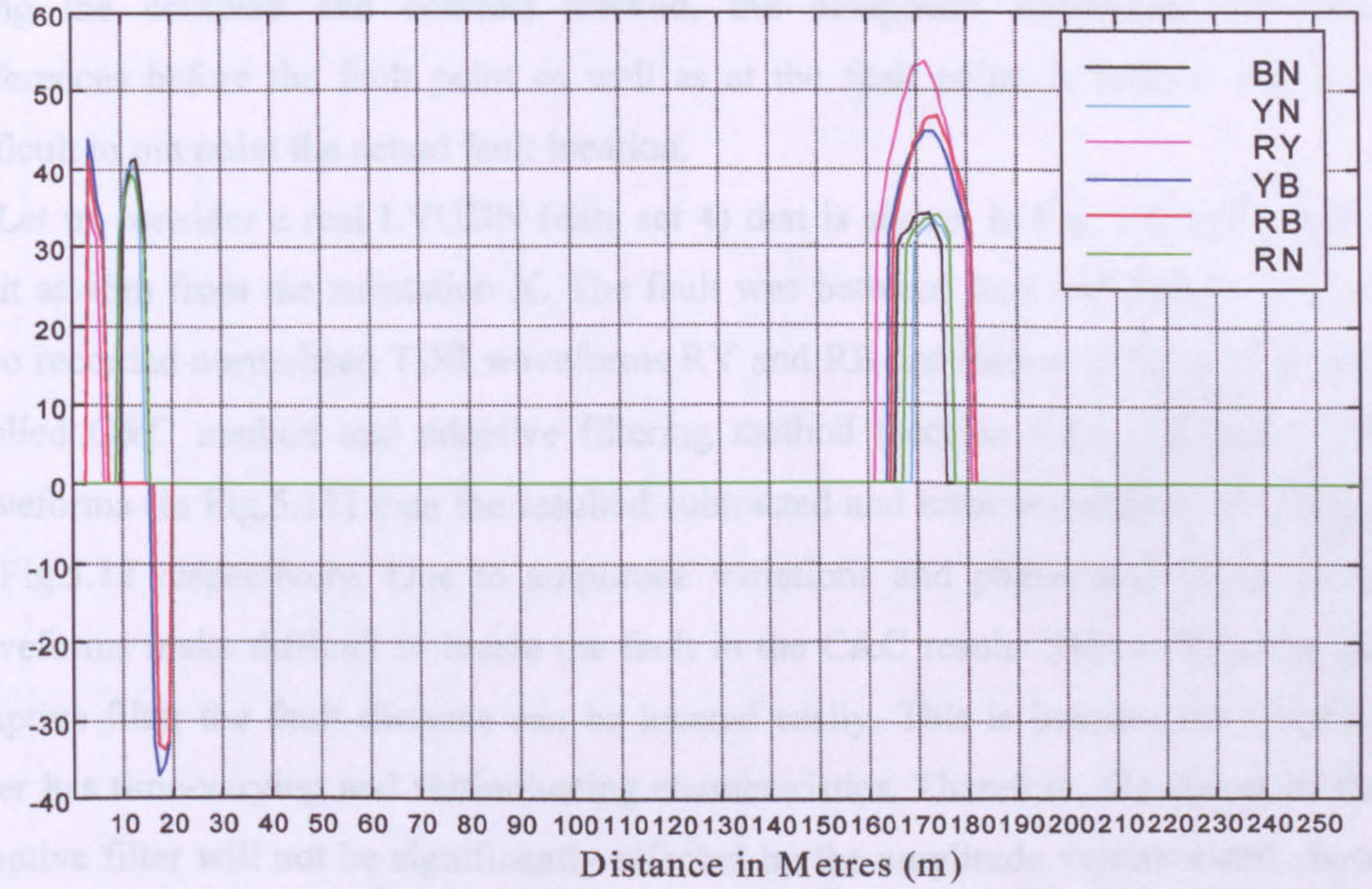

Figure 5.10: Thresholded waveforms of the TDR waveforms that are shown in Fig. 5.9 for locating 3-phase fault

5.4. Intelligent Processing

In the intelligent processing stage, two processes are involved. One is adaptive filtering and the other is the error waveform analysis. The adaptive filtering is to process the TDR waveforms in pairs to produce an error waveform. These error waveforms are then analysed to find the fault location.

5.4.1. Adaptive Filtering Process

5.4.1.1. Adaptive Filtering Vs Compare and Contrast (C&C)

All TDR waveforms from a cable network will have the same characteristics unless there exists any single-phase tee(s) or fault. However, they will have some amplitude variations and phase shift due to the attenuation and dispersion, and different velocity of propagation of each phase. The pulse launched in the cable will attenuate and disperse due to cable loss. Noise also changes the characteristics of the TDR waveforms. Therefore, when analysing the TDR waveforms to locate a fault using the compare and contrast method, the composite waveform will have differences before the fault point as well as at the fault point. It follows that it is difficult to pin point the actual fault location.

Let us consider a real LVUDN (data set 4) that is shown in Fig. 2.5 and it has a fault at 45m from the substation X. The fault was between Red and Yellow phases. Two recorded normalised TDR waveforms RY and RB are shown in Fig.5.11. If one applied C&C method and adaptive filtering method (section 5.4.1.) to both TDR waveforms (in Fig.5.11) then the resulted subtracted and error waveforms are shown in Fig.5.12 respectively. Due to amplitude variations and phase shift in the TDR waveforms make difficult to locate the fault in the C&C result. However, using the adaptive filter the fault distance can be located easily. This is because the adaptive filter has time-varying and self-adjusting characteristics. Therefore, the output of the adaptive filter will not be significantly affected by the amplitude variation and phase shift. The output of the adaptive filter will only have a significant difference at the fault point.

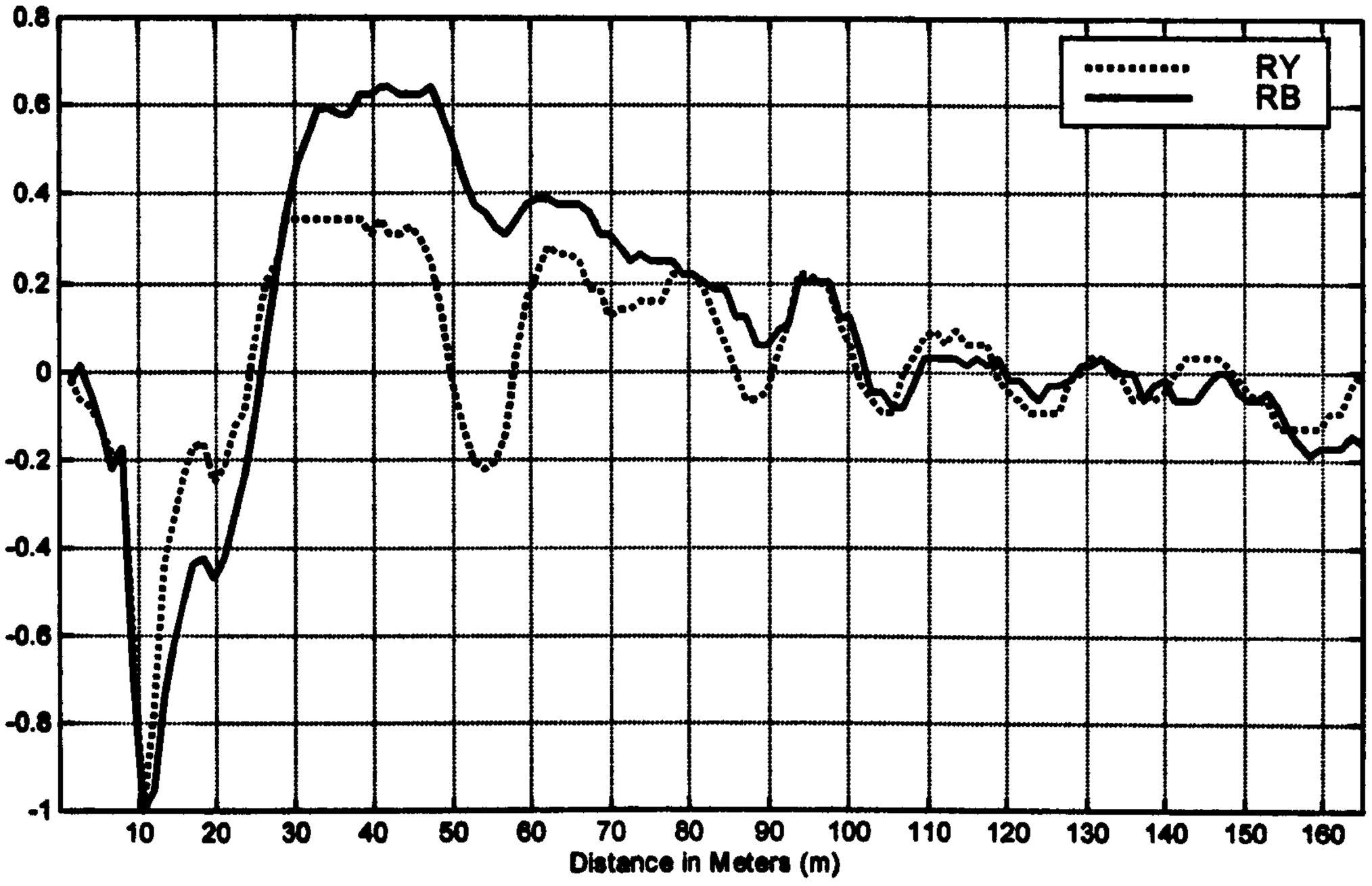

Figure 5.11: TDR waveforms (RY & RB) for the real LVUDN in Fig. 2.5

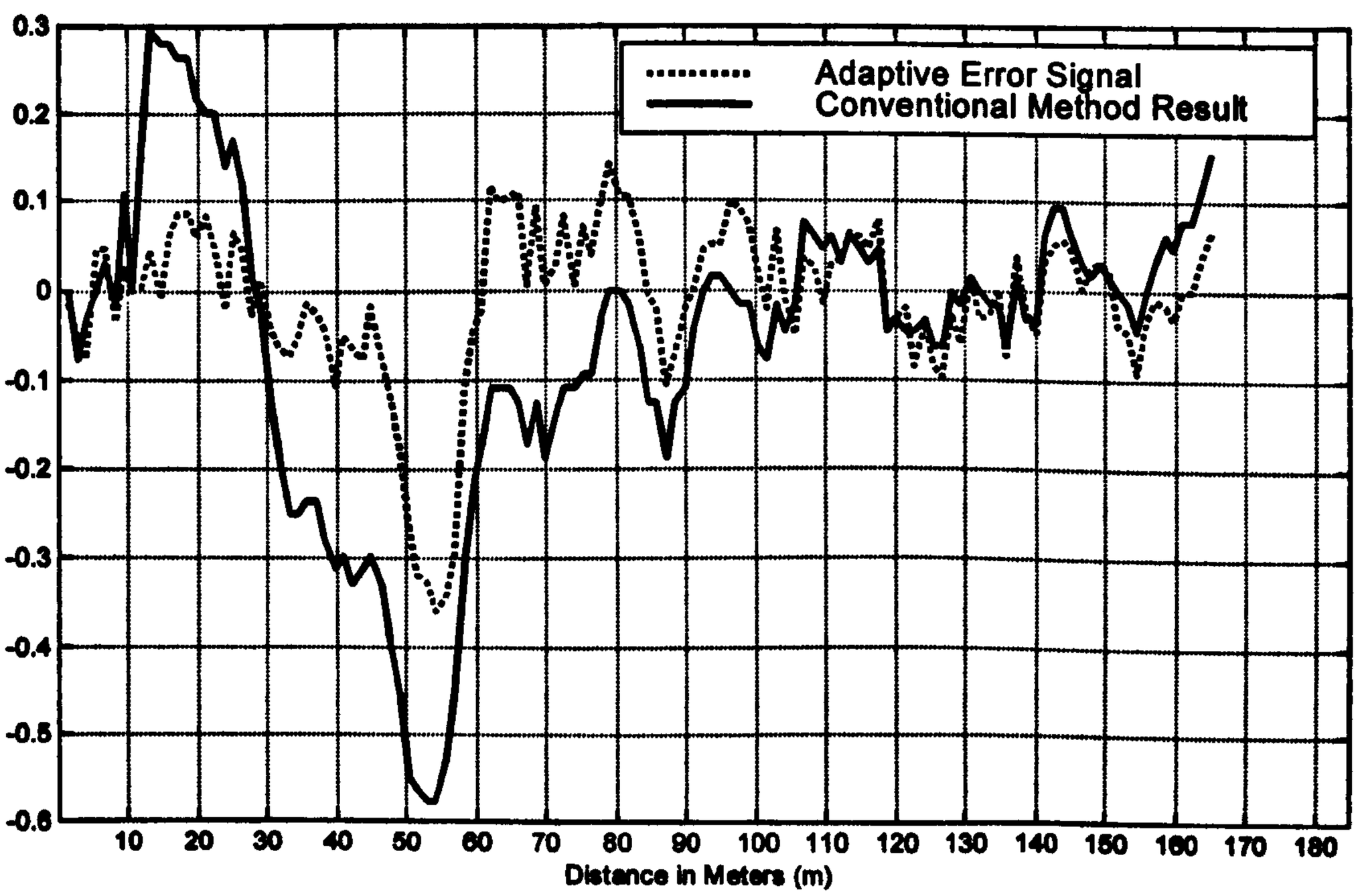

Figure 5.12: C&C and adaptive results for the TDR waveforms in Fig. 5.11

5.4.1.2 Adaptive Filtering

During the pre-processing, if no 3-phase fault is detected then the TDR waveforms are processed with the adaptive filter in pairs. The adaptive filter uses the faulty phase TDR waveform as a reference always and one of the other available TDR waveforms as its input. This adaptive filter process is carried out on all available TDR waveforms. The adaptive filter yields the error waveform as its output for all combinations. The flowchart for the adaptive filtering process is illustrated in Fig. 5.13. Firstly, it checks how many TDR waveforms are available for processing and then normalises all the TDR waveforms. For the case of three TDR waveforms it takes the faulted TDR waveform (2 in Fig. 5.13) and feeds it as a reference (this will be the faulty phase(s) waveform). It also feeds one of the other TDR waveforms (1 in Fig. 5.13) as its input. The adaptive filter yields an error waveform as its output. Similarly, the adaptive filter is again applied, but this time the input is changed with the other TDR waveform (3 in Fig. 5.13) that was not used but the reference is not changed. This time the adaptive filter will yield another error waveform as its output.

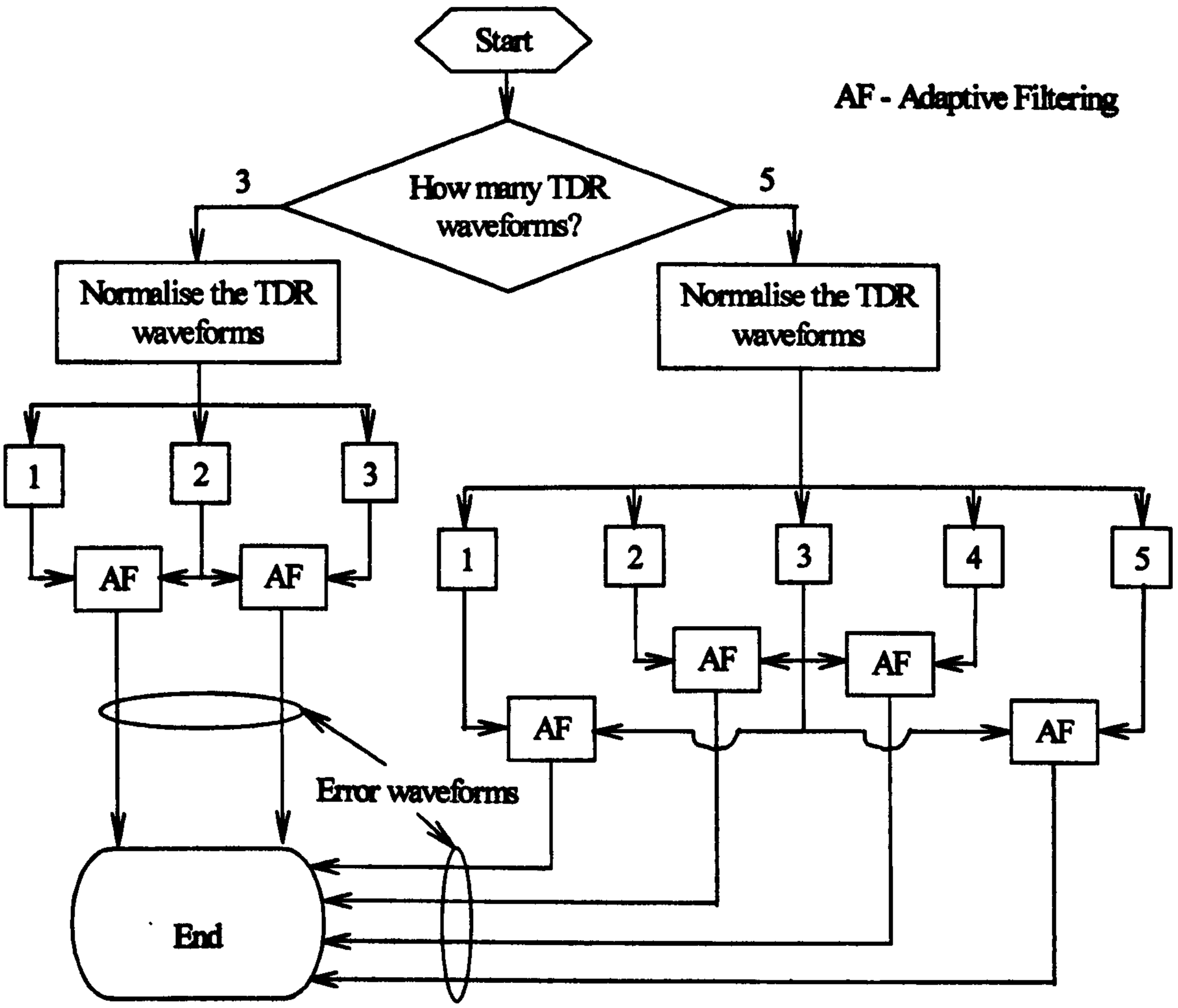

Figure 5.13: Adaptive filtering process

Similarly, for the case of five TDR waveforms the adaptive filter uses the faulted TDR waveform (3 in Fig. 5.13) as reference (this will be the faulty phase waveform) and uses one of the other TDR waveforms (1, 2, 4, or 5 in Fig. 5.13) as input. This adaptive filtering process is repeated by keeping the same reference waveform all the time, changing the input waveforms. For each different input TDR waveform, the adaptive filter will yield an error waveform. Therefore, there will be four error waveforms available for this case. In both cases, the error waveforms gathered are processed in the next section to find the fault location.

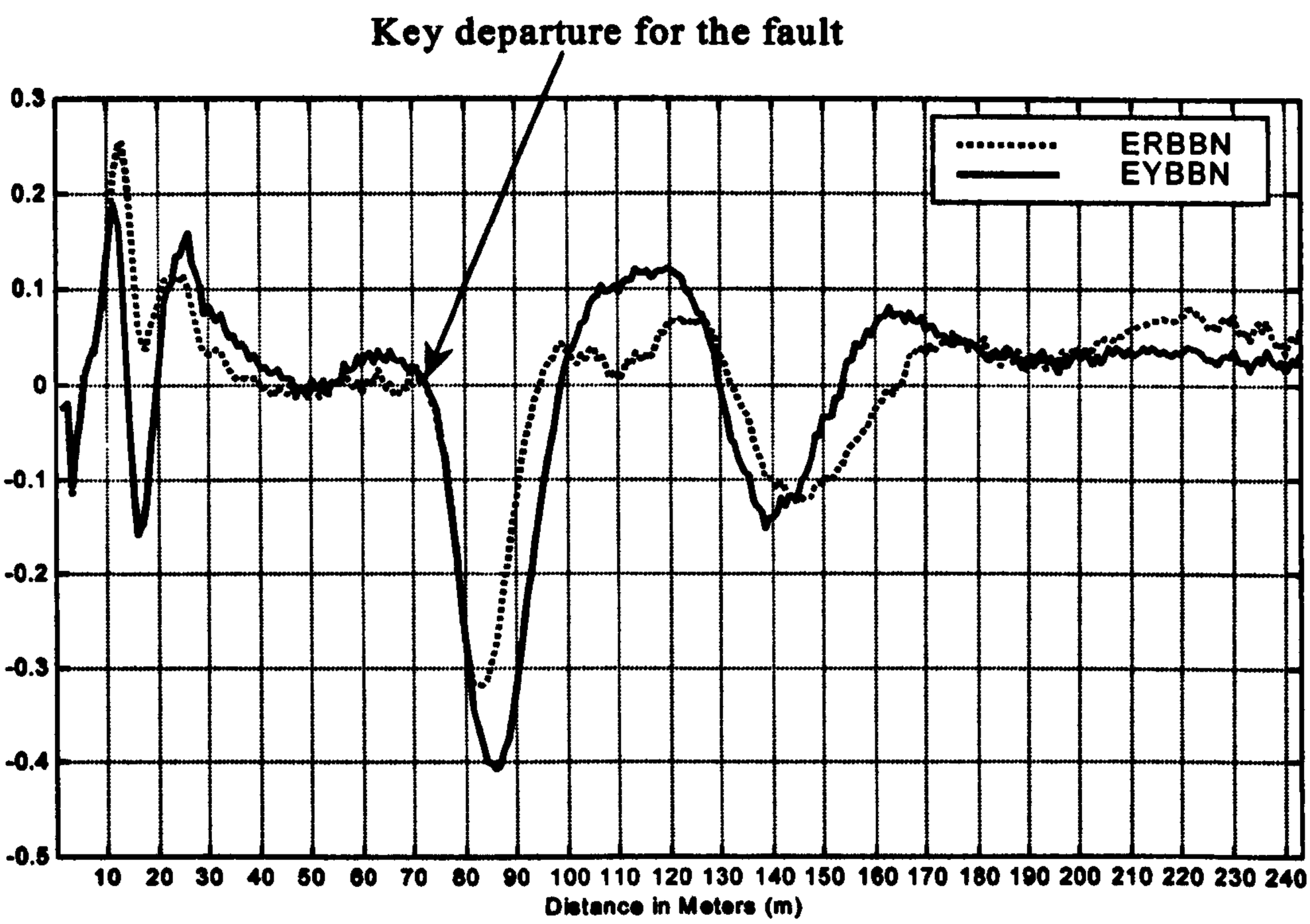

Figure 5.14: The error waveforms for the BN, YB, and RB waveforms in Fig. 5.3

If we take the cable model in Fig. 5.2, it has a short circuit fault between Blue phase and Neutral. If we assume that the fault location is done in the live line as described in section 4.2.1 then only BN, RB, and YB TDR waveforms (in Fig. 5.3) will be available. Therefore, we have a situation where only three TDR waveforms are available, so the faulted waveform is BN (2 in Fig. 5.13) and it will be fed as reference to the adaptive filter. The other two waveforms RB and YB will be fed as input (1 and 3 in Fig.5.13). Since there are two input waveforms, the adaptive filter has to be applied twice as mentioned in section 5.4.1.2. Therefore two error waveforms will be available and are shown in Fig. 5.14. In Fig. 5.14, EYBBN and

ERBBN are the error waveforms between the YB and BN waveforms and RB and BN waveforms respectively.

5.4.2. Process of Error Waveforms Analysis

This process is to find the key departure that is related to the fault so as to locate the fault itself. The flowchart for the error waveform analysis process is shown in Fig.5.15. First, the error waveforms are thresholded with a pre-set threshold value of 0.3. After thresholding, the error waveforms are analysed as below to identify key departures. The thresholded error waveform values are analysed to identify key departures by checking whether their values are equal to zero or not. If a key departure is found in the error waveform then it calculates the fault distance using the fault distance calculation process in section 5.5.

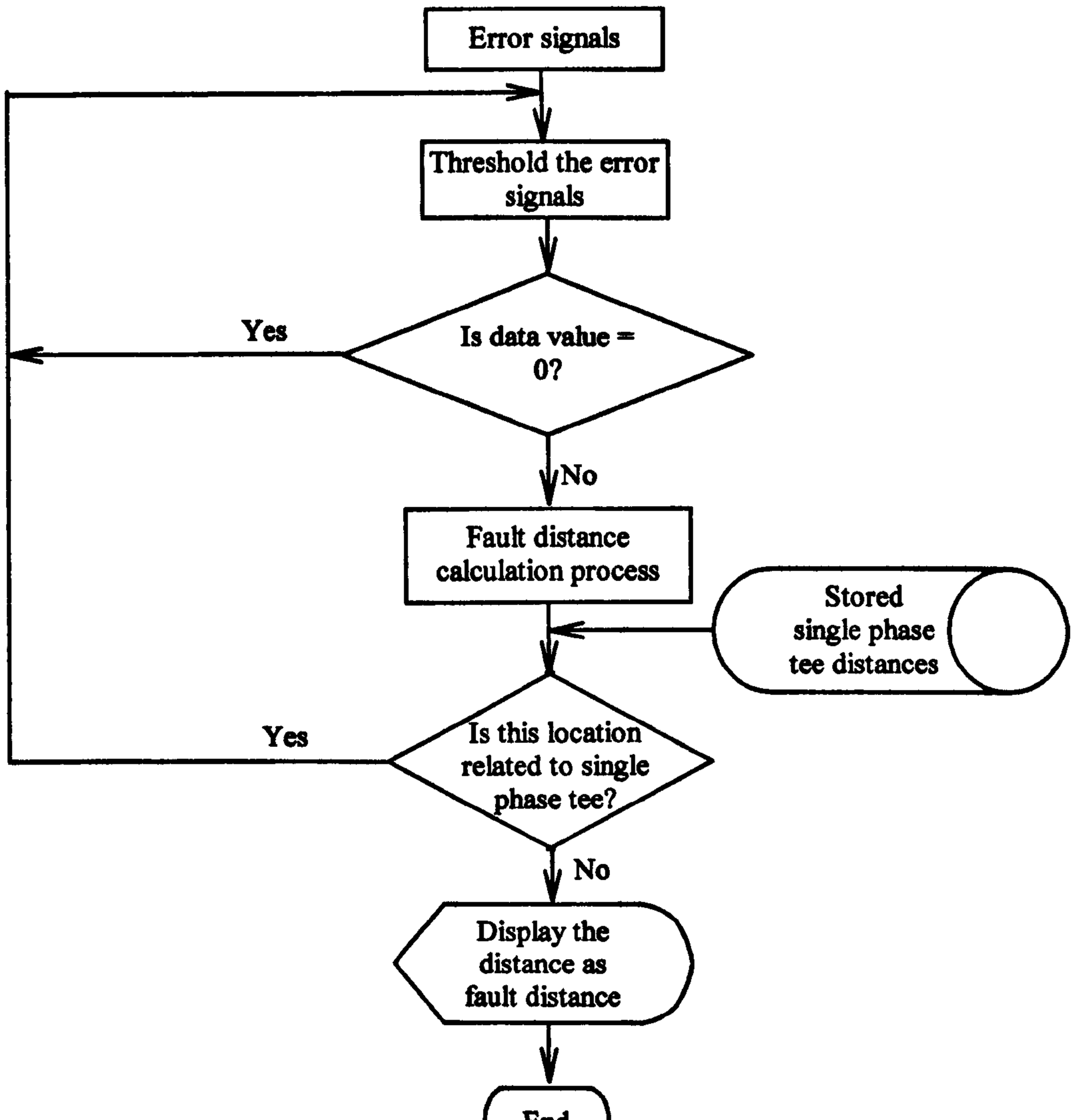

Figure 5.15: Flowchart for the error waveforms processing

This fault distance is then cross-examined with single-phase tee distances that may have been identified during the single phase tee location process (section 5.2.2.1). If this distance is not related (i.e same distance within the range of ±5m) to a single-phase tee then the distance is identified as the fault distance. If this distance is related to a single phase tee distance then is ignored and the process is continued until a fault distance is located. Once the fault is located, it displays the fault distance and ends the fault location process.

Fig. 5.16 shows the thresholded waveforms for the error waveforms in Fig. 5.14 to find the fault departure as mentioned above. The EYBBN and ERBBN waveforms have departures at 86.2m and 85.4m respectively.

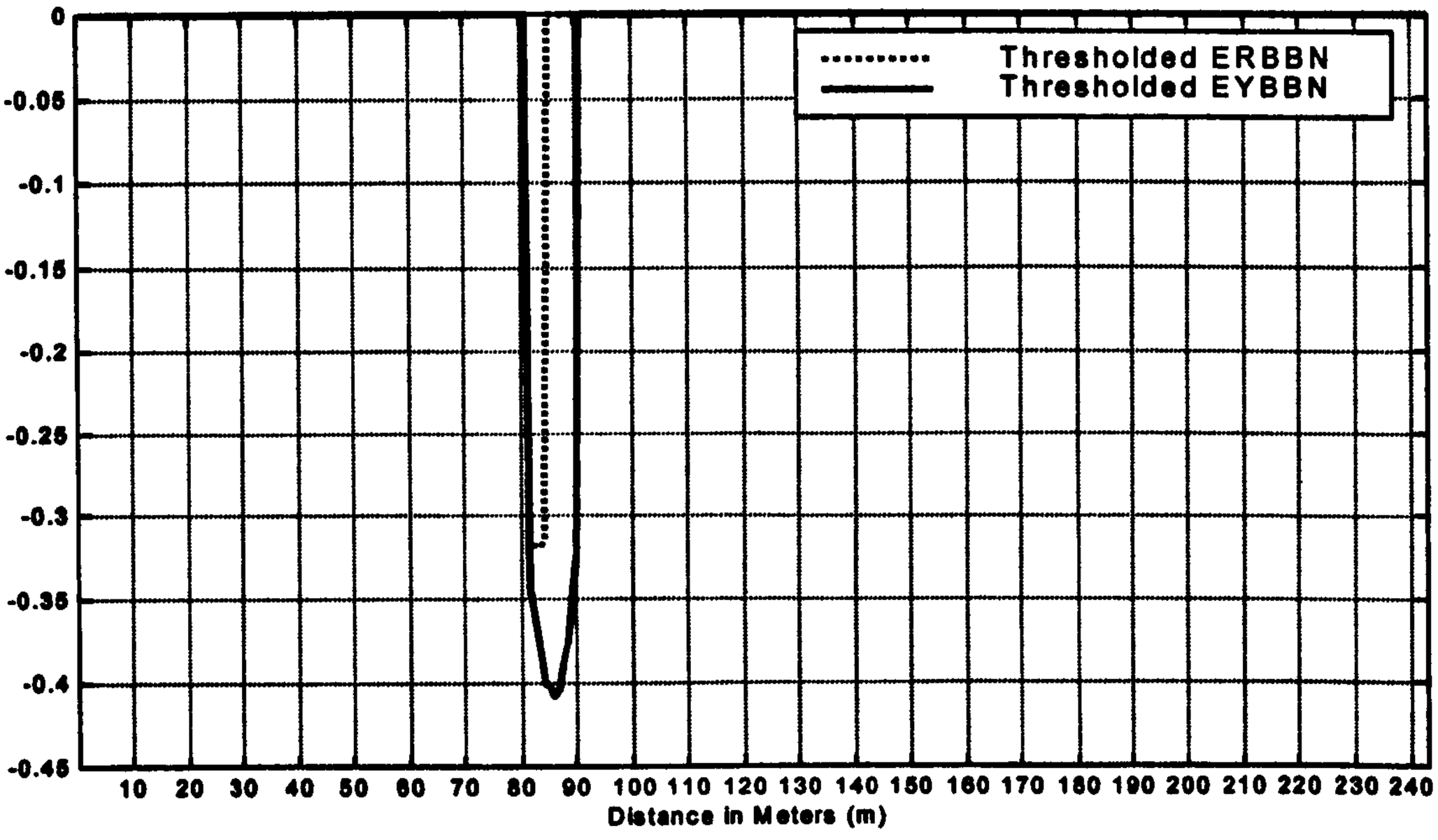

Figure 5.16: Thresholded waveforms for the error waveforms in Fig. 5.14

5.5. Fuzzy Based Distance Calculation Process

This process has three components: distance-axis crossing point calculation, common distance-axis crossing point calculation, and distance calculation as shown in Fig. 5.17. Firstly, the process finds where the departure crosses the distance-axis. It then checks whether it is a single-phase tee distance calculation process. If it is then it moves on to calculating the distance without calculating the common distance-axis crossing point. This is because in single-phase tee distance calculation process only one TDR waveform will be available. Therefore, there is no need to calculate the

common distance-axis crossing point. If it is not a single-phase tee distance calculation process then it proceeds to calculate the common distance-axis crossing point using fuzzy membership. It then calculates the fault distance.

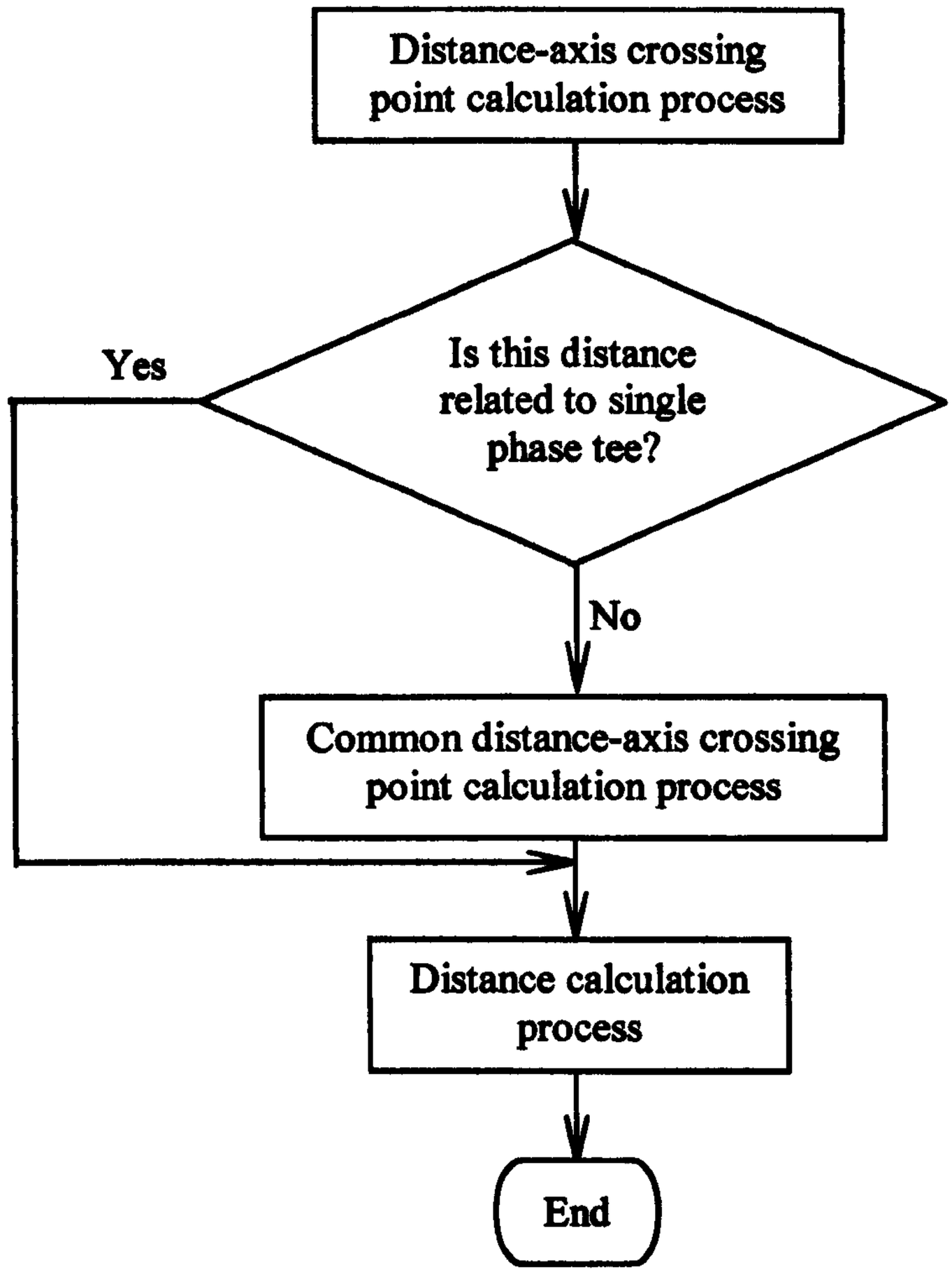

Figure 5.17: Fuzzy based fault distance calculation process

5.5.1. Process of Distance-axis Crossing Point Calculation

A flowchart for distance-axis crossing point calculation process is shown in Fig. 5.18. The distance-axis crossing point is calculated using either the TDR or the error waveforms. For the 3-phase fault and single-phase tee location process, it uses the TDR waveforms whereas in the case of intelligent processing, it uses the error waveforms.

Firstly, the process takes the data value and checks whether it is negative or positive. This is to check whether the departure is positive or negative. If it is a positive value then it decreases the data position one by one until the data value is less than or equal to zero. Similarly, if the initial data value is negative value then it

decreases the data position one by one until the data value is greater than or equal to zero. This is to find where the departure is crossing the distance-axis for a particular waveform. The final value of the data position will give the distance-axis crossing point.

If we take the example from the 3-phase fault location process (Fig. 5.8), it has found a 3-phase fault departure just after 160m. Following this, one needs to find where the 3-phase fault departure crosses the distance-axis in each TDR waveform. It has been calculated as 141.4m, 149.1m, 149.1m, 149.1m, 147.4m, and 144.8m for YB, YN, RN, BN, RB, and RY respectively (velocity of propagation 162m/μs is used). Using these distances, the common distance-axis crossing point calculated in the next section.

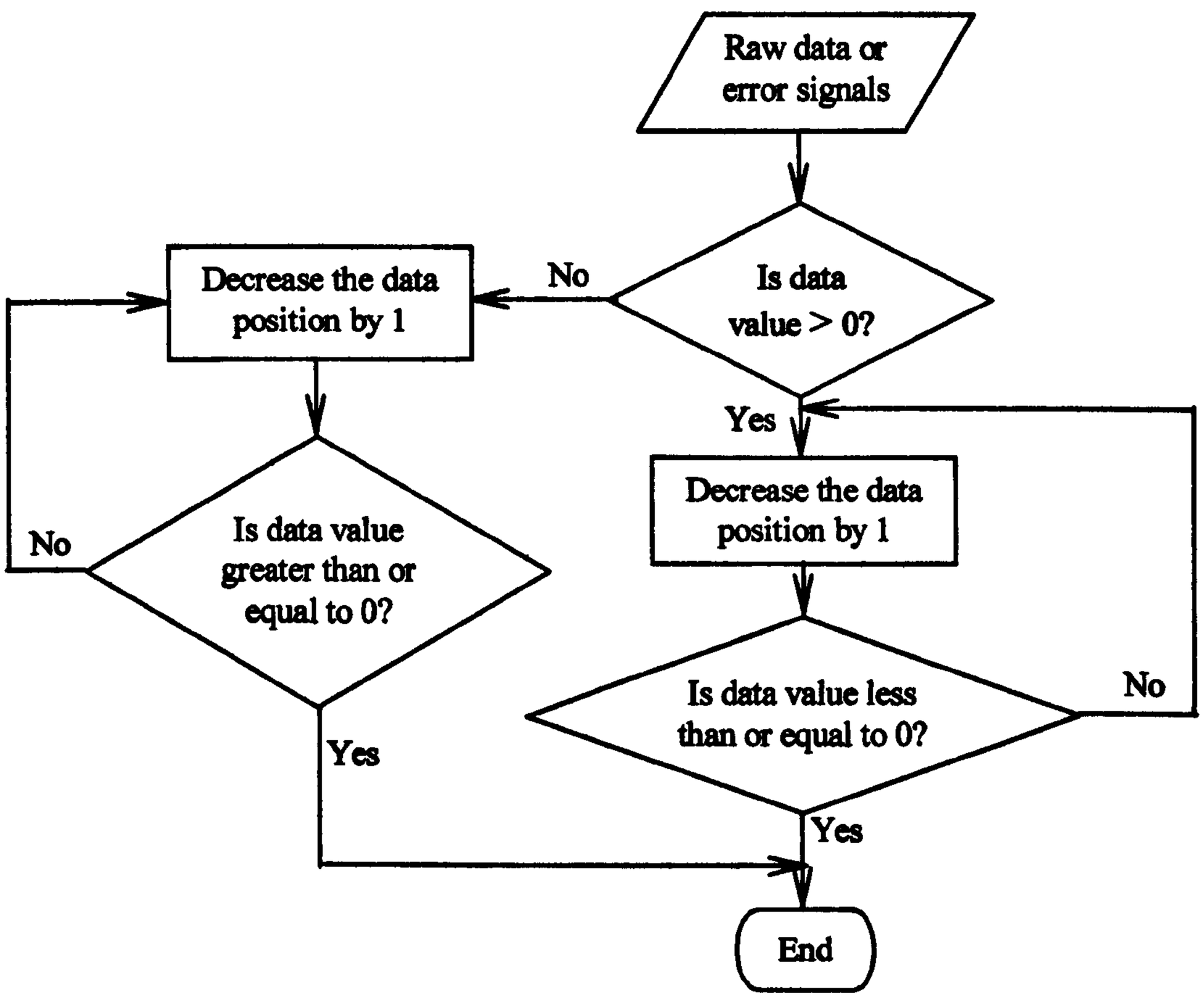

Figure 5.18: Distance-axis crossing point calculation process

5.5.2. Common Distance-axis Crossing Point Calculation Process

The flowchart for the common distance-axis crossing point calculation process is illustrated in Fig. 5.19. This process is to find the common distance-axis crossing point of the error or the TDR waveforms, if there is more than one waveform (TDR or error). This is because each waveform may cross the distance-axis in different positions as seen in the last section for the 3-phase fault example. Therefore, it is necessary to find the common distance-axis crossing point. Adding all the points that are crossing the distance-axis and then taking the average is a simple way, but not the best way. This is because the averaging method will give the average value of all the points. However, the best way of calculating the common point is to choose the point that is closest to most of the points. Fuzzy membership is therefore used to find the common point that crosses the distance-axis, which allows finding the common point that is closest to most of the points.

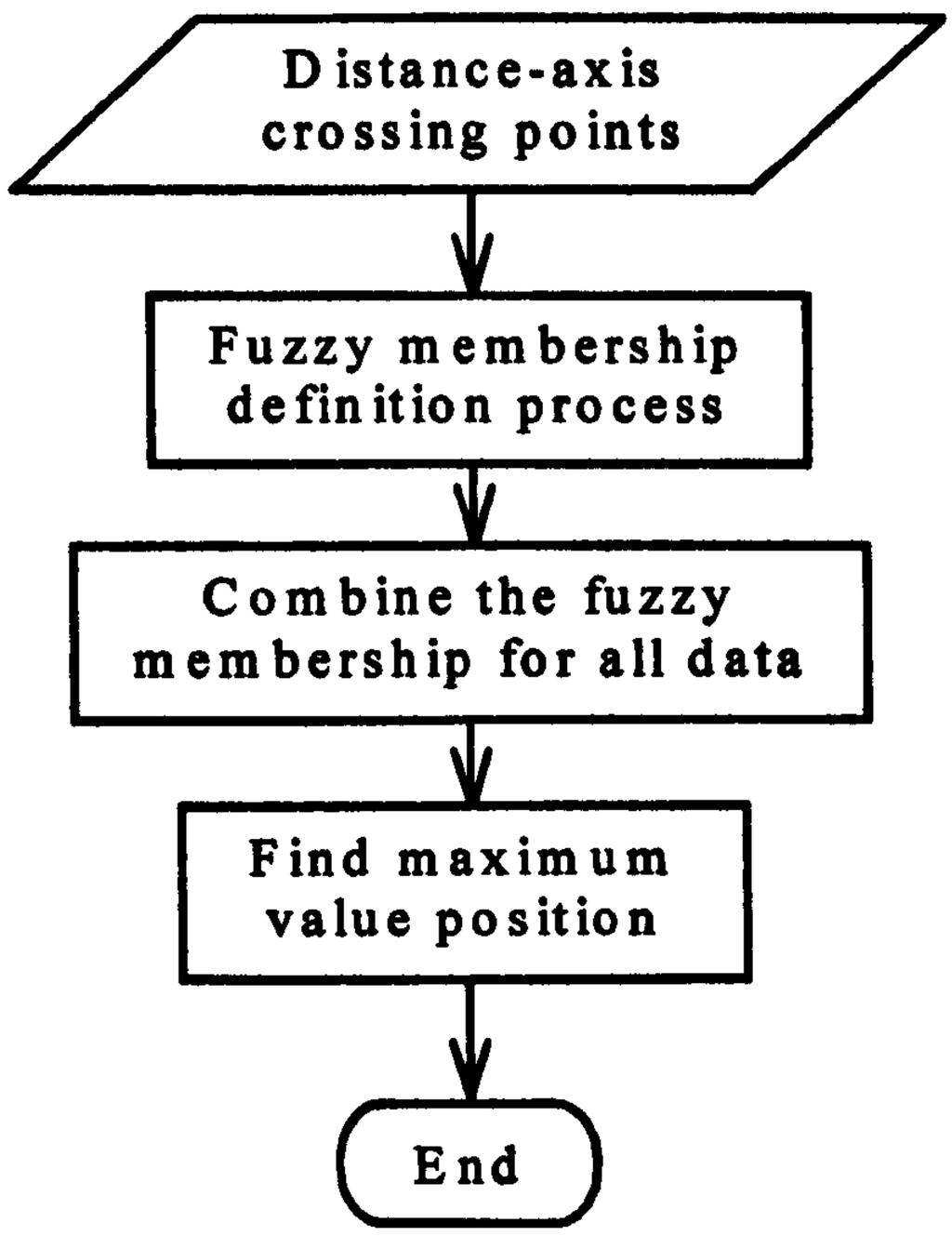

Figure 5.19: Flowchart for common distance-axis crossing point calculation process

We are interested in finding the common point that crosses the distance-axis. So in the fuzzification procedure, the highest membership value (unity) is assigned to the points that reside in the *more likely* distance-axis crossing point region, and no

membership value (zero) to the points outside the *potential* region. For the points residing in the *potential* but not in the *more likely* region a monotonically decreasing membership is considered as the point's distance from the distance-axis crossing increases.

Based on the above definition process, the fuzzy membership function of the distance-axis crossing point, *fdist* produces the fuzzy subset FDIST of the waveform. It defines to what degree any point in the waveform is similar to the fault location based on only its positional information and is defined as follows:

$$\mu dist(i) = fdist(i) = \begin{cases} 1 & i = d \\ \dfrac{0.9}{((i+r)-d)} & d < i \le (d+r) \\ \dfrac{0.9}{(d-(i-r))} & (d-r) \le i < d \\ 0 & otherwise \end{cases} \tag{5.1}$$

where $\mu dist(i)$ is the membership value of the i^{th} point in the fuzzy subset FDIST, d is the distance-axis crossing point for the waveform, and r is the *more likely* and *potential* region that the common distance-axis crossing point will be in. By applying the *fdist* function to the points in the waveform, the fixed fuzzy subset FDIST for all the waveforms can be defined as:

$$FDIST = \{i, \mu dist\}, \quad i = 1,2,3,\ldots\ldots 2r \tag{5.2}$$

These fuzzy membership functions for each waveform are then combined to produce one fuzzy membership function. Following this, the point where the fuzzy membership has a maximum value is found and identified as the fault position (location).

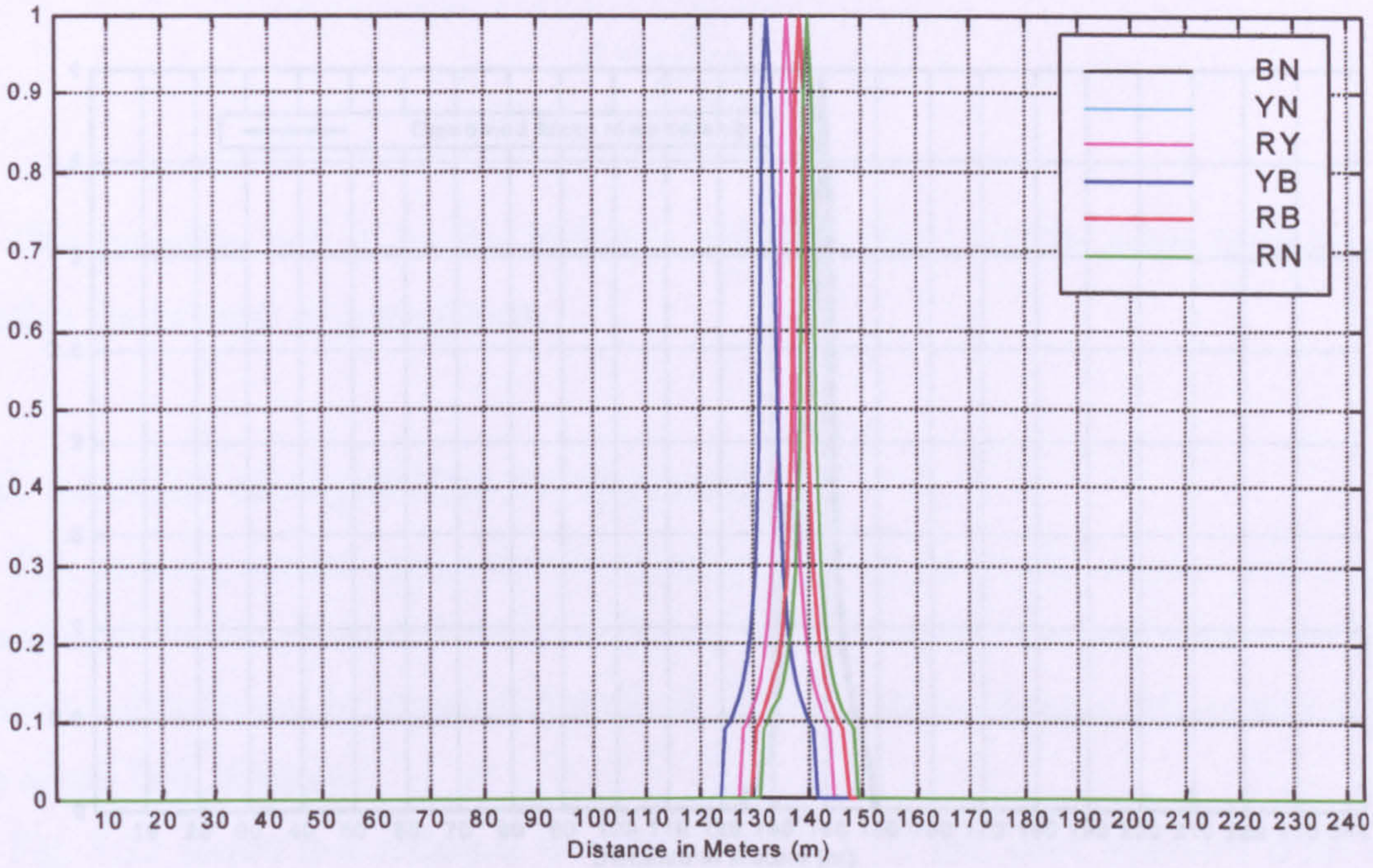

Figure 5.20: Fuzzy membership of the 3-phase fault departure on all TDR waveforms in Fig. 5.9

In the example that is used in the 3-phase fault location process (Fig. 5.9), there is one distance-axis crossing point for each TDR waveform. Therefore, we map them into fuzzy memberships as explained above. For this case, $r = 10$ is used to calculate the fuzzy membership. We will get fuzzy memberships as shown in Fig.5.20. We then combine these fuzzy memberships to obtain a common distance-axis crossing point, getting a fuzzy membership as shown in Fig. 5.21. Finally, the maximum value position for the fuzzy membership in Fig. 5.21 is calculated and it is found to be 148.2m. If we take the average value of all the distance-axis crossings then it will be 146.8m. This is 3.2m short of actual fault distance (150m) whereas the fuzzy method gives better accuracy and is 1.8m from the actual fault. Note that the distance-axis crossing points are given on a metre scale, so that they can be compared easily with the actual fault distance. In the fault location program, they are calculated in samples and only the final fault distance is calculated in metres.

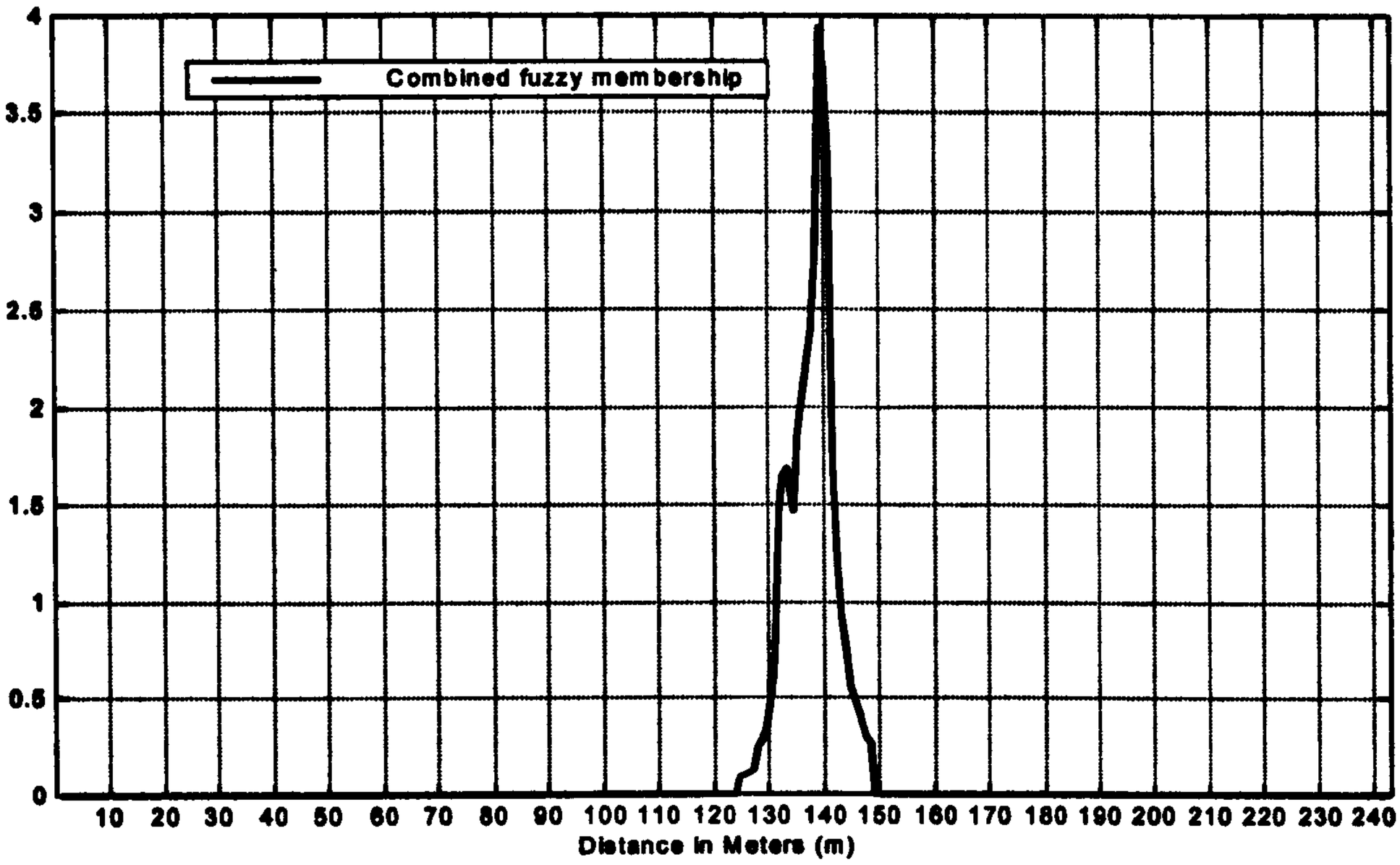

Figure 5.21: Combined result of the fuzzy memberships in Fig. 5.20

Data label	Few value of distance-axis crossing points (m)	Fuzzy membership (m)	Averaging method (m)	Actual location (m)
Model Fig.5.8	141.4, 149.1, 149.1, 149.1, 147.4, 144.8	148.2	146.8	150
Model 2	116.4, 122.4, 122.4, 125.9, 127.6, 127.6	126.7	123.7	129
Model 3	72.4, 72.4, 72.4, 73.3, 74.1, 74.3, 110.3	73.3	79.2	70

Table 5.1: Summary results of fuzzy membership and averaging method results

To determine the robustness of this fuzzy membership, a number of tests were carried out on data sets. Results show that it gives about 97% accuracy of the actual fault distance. The test results for the averaging and fuzzy membership method for three sets of data including model in Fig. 5.8 are shown in Table 5.1.

5.5.3. Distance Calculation process

Using the formula (Eq. 2.4) the distance is calculated as illustrated in Eq. 5.3. Where a is the distance-axis crossing point, $t = \frac{1}{f}$ and f is the sample rate of the instrument (that the TDR waveforms are recorded) and v is the velocity of propagation of the cable under test.

$$d = \frac{a}{t^* \left(\frac{v}{2}\right)} \tag{5.3}$$

The sampling rate, *f*, for the P2000 is 100MHz. For LVUDN cable 162m/μs is used as the velocity of propagation.

5.6. Analysis of Algorithm Performance

This section provides the performance analysis of the automatic adaptive and fuzzy based fault location system that was designed in this chapter. The performance of the system is determined by comparing the fault distance obtained using this system with the actual fault distance.

Fig. 5.22 shows two reflected waveforms (RB, YN) that were recorded from an actual LVUDN (data set 1). It was found that the LVUDN has a fault at 33m from the testing point. Due to the fault at 33m, superimposing both reflected waveforms showing a spilt at 33m. If one applied the adaptive and fuzzy based fault location to these TDR waveforms then the procedure is as follows: First these TDR waveforms are thresholded to detect and locate any single-phase tees and 3-phase faults. The two thresholded reflected waveforms (RB and YN) are shown in Fig. 5.23. The RB has a positive departure at 35.6m and the YN has a negative departure at 37.6m. These are due to the fault. Therefore, no single-phase tees are detected.

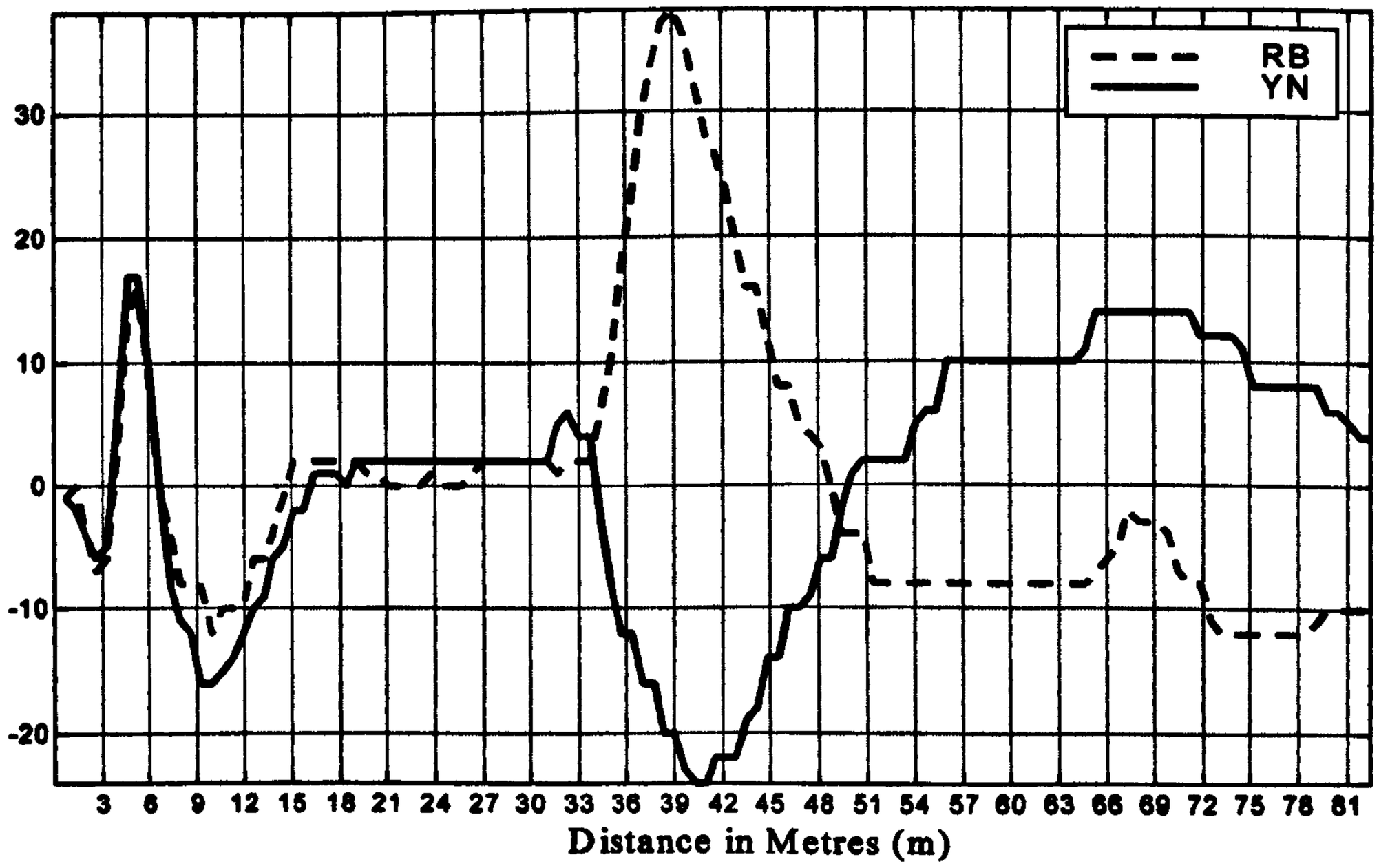

Figure 5.22: First set of field data (RB and YN)

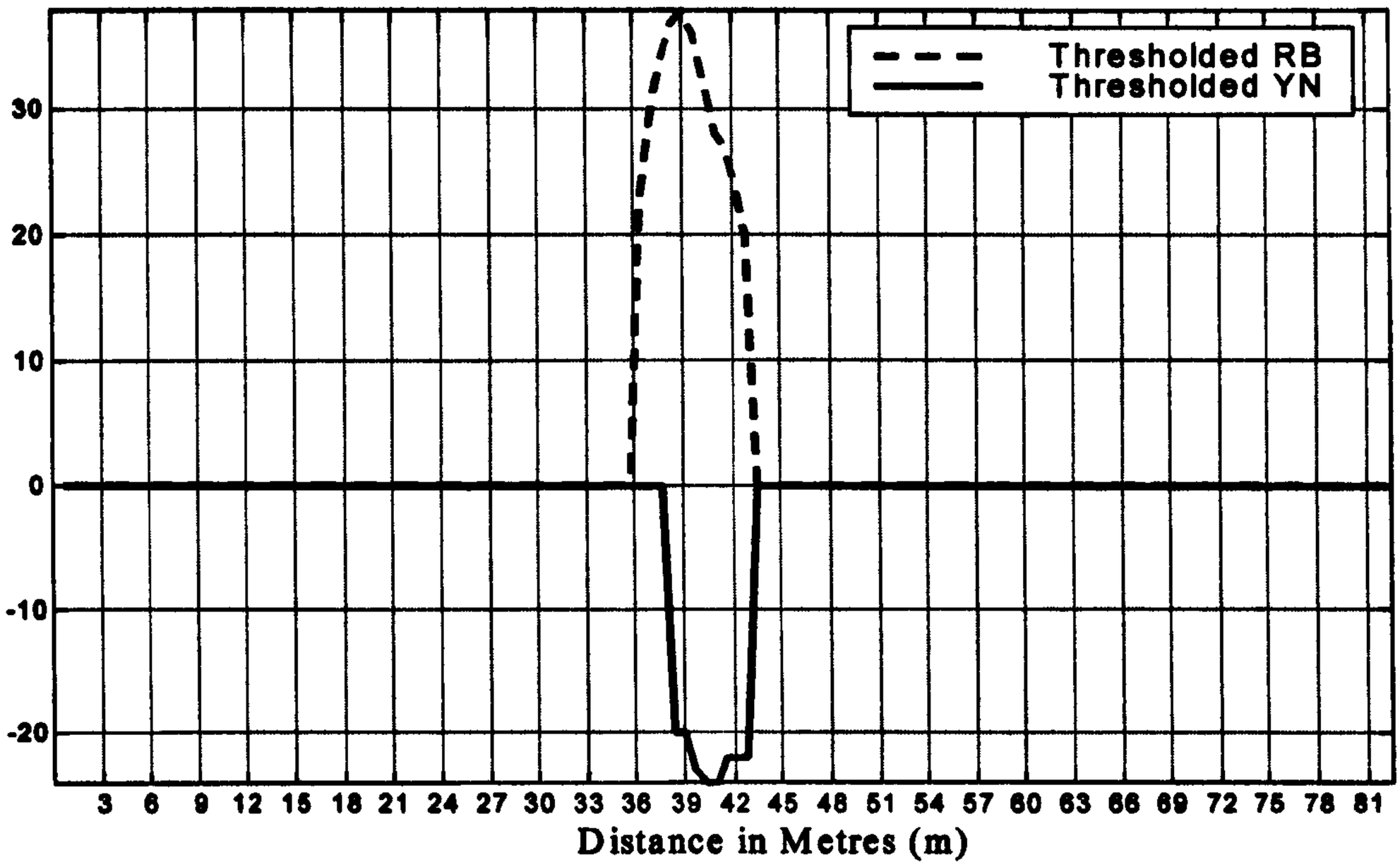

Figure 5.23: Thresholded waveforms for the waveforms in Fig. 5.22

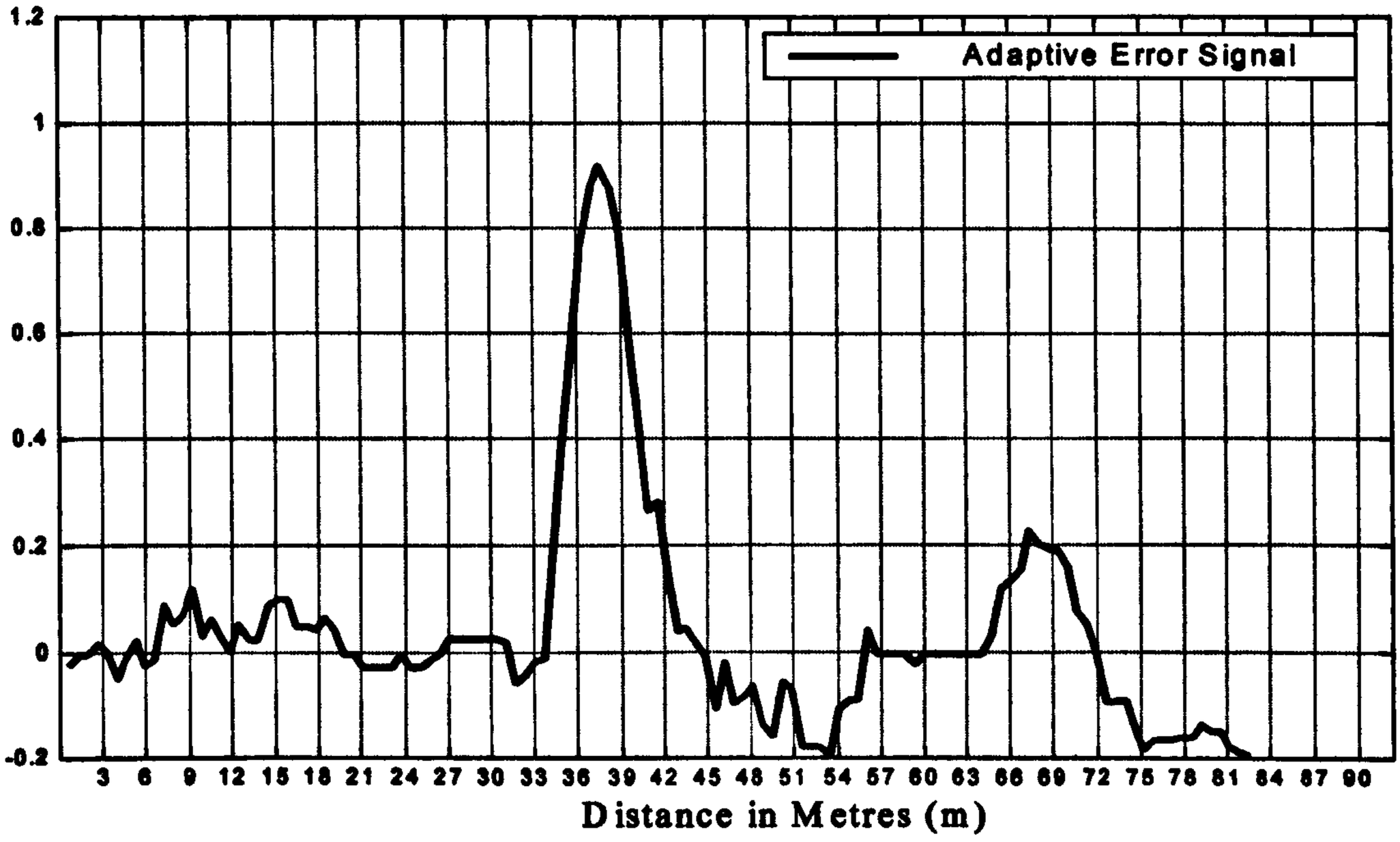

Figure 5.24: Adaptive error waveform for the waveforms in Fig. 5.22

Since there are only two reflected waveforms, the 3-phase fault is ruled out. Following this, intelligent processing is applied to these TDR waveforms. The output of the adaptive filter (error waveform) is shown in Fig. 5.24. Since in this case only two reflected waveforms are available, only one error waveform is produced. The error waveform is then processed to locate the fault. Firstly, this error waveform is thresholded as shown in Fig. 5.25 to extract key departures that belong to the fault. It

has a peak at 34.2m on the thresholded waveform. The distance-axis crossing point for this location is 33.2m. Since there is only one error waveform, this location is identified as the fault distance.

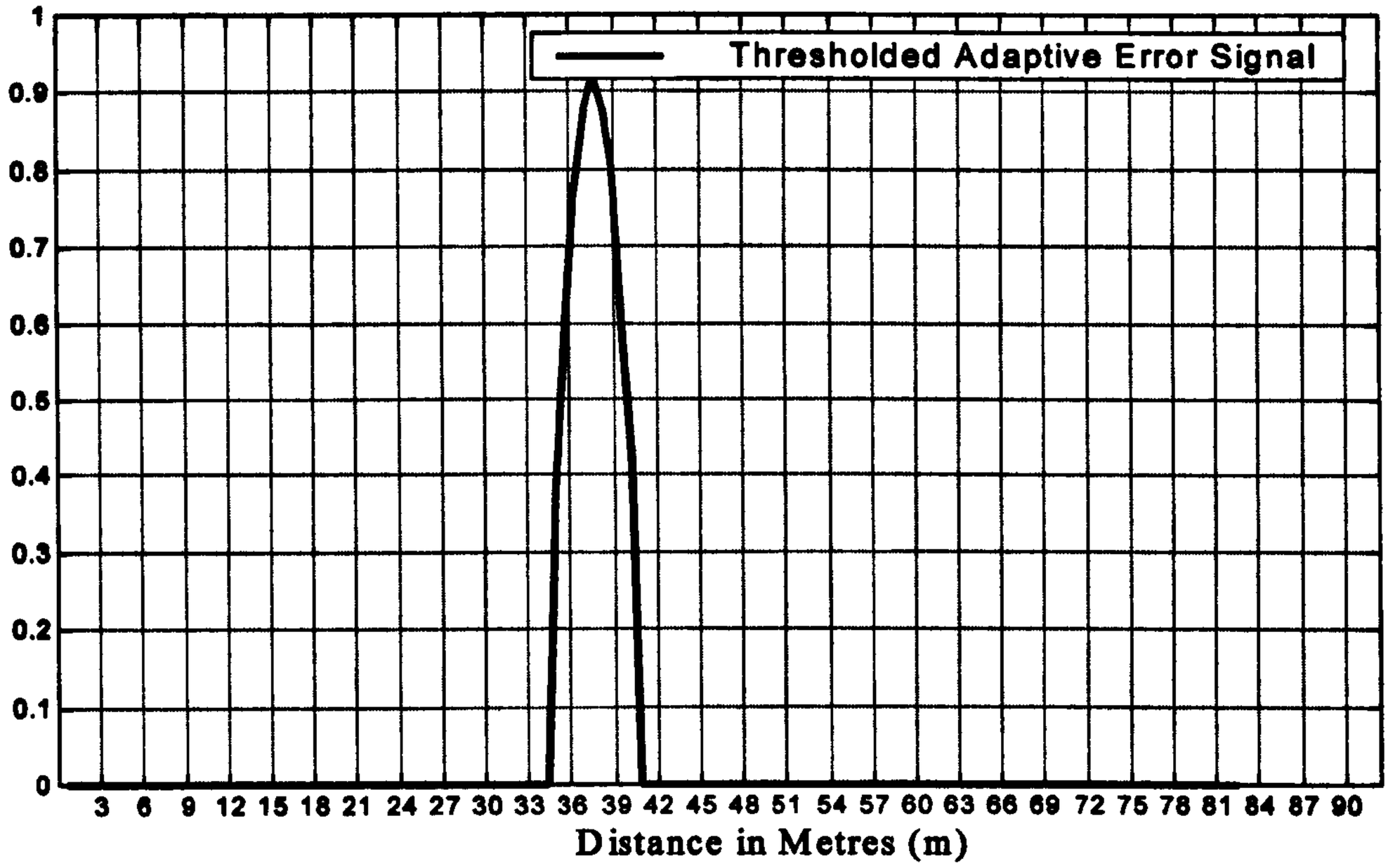

Figure 5.25: Thresholded error waveform of the error waveform in Fig. 5.24

Table 5.2 shows the six sets of real data results. The table shows that the automatic fault location algorithm can locate fault within ± 4.3m.

Data Label	Actual Fault Distance (m)	Fault Distance by Adaptive Method (m)	Difference (m)
Data set 1	33.0	33.2	+0.2
Data set 2	65.5	62.7	-2.8
Data set 3	10.8	10.6	-0.2
Data set 4	45.0	43.9	-1.1
Data set 5	19.6	23.9	+4.3
Data set 6	35.6	35.6	

Table 5.2 Summary of real data sets results

5.7. Optimisation of Adaptive Algorithm Parameters

As described in chapter 3, the adaptive algorithms (LMS, NLMS, and RLS) have two parameters (weight (w) and step size (μ) for LMS, weight (w) and adaptation constant ($\hat{\mu}$) for NLMS, weight (w) and the forgetting factor (λ) for RLS) can changed according to the data, so that better result can be obtained. To achieve better

results, these two parameters need to be optimised. To find optimum parameter values a number of tests were carried out.

For the LMS algorithm weight from 1 to 10 and step size value from 0.1 to 1.0, for the NLMS algorithm weight from 1 to 10 and adaptation constant value from 0.1 to 1.0, and for the RLS algorithm weight from 1 to 10 and forgetting factor value from 0.991 to 1.000 with these parameter test were carried out on data sets 1, 2, 3, 4 and 6. The number of weights was limited to this range, because the optimum result was found within this range. The step size, adaptation constant, and forgetting factor ranges were also limited, because the optimum results were found within the above range. The measure of the optimum parameter values are calculated by the error waveform that gives a maximum peak value for the fault departure (P) and gives the fault distance (D) that is closest to the actual fault distance.

Table 5.3 shows the summary of the optimisation results for the LMS algorithm. It shows that only data sets 1 and 3 gave a fault distance that is close to the actual fault distance and the parameter values (weights and step size) are not consistent for all data sets.

Data Label		LMS			
	Actual Fault distance (m)	D (m)	P	μ	w
Data set 1	33.0	32.8	0.5133	0.9	2
Data set 2	65.0	86.3	0.4371	0.5	2
Data set 3	10.8	10.1	0.3107	1.0	9
Data set 4	45.0	36.0	0.3071	0.4	4
Data set 6	35.6	51.0	0.5080	0.4	10

Table 5.3 Optimisation results for the LMS Algorithm

Table 5.4 shows the summary of the optimisation results for the NMLS algorithm. It shows that data sets 1, 2, 3, and 4 gave the fault distance that is close to the actual fault distance. The parameter values (weight and adaptation constant) are also not consistent for all data sets.

Data Label		NLMS			
	Actual Fault distance (m)	D (m)	P	$\hat{\mu}$	w
Data set 1	33.0	32.9	0.3981	0.1	9
Data set 2	65.0	63.0	0.3890	0.7	2
Data set 3	10.8	10.5	1.1232	0.5	9
Data set 4	45.0	43.7	0.6136	0.1	1
Data set 6	35.6	51.0	0.4973	0.3	10

Table 5.4 Optimisation results for the NLMS Algorithm

Table 5.5 shows the summary of the optimisation results for the RLS algorithm. It shows that all the data sets gave the fault distance that is close to the actual fault distance and the parameter values (weights and forgetting factor) also consistent for all data sets.

Data Label		RLS			
	Actual Fault distance (m)	D (m)	P	λ	w
Data set 1	33.0	33.2	0.4456	0.996	7
Data set 2	65.0	62.7	0.5186	0.996	7
Data set 3	10.8	10.6	0.9939	0.996	7
Data set 4	45.0	43.9	0.4197	0.996	7
Data set 6	35.6	35.6	0.3574	0.996	7

Table 5.5 Optimisation results for the RLS Algorithm

All the above results show that RLS algorithm gave the best results and the parameter values are also consistent. It is important that the parameter values need to be consistent for an automating the fault distance calculation algorithm. Therefore, the RLS algorithm is chosen. Detail optimisation results can be found Appendix-A.

5.8. Conclusion

In this chapter, a new automatic fault location system for locating faults in LVUDN is presented. This system pre-processes the TDR waveform to identify single-phase tees that may exist in the LVUDN and also locates 3-phase faults. If there is no 3-phase fault then the system processes the waveforms with intelligent processing to find the fault. The intelligent processing uses adaptive filtering to produce an output (error) waveform that will show a key departure at the fault point. Since, there may be more than one error waveform, it uses fuzzy membership to find a unique fault distance rather than using arithmetic averaging. Finally, the fault distance is then calculated using an appropriate velocity of propagation that is provided by the user.

The whole process is done automatically. Therefore, it minimises user interpretation. The only information needs to be provided by the user is the velocity of propagation. This is because more than one cable type is installed in LVUDN. Each cable type has a different velocity of propagation. Therefore, the system cannot have a pre-determined velocity of propagation.

The performance of the system was tested using the model data as well as field data. It gave an accuracy of ±4.3m of the actual fault distance on the field data. It shows the robustness of the system and effectiveness of the adaptive filtering and fuzzification in dealing with noisy and complicated TDR waveforms. This algorithm is suitable for permanent and intermittent faults such as persistent and transitory.

Chapter 6

6. Wavelet Enhanced Fault Location and Alternative Methods of Fault Distance Calculation

6.1. Introduction

The Wavelet Transform (WT) is one the most useful signal processing tools that is used to provide both a local and a global view of waveforms. In the WT, frequency resolution is proportional to the frequency level. As a consequence, time localisation is finer at the higher frequencies. The smaller scales decrease the time spread and increase the frequency distribution, thus giving good frequency resolution but poor time resolution at low frequencies whilst at higher frequencies the reverse is true. This chapter discusses how the wavelet transform is used to automate TDR based fault location, and to improve the accuracy of the fault distance calculation. It uses a gradient method to find the zero crossing of the peak in the error waveform to identify the fault position.

Section 6.2 discusses why the WT is used in the fault location system and the use of Mallat [9] filter banks in the WT are also investigated. This section also includes an analysis of multi-scale resolution when the WT is applied to an example TDR waveform.

Section 6.3 presents a "wavelet enhanced" fault location system. In this section, an analysis of the algorithm performance is compared to the adaptive and fuzzy based fault location system.

Section 6.4 discusses how to improve the accuracy of fault distance calculation for both wavelet, and the adaptive and fuzzy based fault location systems. One technique uses the gradient of the fault indication peak to find the zero crossing where the slope of the fault indicating peak changes rapidly. The second technique calculates the local mean at the zero crossing point to calculate the fault distance. This is only used with the adaptive and fuzzy based fault location system because the error

waveforms are noisy and spiky as they consist mainly of high frequency components. Finally, conclusions to this chapter are presented in section 6.5.

6.2. Why Wavelet Transform?

As mentioned earlier, WT multi resolution analysis can yield good time resolution of high frequencies but poor time resolution of low frequencies. Applying WT to TDR waveforms reduces them into multi scales. Each scale will have high and low pass components. The low pass scales give the low frequency components of the waveform and the high pass scales give the high frequency components. Reducing the waveform into multi frequency components minimises the effects of the cable's attenuation and dispersion characteristics [55]. It also reduces noise so that analysis of the waveform is more effective. Therefore, applying adaptive filtering to individual scales waveforms potentially produces better error waveforms.

In practice, the waveforms normally consist of high frequency components of short duration and low frequency components of long duration [78]. The distance to faults in LVUDN can vary from short distances to long distances. Analysis of the low pass scales of a waveform, i.e. the low frequency components, allows faults to be located at both short and long range whereas using the high pass scales only short range faults can be located. However, low pass scales give poor time resolution compared to high pass scales and hence the accuracy of fault location is worse.

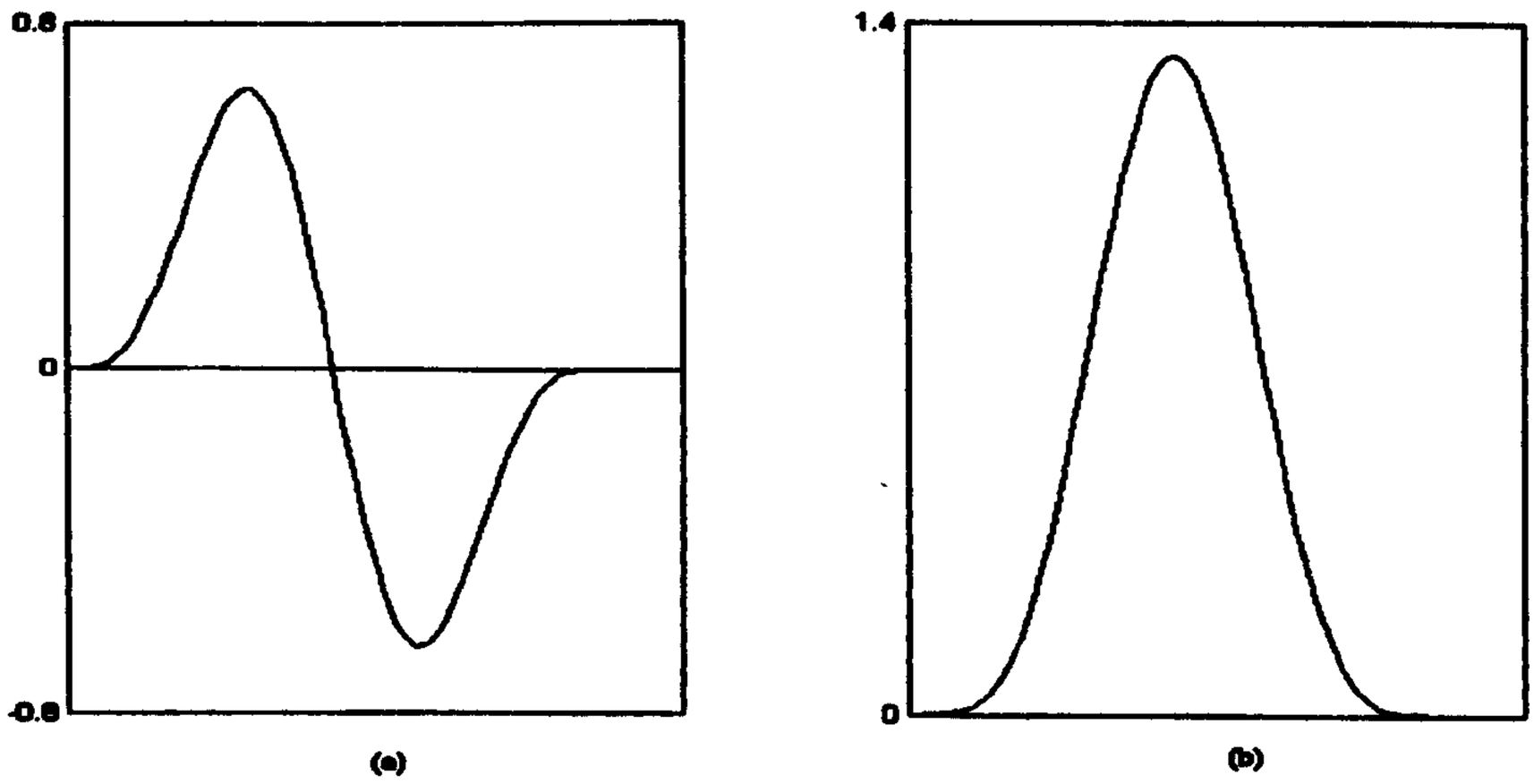

Figure 6.1 (a) Non-orthogonal mother wavelet *h(t)*, this wavelet is a quadratic spline and is the first derivative of the cubic spline function in (b)

Points of sharp variations are often among the most important features for analysing the properties of transient waveforms or images [9]. Mallat's WT algorithm [9] was successfully used for edge detection in images where images have many different types of sharp variations. TDR waveforms contain many discontinuities due to multiple reflections from joints, tees, and faults. Therefore, Mallat's WT algorithm is used in the "wavelet enhanced" fault location system. The non-orthogonal wavelet *h(t)* in Mallat's WT algorithm, shown in Fig. 6.1a, is the first derivative of the cubic spline function shown in Fig 6.1b.

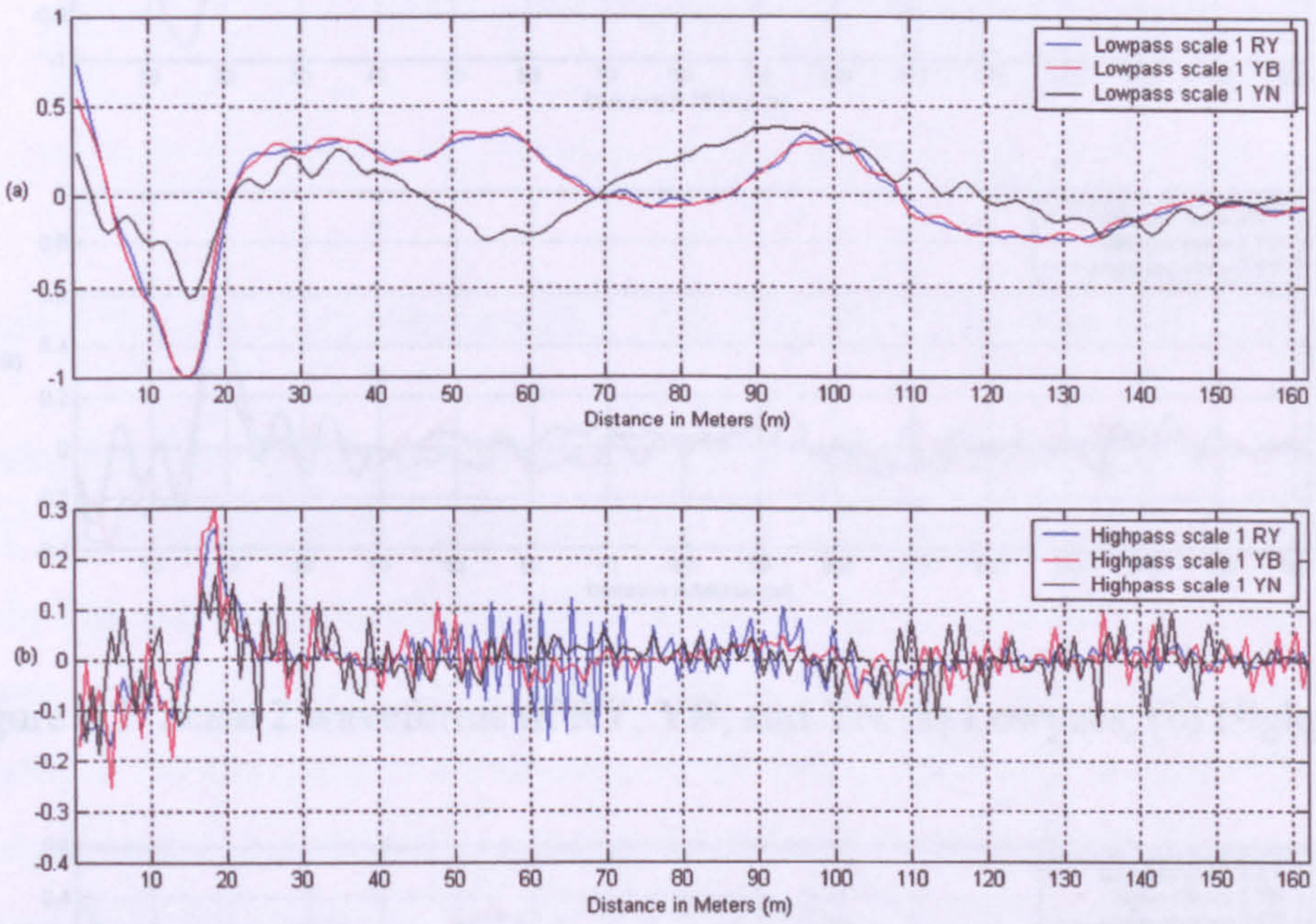

Figure 6.2: Scale 1 waveforms of RY, YB, and YN (a) Lowpass, (b) Highpass

Data set 6 (described in chapter 5) has a short circuit fault between Yellow and Neutral at 35.6m from the test point. This data was recorded with all three phases of the cable de-energised. If the cable is energised on the Red and Blue phases with the Yellow phase de-energised due to a fault then only YN, YB and RY phases will be available for fault location (as explained in chapter 5). When the WT is applied to these three TDR waveforms (YN, YB, and RY) the low and high pass scales (1, 2, 3, and 4) are shown in Fig. 6.2(a, b), 6.3(a, b), 6.4(a, b) and 6.5(a, b) respectively. It can be seen that high pass scale 1 produces spiky waveforms that have very high frequency components but with better time resolution compared to low pass scale 1.

The low pass scale 1 produces clean waveforms, due to the absence of high frequency signals, but it has poor time resolution compared to the high pass scale 1. As the scale increases, the high pass scale waveforms become 'cleaner' but their time resolution deteriorates. Similarly, the low pass scales become 'smoother' and their time resolution also deteriorates.

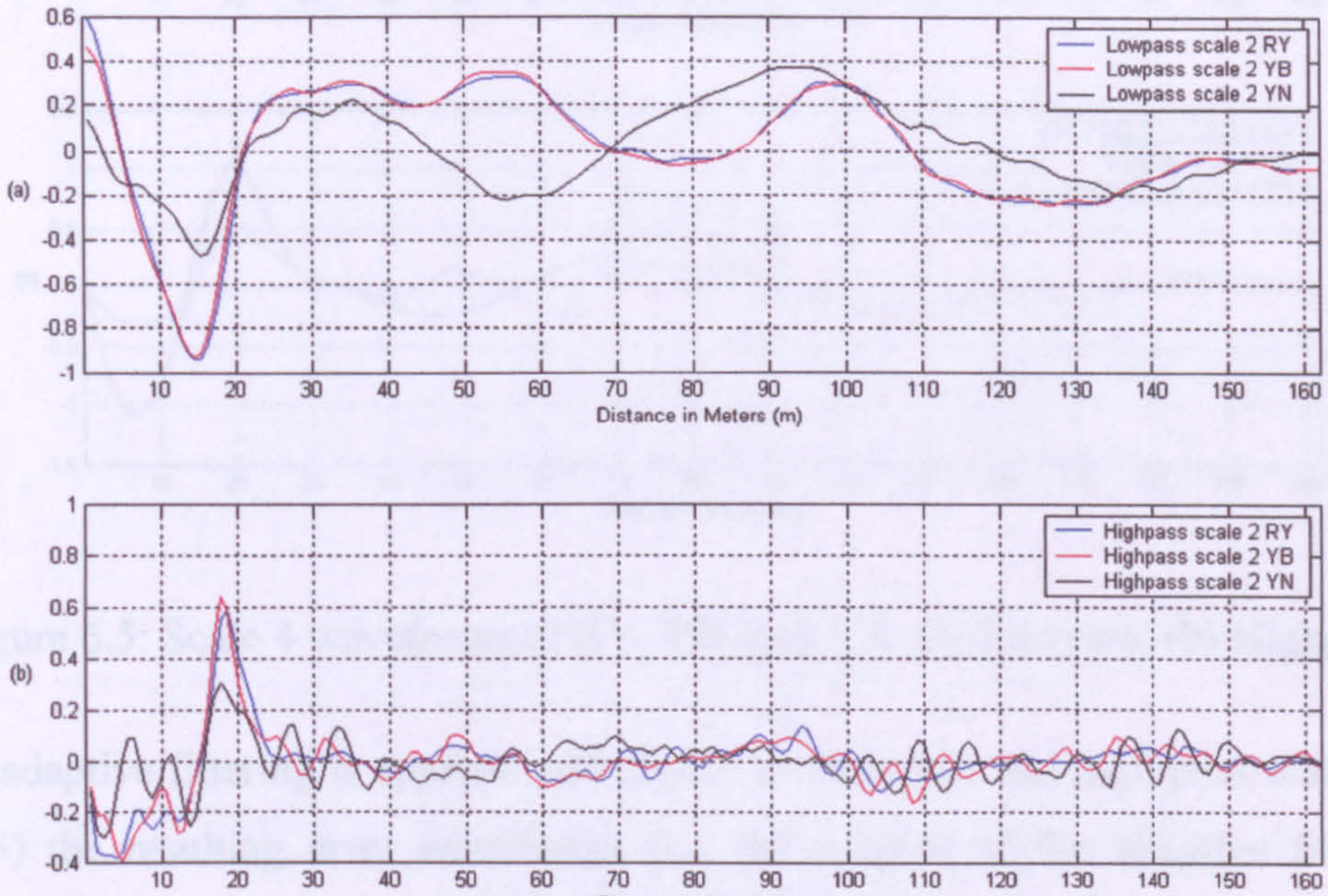

Figure 6.3: Scale 2 waveforms of RY, YB, and YN (a) Lowpass, (b) Highpass

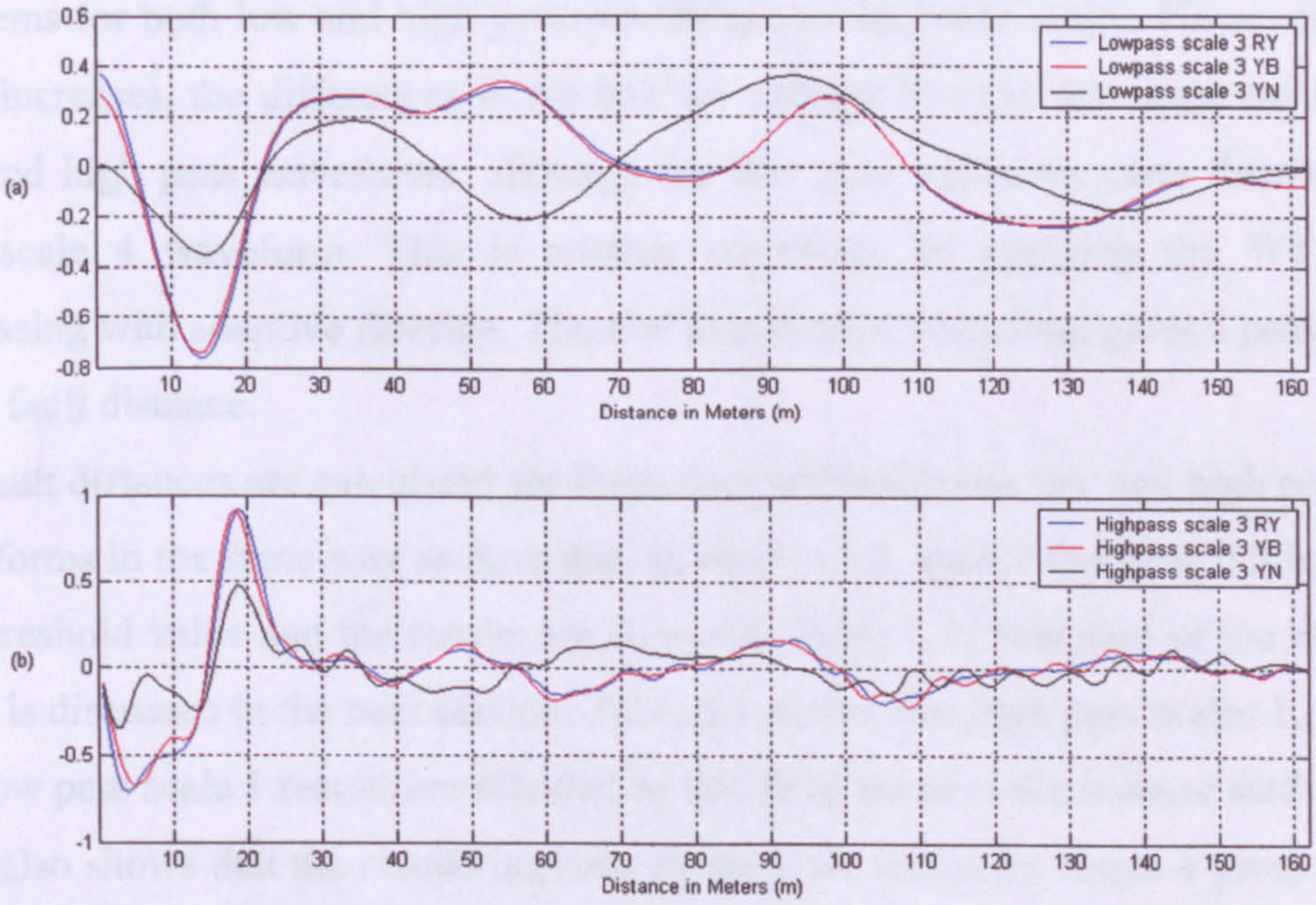

Figure 6.4: Scale 3 waveforms of RY, YB, and YN (a) Lowpass, (b) Highpass

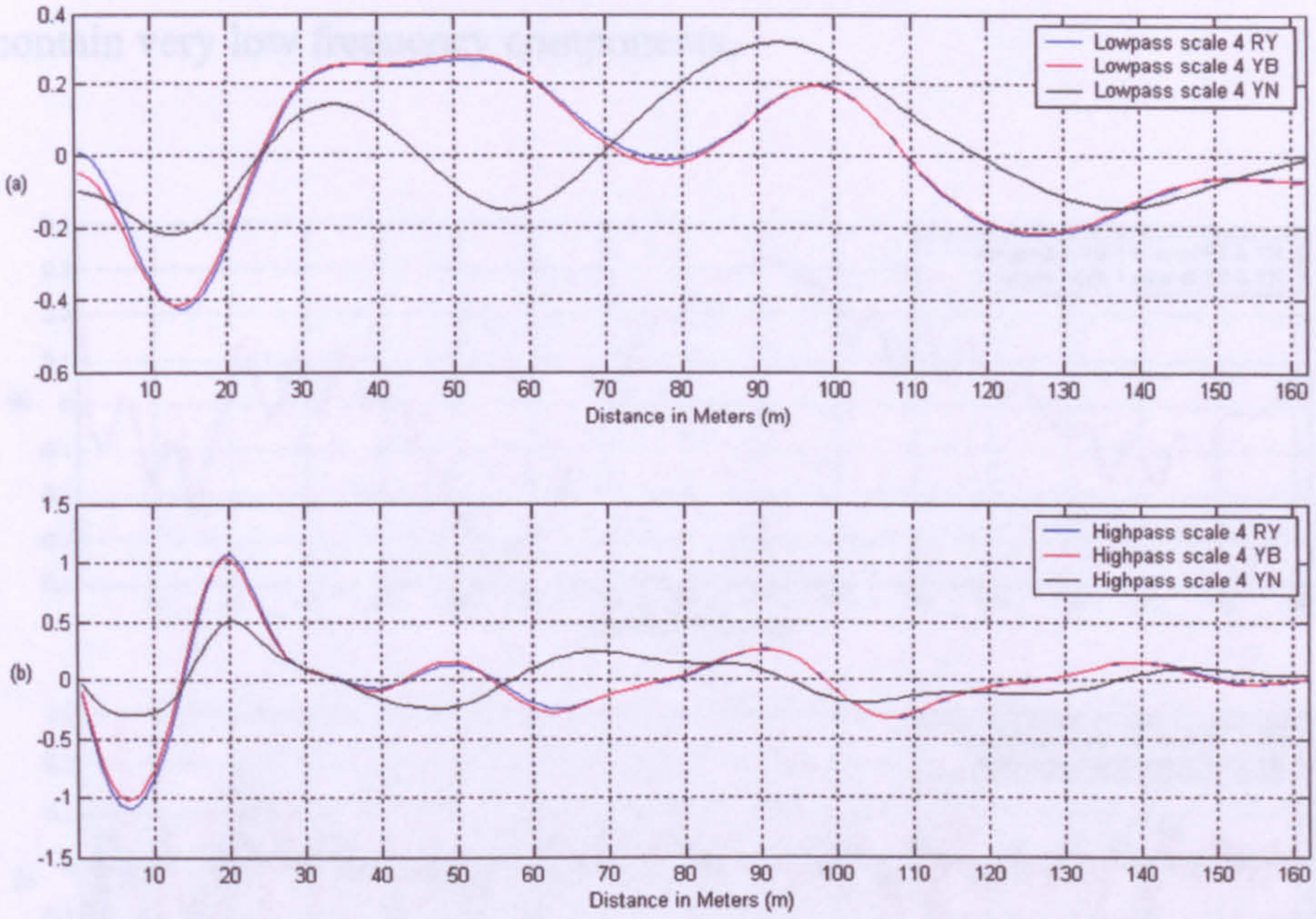

Figure 6.5: Scale 4 waveforms of RY, YB, and YN (a) Lowpass, (b) Highpass

If adaptive filtering is applied individually to these low and high pass scales (Fig. 6.2-6.5) the resulting error waveforms (i.e. the outputs of the adaptive filter) are shown in Fig. 6.6 (a, b), 6.7(a, b), 6.8(a, b) and 6.9(a, b) respectively. It can be seen that there are differences between the 'phase to phase' and 'phase to neutral' waveforms at the start, due to differences in the balance network settings. This causes problems for both low and high pass waveforms at the lower scales. However, as the scale increases, the differences in the balance settings become less apparent for both low and high pass waveforms, although the low pass improves more than the high pass scale 4 waveform. This is another advantage of applying the WT before processing with adaptive filtering. The low pass scale 4 waveform gives a peak almost at the fault distance.

Fault distances are calculated for these four scales of both low and high pass error waveforms in the same way as described in section 5.5, except that here 0.2 is used as the threshold value and the results are shown in Table 6.1. Selection of the threshold value is discussed in the next section. Table 6.1 shows that high pass scales 1, 2, and 3 and low pass scale 1 results are affected by the differences in the balance settings. The table also shows that the results improve as the scale increases. Scale 4 gives the best result, i.e the closest to the actual fault distance (35.6m). Tests were also carried out

for scale 5 and 6, but the results were found to give the lowest accuracy because these scales contain very low frequency components.

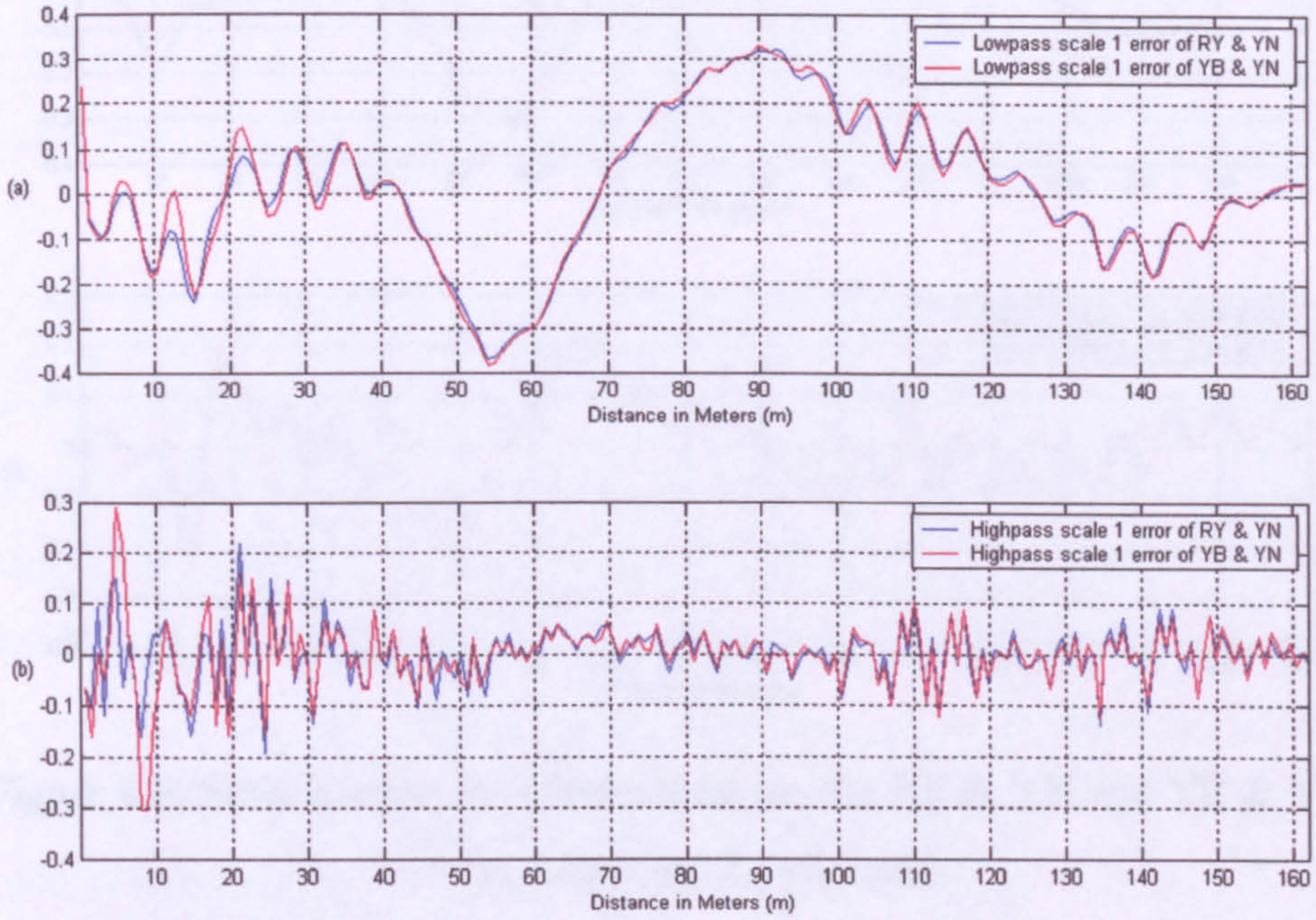

Figure 6.6: Scale 1 error waveforms between the RY & YN and YB & YN (a) Lowpass, (b) Highpass

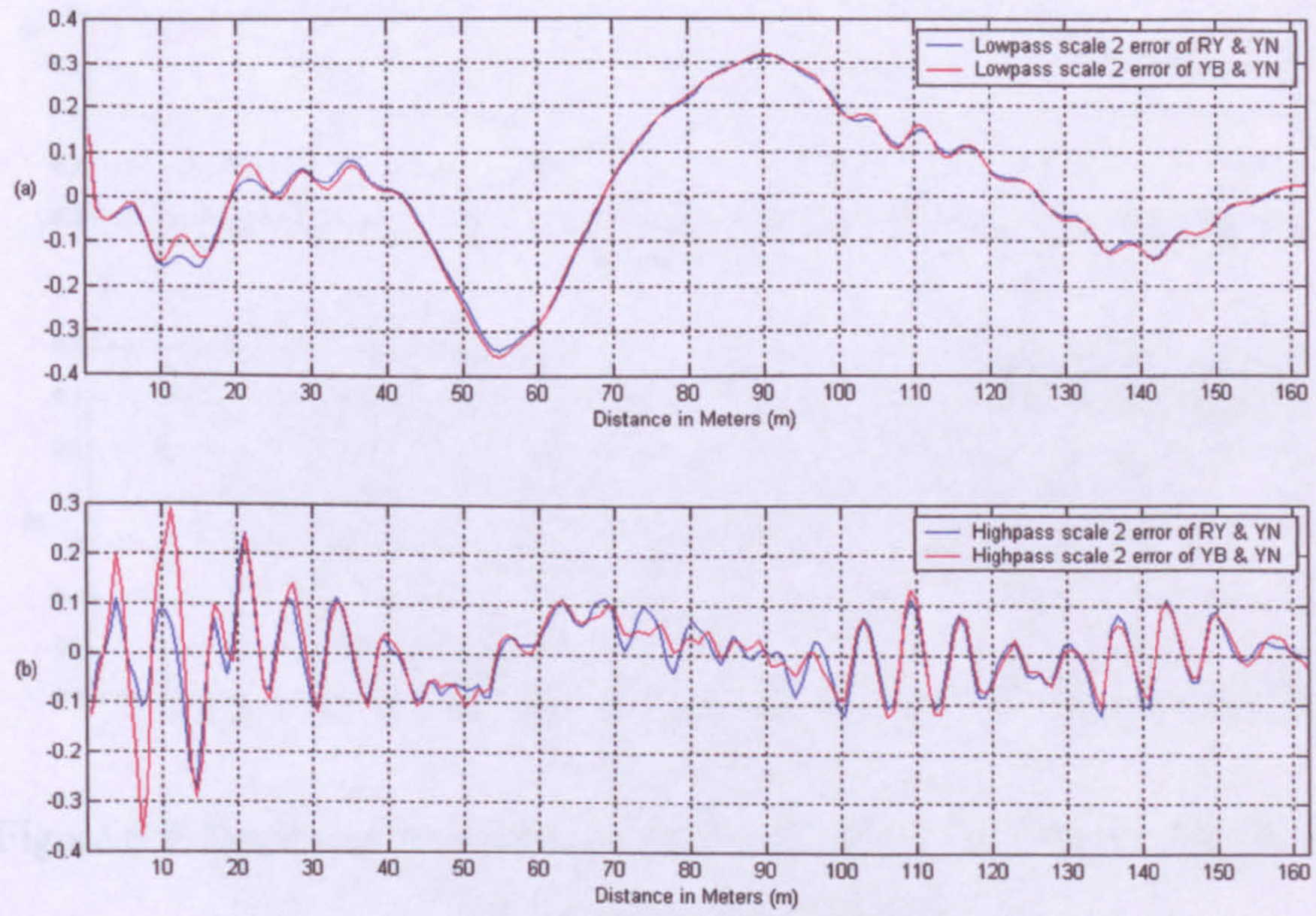

Figure 6.7: Scale 2 error waveforms between the RY & YN and YB & YN (a) Lowpass, (b) Highpass

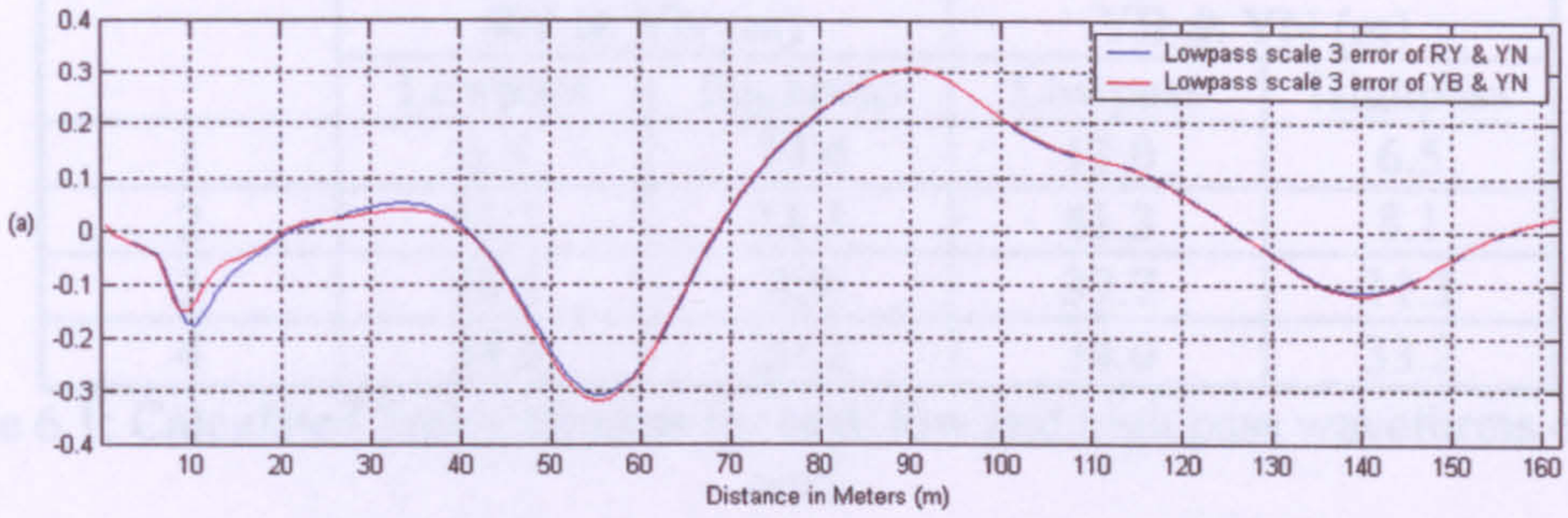

Figure 6.8: Scale 3 error waveforms between the RY & YN and YB & YN

(a) Lowpass, (b) Highpass

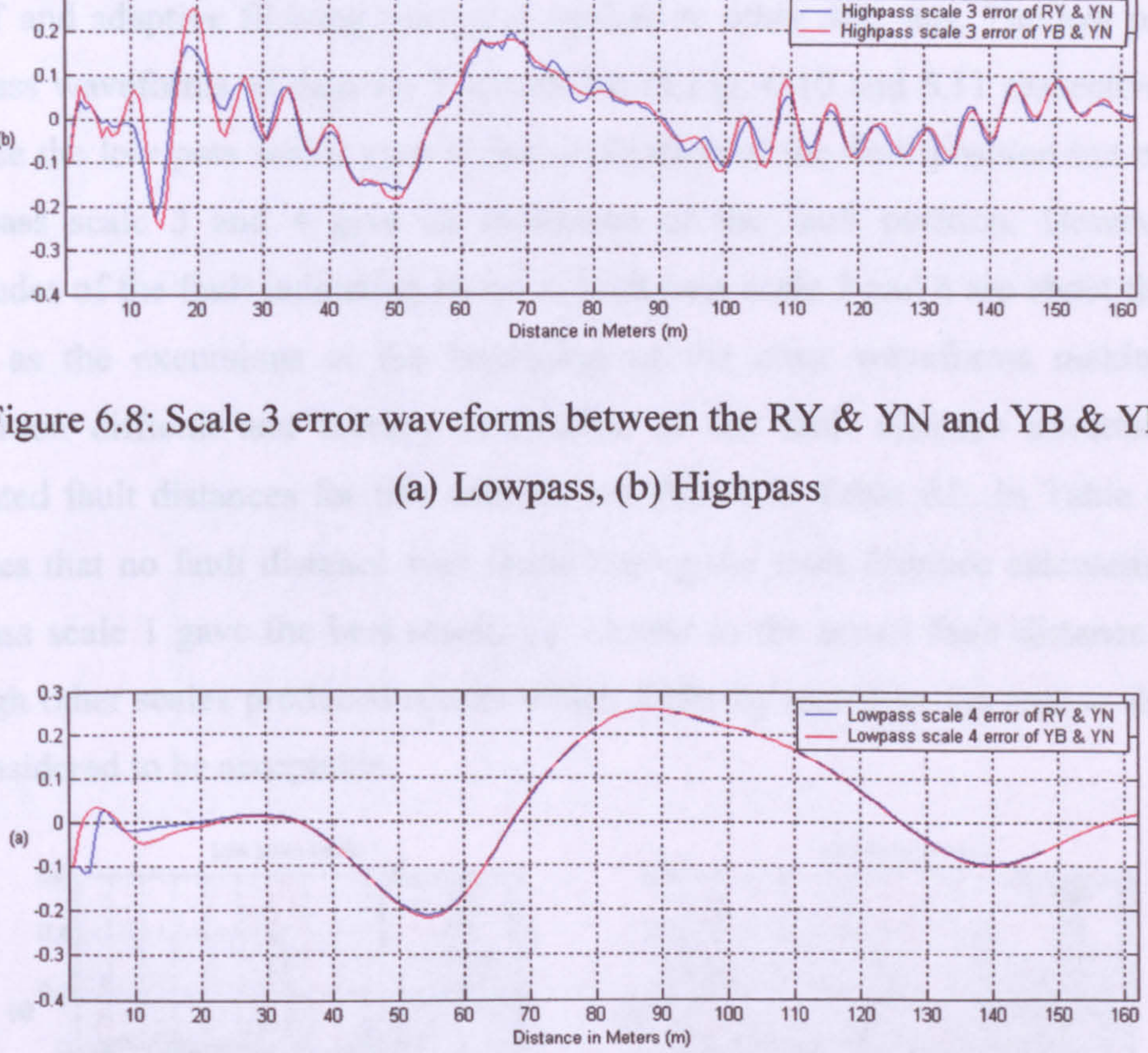

Figure 6.9: Scale 4 error waveforms between the RY & YN and YB & YN

(a) Lowpass, (b) Highpass

Scale No.	Fault Distance between RY & YN (m)		Fault distance between YB & YN (m)	
	Lowpass	Highpass	Lowpass	Highpass
1	6.5	19.4	13.0	6.5
2	42.1	11.3	41.3	8.1
3	40.5	4.9	39.7	11.3
4	34.8	33.2	34.0	33.2

Table 6.1: Calculated fault distances for both low and high pass waveforms of data set6

WT and adaptive filtering were also applied to other data sets. The low pass and high pass waveforms of data set 1 are shown in Fig. 6.10 and 6.11 respectively. In this case the low pass scales give a clear indication of the fault position but only the high pass scale 3 and 4 give an indication of the fault position. However, the amplitudes of the fault indicating peaks in high pass scale 3 and 4 are about the same height as the excursions at the beginning of the error waveforms making their recognition difficult and thereby calculation of the fault distance uncertain. The calculated fault distances for this data set are shown in Table 6.2. In Table 6.2, '*' indicates that no fault distance was found during the fault distance calculation. The low pass scale 1 gave the best result, i.e. closest to the actual fault distance (33m), although other scales produced results which differ by less than 1m and so they also are considered to be acceptable.

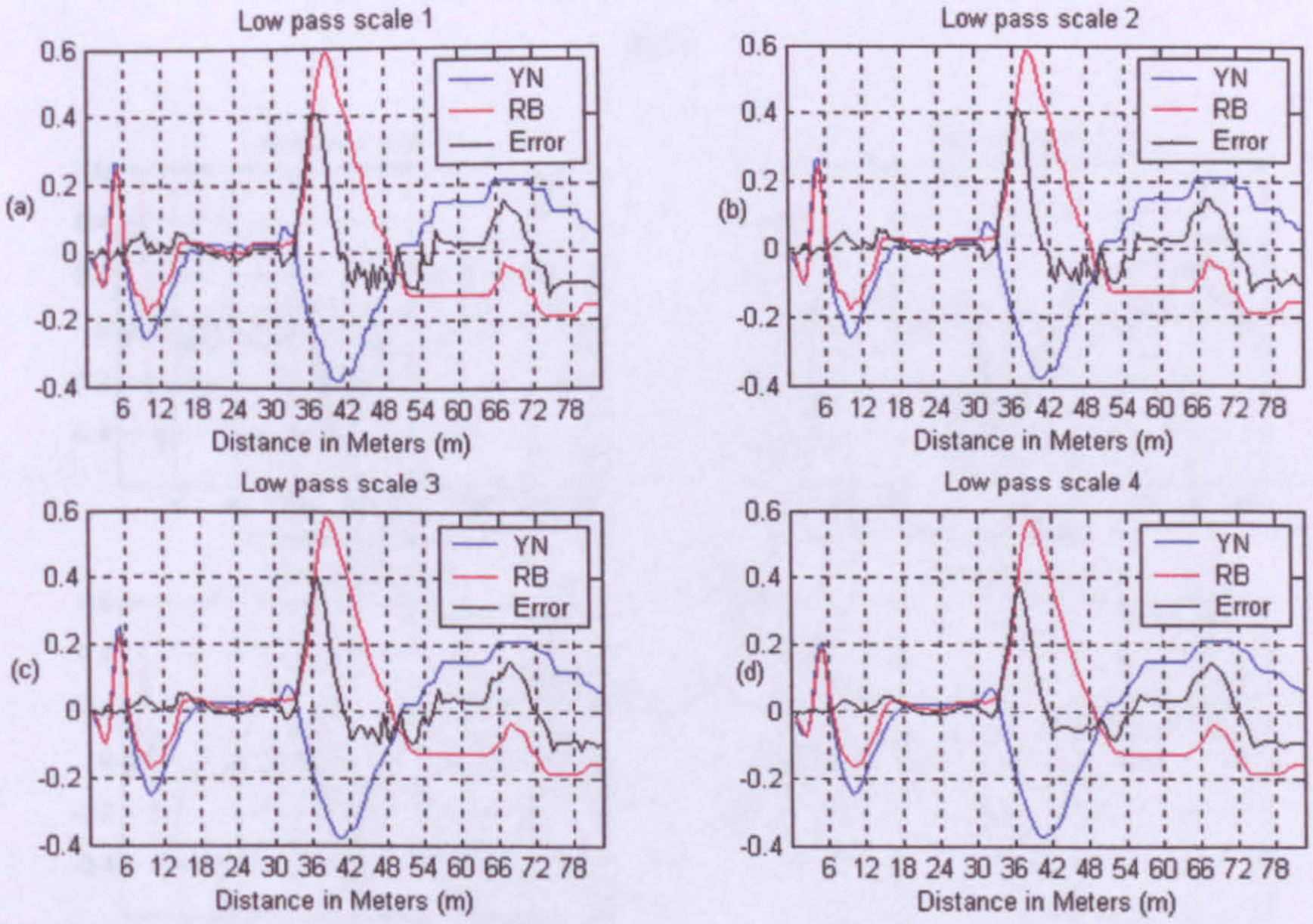

Figure 6.10: Low pass result for data set 1

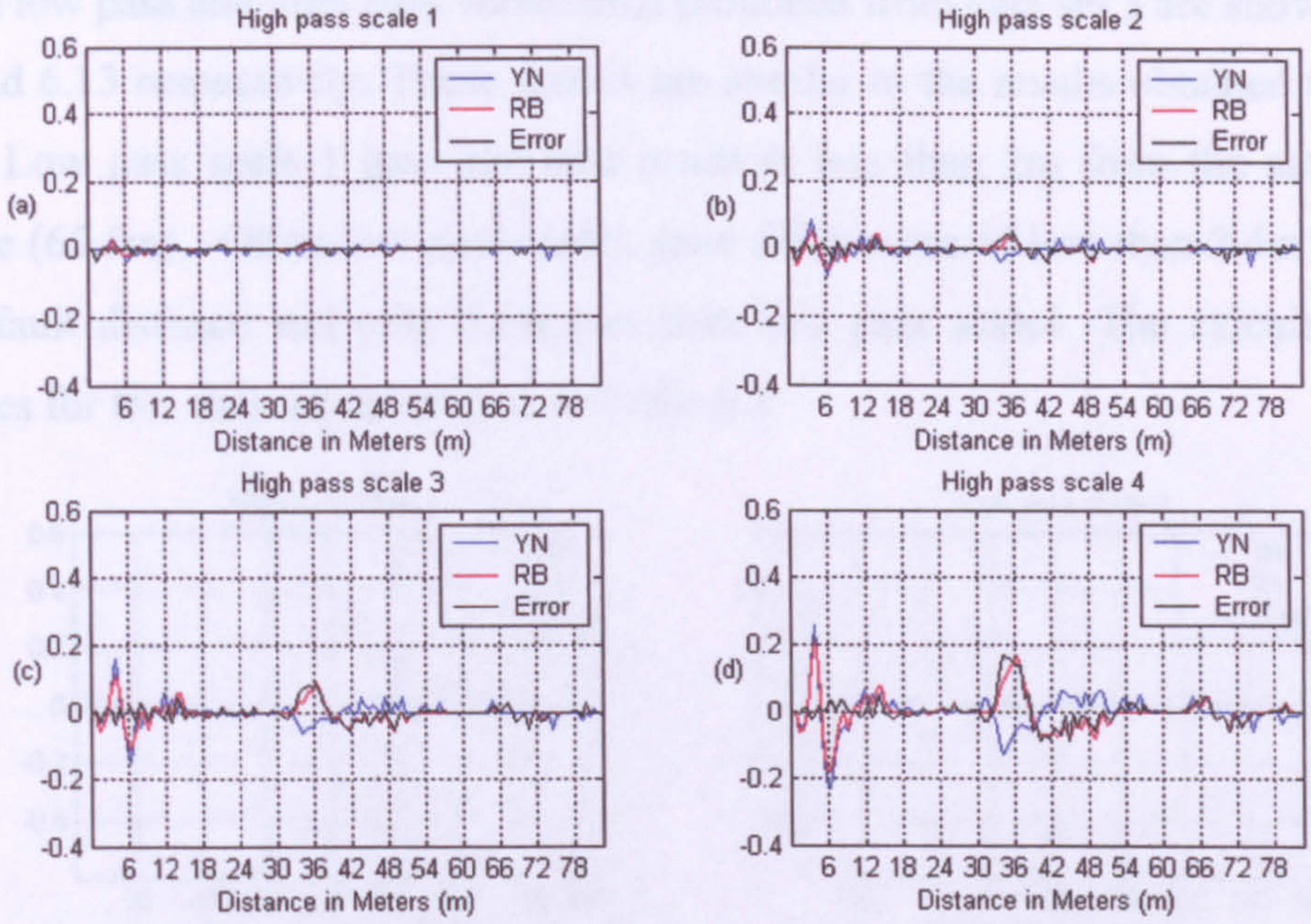

Figure 6.11: High pass result for data set 1

Scale No.	Fault Distance (m)	
	Lowpass	Highpass
1	33.1m	*
2	32.9m	*
3	32.7m	*
4	32.4m	*

Table 6.2: Calculated fault distances for both low and high pass waveforms of data set1

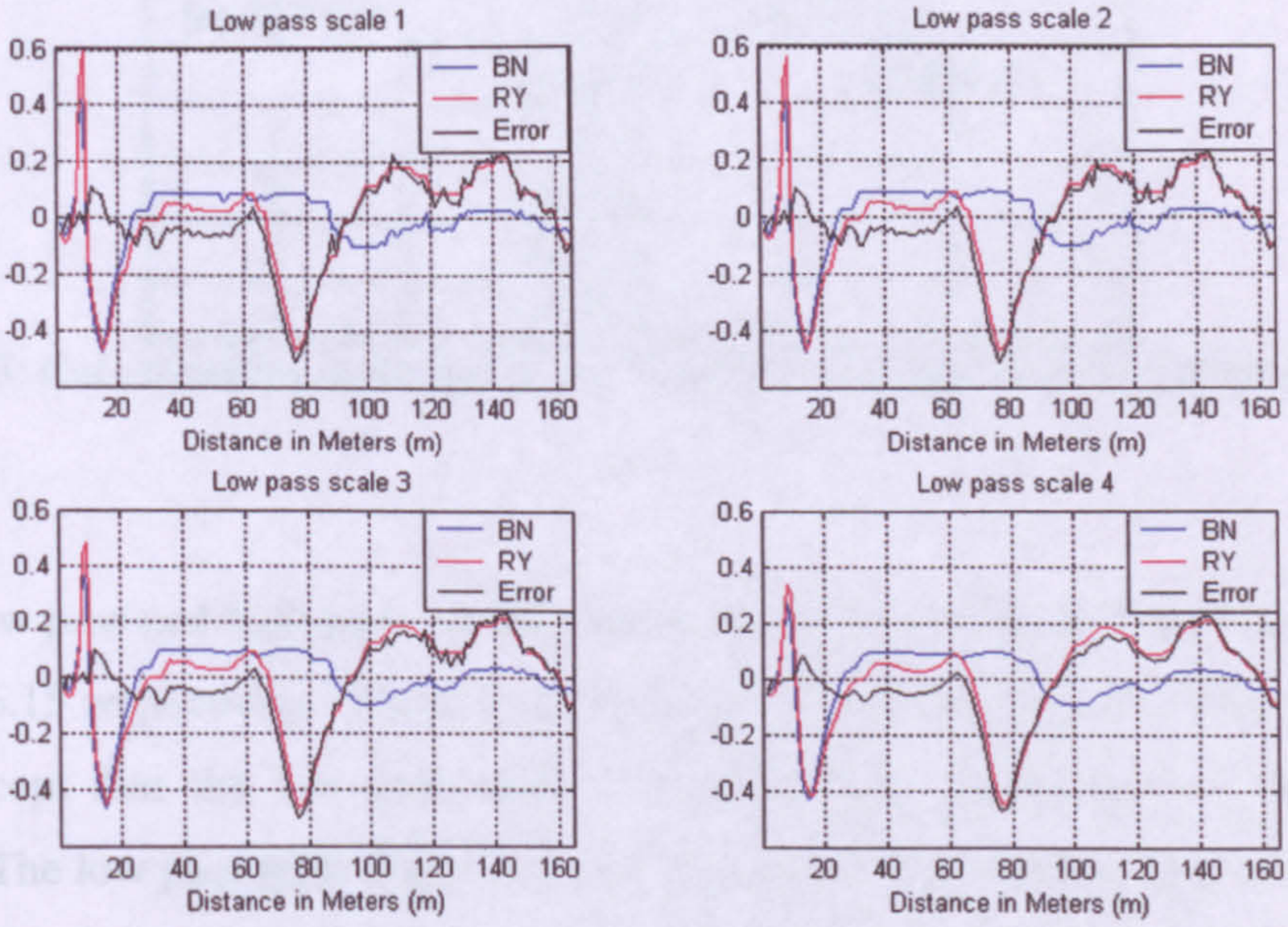

Figure 6.12: Low pass result for data set 2

The low pass and high pass waveforms produced from data set 3 are shown in Fig. 6.12 and 6.13 respectively. These results are similar to the results obtained with data set 1. Low pass scale 1 gave the best result at less than 2m from the actual fault distance (65.5m). Other low pass scales gave differences of less than 2.4m from the actual fault distance and only 0.5m less than low pass scale1. The calculated fault distances for this data set are shown in Table 6.3.

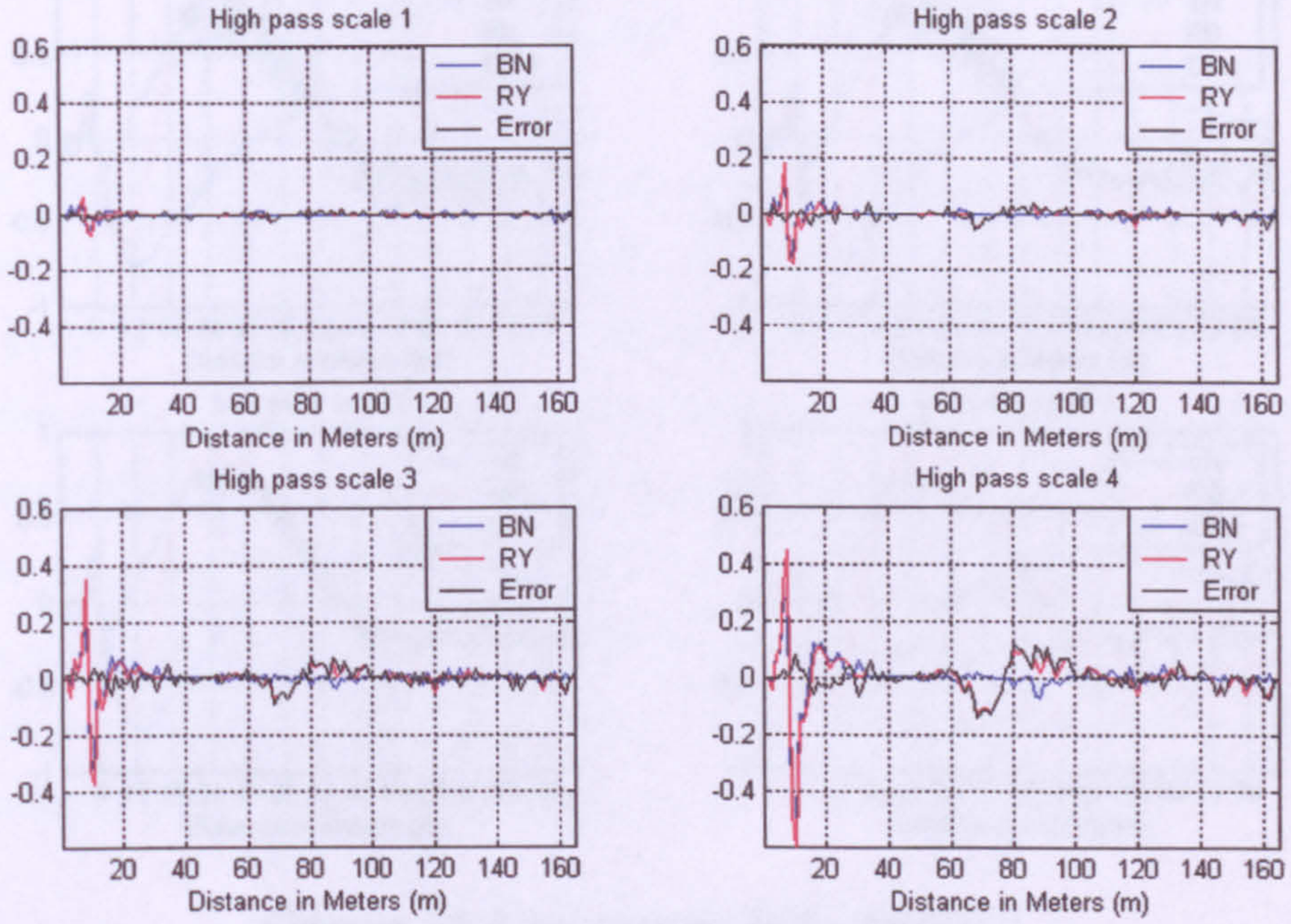

Figure 6.13: High pass result for data set 2

Scale No.	Fault Distance (m)	
	Lowpass	Highpass
1	63.5m	*
2	63.4m	*
3	63.2m	*
4	63.0m	*

Table 6.3: Calculated fault distances for both low and high pass waveforms of data set2

The low pass and high pass waveforms produced from data set 3 are shown in Fig. 6.14 and 6.15 respectively. These results are similar to those obtained from data set 1 and 2 except that the low pass scale 1 is affected by differences in the balance settings. The low pass scale 2 gave a result that is less than 0.9m from the actual fault distance (10.8m). Low pass scale 3 and 4 gave differences of 1m and 1.1m

respectively compared to the actual fault distance, and only 0.2m less than low pass scale2. Low pass scale 1 produced gave a difference of 5.9m from the actual fault distance due differences at the beginning of the waveform resulting from differences on the balance settings. The calculated fault distances are shown in table 6.4 which, as with data sets 1 and 2, shows that the high pass scales did not produce any result.

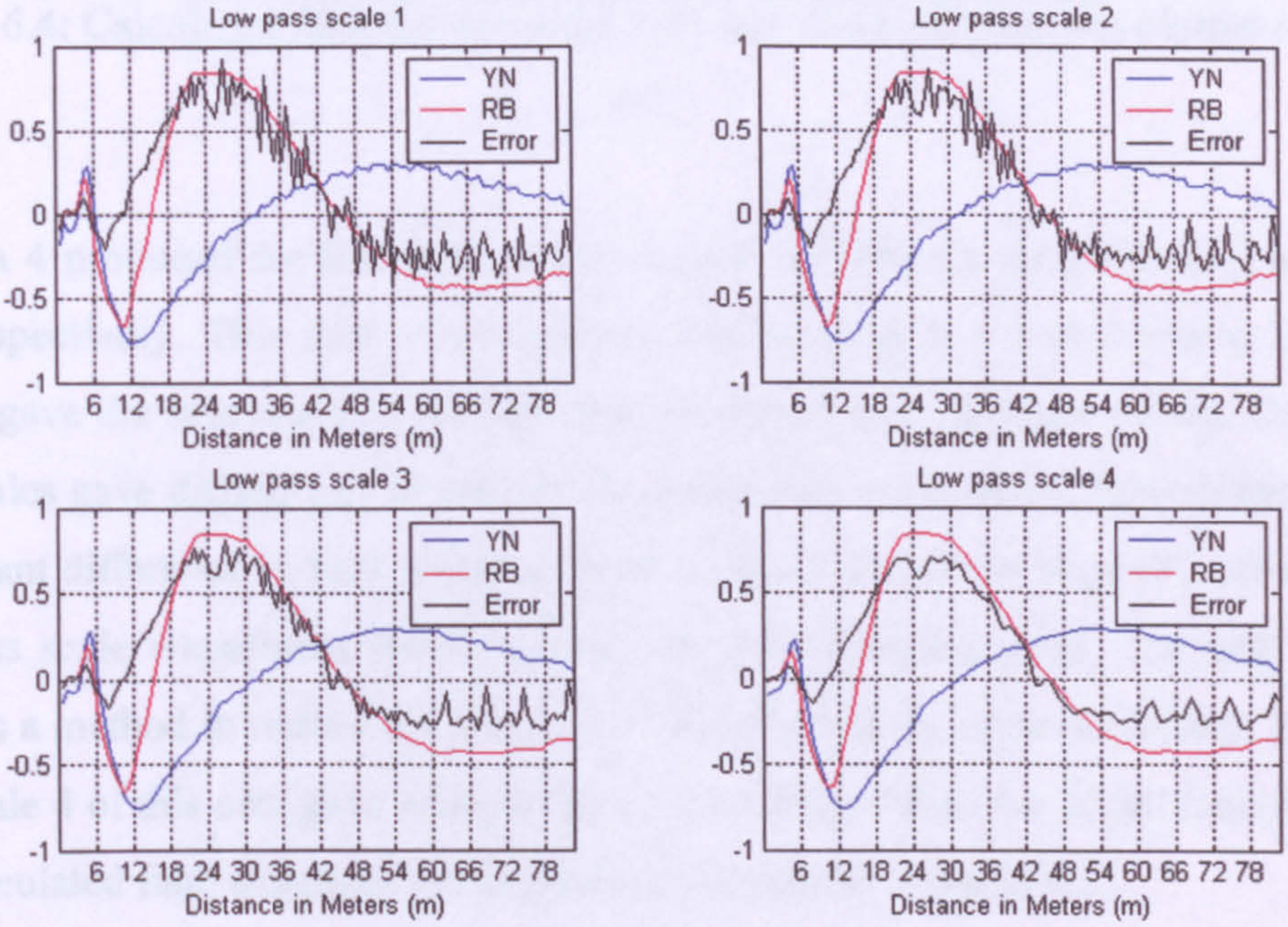

Figure 6.14: Low pass result for data set 3

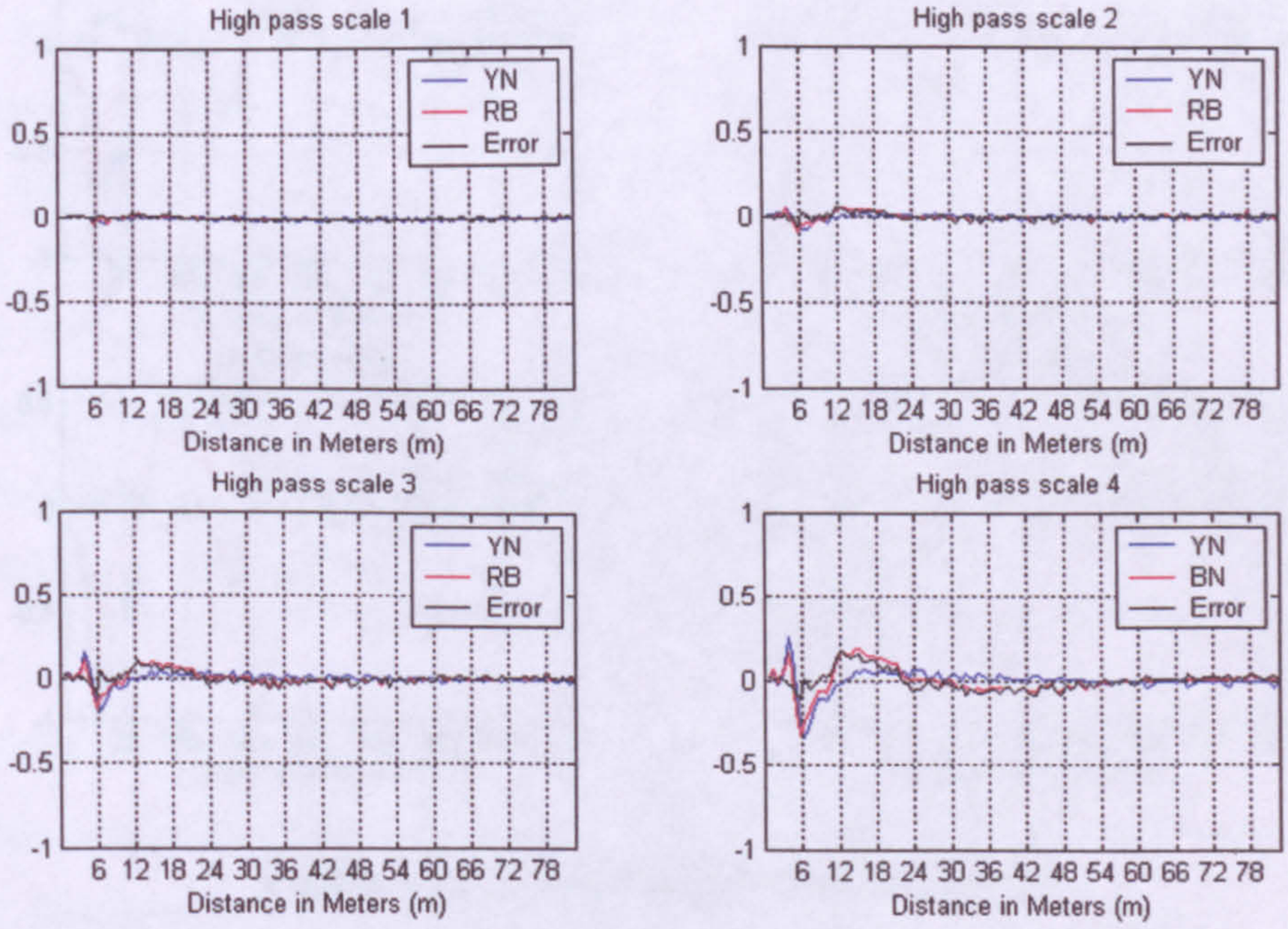

Figure 6.15: High pass result for data set 3

Scale No.	Fault Distance (m)	
	Lowpass	Highpass
1	4.9	*
2	9.9	*
3	9.8	*
4	9.7	*

Table 6.4: Calculated fault distances for both low and high pass waveforms of data set3

Data 4 produced the low pass and high pass waveforms shown in Fig. 6.16 and 6.17 respectively. This data result is again similar to data 1 and 2 where low pass scale 1 gave the best result at 9m less than the actual fault distance (45m). Other low pass scales gave differences of upto 10.7m compared to the actual fault distance. The significant difference in fault distance for this data is due to the large DC offset in the low pass scale waveforms which 'delays' the zero crossing point. The next section presents a method to reduce the effect of a DC offset in the error waveform. The high pass scale 4 of this data gave a result that is 7.1m longer than the actual fault distance. The calculated fault distances for this data set are shown in table 6.5.

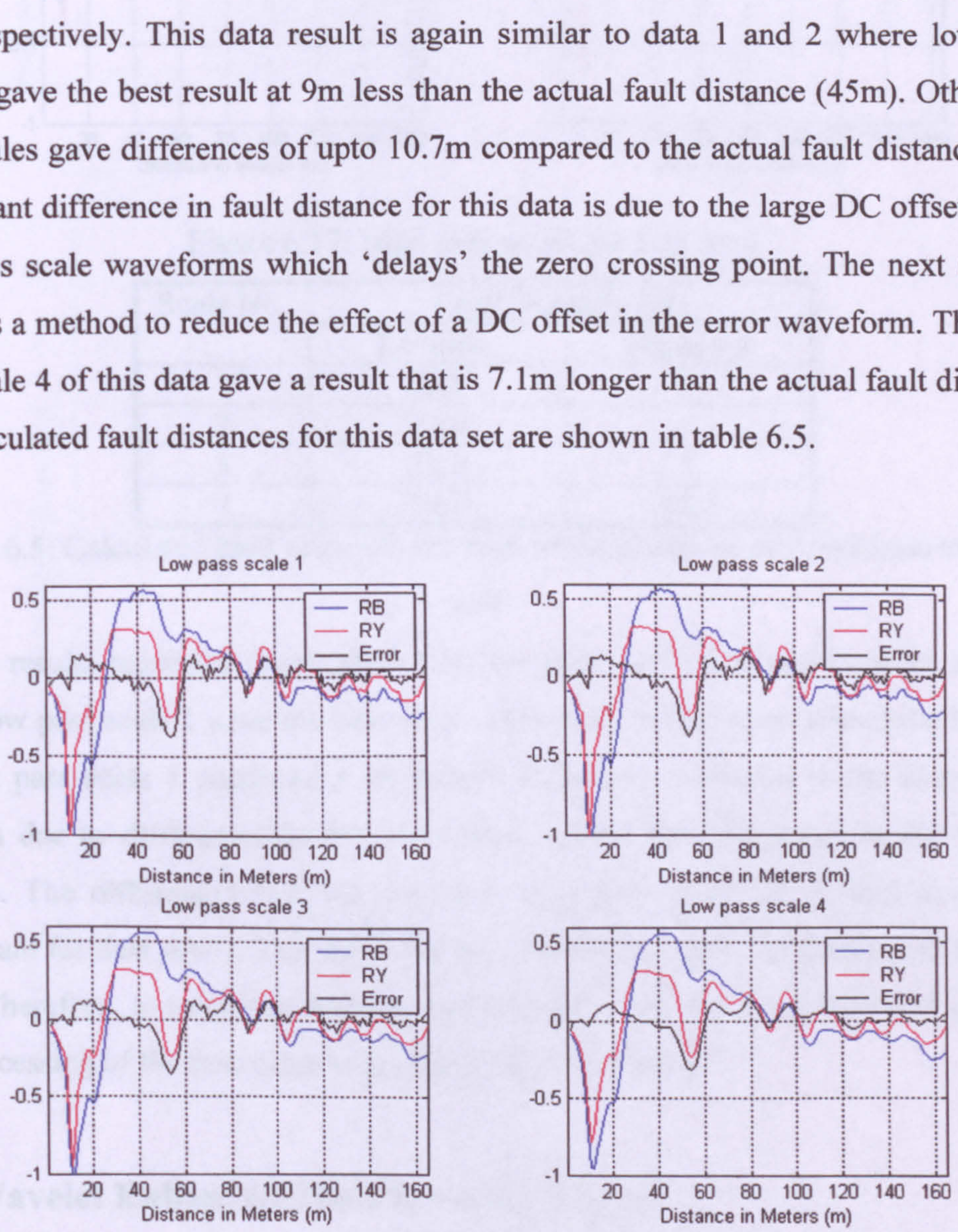

Figure 6.16: Low pass result for data set 4

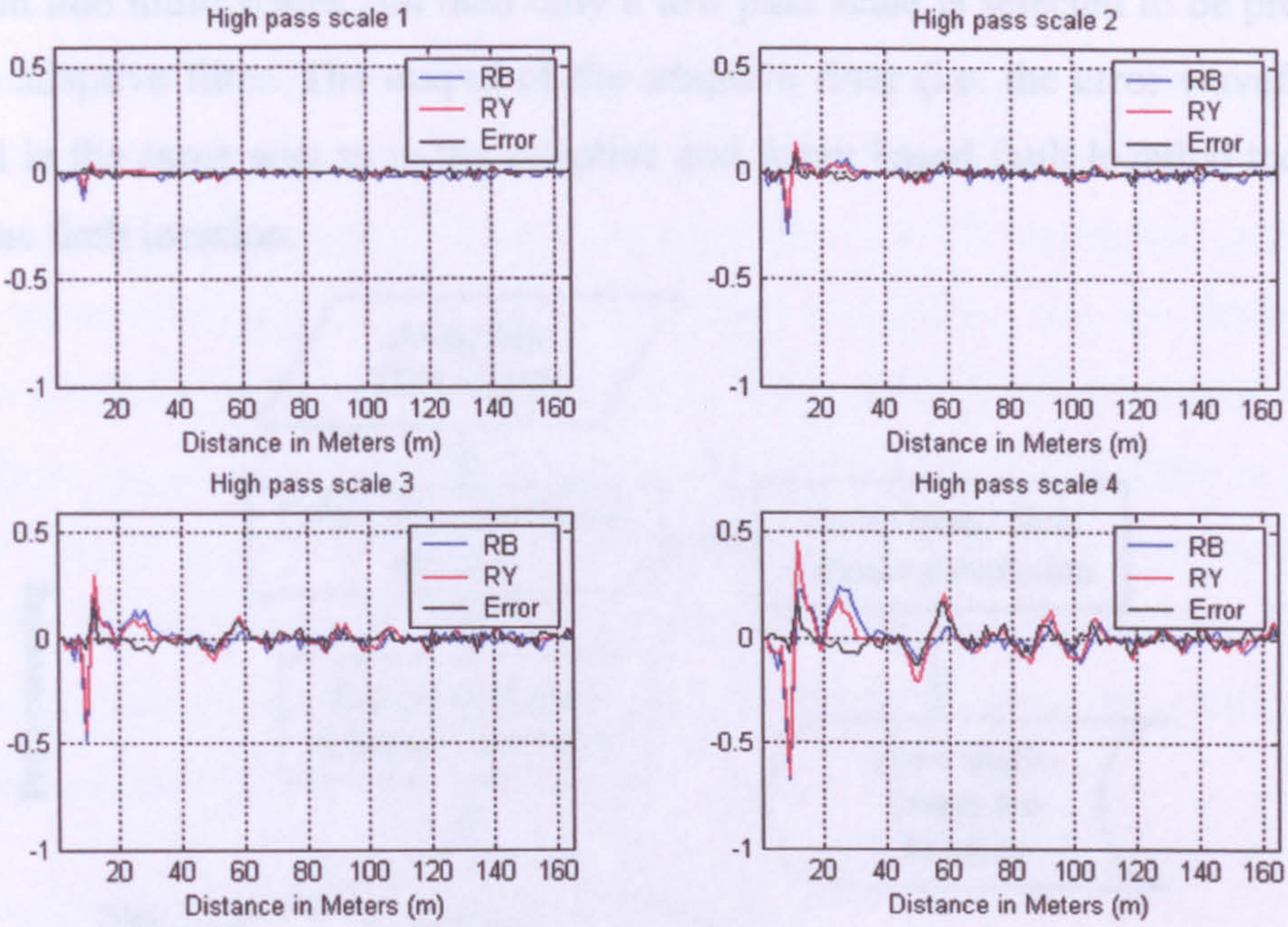

Figure 6.17: High pass result for data set 4

Scale No.	Fault Distance (m)	
	Lowpass	Highpass
1	36.0	*
2	34.5	*
3	35.3	*
4	34.3	52.1

Table 6.5: Calculated fault distances for both low and high pass waveforms of data set4

The results presented above show that low pass scales give good results. In most cases low pass scale 1 gave the best result. However, in two cases (data sets 3 and 6) the low pass scale 1 produced a significant difference compared to the actual fault position due to differences in the waveforms caused by differences in the balance settings. The differences between the other low pass scales (2, 3, and 4) are not significant for data sets 1, 2, 3, and 4 but low pass scale 4 gave the best result for data set 6. Therefore, to minimise the computation time, only low pass scale 4 is used for pre-processing of the data prior to applying adaptive filtering.

6.3. Wavelet Enhanced Fault Location System

In this section, a wavelet based fault location technique is presented. This method of fault location is similar to adaptive and fuzzy based fault location, which is described in section 5.2 except that here the wavelet transform is used to reduce the

waveform into multi scales and then only a low pass scale is selected to be processed with the adaptive filter. The output of the adaptive filter (i.e. the error waveform) is analysed in the same way as in the adaptive and fuzzy based fault location technique to find the fault location.

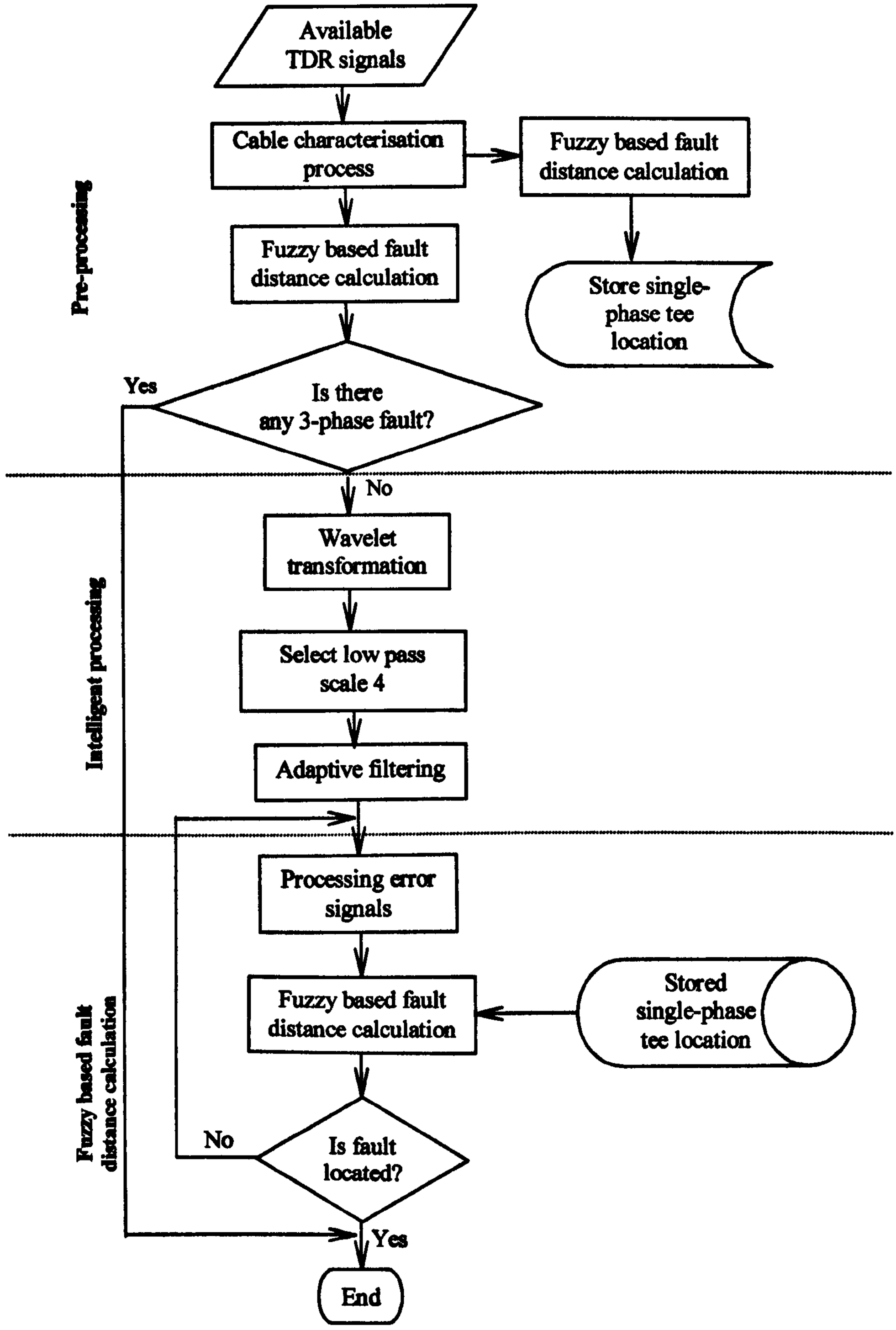

Figure 6.18: An overview flowchart for wavelet enhanced fault location

6.3.1. System Overview

An overview flowchart for this method is shown in Fig. 6.18. First, waveforms are pre-processed, as described in section 5.3, to locate 3-phase faults and to identify single-phase tees. If no 3-phase fault is detected then the WT is applied to the TDR waveforms in four scales. Low pass scale four is selected and the faulty phase waveform, together with a healthy phase waveform (or a reference waveform of the faulty phase in a healthy state), are then processed with the adaptive filter to produce an error waveform. The adaptive filtering process is the same as that described in section 5.4. The error waveforms are then analysed, as described in section 5.4, to find the fault location. Finally, the fault distance is calculated using the fault distance calculation process, described in section 5.5.

6.3.2. An Alternative Wavelet Transformation

Following pre-processing, if no 3- phase fault is located, the TDR waveforms are processed with a wavelet transform using Mallat [9] filter banks to produce 4 scales of low and high pass waveforms. After the wavelet transformation, low pass scale 4 waveforms are selected for processing with the adaptive filter.

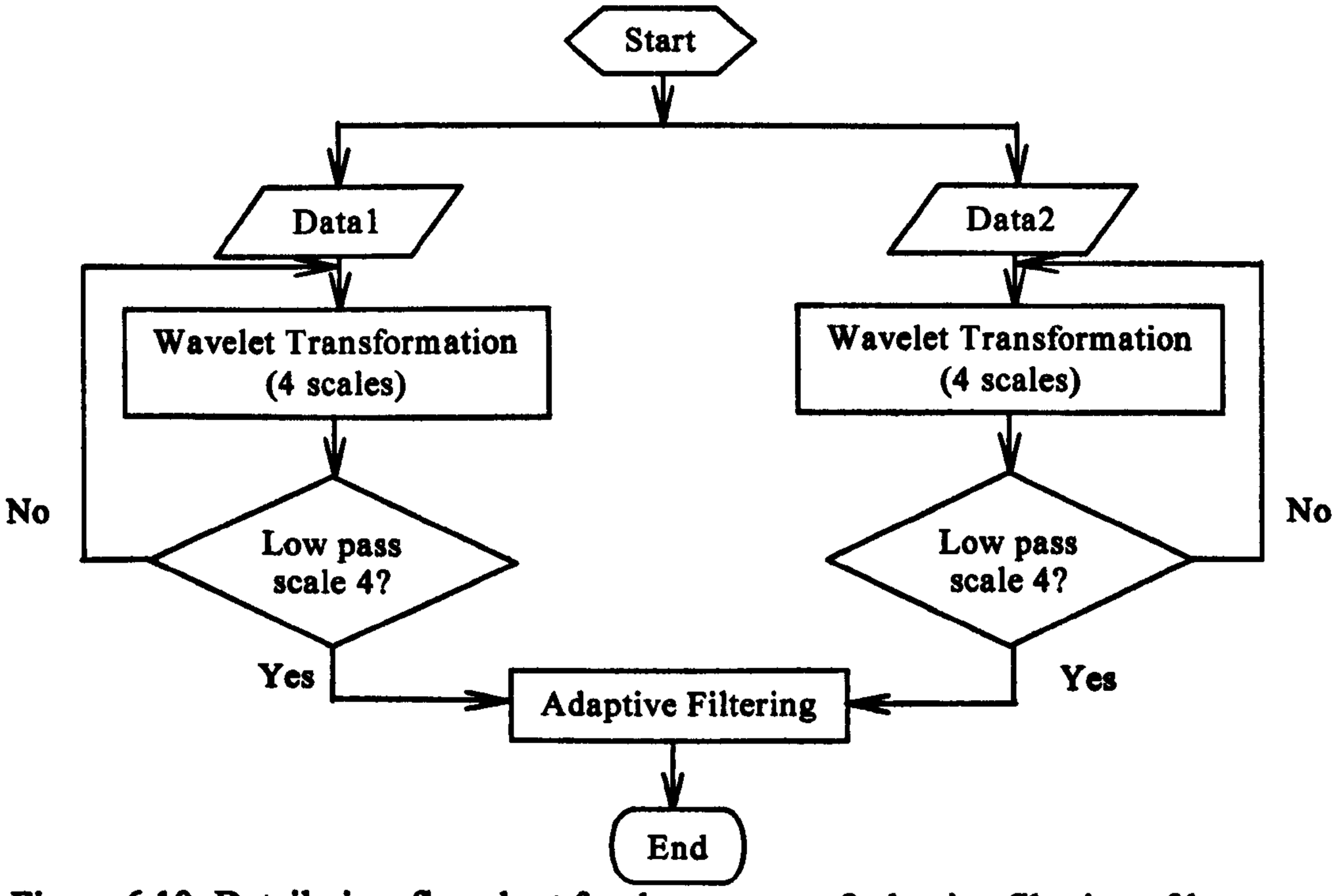

Figure 6.19: Detail view flowchart for the process of adaptive filtering of low pass scale 4

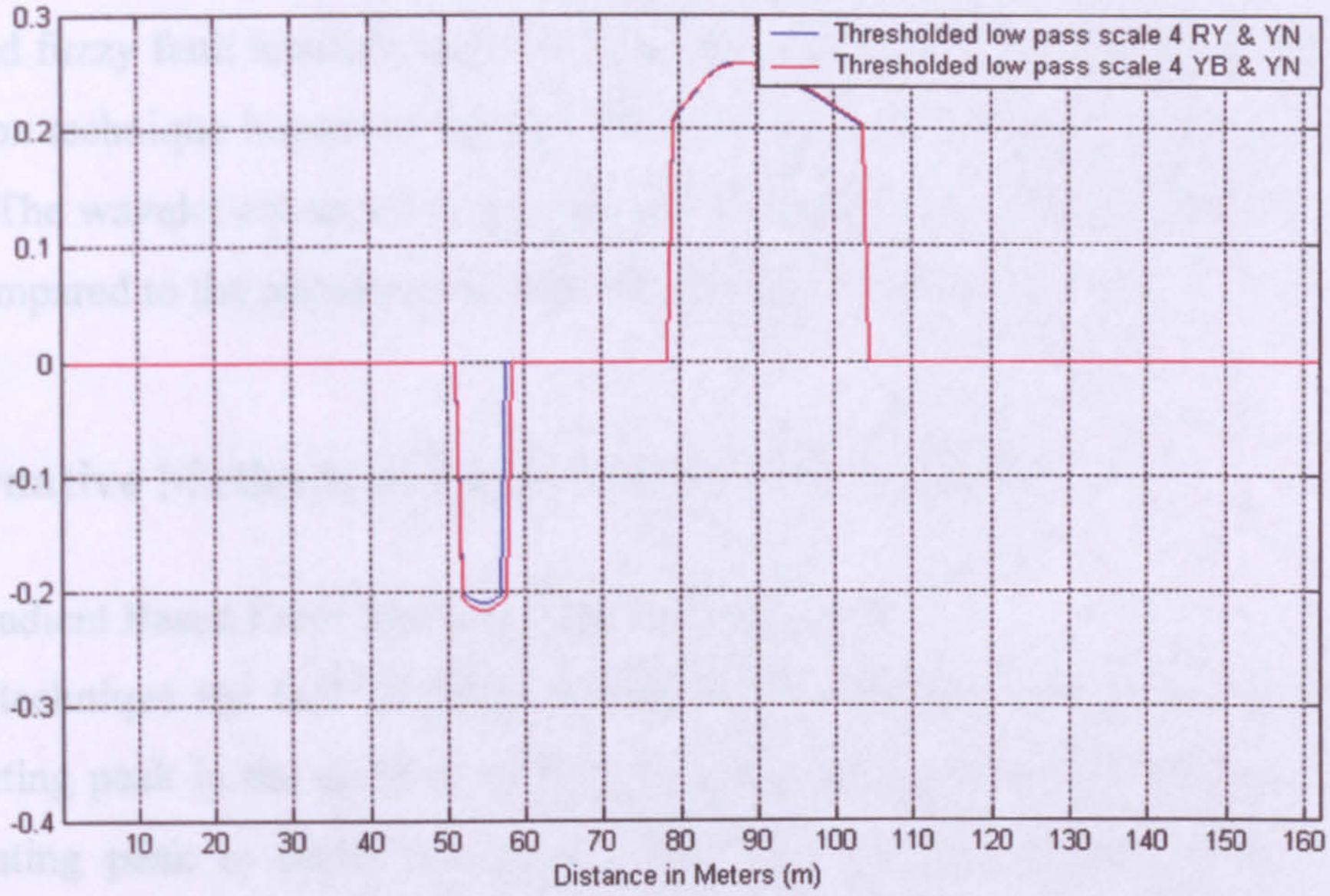

Figure 6.20: Scale 4 thresholded error waveforms between RY & YN and YB & YN

A detail view flowchart for the adaptive filtering of the selecting low pass scale four is shown in Fig. 6.19. This flowchart shows only two TDR waveforms being processed, but normally 3 or 5 TDR waveforms will be used depending on how many TDR waveforms are available, as described in chapter 4.

The outputs of the adaptive filter (low pass scale 4 error waveforms) are then thresholded with 0.2. The resulting waveforms are shown in Fig. 6.20. The threshold value 0.2 is chosen based on the results that were obtained for data sets 1, 2, 3, 4, and 6. The fault distance calculation process, described in section 5.5, produces the final result. For data set 6, the average between the two fault distances is taken as the fault distance.

Data Label	Actual Fault Distance (m)	Fault Distance by Adaptive Method (m)	Fault Distance by Wavelet Method (m)
Data set 1	33.0	33.2	32.4
Data set 2	65.5	63.7	63.0
Data set 3	10.8	10.8	9.7
Data set 4	45.0	43.9	34.3
Data set 5	19.6	23.9	23.9
Data set 6	35.6	39.6	34.4

Table 6.6 Fault distance comparisons between the wavelet and adaptive methods

Table 6.6 shows the comparison of results between the wavelet enhanced and the adaptive and fuzzy fault location systems. The table shows that the wavelet enhanced fault location technique improved the data set 6 result, but produced a poor result for data set 4. The wavelet enhanced technique also produced less accuracy for data sets 1, 2 & 3 compared to the adaptive and fuzzy based fault location system.

6.4. Alternative Methods of Fault Distance Calculation

6.4.1. A Gradient Based Fault Distance Calculation Method

In this technique the fault distance is determined using the zero crossing of the fault-indicating peak in the error waveform. In some cases, the rate of change of the fault indicating peak is stable for some period due to a DC offset in the TDR waveform. This stable period in the fault indicating peak waveform will cause an error in the fault distance calculation. To minimise this error, the gradient of the fault indicating peak is calculated from the peak until a 50% change in the gradient is identified. Once the change in gradient is found then the gradient value is applied to the fault indicating peak from that point of change onwards until the next zero crossing. After identifying the zero crossing point calculated the fault distance is calculated. The flowchart for this technique is shown in Fig. 6.21.

Taking the low pass scale 4 of data set 4,shown in Fig. 6.16 it can be seen that the fault indicating peak starts at about 54m and then decreases steadily up to 45m. After 45m the fault indicating peak waveform changes in slope significantly which delays the zero crossing point. Therefore, the fault distance is calculated to be 34.3m (Table 6.5). However, if the above gradient is calculated to the initial slope of the fault-indicating peak and if any significant changes in slope occur before it crosses zero then by applying this gradient the result can be improved. When this technique was applied to data set 4 in the wavelet enhanced fault location method it produced a fault distance of 44m, i.e. an improvement in the result of 9.7m. Similarly, when the technique was applied to the adaptive and fuzzy based fault location method using data set 4 it produced a fault distance of 45.5m, i.e. an improvement of 0.6m in the fault location.

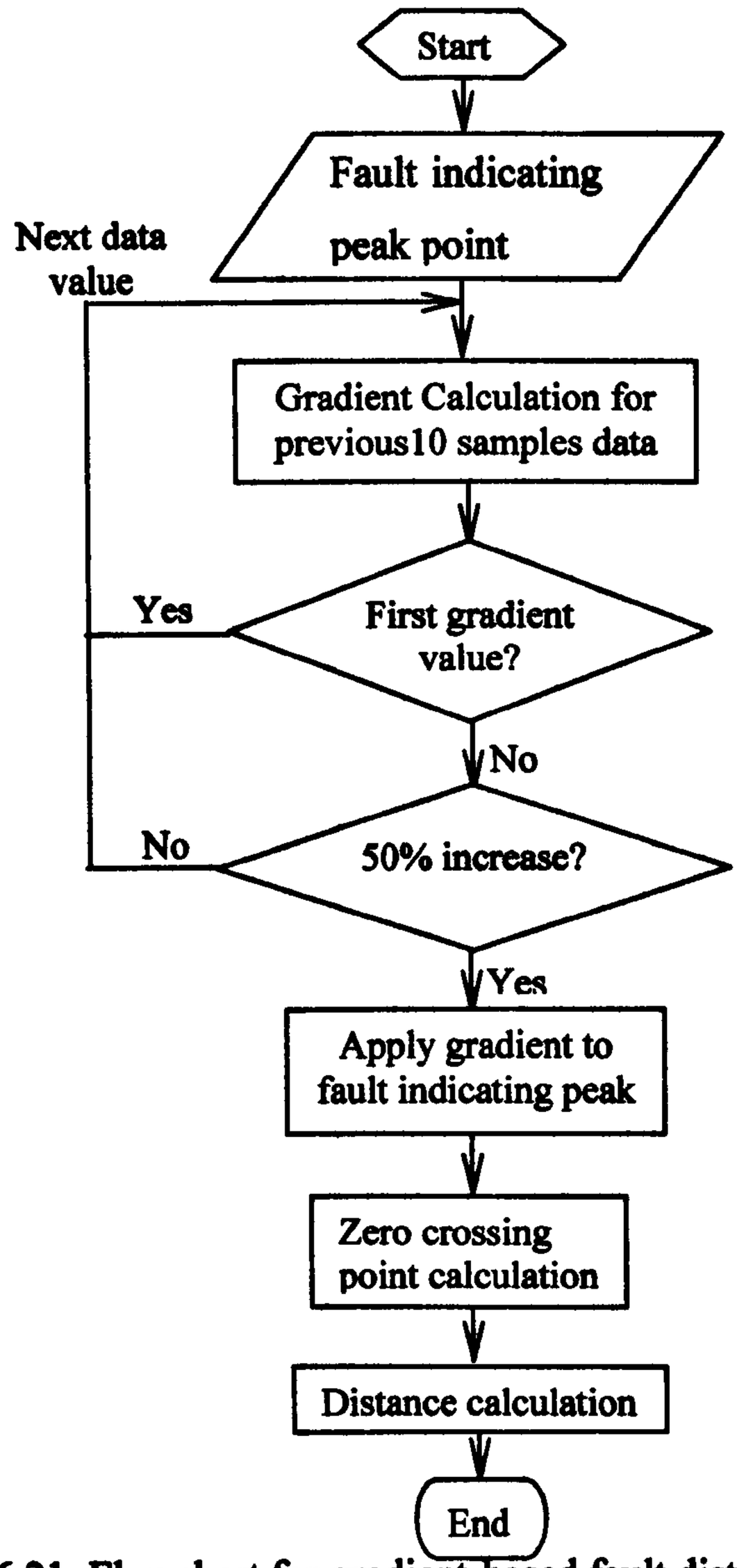

Figure 6.21: Flowchart for gradient-based fault distance calculation

6.4.2. Local Mean Based Fault Distance Calculation

In the fault distance calculation, the point at which the error waveform crosses the zero line is used to calculate the fault distance. However, TDR waveforms contain high frequency components caused by noise and discontinuities in the cable (other than the fault) and therefore the point at which the error waveform crosses the zero line can be 'displaced' resulting in an incorrect fault distance. This problem can be minimised if the 'local mean' of the error curve is used to estimate the point of zero crossing. Fig. 6.22 shows the flowchart for the local mean based fault distance calculation. The local mean is calculated for a period of 5 samples before the zero (distance-axis) crossing point and 5 samples after (i.e. 11 samples in total). The

intersection of the local mean and the zero axis is then calculated and the result used to determine the fault distance.

This approach was applied to all data sets and Table 6.7 shows the comparison between the local mean and zero (distance-axis) crossing based fault distance calculation for both adaptive and fuzzy based fault location systems. The table shows that using the local mean has improved the accuracy of fault distance for data sets 3 and 6 but reduced the accuracy for data set 2 whilst the others are unchanged.

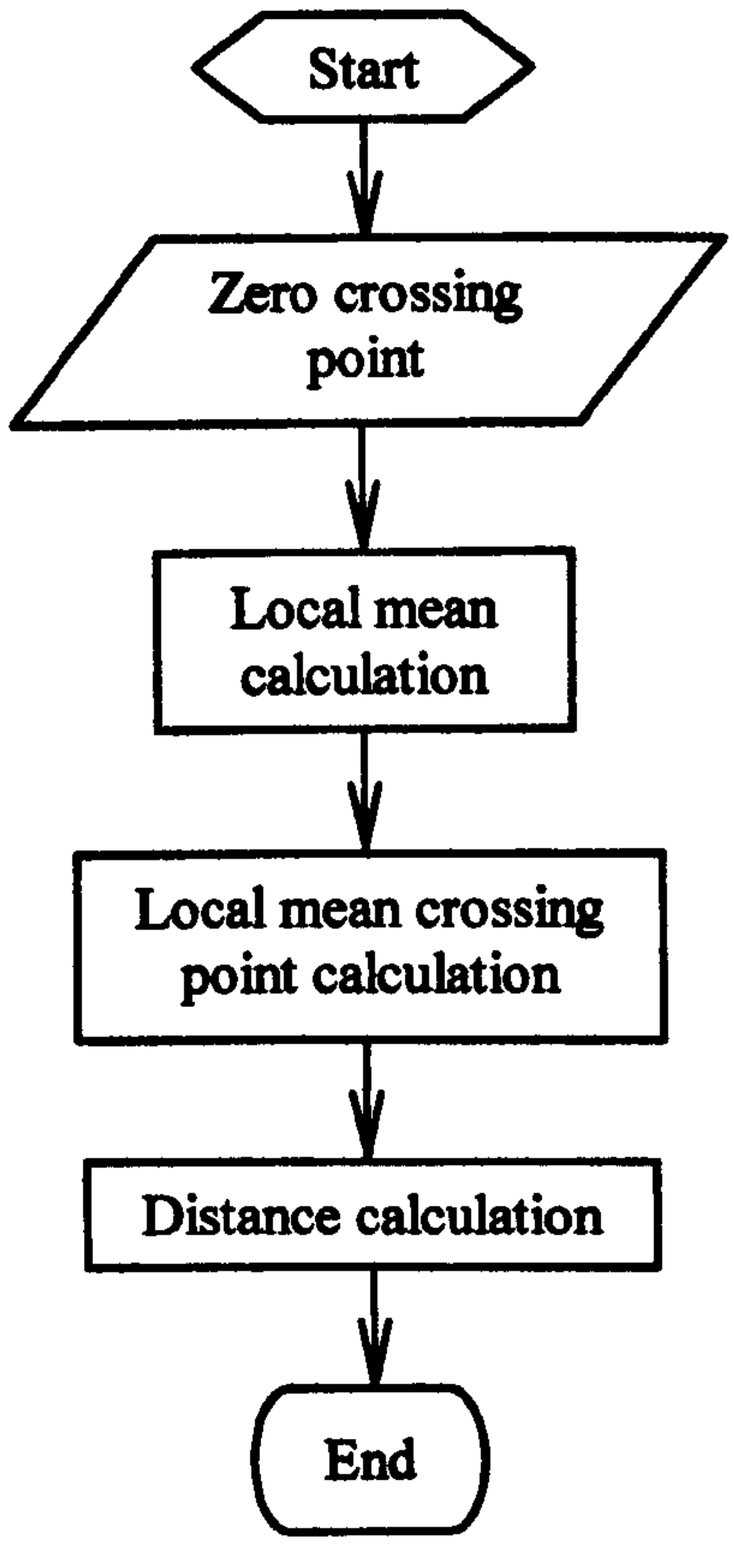

Figure 6.22: Flowchart for local mean based fault distance calculation

Data Label	Actual Fault Distance (m)	Fault Distance using Zero (Distance-axis) crossing (m)	Fault Distance using Local mean crossing (m)
Data set 1	33.0	33.2	33.2
Data set 2	65.5	63.7	62.7
Data set 3	10.8	10.6	10.8
Data set 4	45.0	43.9	43.9
Data set 5	19.6	23.9	23.9
Data set 6	35.6	39.6	35.6

Table 6.7: Fault distance comparisons between the local mean and zero crossing based fault distance calculation methods

6.5. Conclusion

In this chapter, a new wavelet enhanced fault location and alternative methods of fault distance determination are presented. In this system the data is pre-processed using wavelets prior to adaptive filtering which is now carried out in the multiresolution domain. After the wavelet transformation, in fact only the low pass scale 4 is selected for processing by the adaptive filter and thereafter the routines are the same as those used for the system described in chapter 5. When compared with the adaptive and fuzzy based fault location system, the system described in this chapter gives a better result for data set 6, but slightly worse results for data sets 1, 2, 3, and 4.

To improve the accuracy of fault distance calculation in this method, a high pass scale error waveform could be used in conjunction with a low-pass scale waveform. These would together provide better time resolution compared with low-pass scaling alone.

A gradient method is described to improve the accuracy of the fault distance calculation for both methods of fault location. This produced improvements in the results for data set 4 for both methods of fault location. However, the performance of this technique needs to be tested on many more sets of data.

To improve fault distance calculation accuracy, in the adaptive and fuzzy based fault location system, a local mean crossing point method was examined. This method generally exhibited improved results.

Chapter 7

7. Conclusions and Future Directions

7.1. Conclusions

This thesis has been concerned with the development of an automatic fault location system for LVUDN using the TDR waveforms. The original contributions developed in the course of this research work include: automating part of the TDR waveform acquisition process, an automatic adaptive and fuzzy based fault location system using TDR waveforms, and an automatic fault location system using wavelet transform.

The automation of TDR waveform acquisition includes: auto test lead connection check, auto balancing, auto blown fuse and backfeed checks, selection of the appropriate TDR waveforms to record, and auto voltage and current triggering. The auto test lead connection process detects whether the user has connected the test leads properly and reports a message to the user accordingly. In earlier instruments adjusting the setting of the balance network to match the cable surge impedance and to compensate for the effects of the test leads was always done manually. This process has been automated to minimise user interaction. The auto selection of TDR waveforms to be recorded is based on which fuses ruptured and whether there are any backfeeds. Previously the user would use test lamps to check which fuses are blown and then manually select the appropriate TDR waveforms to be recorded. The fuse blown and backfeed checks are automated and the TDR waveforms are recorded automatically, according to which fuses are blown and which phases have a backfeed. For transient fault location, voltage and current triggering are used to record TDR waveforms before and during the fault arcing process. Previously the voltage and current trigger level were set by the user but in the P2000 this is automated. A detailed description of the automation of the TDR waveform acquisition process is given in chapter 4.

The most significant developments of the automatic system are: the use of pre-processing to identify single phase tees and to locate 3-phase faults, adaptive filtering

of 2 TDR waveforms to produce a difference signal that will have an easily identified feature at the fault point, and the use of fuzzy membership to calculate the fault distance. Human experts usually try to locate a fault by looking for a departure in the TDR waveforms produced by the fault. This departure may not be clear due to noise, attenuation, and dispersion. A human observer may also confuse a single phase tee with the fault. Therefore, identifying single-phase tees before processing the TDR waveforms enables differentiation between the reflections from any single-phase tees and the reflection from the fault.

3-phase faults will have a reflection on all TDR waveforms with the same polarity and similar amplitude. Therefore a 3-phase fault may be confused with the reflection from a 3-phase tee if the fault is a short circuit. Another problem with 3-phase faults is that the difference between the waveforms will be almost zero. Therefore, 3-phase faults are located during the pre-processing. A detailed explanation of this process is given in section 5.3.

In trying to subtract two TDR waveforms the difference waveform may not show an obvious difference at the fault point due to attenuation, dispersion and noise. Therefore adaptive filtering is used to produce a difference waveform between the two TDR waveforms so that the difference (error) waveform will show a significant difference at the fault point. If only one fuse is blown then only the three TDR waveforms related to the faulty phase will be available. Therefore at the fault point there will not be a significant difference. This makes it more difficult to locate faults when using conventional methods but the adaptive filtering method has demonstrated that it is possible to locate faults automatically using the limited data available. With conventional methods the fault distance is calculated manually but this has now been automated following the adaptive filtering process. A detailed explanation of the above process is given in section 5.4.

In 3-phase fault location, there will be six TDR waveforms involved but each may indicate slightly different fault distances due to attenuation and dispersion. Similarly, if there is more than one error (difference) waveform produced by the adaptive filtering process there will be more than one fault distance. Therefore a simple method of calculating a common fault distance would be to take the average of all the fault distances but this is hardly an ideal solution. Therefore, fuzzy membership is used to calculate the common fault distance. The automatic adaptive based fault location

system minimises requirements for operator expertise. A detailed explanation of the processes are given in section 5.5.

In section 6.3, a wavelet enhanced fault location method is developed as an alternative to the adaptive based fault location method. This technique was found to improve the accuracy for one set of data whilst for the other sets it produced results close to the actual fault distance. The technique is the same as the adaptive filtering based fault location method other than that the wavelet transform is used to reduce the TDR waveforms into multi-scales of frequency components. Then the optimum low pass scale (4) waveform can be selected and processed with adaptive filtering. By selecting low frequency scale 4 as significant reduction in unwanted reflections and noise can be achieved. Applying adaptive filtering to individual scales allows the waveforms to be processed in limited frequency bands thereby reducing the effects of dispersion. The error (difference) waveform of the low pass scale 4 is then processed in the same way as the adaptive based fault location error waveform to find the fault distance. This method improved the result for one set of data compared to adaptive based fault location, but the disadvantage of selecting low pass scale 4 is that it gives poor time resolution and therefore a less accurate fault distance. However, the advantage of selecting low pass scale 4 is that it does give good frequency resolution and therefore the reflection of the fault is clearer.

To improve the accuracy of fault distance calculation for both methods of fault location systems a gradient based fault distance calculation method is presented in section 6.4.1. A local mean based fault distance calculation method for the adaptive and fuzzy based fault location systems to improve the accuracy of fault distance calculation is presented in section 6.4.2.

In this thesis an automated data acquisition system, and two automatic fault location systems are presented. The performance of the automated fault location systems were tested with both field and model data.

7.2. Directions for Future Research

In all PhD research work there will always be further improvements that could be made if more time was available. The following suggestions are therefore presented for further investigation in future work.

The P2000 incorporates voltage triggering for transient faults. It monitors all three phases all the time but the current trigger monitors only one phase. Current triggering on all three phases would provide higher reliability and additional information regarding the behaviour of the fault.

The adaptive filter parameters that were used in the wavelet enhanced fault location method were the optimised parameter values for the adaptive based fault location method. Further study into the optimum parameter selection for the wavelet enhanced fault location systems may produce improved results. The wavelet enhanced fault location system gives a clear indication of the fault, but with less accuracy compared to the adaptive and fuzzy based fault location systems because it uses low pass scale 4. Further investigation into the use of high pass scales may improve accuracy as they would give better time resolution.

Both automated systems were tested on a limited selection of data and it is essential that many more tests are preformed to check the robustness of the methods.

In radar applications, "pulse compression" has been successfully used to acquire good reflections. This technique should be tried for LVUDN fault location to determine if better fault reflections can be obtained. The automatic fault location systems have only been tested on LVUDN cables. Investigations are needed to see whether the methods could be applied to fault location on MV and HV power cables and also telecommunication cables.

The automatic fault location methods presented in this research are intended for permanent and transient TDR based fault location systems only. For transient fault location, TDR based fault location will give accurate results provided the pulse is injected when the fault is arcing and the fault resistance is low. Initially, transient faults start with a high resistance which then becomes a low resistance. It can take a long time before a transient fault becomes a low resistance, therefore an alternative method to TDR should be considered. Transient faults much more troublesome than permanent faults but they are often the precursors to permanent faults. Transient faults therefore merit further study since if they can be detected and located at an early stage many permanent faults could be prevented.

Appendix-A

Optimisation of Adaptive Filter Parameters

In appendix-A, the optimisation results using three adaptive algorithms (LMS, NLMS, and RLS) for data sets 1, 2, 3, 4, and 6 are given. Optimisation was not applied to data set 5, as it was an open circuit fault. During the optimisation process the threshold value 0.3 was applied to all algorithms. In the tables, '*' indicates that there was no distance and '+' that there was no peak after thresholding the error signal (the output of the adaptive filter). The fault distances that are highlighted in the tables are the best results for each data set. The best results are defined to be those where the calculated distance is closest to the actual fault distance and also has the maximum absolute peak. The results in bold in the RLS algorithm tables are the best results for each data set with a particular common parameter set (λ=0.996 and w=7). For data set 6, RY, YB and YN TDR waveforms are available for processing. It is necessary to process these as the pairs RY & YN and YB & YN, since the fault is between the Yellow phase and Neutral. The results of the LMS shown in table A13 and A14 show that parameter values for both are the same. However, The NLMS results show (Table A15 and A16) the number of weights for both is the same, but the adaptation constant is different. The optimum results for RY & YN were obtained when the adaptation constant is 0.3. The optimum results for YB & YN were obtained when adaptation constant was 0.2, but an adaptation constant of 0.3 gave the same fault distance (51.8m). The only difference was the peak value, which differed by 0.0003. Therefore, the results for the parameter value 0.3 are taken to be the optimum.

It can be seen in the tables that for three data sets, the LMS and NLMS algorithms did not give a full set of results for all parameters, due to thresholding. If the threshold value is smaller than 0.3 then these two algorithms will give better results. For example, if the threshold value is 0.1 for LMS and 0.2 for NLMS algorithm, for data set 1, then they produce a better result as shown in Table A19 and A20 respectively. The disadvantage of using a small threshold value is that when trying to apply the algorithm to phase to phase data with phase to Neutral data and the phase-to-neutral data has a single phase tee (service tee), improper balancing may produce a peak in the error signal (output of the filter). This peak is smaller in magnitude than the peak

that indicates the fault distance. Using a smaller threshold value may indicate this distance as the fault distance, if this single phase tee location was not identified during the pre-processing stage. Using larger threshold values can minimise this problem. It can be seen on both tables that the results have been improved, but at the same time in some cases the results are worse.

In some cases the balancing was not applied properly, this is because the data were recorded by field engineers. Therefore, at the beginning of the data there will be some difference that may produce a peak in the error signal. This may cause inaccurate fault distance calculation. This can be seen in Table A11 for the NLMS results of data set 4. This problem can be overcome by ignoring any calculated fault distance within the first 5m and taking the next fault distance. Table A21 shows that ignoring the first fault distance (0.2m) improves the results of the NLMS significantly.

The results show that the RLS algorithm performs well compared to the other two (LMS and NLMS) algorithms. For data set 6, processing with the RLS algorithm gave the same fault distance for both RY & YN and YB & YN, whereas the other two algorithms gave different values. In this case, the average value is taken to be their optimum value.

	μ = 0.1		μ = 0.2		μ = 0.3		μ = 0.4		μ = 0.5	
w	Abs(P)	D (m)	Abs(P)	D (m)	Abs(P)	D (m)	Abs(P)	D (m)	Abs(P)	D (m)
1	+	*	+	*	+	*	+	*	+	*
2	+	*	+	*	+	*	+	*	+	*
3	+	*	+	*	+	*	+	*	+	*
4	+	*	+	*	+	*	+	*	+	*
5	+	*	+	*	+	*	+	*	+	*
6	+	*	+	*	+	*	+	*	+	*
7	+	*	+	*	+	*	+	*	+	*
8	+	*	+	*	+	*	+	*	+	*
9	+	*	+	*	+	*	+	*	+	*
10	+	*	+	*	+	*	+	*	+	*
	μ = 0.6		μ = 0.7		μ = 0.8		μ = 0.9		μ = 1.0	
w	Abs(P)	D (m)	Abs(P)	D (m)	Abs(P)	D (m)	Abs(P)	D (m)	Abs(P)	D (m)
1	+	*	+	*	0.3917	49.3	0.3278	3.0	0.5188	3.0
2	+	*	0.3268	32.6	0.3996	32.8	0.5133	32.8	0.3410	3.2
3	+	*	+	*	+	*	0.3643	17.5	0.3158	4.0
4	+	*	+	*	+	*	+	*	0.3299	3.5
5	+	*	+	*	+	*	+	*	0.3103	3.7
6	+	*	+	*	+	*	+	*	0.3173	4.0
7	+	*	+	*	+	*	+	*	0.3778	34.4
8	+	*	+	*	+	*	+	*	0.3351	31.7
9	+	*	+	*	+	*	+	*	0.3008	41.2
10	+	*	+	*	+	*	+	*	+	*

Table A.1 LMS result for data set 1

	$\hat{\mu}$ = 0.1		$\hat{\mu}$ = 0.2		$\hat{\mu}$ = 0.3		$\hat{\mu}$ = 0.4		$\hat{\mu}$ = 0.5	
w	Abs(P)	D (m)	Abs(P)	D (m)	Abs(P)	D (m)	Abs(P)	D (m)	Abs(P)	D (m)
1	0.5723	30.9	0.5255	31.9	0.4914	32.3	0.4561	33.2	0.4286	33.2
2	0.5292	32.1	0.4617	32.3	0.4092	33.2	0.3593	33.2	0.3255	33.2
3	0.5038	32.3	0.4169	33.2	0.3491	33.2	0.3055	33.2	+	*
4	0.4764	32.5	0.3773	33.2	0.3122	33.2	+	*	+	*
5	0.4536	32.6	0.3490	33.2	+	*	+	*	+	*
6	0.4372	33.2	0.3267	32.7	+	*	+	*	+	*
7	0.4226	33.2	0.3084	32.7	+	*	+	*	+	*
8	0.4096	32.8	+	*	+	*	+	*	+	*
9	0.3981	32.9	+	*	+	*	+	*	+	*
10	0.3878	32.8	+	*	+	*	+	*	+	*
	$\hat{\mu}$ = 0.6		$\hat{\mu}$ = 0.7		$\hat{\mu}$ = 0.8		$\hat{\mu}$ = 0.9		$\hat{\mu}$ = 1.0	
w	Abs(P)	D (m)	Abs(P)	D (m)	Abs(P)	D (m)	Abs(P)	D (m)	Abs(P)	D (m)
1	0.4008	33.2	0.3737	33.2	0.3514	33.2	0.3324	33.2	0.3175	33.2
2	0.3013	33.2	+	*	+	*	+	*	+	*
3	+	*	+	*	+	*	+	*	+	*
4	+	*	+	*	+	*	+	*	+	*
5	+	*	+	*	+	*	+	*	+	*
6	+	*	+	*	+	*	+	*	+	*
7	+	*	+	*	+	*	+	*	+	*
8	+	*	+	*	+	*	+	*	+	*
9	+	*	+	*	+	*	+	*	+	*
10	+	*	+	*	+	*	+	*	+	*

Table A.2 NLMS result for data set 1

	λ = 0.991		λ = 0.992		λ = 0.993		λ = 0.994		λ = 0.995	
w	Abs(P)	D (m)	Abs(P)	D (m)	Abs(P)	D (m)	Abs(P)	D (m)	Abs(P)	D (m)
1	+	*	+	*	0.3098	33.2	0.3493	33.2	0.3905	33.2
2	+	*	+	*	0.3236	33.2	0.3619	33.2	0.4015	33.2
3	+	*	+	*	0.3310	33.2	0.3688	33.2	0.4076	33.2
4	+	*	0.3020	33.2	0.3313	33.2	0.3664	33.2	0.4024	33.2
5	+	*	0.3074	33.2	0.3333	33.2	0.3633	33.2	0.4018	33.2
6	+	*	0.3141	33.2	0.3390	33.2	0.3647	33.2	0.4064	33.2
7	0.3031	33.2	0.3214	33.2	0.3445	33.2	0.3685	33.2	0.4007	33.2
8	0.3117	33.2	0.3300	33.2	0.3505	33.2	0.3734	33.2	0.4089	32.8
9	0.3189	33.2	0.3376	32.9	0.3569	32.9	0.3785	32.9	0.4082	32.9
10	0.3259	33.2	0.3450	33.0	0.3647	33.0	0.3846	33.0	0.4099	33.0
	λ = 0.996		λ = 0.997		λ = 0.998		λ = 0.999		λ = 1.000	
w	Abs(P)	D (m)	Abs(P)	D (m)	Abs(P)	D (m)	Abs(P)	D (m)	Abs(P)	D (m)
1	0.4316	33.2	0.4727	33.2	0.5184	33.2	0.5599	33.2	0.6085	33.2
2	0.4408	33.2	0.4799	33.2	0.5241	33.2	0.5644	33.2	0.6064	33.2
3	0.4459	33.2	0.4836	33.2	0.5272	33.2	0.5668	33.2	0.6014	33.2
4	0.4429	33.2	0.4877	33.2	0.5303	33.2	0.5691	33.2	0.6030	33.2
5	0.4462	33.2	0.4902	33.2	0.5322	33.2	0.5704	33.2	0.6039	33.2
6	0.4497	33.2	0.4928	33.2	0.5339	33.2	0.5715	33.2	0.6044	33.2
7	**0.4456**	**33.2**	0.4906	33.2	0.5336	33.2	0.5728	33.2	0.6079	33.2
8	0.4513	32.8	0.4938	32.8	0.5347	32.8	0.5722	32.8	0.6097	32.8
9	0.4510	32.9	0.4938	32.9	0.5348	32.9	0.5723	32.9	0.6051	32.9
10	0.4537	33.0	0.4976	33.0	0.5394	33.0	0.5774	33.0	0.6106	33.0

Table A.3 RLS result for data set 1

	μ = 0.1		μ = 0.2		μ = 0.3		μ = 0.4		μ = 0.5	
w	Abs(P)	D (m)	Abs(P)	D (m)	Abs(P)	D (m)	Abs(P)	D (m)	Abs(P)	D (m)
1	0.3936	5.9	0.5433	5.3	0.7098	5.3	0.8698	5.3	1.0253	5.3
2	0.5083	125.6	0.3185	117.0	0.3408	86.5	0.3025	86.3	0.4371	86.3
3	0.4118	125.6	0.3824	117.2	0.3726	117.2	0.3294	118.1	0.3031	118.1
4	0.3243	125.6	0.3675	117.0	0.3880	117.3	0.3742	117.3	0.3433	117.0
5	+	*	0.3181	117.3	0.3594	117.2	0.3579	117.2	0.3361	117.0
6	+	*	+	*	+	*	0.3007	117.2	0.3276	128.4
7	+	*	+	*	+	*	+	*	+	*
8	+	*	+	*	+	*	+	*	+	*
9	+	*	+	*	+	*	+	*	+	*
10	+	*	+	*	+	*	+	*	+	*
	μ = 0.6		μ = 0.7		μ = 0.8		μ = 0.9		μ = 1.0	
w	Abs(P)	D (m)	Abs(P)	D (m)	Abs(P)	D (m)	Abs(P)	D (m)	Abs(P)	D (m)
1	1.1772	5.3	1.3265	5.3	0.3143	0.3	0.3358	0.3	0.3411	0.3
2	0.5701	86.5	0.3411	7.8	0.4778	7.8	0.3221	4.3	0.6048	4.3
3	0.4288	129.0	0.4792	129.0	0.3358	86.6	0.3066	86.6	0.3369	4.3
4	0.3153	118.1	0.3001	118.1	0.3650	126.6	0.3610	118.6	0.3501	1.0
5	0.3109	117.0	0.3038	117.0	0.3551	118.3	0.4205	118.3	0.3444	1.3
6	0.3680	128.4	0.3818	128.9	0.4316	128.9	0.3045	118.5	0.3098	2.5
7	+	*	0.3148	128.5	0.4034	129.0	0.5021	129.0	0.3045	2.5
8	+	*	0.3527	145.9	0.4023	145.9	0.4298	146.7	0.3486	5.4
9	+	*	0.3121	147.2	0.3180	147.2	+	*	0.4169	6.8
10	+	*	+	*	+	*	0.3286	149.8	0.3041	6.1

Table A.4 LMS result for data set 2

	$\hat{\mu}$ = 0.1		$\hat{\mu}$ = 0.2		$\hat{\mu}$ = 0.3		$\hat{\mu}$ = 0.4		$\hat{\mu}$ = 0.5	
w	Abs(P)	D (m)	Abs(P)	D (m)	Abs(P)	D (m)	Abs(P)	D (m)	Abs(P)	D (m)
1	0.6089	4.5	0.5478	4.5	0.4977	4.5	0.4584	4.5	0.4220	4.5
2	0.5642	4.5	0.4840	4.5	0.4214	4.5	0.3698	4.5	0.3367	4.5
3	0.5373	4.5	0.4483	4.5	0.3766	4.5	0.3346	4.5	0.3054	4.5
4	0.5204	4.5	0.4242	4.5	0.3551	4.5	0.3160	4.5	0.3463	62.9
5	0.5111	4.5	0.4085	4.5	0.3444	4.5	0.3072	4.5	0.3161	62.9
6	0.5045	4.5	0.3975	4.5	0.3377	4.5	0.3013	4.5	+	*
7	0.5004	4.5	0.3925	4.5	0.3331	4.5	0.3019	63.0	+	*
8	0.4978	4.5	0.3892	4.5	0.3301	4.5	+	*	+	*
9	0.4959	4.5	0.3871	4.5	0.3279	4.5	+	*	+	*
10	0.4947	4.5	0.3855	4.5	0.3267	4.5	+	*	+	*
	$\hat{\mu}$ = 0.6		$\hat{\mu}$ = 0.7		$\hat{\mu}$ = 0.8		$\hat{\mu}$ = 0.9		$\hat{\mu}$ = 1.0	
w	Abs(P)	D (m)	Abs(P)	D (m)	Abs(P)	D (m)	Abs(P)	D (m)	Abs(P)	D (m)
1	0.3883	4.5	0.3613	4.5	0.3436	4.5	0.3266	4.5	0.3124	4.5
2	0.3129	4.5	0.3890	63.0	0.3728	63.0	0.3578	63.0	0.3438	63.0
3	0.3591	63.0	0.3384	63.0	0.3195	63.0	0.3020	63.0	+	*
4	0.3208	62.9	+	*	+	*	+	*	+	*
5	+	*	+	*	+	*	+	*	+	*
6	+	*	+	*	+	*	+	*	+	*
7	+	*	+	*	+	*	+	*	+	*
8	+	*	+	*	+	*	+	*	+	*
9	+	*	+	*	+	*	+	*	+	*
10	+	*	+	*	+	*	+	*	+	*

Table A.5 NLMS result for data set 2

	λ = 0.991		λ = 0.992		λ = 0.993		λ = 0.994		λ = 0.995	
w	Abs(P)	D (m)	Abs(P)	D (m)	Abs(P)	D (m)	Abs(P)	D (m)	Abs(P)	D (m)
1	0.4446	63.0	0.4622	63.0	0.4791	63.0	0.4949	63.0	0.5091	63.0
2	0.4448	63.0	0.4624	63.2	0.4794	63.7	0.4952	63.7	0.5095	63.0
3	0.4447	62.7	0.4624	62.7	0.4794	62.7	0.4952	62.7	0.5095	62.5
4	0.4447	62.9	0.4624	62.9	0.4793	62.7	0.4951	62.5	0.5094	62.5
5	0.4444	62.9	0.4619	62.7	0.4787	62.7	0.4944	62.5	0.5086	62.5
6	0.4439	62.9	0.4612	62.9	0.4779	62.7	0.4935	62.5	0.5075	62.5
7	0.4431	62.9	0.4602	62.9	0.4768	62.7	0.4923	62.7	0.5063	62.7
8	0.4425	62.9	0.4596	62.9	0.4760	62.9	0.4915	62.9	0.5055	62.9
9	0.4415	62.9	0.4585	62.9	0.4749	62.9	0.4904	62.9	0.5046	62.9
10	0.4408	62.9	0.4577	62.9	0.4742	62.9	0.4897	62.9	0.5040	62.9
	λ = 0.996		λ = 0.997		λ = 0.998		λ = 0.999		λ = 1.000	
w	Abs(P)	D (m)	Abs(P)	D (m)	Abs(P)	D (m)	Abs(P)	D (m)	Abs(P)	D (m)
1	0.5215	63.0	0.5320	63.0	0.5406	62.9	0.5475	62.9	0.5529	62.9
2	0.5219	63.0	0.5324	63.0	0.5410	63.0	0.5480	63.0	0.5536	63.0
3	0.5219	62.5	0.5324	62.5	0.5411	62.5	0.5481	62.5	0.5537	62.5
4	0.5217	62.5	0.5322	62.5	0.5409	62.5	0.5479	62.5	0.5535	62.5
5	0.5209	62.5	0.5314	62.5	0.5400	62.5	0.5471	62.5	0.5527	62.5
6	0.5198	62.5	0.5303	62.5	0.5390	62.5	0.5461	62.5	0.5519	62.5
7	**0.5186**	**62.7**	0.5292	62.7	0.5381	62.7	0.5454	62.7	0.5512	62.5
8	0.5179	62.9	0.5286	62.7	0.5376	62.7	0.5449	62.7	0.5509	62.5
9	0.5172	62.7	0.5280	62.7	0.5371	62.7	0.5446	62.7	0.5507	62.5
10	0.5167	62.7	0.5276	62.7	0.5368	62.7	0.5444	62.7	0.5506	62.7

Table A.6 RLS result for data set 2

	μ = 0.1		μ = 0.2		μ = 0.3		μ = 0.4		μ = 0.5	
w	Abs(P)	D (m)	Abs(P)	D (m)	Abs(P)	D (m)	Abs(P)	D (m)	Abs(P)	D (m)
1	0.3796	6.1	0.4227	5.7	0.3467	3.5	0.3519	2.9	0.4115	2.9
2	0.6576	28.8	0.6361	29.8	0.6305	29.8	0.3395	27.6	0.3483	8.3
3	0.6465	28.9	0.6149	28.9	0.5991	28.9	0.5882	29.9	0.5788	29.9
4	0.6345	29.0	0.5944	29.0	0.5715	29.0	0.5550	29.0	0.5413	29.0
5	0.6226	29.0	0.5748	29.0	0.5458	29.0	0.5247	28.9	0.5075	29.0
6	0.5956	29.0	0.5411	29.0	0.5076	29.0	0.4830	29.0	0.4632	28.9
7	1.3093	28.0	0.5114	29.0	0.4755	29.0	0.4498	29.0	0.4292	29.0
8	1.6525	28.0	0.4845	29.3	0.4474	29.3	0.4210	29.3	0.4001	29.3
9	1.9783	26.6	1.1285	28.9	0.4227	29.4	0.3964	29.4	0.3759	29.4
10	1.9882	26.6	1.1250	29.0	1.1810	29.0	1.2367	29.0	0.3500	29.5
	μ = 0.6		μ = 0.7		μ = 0.8		μ = 0.9		μ = 1.0	
w	Abs(P)	D (m)	Abs(P)	D (m)	Abs(P)	D (m)	Abs(P)	D (m)	Abs(P)	D (m)
1	0.4692	2.9	0.5250	2.9	0.5799	2.9	0.6355	2.9	0.6825	2.8
2	0.4166	8.3	0.4863	8.3	0.3656	6.8	0.3616	6.6	0.4307	6.2
3	0.5699	29.9	0.5615	29.9	0.3332	28.1	0.3653	28.1	0.3150	6.2
4	0.5288	29.0	0.5170	29.9	0.5053	29.9	0.4937	29.9	0.3054	7.3
5	0.4926	29.0	0.4789	29.8	0.4660	29.8	0.4536	29.8	0.3260	6.9
6	0.4460	28.9	0.4301	29.0	0.4150	29.0	0.3998	29.1	0.3158	9.6
7	0.4114	29.0	0.3951	29.0	0.3796	29.0	0.3642	28.9	0.3067	10.1
8	0.3822	29.3	0.3658	29.3	0.3503	29.3	0.3350	29.3	0.3081	13.5
9	0.3583	29.4	0.3424	29.4	0.3272	29.4	0.3121	29.4	0.3107	10.1
10	0.3309	29.5	0.3133	29.5	1.5795	30.9	0.3243	29.5	0.3066	10.1

Table A.7 LMS result for data set 3

	$\hat{\mu}$ = 0.1		$\hat{\mu}$ = 0.2		$\hat{\mu}$ = 0.3		$\hat{\mu}$ = 0.4		$\hat{\mu}$ = 0.5	
w	Abs(P)	D (m)	Abs(P)	D (m)	Abs(P)	D (m)	Abs(P)	D (m)	Abs(P)	D (m)
1	0.4224	4.9	0.3558	4.9	0.3174	4.8	0.9963	9.7	1.0225	9.3
2	0.3747	4.9	0.3084	4.8	1.0192	9.4	1.0463	9.0	1.0706	8.9
3	0.3451	4.8	0.9989	9.4	1.0365	9.0	1.0642	8.5	1.0923	8.8
4	0.3342	4.8	1.0011	9.1	1.0492	8.6	1.0849	8.4	1.1130	8.8
5	0.3318	4.8	0.3028	4.5	1.0678	8.5	1.1043	8.3	1.1325	8.8
6	0.3326	4.8	0.3088	4.5	0.3024	4.5	0.3013	4.4	0.3009	4.3
7	0.3354	4.5	0.3136	4.5	0.3065	4.5	0.3044	4.4	0.3027	4.3
8	0.3392	4.5	0.3164	4.5	0.3088	4.5	0.3047	4.4	0.3015	4.3
9	0.3431	4.5	0.3177	4.5	0.3091	4.5	0.3021	4.4	1.1232	10.5
10	0.3457	4.5	0.3158	4.5	0.3049	4.5	1.0968	9.7	1.1158	11.6
	$\hat{\mu}$ = 0.6		$\hat{\mu}$ = 0.7		$\hat{\mu}$ = 0.8		$\hat{\mu}$ = 0.9		$\hat{\mu}$ = 1.0	
w	Abs(P)	D (m)	Abs(P)	D (m)	Abs(P)	D (m)	Abs(P)	D (m)	Abs(P)	D (m)
1	1.0424	9.3	1.0578	9.7	1.0698	9.7	1.0792	9.7	1.0863	9.7
2	1.0944	9.7	1.1148	9.7	1.1327	11.5	1.1484	11.5	1.1623	11.5
3	1.1155	9.2	1.1350	9.7	1.1516	11.5	1.1658	11.5	1.1781	11.5
4	1.1357	9.3	1.1544	9.7	1.1701	11.5	1.1833	11.5	0.3015	4.0
5	1.1550	9.3	1.1735	11.6	0.3008	4.0	0.3027	4.0	0.3041	4.0
6	1.1641	9.3	1.1805	11.5	1.1938	14.9	1.2046	22.4	1.2134	22.4
7	0.3001	4.3	1.1694	14.9	1.1813	22.4	1.1909	22.4	1.1987	23.1
8	1.1468	16.1	1.1591	18.9	1.1681	22.4	1.1747	23.2	1.1794	23.2
9	1.1385	12.3	1.1497	18.9	1.1579	23.3	1.1637	23.3	1.1677	23.3
10	1.1300	11.6	1.1401	23.3	1.1473	23.3	1.1522	23.3	1.1553	23.3

Table A.8 NLMS result for data set 3

	λ = 0.991		λ = 0.992		λ = 0.993		λ = 0.994		λ = 0.995	
w	Abs(P)	D (m)	Abs(P)	D (m)	Abs(P)	D (m)	Abs(P)	D (m)	Abs(P)	D (m)
1	0.8029	9.3	0.8035	9.3	0.8102	9.3	0.8246	9.3	0.8388	9.3
2	1.0006	10.2	0.9986	10.2	0.9950	10.2	0.9902	10.2	0.9843	10.2
3	1.0813	9.7	1.0735	9.7	1.0636	9.7	1.0521	9.7	1.0394	9.7
4	1.1297	9.7	1.0983	9.7	1.0659	9.7	1.0333	9.7	1.0011	9.7
5	1.1857	10.7	1.1520	10.7	1.1174	10.7	1.0827	10.7	1.0485	10.7
6	1.0909	10.6	1.0614	10.6	1.0322	10.6	1.0037	10.6	0.9765	10.6
7	1.0562	10.6	1.0419	10.6	1.0284	10.6	1.0158	10.6	1.0043	10.6
8	1.0220	10.6	1.0100	10.6	0.9989	10.6	0.9886	10.6	0.9793	10.6
9	0.9696	10.6	0.9600	10.6	0.9511	10.6	0.9428	10.6	0.9354	10.6
10	0.9669	10.6	0.9584	10.6	0.9503	10.6	0.9429	10.6	0.9361	10.6
	λ = 0.996		λ = 0.997		λ = 0.998		λ = 0.999		λ = 1.000	
w	Abs(P)	D (m)	Abs(P)	D (m)	Abs(P)	D (m)	Abs(P)	D (m)	Abs(P)	D (m)
1	0.8529	9.3	0.8668	9.4	0.8804	9.7	0.8937	9.7	0.9068	9.7
2	0.9777	10.2	0.9707	10.2	0.9636	10.2	0.9659	10.2	0.9694	10.2
3	1.0261	9.7	1.0127	9.7	1.0097	9.7	1.0101	9.7	1.0109	10.2
4	0.9699	9.7	0.9402	9.7	0.9246	9.7	0.9257	9.7	0.9318	10.0
5	1.0157	10.7	0.9845	10.7	0.9553	10.7	0.9321	10.7	0.9370	10.7
6	0.9508	10.6	0.9279	10.6	0.9245	10.6	0.9290	10.6	0.9346	10.6
7	**0.9939**	**10.6**	0.9848	10.6	0.9768	10.6	0.9699	10.6	0.9641	10.6
8	0.9709	10.6	0.9637	10.6	0.9574	10.6	0.9520	10.6	0.9476	10.6
9	0.9288	10.6	0.9230	10.6	0.9181	10.6	0.9141	10.6	0.9125	10.6
10	0.9299	10.6	0.9246	10.6	0.9199	10.6	0.9160	10.6	0.9128	10.6

Table A.9 RLS result for data set 3

	μ = 0.1		μ = 0.2		μ = 0.3		μ = 0.4		μ = 0.5	
w	Abs(P)	D (m)	Abs(P)	D (m)	Abs(P)	D (m)	Abs(P)	D (m)	Abs(P)	D (m)
1	0.4515	21.8	0.4889	21.8	0.6122	21.6	0.7277	21.6	0.8375	21.6
2	0.3512	89.8	0.4628	89.9	0.3622	34.5	0.3327	27.6	0.3980	27.6
3	0.3063	89.8	0.3884	88.8	0.3069	32.7	0.3538	32.7	0.3680	32.7
4	+	*	+	*	0.3152	96.2	0.3071	36.0	0.3106	32.7
5	+	*	+	*	+	*	0.3269	96.2	0.3628	96.2
6	+	*	+	*	+	*	+	*	+	*
7	+	*	+	*	+	*	+	*	+	*
8	+	*	+	*	+	*	+	*	+	*
9	+	*	+	*	+	*	+	*	+	*
10	+	*	+	*	+	*	+	*	+	*
	μ = 0.6		μ = 0.7		μ = 0.8		μ = 0.9		μ = 1.0	
w	Abs(P)	D (m)	Abs(P)	D (m)	Abs(P)	D (m)	Abs(P)	D (m)	Abs(P)	D (m)
1	0.9431	22.1	1.0457	22.1	1.1464	24.6	1.2469	24.6	0.3065	6.9
2	0.3983	25.4	0.4644	25.4	0.4429	25.4	0.4018	25.4	0.3217	4.0
3	0.3032	27.6	0.3590	27.6	0.4063	27.6	0.3785	25.6	0.3093	4.6
4	0.3108	32.7	0.3152	32.7	0.3014	32.7	0.3273	58.9	0.3027	6.9
5	0.3705	96.2	0.3561	96.2	0.3016	96.2	0.3887	92.2	0.3146	5.0
6	+	*	+	*	0.3514	114.0	0.4369	114.0	0.3160	5.3
7	+	*	+	*	+	*	0.3033	130.7	0.3101	5.3
8	+	*	+	*	+	*	0.3330	126.1	0.3177	5.9
9	+	*	+	*	+	*	0.3294	125.7	0.3113	5.9
10	+	*	+	*	+	*	+	*	0.3044	5.9

Table A.10 LMS result for data set 4

	$\hat{\mu}$ = 0.1		$\hat{\mu}$ = 0.2		$\hat{\mu}$ = 0.3		$\hat{\mu}$ = 0.4		$\hat{\mu}$ = 0.5	
w	Abs(P)	D (m)	Abs(P)	D (m)	Abs(P)	D (m)	Abs(P)	D (m)	Abs(P)	D (m)
1	0.6136	0.2	0.4089	0.2	+	*	+	*	+	*
2	0.4843	0.2	+	*	+	*	+	*	+	*
3	0.4052	0.2	+	*	+	*	+	*	+	*
4	0.3665	0.2	+	*	+	*	+	*	+	*
5	0.3463	0.2	+	*	+	*	+	*	+	*
6	0.3365	0.2	+	*	+	*	+	*	+	*
7	0.3320	0.2	+	*	+	*	+	*	+	*
8	0.3294	0.2	+	*	+	*	+	*	+	*
9	0.3294	0.2	+	*	+	*	+	*	+	*
10	0.3309	0.2	+	*	+	*	+	*	+	*
	$\hat{\mu}$ = 0.6		$\hat{\mu}$ = 0.7		$\hat{\mu}$ = 0.8		$\hat{\mu}$ = 0.9		$\hat{\mu}$ = 1.0	
w	Abs(P)	D (m)	Abs(P)	D (m)	Abs(P)	D (m)	Abs(P)	D (m)	Abs(P)	D (m)
1	+	*	+	*	+	*	+	*	+	*
2	+	*	+	*	+	*	+	*	+	*
3	+	*	+	*	+	*	+	*	+	*
4	+	*	+	*	+	*	+	*	+	*
5	+	*	+	*	+	*	+	*	+	*
6	+	*	+	*	+	*	+	*	+	*
7	+	*	+	*	+	*	+	*	+	*
8	+	*	+	*	+	*	+	*	+	*
9	+	*	+	*	+	*	+	*	+	*
10	+	*	+	*	+	*	+	*	+	*

Table A.11 NLMS result for data set 4

	λ = 0.991		λ = 0.992		λ = 0.993		λ = 0.994		λ = 0.995	
w	Abs(P)	D (m)	Abs(P)	D (m)	Abs(P)	D (m)	Abs(P)	D (m)	Abs(P)	D (m)
1	0.3913	36.0	0.3964	36.0	0.4016	36.0	0.4068	36.0	0.4119	36.0
2	0.4479	39.8	0.4496	39.8	0.4515	39.8	0.4534	36.0	0.4554	36.0
3	0.4271	43.2	0.4291	39.9	0.4312	39.9	0.4335	39.9	0.4359	36.0
4	0.4377	36.0	0.4375	36.0	0.4377	36.0	0.4383	36.0	0.4393	36.0
5	0.4157	43.7	0.4168	43.7	0.4183	43.7	0.4202	43.7	0.4224	36.1
6	0.4092	43.7	0.4103	43.7	0.4119	43.7	0.4139	43.7	0.4163	43.7
7	0.4081	43.9	0.4097	43.9	0.4117	43.9	0.4141	43.9	0.4168	43.9
8	0.3829	36.5	0.3850	36.5	0.3875	36.5	0.3903	36.5	0.3933	36.5
9	0.3692	36.1	0.3710	36.1	0.3730	36.1	0.3752	36.1	0.3776	36.1
10	0.3572	36.0	0.3593	36.0	0.3615	36.0	0.3663	36.0	0.3716	36.0
	λ = 0.996		λ = 0.997		λ = 0.998		λ = 0.999		λ = 1.000	
w	Abs(P)	D (m)	Abs(P)	D (m)	Abs(P)	D (m)	Abs(P)	D (m)	Abs(P)	D (m)
1	0.4170	36.0	0.4220	36.0	0.4268	36.0	0.4315	36.0	0.4359	36.0
2	0.4574	36.0	0.4596	36.0	0.4617	36.0	0.4638	36.0	0.4659	36.0
3	0.4385	36.0	0.4411	36.0	0.4438	36.0	0.4466	36.0	0.4493	36.0
4	0.4407	36.0	0.4423	36.0	0.4441	36.0	0.4460	36.0	0.4481	36.0
5	0.4249	36.1	0.4277	36.1	0.4306	36.1	0.4336	36.1	0.4366	36.1
6	0.4190	43.7	0.4220	43.7	0.4252	43.7	0.4285	43.7	0.4318	36.1
7	**0.4197**	**43.9**	0.4228	36.0	0.4259	36.0	0.4291	36.0	0.4323	36.0
8	0.3966	36.0	0.3999	36.0	0.4034	36.0	0.4069	36.0	0.4103	36.0
9	0.3802	36.1	0.3828	36.1	0.3856	36.1	0.3884	36.1	0.3919	36.1
10	0.3777	36.0	0.3834	36.0	0.3887	36.0	0.3936	36.0	0.3982	36.0

Table A.12 RLS result for data set 4

	μ = 0.1		μ = 0.2		μ = 0.3		μ = 0.4		μ = 0.5	
w	Abs(P)	D (m)	Abs(P)	D (m)	Abs(P)	D (m)	Abs(P)	D (m)	Abs(P)	D (m)
1	0.3552	72.0	0.3892	71.2	0.4170	70.4	0.4412	70.4	0.4354	0.8
2	0.4625	71.2	0.4294	70.4	0.3885	70.4	0.3827	70.4	0.3724	70.4
3	0.4352	72.0	0.5403	71.2	0.6348	70.4	0.7411	69.6	0.3524	69.6
4	0.4392	64.7	0.5952	71.2	0.7186	70.4	0.8010	70.4	0.8536	70.4
5	0.4469	63.1	0.5839	71.2	0.6834	71.2	0.7405	71.2	0.7701	70.4
6	0.4541	61.5	0.5936	72.0	0.6660	71.2	0.6893	71.2	0.6848	71.2
7	0.4606	58.3	0.5793	54.2	0.6330	72.0	0.6402	72.0	0.6241	72.0
8	0.4609	56.6	0.5598	53.4	0.5949	72.8	0.5872	72.8	0.5608	72.8
9	0.4588	55.8	0.5415	52.6	0.5621	51.8	0.5448	51.0	0.5126	72.8
10	0.4645	55.0	0.5241	52.6	0.5325	51.0	0.5080	50.2	0.4722	50.2
	μ = 0.6		μ = 0.7		μ = 0.8		μ = 0.9		μ = 1.0	
w	Abs(P)	D (m)	Abs(P)	D (m)	Abs(P)	D (m)	Abs(P)	D (m)	Abs(P)	D (m)
1	0.5953	0.8	0.7630	0.8	0.9365	0.8	1.1134	0.8	1.2914	0.8
2	0.3580	72.8	0.3399	72.8	0.3182	75.2	0.4399	4.0	0.3487	0.8
3	0.3480	69.6	0.3414	68.8	0.3327	72.8	0.3220	73.6	0.3556	8.1
4	0.8834	70.4	0.8957	69.6	0.8949	69.6	0.8847	93.9	0.3382	89.8
5	0.7818	70.4	0.7817	70.4	0.7740	70.4	0.7615	70.4	0.7577	76.9
6	0.6678	71.2	0.6528	71.2	0.6339	71.2	0.6141	71.2	0.6185	97.1
7	0.5966	72.0	0.5634	72.0	0.5346	72.0	0.5109	72.0	0.4839	78.5
8	0.5268	72.8	0.4937	72.8	0.4681	72.8	0.4451	72.8	0.4429	72.0
9	0.4758	72.8	0.4448	72.8	0.4187	72.8	0.3952	72.8	0.3908	75.2
10	0.4359	59.9	0.4080	59.9	0.3828	72.8	0.3611	72.8	0.3660	73.6

Table A.13 LMS result for data set 6 for RY & YN

	μ = 0.1		μ = 0.2		μ = 0.3		μ = 0.4		μ = 0.5	
w	Abs(P)	D (m)	Abs(P)	D (m)	Abs(P)	D (m)	Abs(P)	D (m)	Abs(P)	D (m)
1	1.5095	0.8	1.8800	0.8	2.4120	0.8	3.1436	0.8	3.8684	0.8
2	0.5695	63.9	0.5840	72.8	0.6116	72.0	0.6603	71.2	0.3257	65.5
3	0.5678	63.1	0.5177	57.4	0.5429	76.9	0.5785	80.9	0.6028	80.9
4	0.5762	61.5	0.5463	58.3	0.5952	57.4	0.7307	76.9	0.8368	76.9
5	0.6069	61.5	0.5493	59.9	0.6053	78.5	0.5137	76.9	0.4910	76.9
6	0.6186	59.1	0.5318	54.2	0.6514	58.3	0.7258	60.7	0.7595	78.5
7	0.6184	57.4	0.5409	54.2	0.6319	53.4	0.6827	59.1	0.6998	78.5
8	0.6113	56.6	0.5528	53.4	0.6330	53.4	0.6564	53.4	0.6484	72.8
9	0.6017	55.8	0.5716	53.4	0.6311	51.8	0.6335	53.4	0.6247	53.4
10	0.5920	55.8	0.5719	53.4	0.6275	51.8	0.6321	51.8	0.6135	53.4
	μ = 0.6		μ = 0.7		μ = 0.8		μ = 0.9		μ = 1.0	
w	Abs(P)	D (m)	Abs(P)	D (m)	Abs(P)	D (m)	Abs(P)	D (m)	Abs(P)	D (m)
1	4.5876	0.8	5.3027	0.8	6.0151	0.8	6.7261	0.8	7.4371	0.8
2	0.3784	65.5	0.4335	65.5	0.4909	66.3	0.4080	4.0	0.3329	0.8
3	0.6147	80.9	0.6119	80.9	0.4029	71.2	0.3679	71.2	0.3031	63.9
4	0.9132	76.9	0.9627	80.9	0.9898	80.1	0.5602	80.1	0.3145	76.9
5	0.4637	80.9	0.4348	80.9	0.4099	80.9	0.3927	80.9	0.3138	72.8
6	0.7643	78.5	0.3625	78.5	0.3827	78.5	0.4769	80.1	0.4243	80.1
7	0.6951	78.5	0.6772	78.5	0.6518	80.9	0.6221	80.9	0.6075	98.7
8	0.6246	72.8	0.5999	72.8	0.5750	79.3	0.5492	80.9	0.5189	98.7
9	0.6050	73.6	0.5809	73.6	0.5561	73.6	0.5328	73.6	0.3177	91.4
10	0.5850	74.4	0.5526	74.4	0.5190	80.9	0.4847	80.9	0.4658	80.9

Table A.14 LMS result for data set 6 for YB & YN

	$\hat{\mu}$ = 0.1		$\hat{\mu}$ = 0.2		$\hat{\mu}$ = 0.3		$\hat{\mu}$ = 0.4		$\hat{\mu}$ = 0.5	
w	Abs(P)	D (m)	Abs(P)	D (m)	Abs(P)	D (m)	Abs(P)	D (m)	Abs(P)	D (m)
1	0.5006	71.2	0.5107	71.2	0.5196	71.2	0.5273	71.2	0.5342	71.2
2	0.4495	71.2	0.4368	71.2	0.4440	71.2	0.4510	71.2	0.4576	71.2
3	0.4176	71.2	0.4090	71.2	0.3990	71.2	0.3878	71.2	0.3755	70.4
4	0.5787	71.2	0.6132	71.2	0.6422	71.2	0.6667	71.2	0.6872	71.2
5	0.5936	72.0	0.6211	71.2	0.6423	71.2	0.6586	71.2	0.6708	71.2
6	0.6120	72.0	0.6275	72.0	0.6356	72.0	0.6379	72.0	0.6357	72.0
7	0.5961	72.8	0.6043	72.8	0.6053	72.0	0.6013	72.0	0.5936	72.0
8	0.5696	51.8	0.5704	72.8	0.5647	72.8	0.5548	72.8	0.5420	72.8
9	0.5442	51.8	0.5396	51.0	0.5295	51.0	0.5159	72.8	0.5002	72.8
10	0.5195	51.0	0.5107	51.0	0.4973	50.2	0.4812	50.2	0.4637	50.2
	$\hat{\mu}$ = 0.6		$\hat{\mu}$ = 0.7		$\hat{\mu}$ = 0.8		$\hat{\mu}$ = 0.9		$\hat{\mu}$ = 1.0	
w	Abs(P)	D (m)	Abs(P)	D (m)	Abs(P)	D (m)	Abs(P)	D (m)	Abs(P)	D (m)
1	0.5403	71.2	0.5458	71.2	0.5508	70.4	0.5552	70.4	0.5593	70.4
2	0.4641	70.4	0.4703	70.4	0.4764	70.4	0.4824	70.4	0.4882	70.4
3	0.3623	70.4	0.3596	70.4	0.3607	70.4	0.3615	70.4	0.3622	70.4
4	0.7042	70.4	0.7182	70.4	0.7294	70.4	0.7382	70.4	0.7449	70.4
5	0.6797	71.2	0.6859	71.2	0.6898	71.2	0.6919	71.2	0.6925	71.2
6	0.6301	71.2	0.6217	71.2	0.6118	71.2	0.6065	71.2	0.6002	71.2
7	0.5833	72.0	0.5711	72.0	0.5574	72.0	0.5428	72.0	0.5275	72.0
8	0.5274	72.8	0.5116	72.8	0.4952	72.8	0.4792	72.8	0.4675	72.8
9	0.4834	72.8	0.4660	72.8	0.4486	72.8	0.4358	72.8	0.4233	72.8
10	0.4455	50.2	0.4285	59.9	0.4150	59.9	0.4020	59.9	0.3896	59.9

Table A.15 NLMS result for data set 6 for RY & YN

	$\hat{\mu}$ = 0.1		$\hat{\mu}$ = 0.2		$\hat{\mu}$ = 0.3		$\hat{\mu}$ = 0.4		$\hat{\mu}$ = 0.5	
w	Abs(P)	D (m)	Abs(P)	D (m)	Abs(P)	D (m)	Abs(P)	D (m)	Abs(P)	D (m)
1	0.5707	65.5	0.5808	65.5	0.5892	65.5	0.5964	65.5	0.3053	0.8
2	0.5042	63.1	0.4900	63.1	0.4991	63.1	0.5077	63.1	0.5159	72.8
3	0.4805	62.3	0.4692	62.3	0.4556	57.4	0.4542	55.8	0.4621	63.1
4	0.4820	57.4	0.4793	57.4	0.4745	57.4	0.4679	57.4	0.4598	57.4
5	0.4577	57.4	0.4559	57.4	0.4521	57.4	0.4467	76.9	0.4401	76.9
6	0.5702	58.3	0.6033	59.1	0.6283	60.7	0.6460	60.7	0.6577	60.7
7	0.5777	53.4	0.5996	58.3	0.6182	57.4	0.6299	59.1	0.6361	59.1
8	0.5918	53.4	0.6086	53.4	0.6163	53.4	0.6170	53.4	0.6128	60.7
9	0.6017	51.8	0.6090	51.8	0.6073	53.4	0.6024	53.4	0.5982	53.4
10	0.6031	51.8	0.6108	51.8	**0.6105**	**51.8**	0.6048	51.8	0.5955	53.4
	$\hat{\mu}$ = 0.6		$\hat{\mu}$ = 0.7		$\hat{\mu}$ = 0.8		$\hat{\mu}$ = 0.9		$\hat{\mu}$ = 1.0	
w	Abs(P)	D (m)	Abs(P)	D (m)	Abs(P)	D (m)	Abs(P)	D (m)	Abs(P)	D (m)
1	0.3167	0.8	0.3274	0.8	0.3377	0.8	0.3474	0.8	0.3566	0.8
2	0.5237	72.8	0.5311	72.8	0.5381	72.8	0.5448	72.8	0.5512	76.9
3	0.4694	76.9	0.4763	76.9	0.4827	76.9	0.4888	76.9	0.4945	76.9
4	0.4504	64.7	0.4397	76.9	0.4279	76.9	0.4152	76.9	0.4177	76.9
5	0.4325	76.9	0.4242	76.9	0.4153	76.9	0.4059	78.5	0.3961	80.9
6	0.6641	63.9	0.6661	77.7	0.3430	77.7	0.3305	77.7	0.3177	77.7
7	0.6376	78.5	0.6355	78.5	0.6304	78.5	0.6230	78.5	0.6138	78.5
8	0.6048	60.7	0.5943	60.7	0.5821	62.3	0.5697	62.3	0.5594	62.3
9	0.5911	63.1	0.5822	63.1	0.5722	63.1	0.5614	73.6	0.5504	73.6
10	0.5837	53.4	0.5704	53.4	0.5560	53.4	0.5409	74.4	0.5253	74.4

Table A.16 NLMS result for data set 6 for YB & YN

	λ = 0.991		λ = 0.992		λ = 0.993		λ = 0.994		λ = 0.995	
w	Abs(P)	D (m)	Abs(P)	D (m)	Abs(P)	D (m)	Abs(P)	D (m)	Abs(P)	D (m)
1	0.3458	35.6	0.3473	35.6	0.3486	35.6	0.3499	35.6	0.3512	35.6
2	0.3476	35.6	0.3488	35.6	0.3502	35.6	0.3515	35.6	0.3528	35.6
3	0.3498	35.6	0.3510	35.6	0.3522	35.6	0.3534	35.6	0.3545	35.6
4	0.3504	35.6	0.3517	35.6	0.3529	35.6	0.3542	35.6	0.3556	35.6
5	0.3503	35.6	0.3516	35.6	0.3529	35.6	0.3541	35.6	0.3555	35.6
6	0.3498	35.6	0.3512	35.6	0.3525	35.6	0.3538	35.6	0.3553	35.6
7	0.3514	35.6	0.3526	35.6	0.3539	35.6	0.3551	35.6	0.3562	35.6
8	0.3007	0.8	0.3016	0.8	0.3025	0.8	0.3033	0.8	0.3042	0.8
9	0.4105	0.8	0.4105	0.8	0.4104	0.8	0.4104	0.8	0.4104	0.8
10	0.5451	0.8	0.5451	0.8	0.5450	0.8	0.5450	0.8	0.5450	0.8
	λ = 0.996		λ = 0.997		λ = 0.998		λ = 0.999		λ = 1.000	
w	Abs(P)	D (m)	Abs(P)	D (m)	Abs(P)	D (m)	Abs(P)	D (m)	Abs(P)	D (m)
1	0.3525	35.6	0.3536	35.6	0.3548	35.6	0.3559	35.6	0.3570	35.6
2	0.3540	35.6	0.3552	35.6	0.3564	35.6	0.3575	35.6	0.3586	35.6
3	0.3556	35.6	0.3566	35.6	0.3576	35.6	0.3586	35.6	0.3595	35.6
4	0.3569	35.6	0.3583	35.6	0.3595	35.6	0.3608	35.6	0.3619	35.6
5	0.3570	35.6	0.3583	35.6	0.3596	35.6	0.3609	35.6	0.3621	35.6
6	0.3567	35.6	0.3581	35.6	0.3595	35.6	0.3608	35.6	0.3620	35.6
7	**0.3574**	**35.6**	0.3585	35.6	0.3596	35.6	0.3606	35.6	0.3616	35.6
8	0.3051	0.8	0.3060	0.8	0.3069	0.8	0.3077	0.8	0.3086	0.8
9	0.4104	0.8	0.4104	0.8	0.4104	0.8	0.4104	0.8	0.4104	0.8
10	0.5449	0.8	0.5449	0.8	0.5449	0.8	0.5448	0.8	0.5448	0.8

Table A.17 RLS result for data set 6 for RY & YN

	λ = 0.991		λ = 0.992		λ = 0.993		λ = 0.994		λ = 0.995	
w	Abs(P)	D (m)	Abs(P)	D (m)	Abs(P)	D (m)	Abs(P)	D (m)	Abs(P)	D (m)
1	0.3430	35.6	0.3441	35.6	0.3453	35.6	0.3463	35.6	0.3474	35.6
2	0.3416	35.6	0.3429	35.6	0.3441	35.6	0.3452	35.6	0.3463	35.6
3	0.3435	35.6	0.3448	35.6	0.3460	35.6	0.3471	35.6	0.3482	35.6
4	0.3440	35.6	0.3453	35.6	0.3465	35.6	0.3477	35.6	0.3489	35.6
5	0.3439	35.6	0.3452	35.6	0.3464	35.6	0.3476	35.6	0.3488	35.6
6	0.3427	35.6	0.3441	35.6	0.3455	35.6	0.3468	35.6	0.3481	35.6
7	0.3428	35.6	0.3442	35.6	0.3456	35.6	0.3469	35.6	0.3482	35.6
8	0.3060	0.8	0.3066	0.8	0.3071	0.8	0.3077	0.8	0.3082	0.8
9	0.3333	0.8	0.3343	0.8	0.3353	0.8	0.3363	0.8	0.3373	0.8
10	0.4088	0.8	0.4088	0.8	0.4088	0.8	0.4088	0.8	0.4088	0.8
	λ = 0.996		λ = 0.997		λ = 0.998		λ = 0.999		λ = 1.000	
w	Abs(P)	D (m)	Abs(P)	D (m)	Abs(P)	D (m)	Abs(P)	D (m)	Abs(P)	D (m)
1	0.3484	35.6	0.3494	35.6	0.3503	35.6	0.3512	35.6	0.3521	35.6
2	0.3474	35.6	0.3484	35.6	0.3494	35.6	0.3503	35.6	0.3512	35.6
3	0.3493	35.6	0.3504	35.6	0.3513	35.6	0.3523	35.6	0.3532	35.6
4	0.3500	35.6	0.3511	35.6	0.3521	35.6	0.3531	35.6	0.3541	35.6
5	0.3500	35.6	0.3511	35.6	0.3521	35.6	0.3531	35.6	0.3541	35.6
6	0.3494	35.6	0.3506	35.6	0.3518	35.6	0.3529	35.6	0.3540	35.6
7	**0.3494**	**35.6**	0.3506	35.6	0.3518	35.6	0.3529	35.6	0.3539	35.6
8	0.3088	0.8	0.3093	0.8	0.3098	0.8	0.3104	0.8	0.3109	0.8
9	0.3383	0.8	0.3394	0.8	0.3404	0.8	0.3414	0.8	0.3424	0.8
10	0.4088	0.8	0.4088	0.8	0.4088	0.8	0.4088	0.8	0.4088	0.8

Table A.18 RLS result for data set 6 for YB & YN

	μ = 0.1		μ = 0.2		μ = 0.3		μ = 0.4		μ = 0.5	
w	Abs(P)	D (m)	Abs(P)	D (m)	Abs(P)	D (m)	Abs(P)	D (m)	Abs(P)	D (m)
1	0.1148	32.0	0.1294	31.9	0.1424	31.9	0.1542	31.9	0.1649	32.3
2	0.1068	32.1	0.1135	31.9	0.1187	32.0	0.1227	32.3	0.1258	32.4
3	0.1730	52.9	0.1059	34.2	0.1040	32.3	0.1601	32.3	0.1073	16.2
4	0.1235	32.3	0.1194	33.7	0.1374	33.7	0.1519	33.7	0.1507	33.7
5	0.1366	32.3	0.1300	32.2	0.1278	31.8	0.1214	32.5	0.1092	32.7
6	0.1430	32.3	0.1216	31.9	0.1052	32.3	+	*	+	*
7	0.1400	32.1	0.1111	32.3	+	*	+	*	+	*
8	0.1462	32.2	0.1085	32.8	+	*	+	*	+	*
9	0.1527	32.8	0.1202	32.7	+	*	+	*	+	*
10	0.1585	32.8	0.1268	32.8	0.1047	32.8	+	*	+	*
	μ = 0.6		μ = 0.7		μ = 0.8		μ = 0.9		μ = 1.0	
w	Abs(P)	D (m)	Abs(P)	D (m)	Abs(P)	D (m)	Abs(P)	D (m)	Abs(P)	D (m)
1	0.1094	2.6	0.1192	2.6	0.1301	2.6	0.1438	3.0	0.1026	1.0
2	0.1081	16.1	0.1413	16.1	0.1100	16.3	0.1016	3.2	0.1025	0.9
3	0.1307	16.2	0.1674	16.2	0.2195	16.2	0.2862	16.2	0.1318	3.4
4	0.1056	33.7	0.1130	16.2	0.1347	16.2	0.1641	16.2	0.1149	1.2
5	0.1012	32.7	0.1011	33.7	0.1121	16.2	0.1291	16.2	0.1119	1.6
6	+	*	+	*	+	*	+	*	0.1006	1.7
7	+	*	+	*	0.1104	15.3	0.1234	15.4	0.1108	3.4
8	+	*	+	*	+	*	0.1249	33.0	0.1057	3.9
9	+	*	+	*	+	*	0.1026	49.4	0.1003	3.7
10	+	*	+	*	+	*	+	*	0.1117	4.0

Table A.19 LMS result for data set 1 with threshold value of 0.1

	$\hat{\mu}$ = 0.1		$\hat{\mu}$ = 0.2		$\hat{\mu}$ = 0.3		$\hat{\mu}$ = 0.4		$\hat{\mu}$ = 0.5	
w	Abs(P)	D (m)	Abs(P)	D (m)	Abs(P)	D (m)	Abs(P)	D (m)	Abs(P)	D (m)
1	0.2358	3.0	0.2220	3.0	0.2090	3.0	0.4561	33.2	0.4286	33.2
2	0.2235	3.0	0.4617	32.3	0.4092	33.2	0.3593	33.2	0.3255	33.2
3	0.2132	3.0	0.4169	33.2	0.3491	33.2	0.3055	33.2	0.2842	32.4
4	0.2050	3.0	0.3773	33.2	0.3122	33.2	0.2824	32.5	0.2591	32.4
5	0.4536	32.6	0.3490	33.2	0.2924	32.6	0.2654	32.5	0.2422	32.4
6	0.4372	33.2	0.3267	32.7	0.2806	32.5	0.2528	32.4	0.2314	32.4
7	0.4226	33.2	0.3084	32.7	0.2716	32.5	0.2432	32.4	0.2274	32.3
8	0.4096	32.8	0.2981	32.6	0.2647	32.4	0.2366	32.3	0.2257	32.3
9	0.3981	32.9	0.2932	32.6	0.2595	32.4	0.2356	32.3	0.2255	32.3
10	0.3878	32.8	0.2895	32.5	0.2556	32.3	0.2360	32.3	0.2264	32.3
	$\hat{\mu}$ = 0.6		$\hat{\mu}$ = 0.7		$\hat{\mu}$ = 0.8		$\hat{\mu}$ = 0.9		$\hat{\mu}$ = 1.0	
w	Abs(P)	D (m)	Abs(P)	D (m)	Abs(P)	D (m)	Abs(P)	D (m)	Abs(P)	D (m)
1	0.4008	33.2	0.3737	33.2	0.3514	33.2	0.3324	33.2	0.3175	33.2
2	0.3013	33.2	0.2859	33.2	0.2714	32.3	0.2580	32.3	0.2464	32.3
3	0.2644	32.4	0.2477	32.4	0.2339	32.3	0.2255	32.3	0.2186	32.3
4	0.2402	32.4	0.2272	32.3	0.2187	32.3	0.2107	32.3	0.2031	32.3
5	0.2272	32.3	0.2175	32.3	0.2084	32.3	+	*	+	*
6	0.2207	32.3	0.2108	32.3	0.2015	32.3	+	*	+	*
7	0.2170	32.3	0.2073	32.3	+	*	+	*	+	*
8	0.2158	32.3	0.2065	32.3	+	*	+	*	+	*
9	0.2160	32.3	0.2071	32.3	0.2000	32.3	+	*	+	*
10	0.2173	32.3	0.2086	32.3	0.2022	32.3	+	*	+	*

Table A.20 NLMS result for data set 1 with threshold value of 0.2

	$\hat{\mu}$ = 0.1		$\hat{\mu}$ = 0.2		$\hat{\mu}$ = 0.3		$\hat{\mu}$ = 0.4		$\hat{\mu}$ = 0.5	
w	Abs(P)	D (m)	Abs(P)	D (m)	Abs(P)	D (m)	Abs(P)	D (m)	Abs(P)	D (m)
1	0.3418	43.7	0.4089	0.2	+	*	+	*	+	*
2	0.4843	0.2	+	*	+	*	+	*	+	*
3	0.4052	0.2	+	*	+	*	+	*	+	*
4	0.3665	0.2	+	*	+	*	+	*	+	*
5	0.3463	0.2	+	*	+	*	+	*	+	*
6	0.3365	0.2	+	*	+	*	+	*	+	*
7	0.3320	0.2	+	*	+	*	+	*	+	*
8	0.3294	0.2	+	*	+	*	+	*	+	*
9	0.3294	0.2	+	*	+	*	+	*	+	*
10	0.3309	0.2	+	*	+	*	+	*	+	*
	$\hat{\mu}$ = 0.6		$\hat{\mu}$ = 0.7		$\hat{\mu}$ = 0.8		$\hat{\mu}$ = 0.9		$\hat{\mu}$ = 1.0	
w	Abs(P)	D (m)	Abs(P)	D (m)	Abs(P)	D (m)	Abs(P)	D (m)	Abs(P)	D (m)
1	+	*	+	*	+	*	+	*	+	*
2	+	*	+	*	+	*	+	*	+	*
3	+	*	+	*	+	*	+	*	+	*
4	+	*	+	*	+	*	+	*	+	*
5	+	*	+	*	+	*	+	*	+	*
6	+	*	+	*	+	*	+	*	+	*
7	+	*	+	*	+	*	+	*	+	*
8	+	*	+	*	+	*	+	*	+	*
9	+	*	+	*	+	*	+	*	+	*
10	+	*	+	*	+	*	+	*	+	*

Table A.21 NLMS result for data set 4 after ignoring the first fault distance

Actual fault distances for data sets 1, 2, 3, 4, and 6 were 33, 65.5, 10.8, 45, and 35.6m respectively. The best calculated fault distances by all three algorithms are shown in Table A22.

Data Label	Actual Fault Distance (m)	Fault distance by LMS (m)	Fault distance by NLMS (m)	Fault distance by RLS (m)
Data 1	33	32.8	32.9	33.2
Data 2	65.5	86.3	63.0	62.7
Data 3	10.8	10.1	10.5	10.6
Data 4	45	36.0	43.7	43.9
Data 6	35.6	51.0	51.0	35.6

Table A.22 Summary of results for the three adaptive algorithms

Figures A1, A2, A3, A4, and A5 show waveforms of data sets 1, 2, 3, 4, and 6 respectively. Figures A6, A7, A8, and A9 show the three adaptive algorithms' best results (error waveforms) for data sets 1, 2, 3, and 4 respectively. Figures A10 and A11 show the three adaptive algorithms' results (error waveforms) for data set 6, for RY & YN and RB & YN respectively.

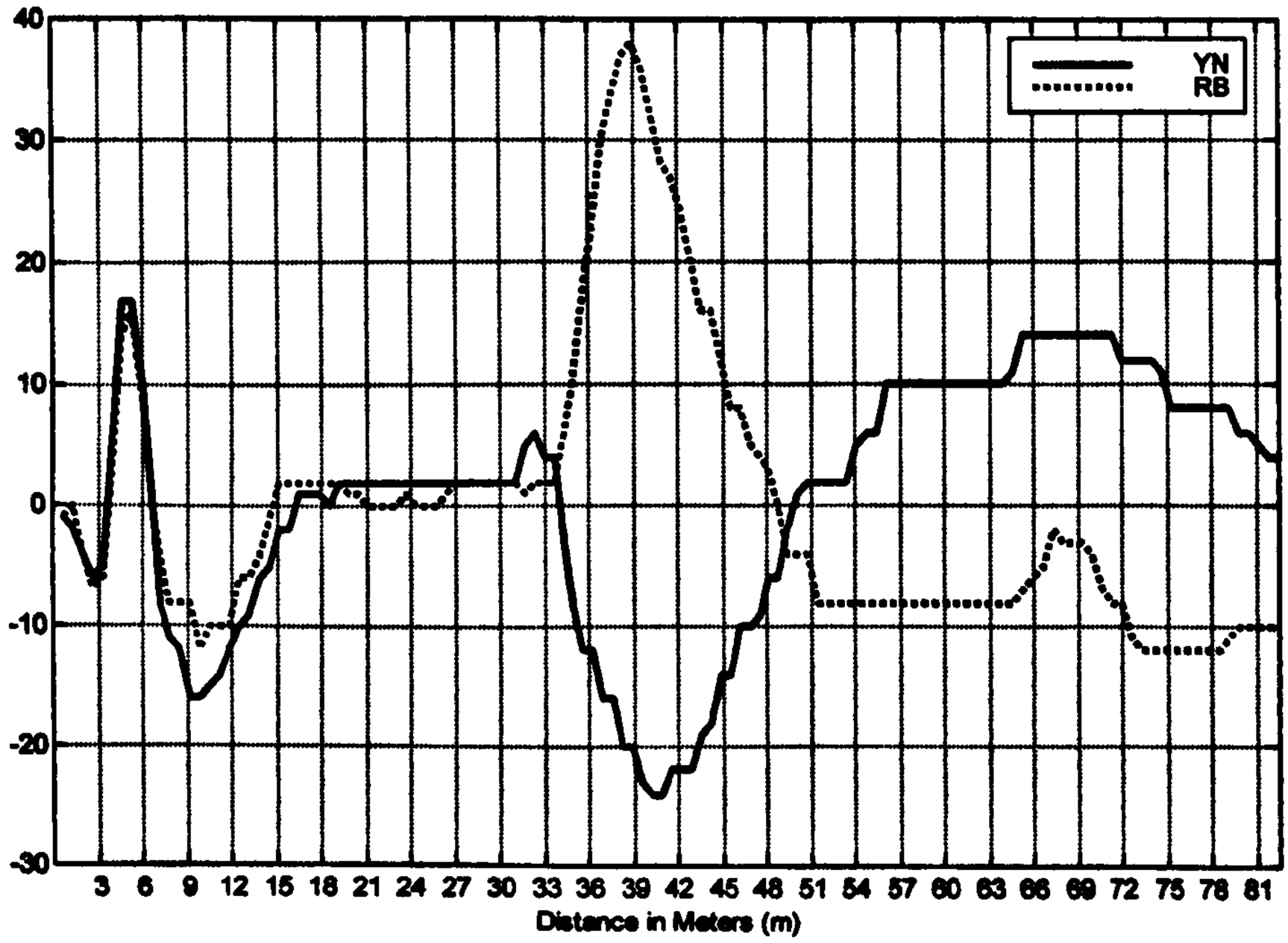

Figure A.1: TDR waveforms of data set 1 (RB and YN)

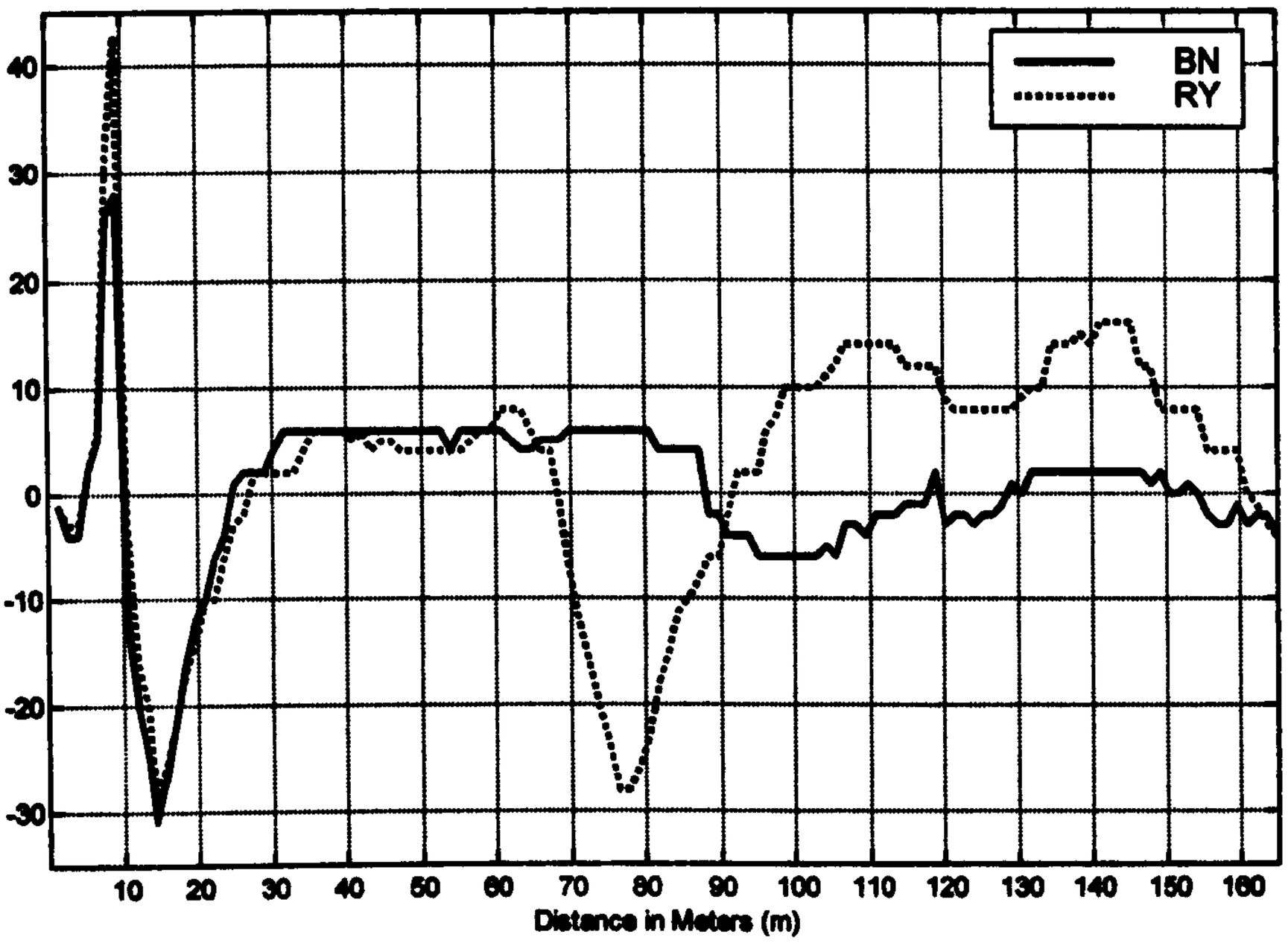

Figure A.2: TDR waveforms of data set 2 (BN and RY)

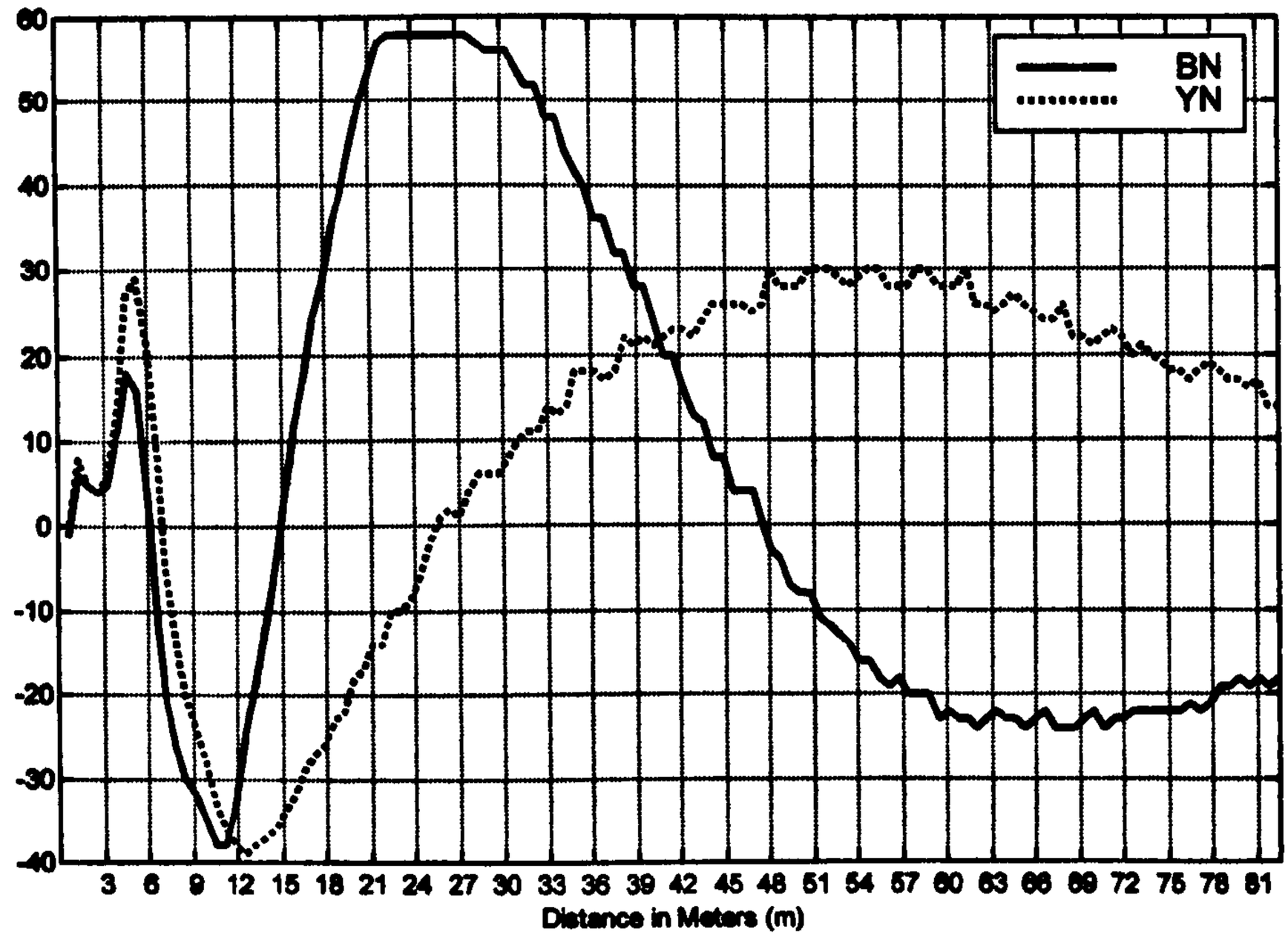

Figure A.3: TDR waveforms of data set 3 (BN and YN)

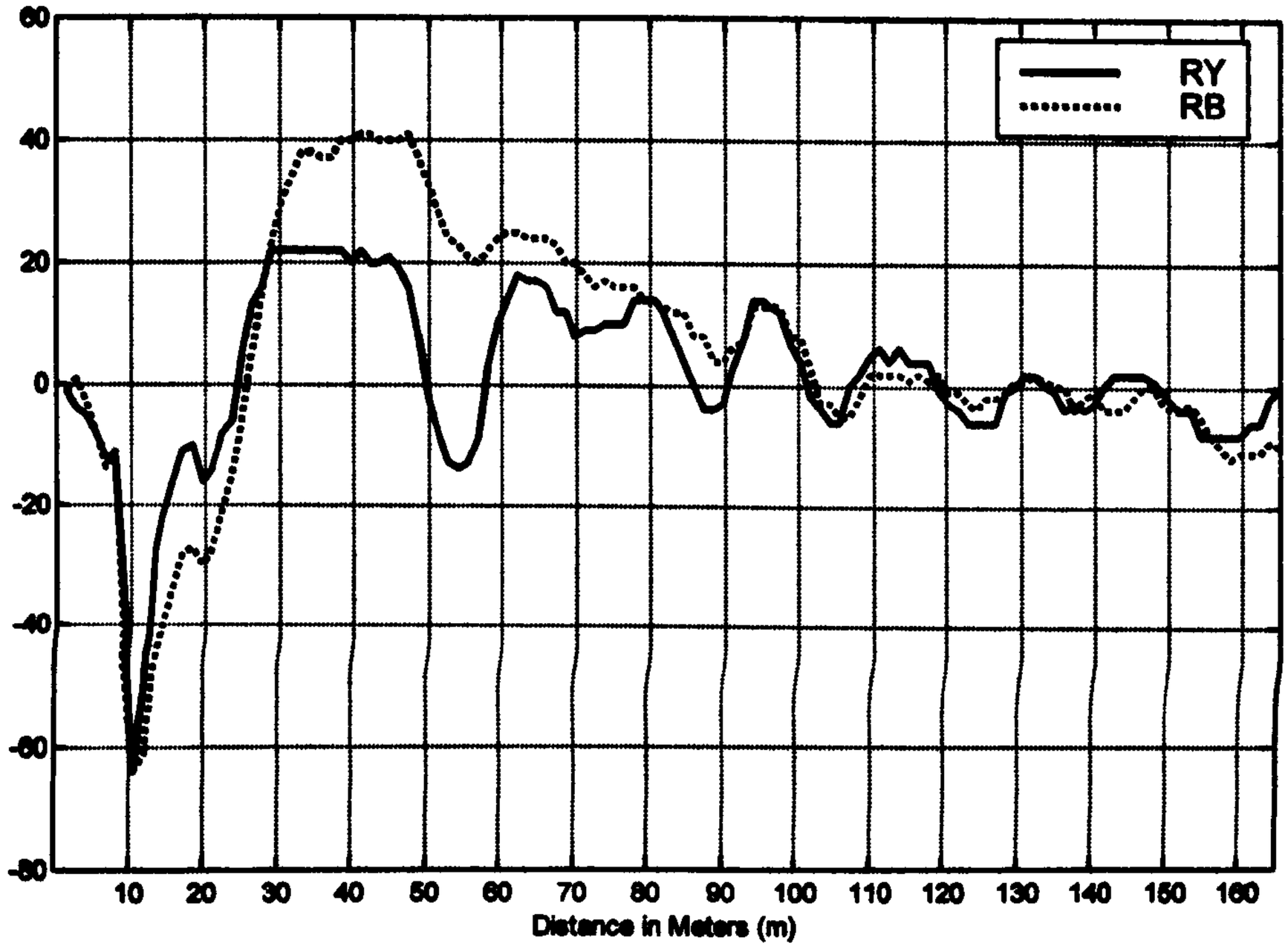

Figure A.4: TDR waveforms of data set 4 (RY and RB)

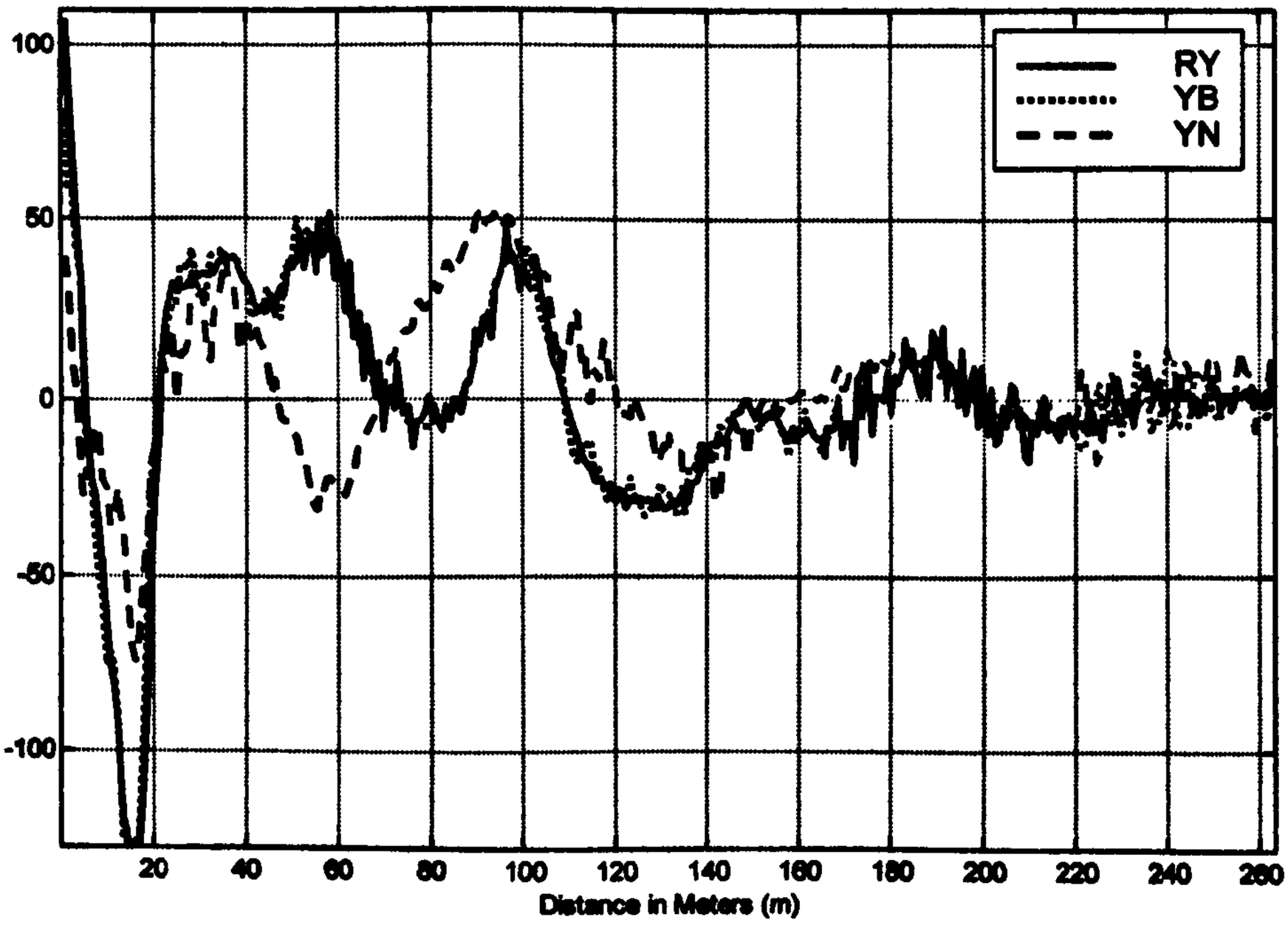

Figure A.5: TDR waveforms of data set 6 (RY, YB, and YN)

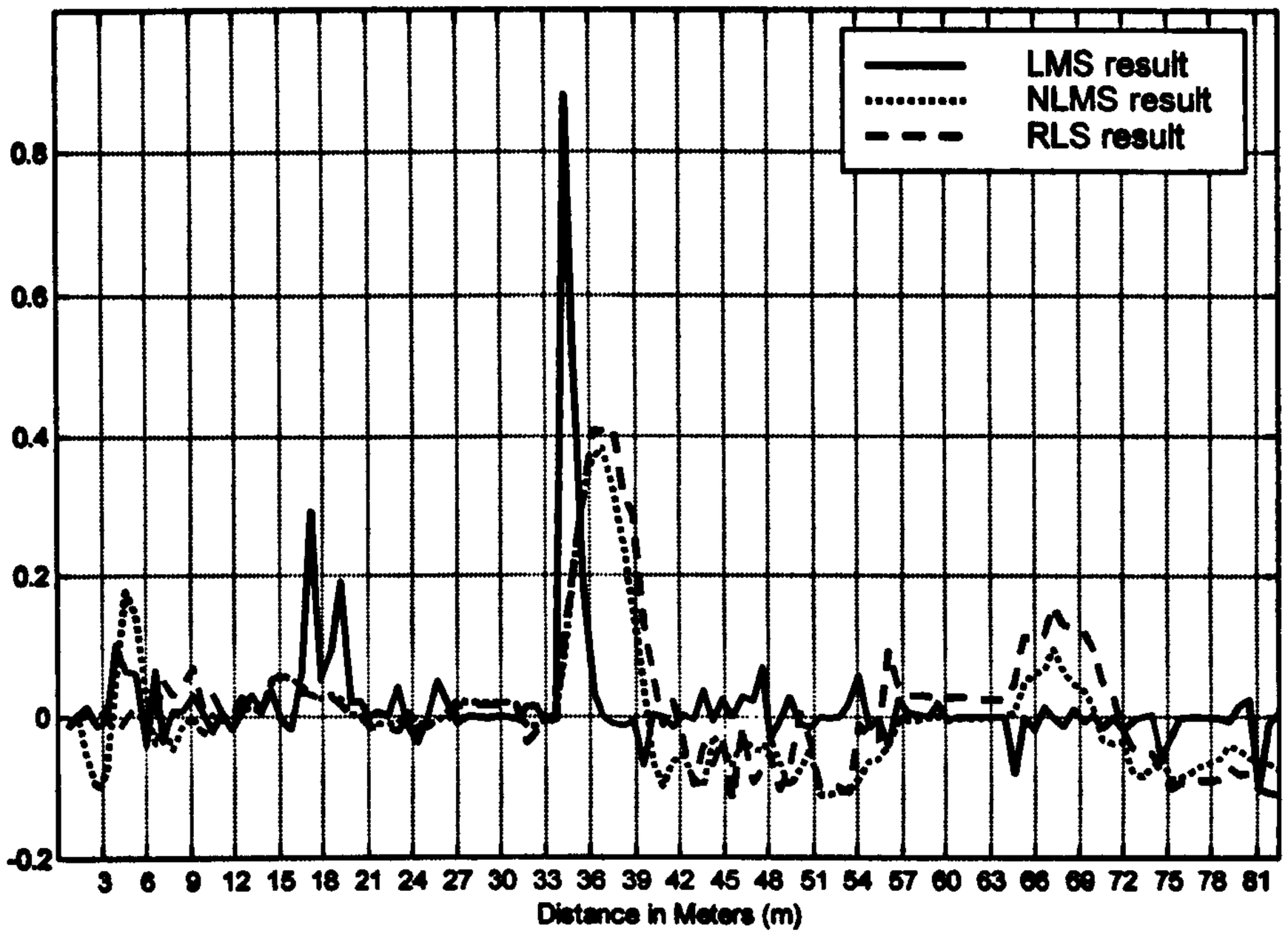

Figure A.6: Summary results for data set 1 of the three adaptive algorithms

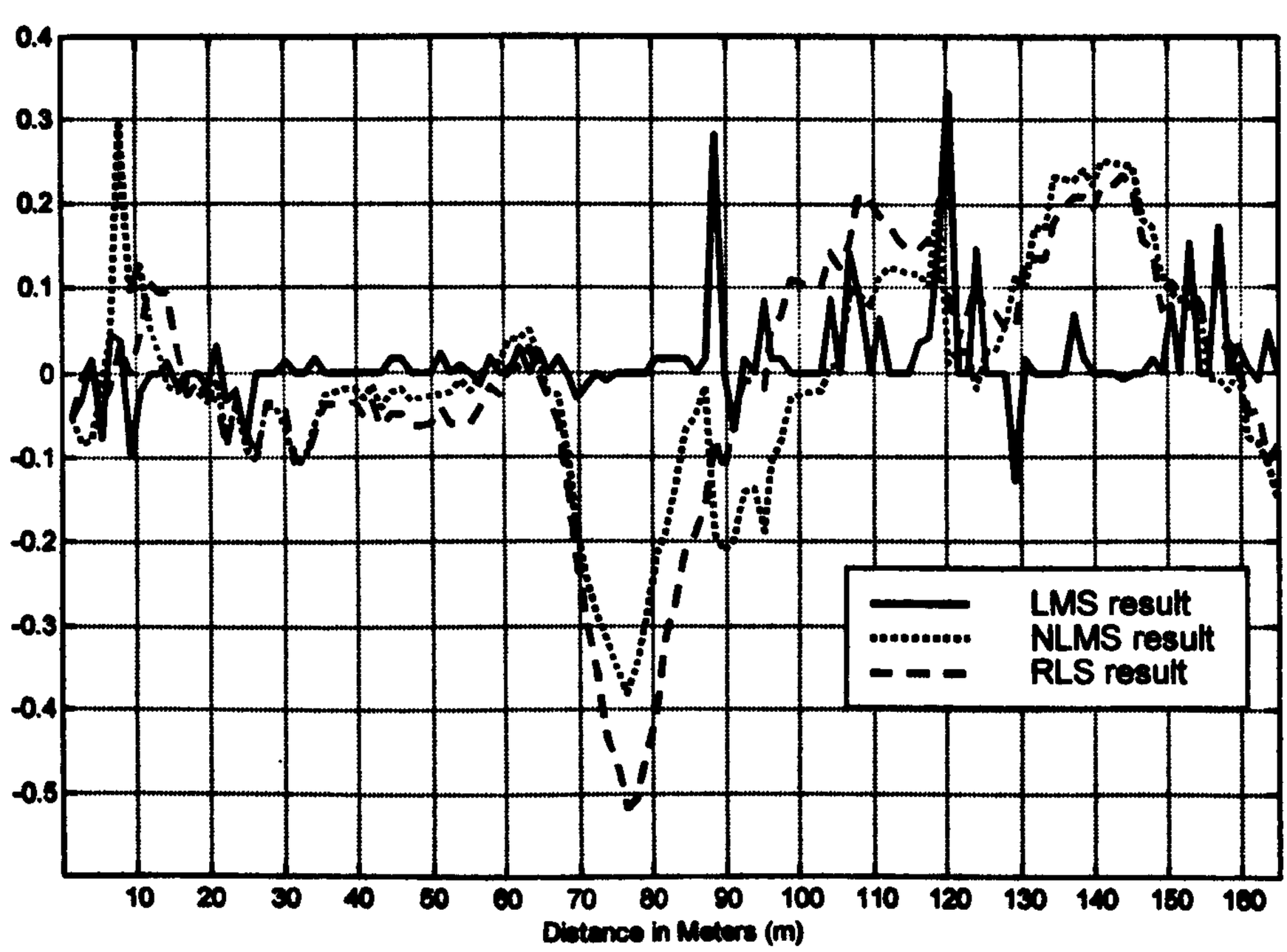

Figure A.7: Summary results for data set 2 of the three adaptive algorithms

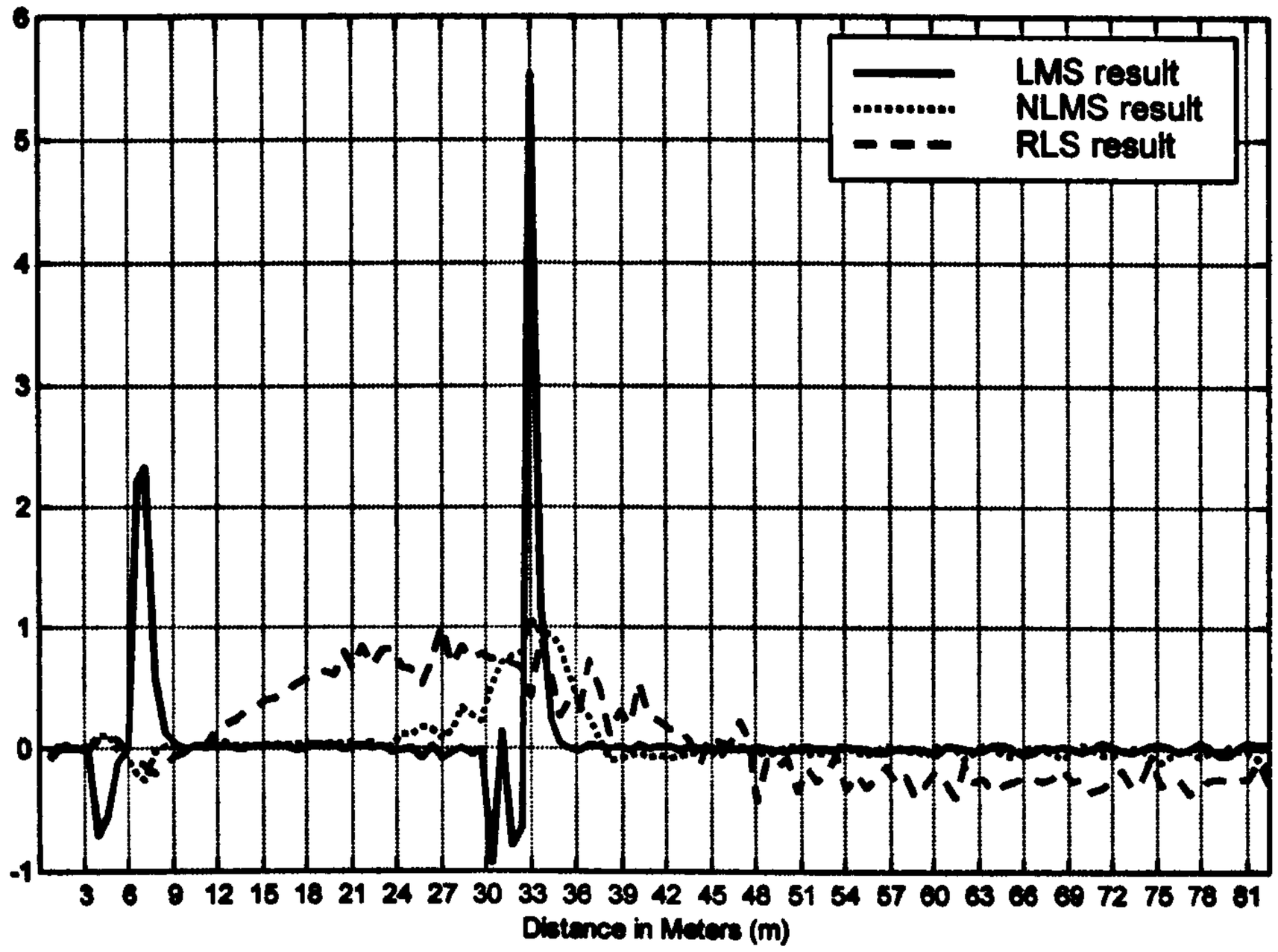

Figure A.8: Summary results for data set 3 of the three adaptive algorithms

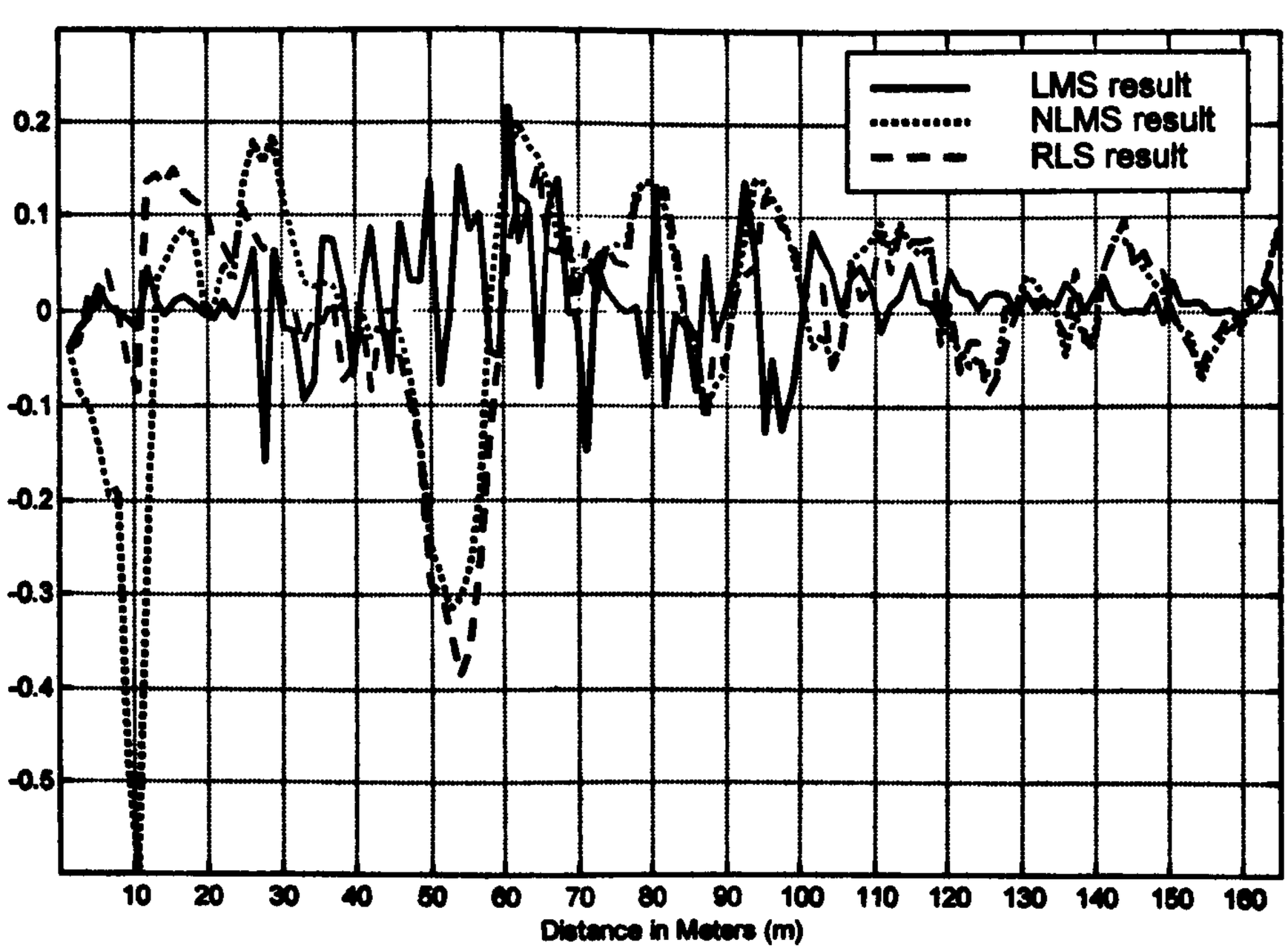

Figure A9: Summary results for data set 4 of the three adaptive algorithms

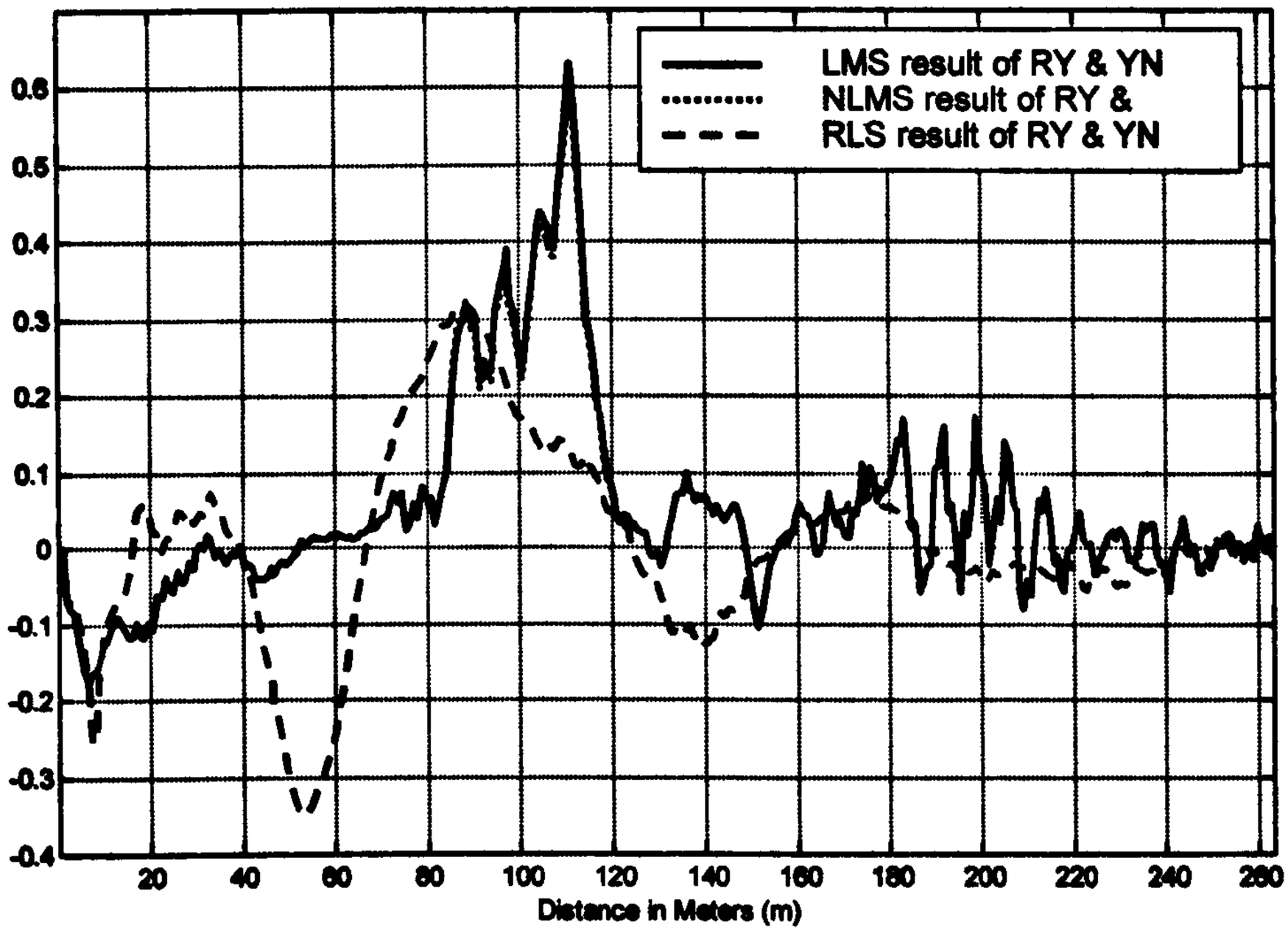

Figure A.10: Summary results for data set 6 (RY and YN) of the three adaptive algorithms

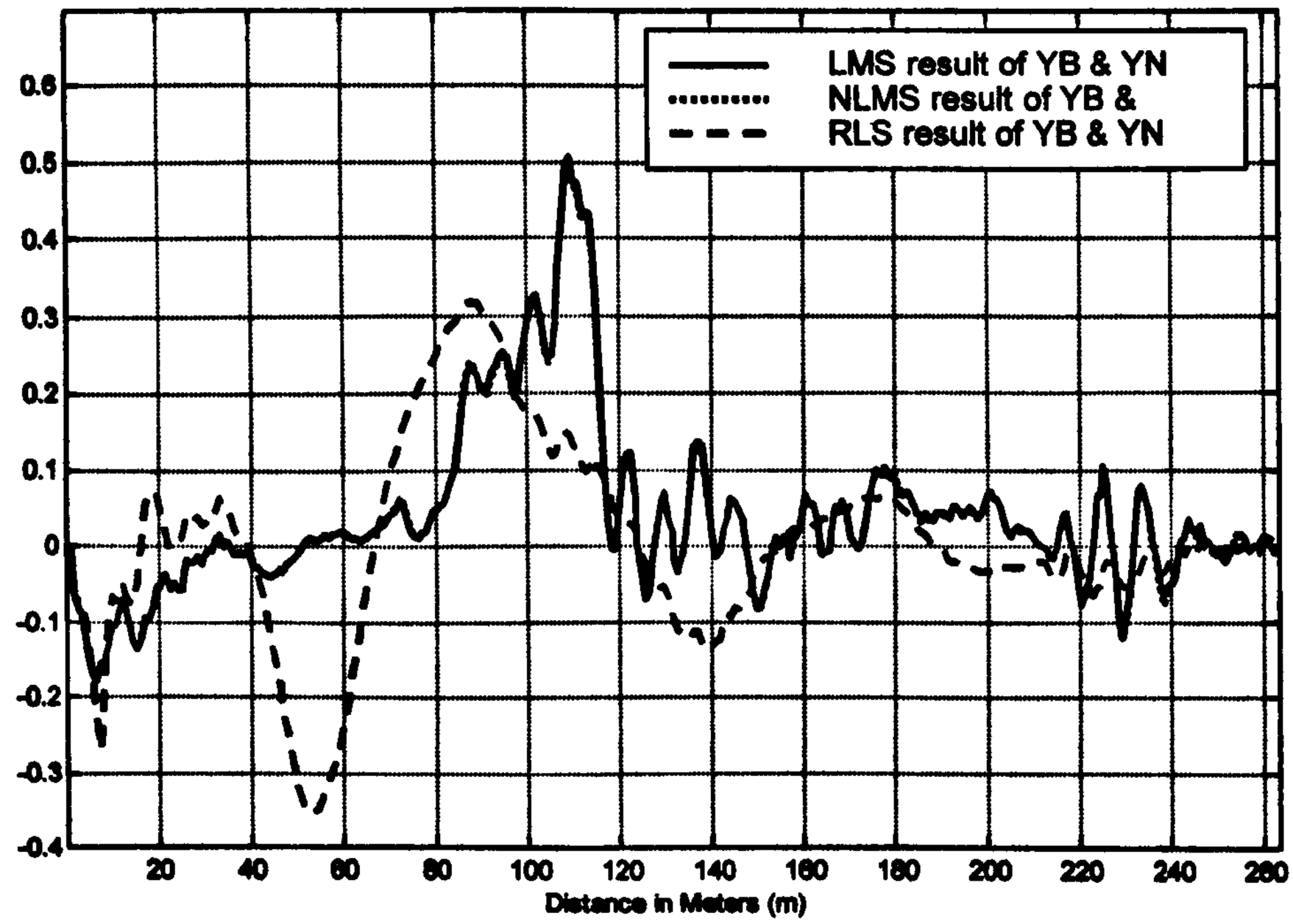

Figure A11: Summary results for data set 6 (YB and YN) of the three adaptive algorithms

Appendix B

Author's Publications

1. Navaneethan, S., Soraghan, J.J., Siew, W.H., Muirhead, R., Livie, J., "An automatic Fault Detection and Location Technique in Low Voltage Distribution Networks", IEEE International Conference on Energy Management and power Delivery, Raffles City Convention Centre, Singapore, 3-5 March 1998, pp732-736.

2. Navaneethan, S., Soraghan, J.J., Siew, W.H., McPherson, F., Gale, P., "Automatic Fault Location Using Intelligent Processing", Proceedings of IEEE International Conference on Power Tech '99, Aug 29 - Sep 2 1999, Budapest, Hungary, Paper No. BPT99-368-23.

3. Siew, W.H., Navaneethan, S., Soraghan, J.J., McPherson, F., Gale, P.F., "Automatic Fault Location for Underground Low Voltage Distribution Networks", IEEE Transactions on Power Delivery, Vol.16, No.2, April 2001, pp346-351.

4. Siew, W.H., Navaneethan, S., Soraghan, J.J., McPherson, F., Gale, P.F., "Automatic Fault Location for Underground Low Voltage Distribution Networks", IEEE Power Engineering Society Winter Meeting, New York, USA, 28 – 31 January 2002, paper no. PE-057PRD (09-2000).

References

[1] J. Bertrand, P. Bertrand, and J. P, "Discrete Mellin Transform for Signal Analysis," in *Proc. 1990 IEEE Int. Conf. Acoust., Speech, Signal Processing*, Albuquerque, NM, Apr. 3-6, 1990, pp. 1603-1606.

[2] P. Flandrin, "Some Aspects of Non-Stationary Signal Processing with Emphasis on Time-Frequency and Time Scale Methods," in *Wavelets, Time-Frequency Methods and Phase Space*. J. M. Combes, A. Grossmann, and Ph. Tchamitchian, Eds. Berlin: Springer, IPTI, 1989, pp. 68-98.

[3] P. Goupillaud, A. Grossmann, and J. Morlet, "Cycle-Octave and Related Transforms in Seismic Signal Analysis," *Geoexploration*, vol. 23, 1984/85, pp. 85-102.

[4] A. Grossmann and R. Kronland-Martinet, "Time and Scale Representaions Obtained Through Continuous Wavelet Transforms," in *Proc. Int Conf. EUSIPCO'88, Signal Processing IV: Theories and Applications*, J. L. Lacoume et al., Eds. New York: Elsevier Science Pub., 1988, pp. 475-482.

[5] M. Holschneider, R. Kronland-Martinet, J. Morlet, and Ph. Tchamitchian, "A Real-Time Algorithm for Signal Analysis with the Help of the Wavelet Transform," in *Wavelet, Time-Frequency Methods and Phase Space*. J. M. Combes, A. Grossmann, and Ph. Tchamitchian, Eds. Berlin: Springer, IPTI, 1989, pp. 286-297.

[6] R. Kronland-Martinet, J. Morlet, and A. Grossmann, "Analysis of Sound Patterns Through Wavelet Transform," in *Int. J. Pattern Recogn. Artificial Intell.*, vol. 1, no. 2, 1987, pp. 273-302.

[7] J. M. Combes, A. Grossmann, and Ph. Tchamitchian, Eds., *Wavelet, Time-Frequency Methods and Phase Space*, Berlin: Springer, IPTI, 1989.

[8] M. Antonini, M. Barlaud, P. Mathieu, and I. Daubechies, "Imaging Coding Using Vector Quantization in the Wavelet Transform Domain," in *Proc. 1990 IEE Int. Conf. Acoust., Speech, Signal Processing*, Albuquerque, NM, Apr. 3-6, 1990, pp. 2297-2300.

[9] S. Mallat and S.Zhong, "Characterization of Signals from Multiscale Edges," *IEEE Trans. Pattern Anal. and Machine Intell.*, vol. 14, no. 7, July 1992, pp. 710-732.

[10] S. Mallat, "A Theory for Multiresolution Signal Decomposition: The Wavelet Representation," *IEEE Trans. Pattern Anal. and Machine Intell.*, vol. 11, no. 7, July 1989, pp. 674-693.

[11] S. Mallat, "Multifrequency Channel Decomposition of Images and Wavelet Models," *IEEE Trans. Acoust., Speech, Signal Processing*, vol. 37, Dec. 1989, pp. 2091-2110.

[12] F. H. Magnago, and A. Abur, "Fault Location Using Wavelets," *IEEE Trans. Power Delivry*, vol. 13, no. 4, Oct., 1998, pp. 1475-1480.

[13] O. Chaari, M. Meunier, and F. Brouaye,"Wavelets: A New Tool for the Resonant Grounded Power Distribution Syatems Relaying," *IEEE Trans. Power Delivery*, vol.11, no.3, July, 1996, pp.1301-1308.

[14] O. Rioul and M. Vetterli, "Wavelets and Signal Processing," *IEEE Signal Processing Magazine*, vol. 8, Oct., 1991, pp. 14-38.

[15] A. Grossmann and J. Morlet, "Decomposition of Hardy Functions into Square Integrable Wavelets of Constant Shape," *SIAM J. Math.*, vol.15, 1984, pp. 723-736.

[16] A. Laine, J. Fan and W. Yang, " Wavelets for Contrast Enhancement of Digital Mammography," *IEEE Engineering in Medicine and Biology*, Sep., 1995, pp. 536-550.

[17] D. Gabor, "Theory of Communication," *Journal of the IEE*, vol. 93, 1946, pp. 429-457.

[18] J. B. Allen and L. R. Rabiner, " A Unified Approach to Short-Time Fourier Analysis and Synthesis," *Proc. IEEE*, vol. 65, 1977, pp. 1558-1564.

[19] M. R. Porrtnoff, "Time-Frequency Representation of Digital Signals and Systems Based on Short-Time Fourier Analysis," *IEEE Trans. on ASSP*, vol. 28, Feb., 1980, pp. 55-69.

[20] A. Croisier, D. Esteban, and C. Galand, "Perfect Channel Splitting by Use of Interpolation, Decimation, Tree Decomposition Techniques," *Int. Conf. on Information Sciences/Systems*, Patraas, Aug., 1976, pp. 443-446.

[21] R. E. Crochiere, S. A. Weber, and J. L. Flanagan, "Digital Coding of Speech in Subbands," *Bell Syst. Tech. J.*, vol. 55, Oct. 1976, pp. 1069-1085.

[22] D. Esteban and C. Galand, "Application of Quadrature Mirror Filter to Split-Band Voice Coding Schemes," *Int. Conf. ASSP*, Hartford, Connecticut, May, 1977, pp. 191-195.

[23] A. Grossmann, R. Kronland-Martinet and J. Morlet, "Reading and Understanding Continuous Wavelet Transform," *In Wavelets: Time-Frequency Methods and Phase Space*, J. M. Combes, A. Grossmann and Ph. Tchamitchian, (eds.), Second Edition, Springer-Verlag, NY, 1989.

[24] I. Daubechies, "The Wavelet Transform, Time-Frequency Localisation and Signal Analysis," *IEEE Trans. Info. Theory*, vol. 36, no.5, Sep., 1990, pp. 961-1005.

[25] Y. Meyer, "Orthonormal Wavelets," *In Wavelets: Time-Frequency Methods and Phase Space*, J. M. Combes, A. Grossmann and Ph. Tchamitchian, (eds.), Second Edition, Springer-Verlag, NY, 1989, pp. 21-37.

[26] I. Daubechies, "Orthogonal Bases of Compactly Supported Wavelets," *Comm. in Pure and Applied Math.*, vol. 41, no. 7, 1988, pp. 909-996.

[27] F. Mintzer, "Filters for Distortion-Free Two-Band Multirate Filter Banks," *IEEE Trans. ASSP. Proc.*, vol. 33, June 1985, pp. 626-630.

[28] M. J. T. Smith and T. P. Barnwell, "Exact Reconstruction for Tree Structured Subband Coders," *IEEE Trans. ASSP. Proc.*, vol. ASSP-34, June 1986, pp. 434-441.

[29] P. P. Vaidyanathan and P. Q. Hoang, "Latice Structures for Optimal Design and Robust Implementation of Two-Band Perfect Reconstruction QMF Banks," *IEEE Trans. ASSP. Proc.*, vol. ASSP-36, no.1, Jan. 1988, pp. 81-94.

[30] M. Vetterli, "Filter Banks Allowing Prefect Reconstruction," *Signal Processing*, vol. 10, no. 3, April 1986, pp. 219-244.

[31] A. Calderon, "Intermediate Spaces and Interpolation, the Complex Method,"*Studia Math.*, vol.24, 1964, pp. 113-190.

[32] A. Harr, "Zur Theorie der Orthogonal Funktionensysteme,"*Math. Annal.*, vol. 69, 1910, pp. 331-371.

[33] B. Widrow and S. M. Stearns, Adaptive Signal Processing, Prentice-Hall, 1985.

[34] E. C. Ifeachor and B. W. Jervis, Digital Signal Processing: A Practical Approach, Addison Wisely, 1994.

[35] B. Widrow, J. R. Glover, J. M. McCool, J. Kaunitz, C. S. Williams, R. H. Hearn, J. R. Zeidler, E. Dong and R. C. Goodlin, "Adaptive Noise Cancelling: Principles and Applications," Proc. IEEE, Vol. 63, 1975a, pp.1692-76.

[36] S. Haykin, Adaptive Filter Theory, 3rd ed., Prentice Hall, 1996.

[37] Wiener Norbert, Interpolation, Interpretation and Smoothing of Stationary Time Series, Wiley Publications, New York, 1949.

[38] L. A. Zadeh, "Fuzzy Set," *Inform. And Contr.*, 1965, 8:338-353.

[39] K. Tomsovic, and J. M. Ling, "A Proposed Fuzzy Information Approach to Power Systems Security," *3rd Symposium on Expert Systems Applications to Power Systems*, Tokyo-Kobe, Japan, April 1991, pp. 427-432.

[40] D. Dubois, and H. Prade, *Fuzzy Sets and Systems: Therory and applications.* Academic Press, Inc., 1980.

[41] R. E. Bellman, and M. Giertz, "On the Analytic Formalism of the Theory of Fuzzy Sets,"*Inf. Sci.*, 1973, 5:149-157.

[42] L. A. Zadeh, "The Concept of a Linguistic Variable and its Application to Approximate Reasoning," Parts 1, 2, and 3, *Inf. Sci.*, 1975, 8:199-249; 8:301-357, 9:43-80.

[43] R. E. Bellman, and Z. A. Zadeh, "Decision-making in Fuzzy Environment," *Manage. Sci*, 1970, 17(4): B141-B164.

[44] P. Deepal, A. Pahwa, J. E. Boyer, "Location of Outages in Distribution Systems Based on Statistical Hypothesis Testing," IEEE Trans. on Power Delivery, Vol. 11, No. 1, Jan. 1996, pp. 546-551.

[45] P. Jarventausta, P. Verho, J. Partanen, " Using Fuzzy Sets to Model the Uncertainty in the Fault Location Process of Distribution Networks," *IEEE Trans. On Power Delivery*, vol. 9, No. 2, April 1994, pp. 954-960.

[46] B. Clegg, Underground Cable Fault Location, McGraw-Hill, 1993.

[47] C. Fukui and J. Kawakami, "An Expert System for Fault Section Estimation Using Information from Protective Relays and Circuit Breakers," *IEEE Trans. On Power Delivery*, Oct. 1986, pp.83-91.

[48] K. Tomsovic, P. Ackerman, and S. Pope, "An Expert System as a Dispatchers' Aid for Isolation of Line Section Faults," *IEEE Trans. On Power Delivery*, vol. PWRD-2, July 1987, pp. 736-743.

[49] E. Cardozo and S. N. Talukdar, "A Distributed Expert System for Fault Diagnosis," *IEEE Trans. On Power Systems*, Aug. 1988, pp. 641-646.

[50] A. A. Girgis and M. B. Johns, "A Hybrid Expert System for Faulted Section Identification, Fault Type Classification, and Selection of Fault Location Algorithms," *IEEE Trans. On Power Delivery*, April 1989, pp. 978-985.

[51] K. Srinivasan and A. St. Jacques, "A New Fault Location Algorithm for Radial Transmission Lines Loads," *IEEE Trans. On Power Delivery*, July 1989, pp. 1676-1682.

[52] F. N. Chowdhury, J. P. Christensen, and J. L. Aravena, "Power System Fault Detection and State Estimation Using Kalman Filter with Hypothesis Testing," *IEEE Trans. On Power Delivery*, July 1991, pp. 1025-1030.

[53] F. Eickoff, E. Handschin, and W. Hoffman, "Knowledge Based Alarm and Fault Location in Distribution Networks," *IEEE Trans. On Power Systems*, May 1992, pp. 770-776.

[54] O. L. Wills, "A Review of Fault Locating Technique in Medium Voltage Power Cable," *IEEE Trans. On Electrical Insulation*, vol. 26, no.9, Jan. 1991, pp. 225-228.

[55] P. F. Gale, "A New Fault Location Technique for Power Cable," PhD Thesis, University of Bradford, U.K, Aug. 1974.

[56] H. R. Gnerlich, "Fault Locating: What's Effect on the Cable," *Electrical World*, vol. 204, no.6, June 1990, Supplement Section, pp. S-6.

[57] G. B. Ancell, and N. C. Pahalawaththa, "Effects of Frequency Dependence and Line Parameters on Single-phase Ended Traveling Wave Based Fault Location", *IEE Proceedings-C*, Vol. 139, No. 4, pp.332-342, July 1992.

[58] M. Komoda and M. Aihara, "Development of a Current Detection Type Cable Fault Locator," *IEEE Trans. on Power Delivery*, Vol.6, No.2, pp.541-545, April 1991.

[59] F. H. Magnago, and A. Abur, "Fault Location Using Wavelets", *IEEE Trans. on Power Delivery*, Vol. 13, No. 4, pp.1475-1480, Oct. 1998.

[60] K. K. Kuan, and K. Warwick, "Real -time Expert System for Fault Location on High Voltage Underground Distribution Cables", *IEE Proceedings-C*, Vol. 139, N0. 3, pp.235-240, May 1992.

[61] J. P. Steiner, W. L. Weeks, and H. W. Ng, "An Automated Fault Locating System," *IEEE Trans. on Power Delivery*, Vol. 7, No. 2, pp. 967-978, April 1992.

[62] W. E. Anderson, J. D. Ramboz, and A. R. Ondrejka, "The Detection of Incipient Faults in Transmission Cables Using Time Domain Reflectometry Techniques: Technical Challenges," IEEE Trans. on Power Apparatus and Systems, Vol. PAS-101, No. 7, pp.1928-1934, July 1982.

[63] H. T. Gooding, "Cable Fault Location on Power Systems," *Proc. of IEE*, Vol. 113, No. 1, pp. 111-120, Jan. 1966.

[64] K. Kato and et al, "Distribution Automation Systems for High Quality Power," *IEEE Trans. on Power Delivery*, pp.1196-1203, July 1991.

[65] P. F. Gale, "Cable -Fault Location by Impulse Current Method," *Proc. IEE*, vol.122, no.4, April 1975, pp.403-408.

[66] E. W. Bungay, and D. McAllister, Electric Cables Handbook, 2nd Ed., Blackwell Science, 1995.

[67] C. J. Kim, B. D. Russell, " High Impedance Fault Detection System Using an Adaptive Element Model," *IEE Proceedings-C*, Vol. 140, No. 2, March 1993, pp. 153-159.

[68] D. C. Yu, S. H. Khan, " An Adaptive High and Low Impedance fault Detection Method," *IEEE Trans. On Power Delivery*, Vol. 9, No. 4, October 1994, pp. 1812-1820.

[69] "Detection of Arcing Faults on Distribution Feeders," EPRI Final Report (prepared by Texas A&M University), *EPRI EL-2757*, 1982.

[70] C. Benner, P. Carswell, and B. D. Russell, "Improved Algorithm for Detecting Arcing Faults Using Random Fault Behavior," *Electr,. Power Syst. Res.*, Vol. 17, 1989, pp. 49-56.

[71] "High Impedance Fault Detection Using Third Harmonic Current," EPRI Final Report (prepared by Hughes Aircraft Co.), *EPRI EL-2430*, 1982.

[72] "Detection of High Impedance Faults," EPRI Final Report (prepared by Power Technologies, Inc.), *EPRI EL-2413*, 1982.

[73] C. J. Kim, and B. D. Russell, " Harmonic Behavior During Arcing Faults on Power Distribution Feeders," *Electr. Power Syst. Res.*, Vol. 14, 1988, pp. 219-225.

[74] D. H. Staelin, A. W. Morgenthaler, and J. A. Kong, Electromagnetic Waves, Prentice-Hall, 1994.

[75] R. Balakrishnan and A. Pahwa, "A Computer Assisted Intelligent Storm Outage Evaluator for Power Distribution Systems," *IEEE Trans. on Power Delivery*, pp. 1591-1597, July 1990.

[76] R. F. Wolff, "Automatic Storm Data to Cut Outage Time," *Electrical World*, pp. 93-94, November 1981.

[77] Y. Hsu and et al, " An Expert System for Locating Distribution Systems Faults," *IEEE Trans. on Power Delivery*, pp. 366-372, Jan. 1991.

[78] R. Polikar," The Wavelet Tutorial," ***http://engineering.rowan.edu/~polikar/wavelets/.***